DTU Library

Studies of coherent lamentary structures in magnetically conned plasmas

Olsen, Jeppe Miki Busk

Publication date:
2018

Document Version
Publisher's PDF, also known as Version of record

[Link back to DTU Orbit](#)

Citation (APA):
Olsen, J. M. B. (2018). Studies of coherent lamentary structures in magnetically conned plasmas. Lyngby, Denmark: Technical University of Denmark (DTU).

Studies of coherent filamentary structures in magnetically confined plasmas

Thesis submitted for the degree of
Doctor of Philosophy

Department of Physics
Technical University of Denmark

DTU

Technical University of Denmark

Jeppe Miki Busk Olsen

Studies of coherent filamentary structures in magnetically confined plasmas

Supervisor:	Professor Jens Juul Rasmussen
Co-supervisors:	Senior scientist Anders Henry Nielsen Researcher Jens Madsen *Technical University of Denmark, Lyngby, Denmark*
Examiners:	Dr. Carlos Hidalgo *CIEMAT. Madrid, Spain* Dr. Nicola Vianello *Consorzio RFX, Padova, Italy*
Chairman:	Senior scientist Stefan Kragh Nielsen *Technical University of Denmark, Lyngby, Denmark*

Submitted to the Technical University of Denmark
on June 30th 2018.

Preface

This thesis has been carried out in accordance with the requirements for obtaining the PhD degree at the Technical University of Denmark (DTU). The research was conducted within the framework of the EUROfusion Consortium and has received funding by the Euratom research and training programme 2014-2018 under grant agreement No. 633053. The views and opinions expressed herein do not necessarily reflect those of the European Commission. The research described in this thesis was supervised by professor Jens Juul Rasmussen, senior scientist Anders Henry Nielsen and researcher Jens Madsen between the 1st of July 2015 and the 30th of June 2018. The majority of the work was carried out at DTU in the plasma physics and fusion energy (PPFE) group within the physics department. Seven months of external research stays were spent at the Max-Planck Institute for Plasma Physics (IPP) in Garching bei München, Germany.

I would sincerely like to thank my supervisors, Jens Juul Rasmussen, Anders Henry Nielsen and Jens Madsen for the guidance and support I have received throughout this entire project. It has been a great help always being able to knock on their door when issues arose, and their great expertise within the field of plasma physics has been both educational and inspiring.

I have been fortunate to share an office with many great colleagues with whom I've shared many laughs, Alexander Simon Thrysøe, Asger Schou Jacobsen, Aslak Sindbjerg Poulsen, Galina Avdeeva, Mads Givskov Senstius, Michael Løiten Magnussen and Søren Kjer Hansen. Thank you all for that.

I would also like to thank Aske Anguasak Busk Olsen, Matthias Wiesenberger, Jakob Gath, Alexander Simon Thrysøe and Silja Kaldan Back for proof-reading the manuscript.

Finally I would like to thank my family and friends for always supporting me. And last but not least I would like to thank my girlfriend, Silja Kaldan Back, for always believing in me, for always making me laugh and for being part of my life.

Abstract

Thermonuclear fusion has been proposed as a sustainable, clean and safe energy source to meet the energy demands of the future. There are, however, still several challenges that need to be overcome in order to realise a viable fusion power plant. One of the challenges are so-called coherent filaments or blobs. These filaments constitute a significant fraction of the transport of plasma towards the outer vessel walls of fusion relevant magnetic confinement devices. It is thus crucial for the realisation of a fusion power plant to gain a better understanding of such coherent filaments.

In this study the propagation of coherent plasma filaments is investigated by means of numerical simulations. The investigations are carried out using both a two-dimensional drift-fluid model which includes the effects of dynamic electron and ion temperatures, and a three-dimensional model derived from first principles, which excludes the effects of dynamic temperatures.

The results from the two-dimensional model reveal that the inclusion of dynamic temperatures has a significant impact on the propagation of blobs. Especially the inclusion of finite ion temperatures is found to strongly impact the blob propagation. Finite ion temperatures break the up-down symmetry seen for cold ions blobs and causes blobs to propagate faster and remain more coherent.

The results from the three-dimensional model reveals that dynamics along the magnetic field lines in a magnetic confinement device also influences the propagation of blobs. A connection to the so-called sheath causes blobs to rotate due to Boltzmann spinning. It is also found that the width of the blob fronts parallel to the magnetic field does not strongly influence the blob propagation, however the parallel extend of the blobs does have an effect. The blobs with larger parallel extend propagate faster than the smaller blobs and they are found to break into smaller fragments at the later stages of propagation. An effect that is not observed for smaller blobs.

Finally we investigate how the so-called scrape-off layer power fall-off length, λ_q, scales with a range of parameters. It is found that coherent structures significantly influence λ_q, and a simple scaling for how λ_q scales with the electron temperature and the safety factor is found. This scaling is found to compare well with experimental results.

Keywords: Coherent filaments, plasma blobs, drift-fluid equations, numerical modelling, scrape-off layer, power fall-off length

Resumé

Kernefusion er blevet foreslået som en vedvarende, ren og sikker energikilde til at imøde-komme fremtidens energibehov. Der er dog stadigvæk udfordringer, der skal overkommes før et fusionskraftværk kan realiseres. En udfordring er det, der kaldes kohærente stuk-turer eller blobs. Disse strukturer bidrager til en betydelig andel af transporten af plasma mod de ydre vægge på fusionsrelevante magnetisk indesluttende reaktorer. Det er derfor afgørende at få en bedre forståelse for disse kohærente strukturer for at kunne realisere et fusionskraftværk.

I denne afhandling bliver bevægelsen af kohærente plasmastrukturer undersøgt ved hjælp af numeriske simuleringer. Undersøgelserne bliver udført både med en todimensionel drift-fluid model, som inkluderer effekterne af dynamiske elektron og ion temperaturer, og med en tredimensionel model udledt fra første principper, som ikke indeholder effekterne af dynamiske temperaturer.

Resultaterne fra den todimensionelle model afslører at inklusionen af dynamiske temper-aturer har en betydelig effekt på hvordan blobs bevæger sig. Især inklusionen af endelige ion temperaturer viser sig at influere stærkt på hvordan blobs bevæger sig. Endelige ion temperaturer bryder op-ned symmetrien, der ses for blobs med kolde ioner, og forårsager at blobsene bevæger sig hurtigere og forblive mere sammenhængende.

Resultaterne fra den tredimensionelle model viser, at dynamikken langs magnetfeltlinierne i en magnetisk indesluttende reaktor også influerer på, hvordan blobs bevæger sig. En forbindelse til det såkaldte sheath forårsager, at blobs roterer grundet Boltzmann rotation. Det vises også, at bredden af fronterne af disse blobs i retningen parallelt med magnetfeltet ikke har nogen stor indflydelse på, hvordan blobs bevæger sig, men den parallelle længde af disse blobs har en indflydelse. Blobs, der er større i den parallelle retning bevæger sig hurtigere end de mindre blobs, og de større blobs deler sig ind i mindre dele i de senere faser af bevægelsen. En effekt der ikke ses for mindre blobs.

Endeligt undersøger vi, hvordan den såkaldte scrape-off layer power fall-off length, λ_q, skalerer med en række parametre. Undersøgelsen viser, at kohærente strukturer har stor indflydelse på λ_q, og en simpel skalering for, hvordan λ_q skalerer med elektron tempera-turen og den såkaldte safety factor, findes. Denne skalering viser sig at passe godt med eksperimentelle resultater.

Nøgleord: Kohærente strukturer, plasma blobs, drift-fluid ligninger, numerisk model-lering, scrape-off layer, power fall-off length

Contents

Chapter 1

Introduction

1.1 The energy problem

Since the beginning of the industrial revolution, the world has seen an almost exponential increase in energy consumption, and with continuously growing populations in Africa and Asia, this increase is expected to continue in the coming decades[1]. The main part of the energy production comes from fossil fuels in the form of oil, coal and natural gas, which all produce vast amounts of CO_2 leading to a greenhouse effect and thus global warming[2]. Despite the expectation that coal consumption is going to stagnate and that renewable energy sources are going to be the fastest growing energy sources, the renewables will not be able to cover the energy demand[1] as illustrated in fig. 1.1. Even if one was to

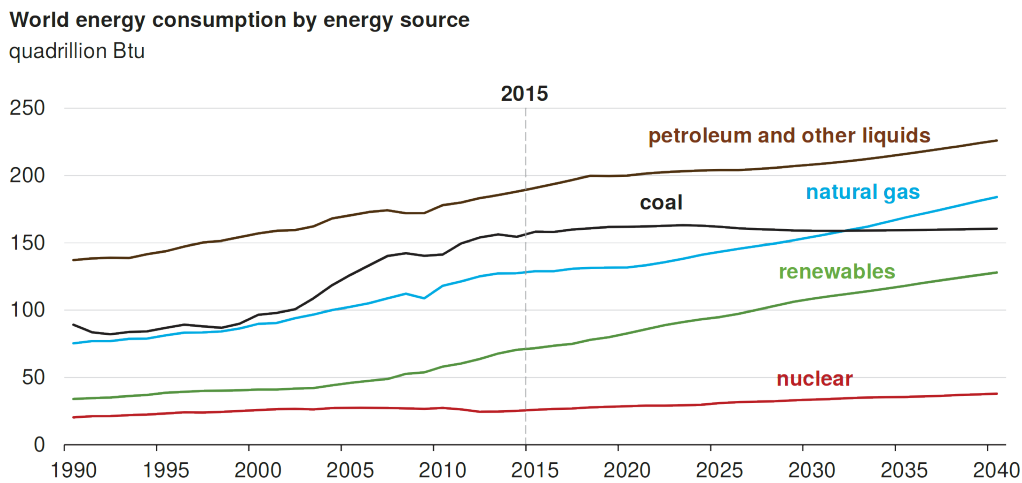Figure 1.1: Global energy consumption for different energy sources. The numbers from 1990-2015 are from statistical data, and from 2015-2040 are projections based on current models[1].

neglect the effects of CO_2 emission, fossil fuels are a limited resource, so it is clear that a new energy source is required to fulfil the future energy demand. One possible energy source is by using the process of nuclear fusion.

1.2 Nuclear fusion

Nuclear fusion is the process that takes place in the sun giving us the light and heat we experience here on earth. It occurs when light nuclei collide at temperatures high enough to overcome the Coulomb barrier and fuse together to create heavier elements. A small amount of mass is lost in this process and this mass is then converted to energy following Einstein's theory of relativity[3]

$$E = mc^2, \tag{1.1}$$

where m is the mass lost and c is the speed of light. This means that even a tiny amount of lost mass generates a large amount of energy relative to the mass lost. Fusion processes are in principle viable up to two lighter elements fusing into iron, which is the most stable element, but the most efficient reaction at low temperatures is the one of the hydrogen isotopes deuterium fusing with tritium to create helium and an excess neutron[4]

$$^{2}_{1}\text{H} +^{3}_{1}\text{H} \rightarrow^{4}_{2}\text{He} +^{1}_{0}\text{n}, \tag{1.2}$$

which generates 17.6 MeV of energy. In the reaction 3.5 MeV is stored in the helium nucleus and 14.1 MeV is in the neutron. The energetic neutrons can be harvested in a liquid blanket around a fusion reactor resulting in steam generation, which can drive turbines and thus generate electricity. To put the energy output of the deuterium-tritium fusion process into perspective, the energy output from just 1 g of reactants in this process is equivalent to the energy in 4 tonnes of oil[5]. Deuterium is abundant on earth, for every litre of seawater there is 0.033 g of deuterium. Tritium is not naturally occurring, since it is radioactive with a half-life of 12.5 years, but it can be bred from lithium, a common, abundant metal.

The advantages of nuclear fusion is, on top of the massive energy output, that the radioactive components generated by the energetic neutrons bombarding the vessel walls have a half-life short enough for the components to be considered safe after 50-100 years[6]. This is in sharp contrast to the half life of 700 million years of the uranium used in conventional fission nuclear power plants. Furthermore, runaway processes such as those seen in Chernobyl and Fukushima are not possible. The fusion reaction requires very specific controlled conditions to run and a fusion power plant will only contain small amounts of deuterium and tritium at a time. If the conditions are not met and the reactants are not continuously supplied, the fusion reactions stop[7].

In order for a fusion power plant to be viable, however, there a criteria which need to be fulfilled. One of the criteria is the so-called triple product, described in the following section.

1.2.1 The triple product

In order for a fusion power plant to be viable, it needs to produce more energy than it consumes. A criterion for such a power producing fusion reactor was derived by Lawson in 1956[8]. He states that the energy released per unit time per volume in a fusion reaction is

$$P_R = n_1 n_2 \overline{v\sigma}(T)E, \tag{1.3}$$

2

where n_1 and n_2 are the densities of the given species, $\overline{v\sigma}(T)$ is the averaged product of the relative velocity between the species and the reaction cross section, E is the energy released per reaction and T is the temperature. This value is largest when $n_1 = n_2 \equiv n/2$, where n is the total density, in which case we have

$$P_R = \frac{1}{4}n^2\overline{v\sigma}(T)E. \tag{1.4}$$

The energy loss per unit volume in a plasma is given by[9]

$$P_L = \frac{3\overline{nT}}{\tau_e}, \tag{1.5}$$

where $\overline{nT}$ is the average product of the density and the temperature of the plasma and τ_e is a characteristic energy loss time. The power loss needs to be balanced by the heating power, which can be supplied externally and in the case of deuterium-tritium, the heating can be supplied by the helium (alpha) particles created in the fusion process. As mentioned above, for every fusion reaction between deuterium and tritium, 14.1 MeV are stored in the neutron, which is difficult to confine, and 3.5 MeV is in the alpha particle, which can be confined using, e.g., magnetic fields. This alpha particle can then be used to heat up the deuterium and tritium. The heating power produced by alpha heating is given by

$$P_\alpha = \frac{1}{4}n^2\overline{v\sigma}(T)E_\alpha, \tag{1.6}$$

where E_α is the energy stored in the alpha particle in every fusion reaction, i.e., the 3.5 MeV. In order to have power balance we must have that

$$P_H + P_\alpha = P_L, \tag{1.7}$$

where P_H is the externally applied heating per unit volume. For the plasma to generate more energy than what is applied we need to have that

$$\frac{P_R}{P_H} = \frac{n^2\overline{v\sigma}(T)E}{4P_H} \equiv Q > 1. \tag{1.8}$$

For the fusion reaction to generate more power than it consumes it is theoretically enough that $Q > 1$. Ideally, however, after an initial start-up phase, the alpha heating could supply enough power for no external heating sources to be required, corresponding to $Q = \infty$, also known as ignition[9].

The heating power required to heat up the plasma is given by the power balance equation, eq. (1.7). This means that

$$P_H = P_L - P_\alpha = \frac{3}{\tau_e}\overline{nT} - \frac{1}{4}n^2\overline{v\sigma}(T)E_\alpha. \tag{1.9}$$

Using this expression, the ignition criterion, assuming constant n and T, becomes

$$0 > \frac{3}{\tau_e}T - \frac{1}{4}n\overline{v\sigma}(T)E_\alpha \Rightarrow n\tau_e > \frac{12}{\overline{v\sigma}(T)}\frac{T}{E_\alpha}. \tag{1.10}$$

Here $n\tau_e$ is only dependent on the temperature and can be plotted to find an optimum condition for ignition. For deuterium-tritium fusion this condition has a minimum at around $T = 30$ keV given by[9]

$$n\tau_e > 1.5 \times 10^{20}\text{m}^{-3}\text{s}. \tag{1.11}$$

However, τ_e itself is also a function of T. This means that the optimum condition for deuterium-tritium fusion is somewhat smaller than the $T = 30$ keV stated above, and it rather lies in the range $T = 10\text{-}20$ keV[9]. In this range, the cross-section can be estimated within 10% to be[9]

$$\overline{v\sigma}(T) = 1.1 \times 10^{-24}T^2\text{m}^3\text{s}^{-1}, \tag{1.12}$$

which leads to the ignition condition

$$n\tau_e T > 5 \times 10^{21}\text{m}^{-3}\text{keVs}, \tag{1.13}$$

where $n\tau_e T$ is called the triple product and is a general criterion that needs to be met for viable fusion power plants.

However, the 10-20 keV needed to fulfil the ignition condition correspond to approximately 100 mio.-200 mio.°C. No materials can withstand such temperatures, and instead alternative confinement methods need to be used. In the following section we discuss possible methods for confining the fusion reaction.

1.2.2 Magnetic confinement

In the previous section, we saw that the optimum condition for ignition was more than 100 mio.°C. At these temperatures, the fusion reactants become so hot that electrons are separated from ions creating what is called a plasma. Several approaches have been suggested for confining such a plasma, but so far the most promising confinement methods are by the use of magnetic fields. Since electrons and ions are separated in a plasma, the plasma will consist of a mix of charged particles. These charged particles can be confined to gyrating in orbits around magnetic field lines when a magnetic field is applied due to the Lorentz force

$$\mathbf{F}_{Lorentz} = q\left(\mathbf{E} + \mathbf{v} \times \mathbf{B}\right), \tag{1.14}$$

where q is the charge of the particle, $\mathbf{E}$ is the electric field, $\mathbf{v}$ is the velocity of the particle and $\mathbf{B}$ is the magnetic field. Many attempts for magnetic confinement devices have been attempted such as the Z-pinch[10] and magnetic mirror machines[11]. One of the issues with magnetic confinement devices, however, is how to close the magnetic field, since terminating the field lines at a vessel wall would lead to significant heat loads at that wall. A way to overcome this issue is by creating magnetic fields that close on themselves in a doughnut-like shape. This, however, creates the issue that near the inner boundary of the doughnut shape, the magnetic field coils are wound tighter than at the outer boundary, which causes the plasma particles to drift towards the outer wall when travelling along the magnetic field lines. This region at the inner wall is called the high-field side (HFS) while the outer region with further distance between the magnetic field coils is called the low-field side (LFS). To avoid the particles drifting to the outer wall, it is necessary to introduce a twist in the magnetic field so the particles shift between the

inner and outer wall region. So far, the two most successful magnetic confinement devices, the stellarator and the tokamak, create this twist in different ways. The stellarator does it by twisting the applied magnetic field with specially shaped external magnetic field coils and the tokamak does it by inducing a current in the plasma, which in turn creates a twisted magnetic field.

In the following sections, we briefly introduce the stellarator and the tokamak.

The Stellarator

The stellarator was developed in the post war era by Lyman Spitzer at Princeton university with the first prototype finished in 1951[12]. To create the required twist in the plasma, the stellarator uses specially designed magnetic field coils. This creates a winding magnetic field, which ensures that the charged particles alternate between the LFS and the HFS. The fact that all the confining magnetic fields are applied externally means that in theory, the stellarator could run continuously, whereas the tokamak, which uses induced currents, needs to operate in pulses. The lack of induced currents means that the stellarator does not risk current disruptions like tokamaks do. However, due to the twisting magnetic field, the stellarator has historically suffered from high diffusion and worse plasma confinement than tokamaks[13]. Furthermore, the construction of stellarators is notoriously difficult, where specially designed magnetic field coils need to be assembled with millimetre precision. This means that the majority of the fusion research in the last five decades has been focused on tokamaks. Recently, however, there has been an increased interest in stellarators due to the promising results of Wendelstein 7-X (see fig. 1.2) and other recent stellarators designed and optimised using computer models.
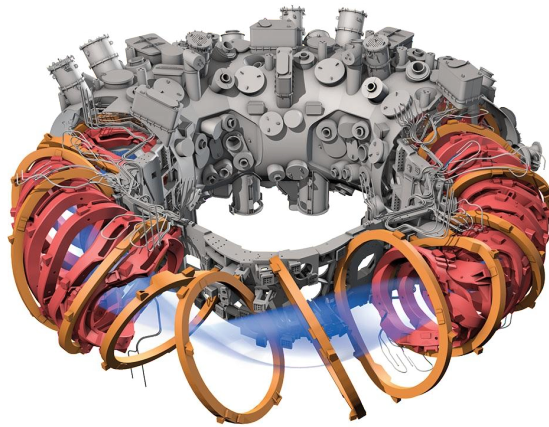
Figure 1.2: A 3D rendered image of the W7-X stellarator. Image from [13].

The Tokamak

The approach to solving the issue with particles drifting radially towards the outer wall at the LFS in a tokamak is quite different from the stellarators. Instead of carefully designing each magnet, the doughnut shape is retained in the tokamak and a solenoid is placed in the centre of the doughnut which induces a current in the plasma. The induced

current generates a magnetic field in the poloidal (axisymmetric) direction. The concept, which is illustrated in fig. 1.3, was evolved in the 1950's in the Soviet Union, and the design showed much better results than any other designs at the time[14]. The success of the tokamak has resulted in most fusion experiments built since the 1970's being based on the tokamak design, culminating in the ITER tokamak currently being built in Cadarache in France, which is designed to reach $Q = 10$.

Modern tokamaks operate with two regions, one with closed magnetic field lines known as the core region and one with open magnetic field lines known as the scrape-off layer (SOL), where the magnetic field lines terminate on a so-called divertor. The divertor is designed to withstand the heat loads of the plasma exhausted from the core region across the last closed flux surface (LFCS) into the SOL. The drawbacks of the tokamak
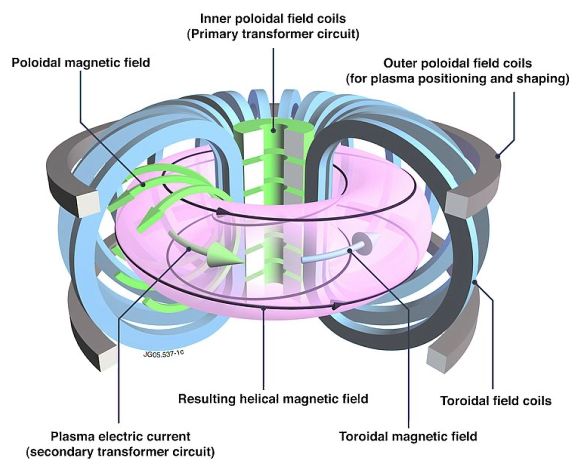
Figure 1.3: An illustration of the tokamak design. Image from [15].

is that due to the induced current, it needs to be pulsed and can be subject to current disruptions, which result in large magnetic forces on the reactor and massive heat loads reaching the outer wall of the vessel. However, the first large stellarator was not built until 1998 and the tokamak design has shown promising results over the last many decades, so the tokamak is still the main focus of the fusion community[16], and it is therefore this design we will focus on in this thesis.

1.2.3 Plasma filaments

The application of a strong magnetic field is a way to confine the 100 mio.°C hot plasma in fusion reactors. However, the application of a magnetic field to a plasma consisting of both ions and electrons causes the oppositely charged particles to drift in opposite directions. This causes a charge separation in the region of open magnetic field lines, inducing an electric field, which in turn can cause a collection of plasma particles to drift towards the outer wall of the vessel. This collection of plasma is known as coherent plasma filaments or blobs (see fig. 1.4 for an image of such filaments in the MAST tokamak). It turns out that these filaments significantly contribute to the particle flux towards the outer vessel wall, and studies[17, 18, 19] have shown that a significant fraction of the transport across the LCFS into the SOL can be attributed to intermittent transport in the form of blobs.
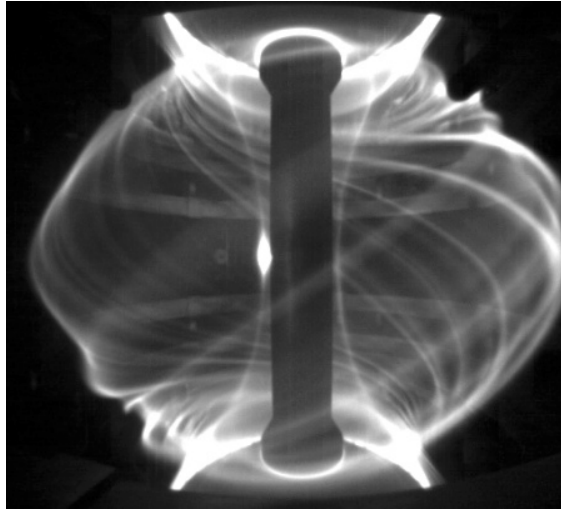
Figure 1.4: Image from the Mega Ampere Spherical Tokamak (MAST). Field aligned plasma filaments (blobs) are clearly visible as the elongated stripes of light in the image. Image from [23]

They are generated in the so-called edge region, the region between open and closed field lines in a tokamak and propagate toward the outer wall at high speeds. If the blobs reach the main chamber wall they can lead to erosion, causing sputtering and thus impurities in the plasma, which in the worst case scenario can lead to disruptions[20]. It is therefore crucial to gain an understanding of these filaments, how they are generated and how they propagate in the SOL. However, filaments do not only propagate towards the outer vessel wall in a direction perpendicular to the applied magnetic field. Blobs are field-aligned structures as is seen in fig. 1.4, and they thus also contribute to the transport of plasma parallel to the magnetic field. A measure for this parallel transport is the so-called SOL power fall-off length, denoted as λ_q. This parameter is the radial width of the channel transporting plasma towards the divertor[21] and knowing this parameter is essential if a fusion power plant is to be realised. If this radial width is too narrow, the heat loads reaching the divertor will exceed the material limits causing the divertor to fail[22].

The significance of these plasma filaments both in the direction parallel and perpendicular to the magnetic field means that it is crucial to gain a better understanding of them if a fusion power plant is to be realised. There are two ways one can investigate such plasma filaments, namely by doing experiments and by means of numerical simulations. However, in typical fusion grade plasma experiments, the high temperatures of the plasma makes measurements difficult and diagnostics are often subject to large uncertainties. Furthermore, experiments are expensive to conduct, so a way to gain a better understanding of filamentary transport without doing expensive experiments is by simulating the plasma filaments using numerical models. The advantage of this approach is that all plasma parameters are known exactly in the simulations and the individual effects of each parameter can be determined. This thesis therefore sets out to study plasma filaments by means of numerical simulations. The effects of electron and ion temperature dynamics on blobs are investigated as well as how their radial velocity scales with different parameters. The effects of three-dimensional dynamics are briefly addressed and finally a study of how the scrape-off layer power fall-off length scales with different parameters is carried out.

1.3 Outline of thesis

The work presented in this thesis concerns a wide range of studies concerning filamentary structures. Both effects concerning blobs in a two-dimensional and in a three-dimensional geometry are investigated. These investigation include how blobs are influenced by the inclusion of dynamic temperatures, how different initial parameters influence the maximum centre of mass velocity of the blobs as well as how three-dimensional dynamics influence blob propagation. The investigations are carried out using the so-called HESEL model[24, 25] and a model derived from first principles to include three-dimensional effects. Finally a study of how the scrape-off layer power fall-off length scales with a range of parameters is investigated. We believe that the results presented in this thesis contribute to a better understanding of how coherent filaments propagate in the scrape-off layer of magnetically confined plasmas and we believe that the results can act as a foundation for future investigations.

The outline of the thesis is as follows;

In chapter 2 we derive a theoretical model designed to simulate the three-dimensional effects on blob dynamics. In sec. 2.1 we present the geometry used in this thesis. In sec. 2.2 we present the so-called two-fluid equations, which act as the foundation for the derivation of the three-dimensional model. In sec. 2.3 we introduce a series of assumptions in order to derive a set of particle drifts expressed in terms of plasma parameters. In sec. 2.4 we derive the perpendicular components of the three-dimensional model. The parallel components of the model are derived in sec. 2.5, and finally the assumptions used and the three-dimensional model are recapped in sec. 2.6. In sec. 2.7 the two-dimensional HESEL model is described.

In chapter 3 the numerics used in this thesis are accounted for, starting in sec. 3.1 with a thorough description of the BOUT++ framework which is used to implement the 3D model derived in chapter 2. This description is followed in sec. 3.2 by a brief explanation of the numerical implementation of HESEL.

In chapter 4 the dynamics of plasma filaments in a two-dimensional geometry are investigated. In sec. 4.1 a recap of two papers which I have co-authored is presented. The papers concern multi code validations of two different plasma experiments, namely the TORPEX experiment and the MAST tokamak, where five different numerical models are compared with the experimental results. In sec. 4.2, the influence of temperature dynamics on blobs and the relation to velocity scaling laws is examined in a published article, on which I am main author.

Chapter 5 is dedicated to preliminary, unpublished work on numerical simulations of three-dimensional effects on plasma filaments. We start the chapter in sec. 5.1 with a description of the parameters used in the simulations as well as how the simulations are initialised. In sec. 5.2 we discuss the steady-state of the three-dimensional system, before we move on to investigate three-dimensional seeded blobs in sec. 5.3.

In chapter 6 we discuss the scrape-off layer power fall-off length, λ_q, in a published article on which I am main author. Specifically we discuss how λ_q scales with a series of different parameters and state the importance of intermittent transport when determining the width of the scrape-off layer power fall-off length.

Finally in chapter 7 the thesis is summarised and concluded and a discussion of future work and possible improvements is presented.

Chapter 2

Theory

In order to study coherent filaments in magnetically confined plasmas by means of numerical simulations, a set of equations are required. In this chapter we derive a self-consistent three-dimensional model based on first principles and briefly explain the HESEL model which is used to simulate plasma filaments in a two-dimensional slab geometry. Both the HESEL model and the derived 3D model are based on the Braginskii two-fluid equations and are designed to model plasmas in the edge and SOL region of a tokamak.

2.1   Coordinate system

Before deriving a set of equations, we define the geometry of the system we wish to solve. For simplicity we will restrain the analysis in this thesis to a slab at the out-board midplane of a tokamak as illustrated in fig. 2.1. The slab is indicated in red and is
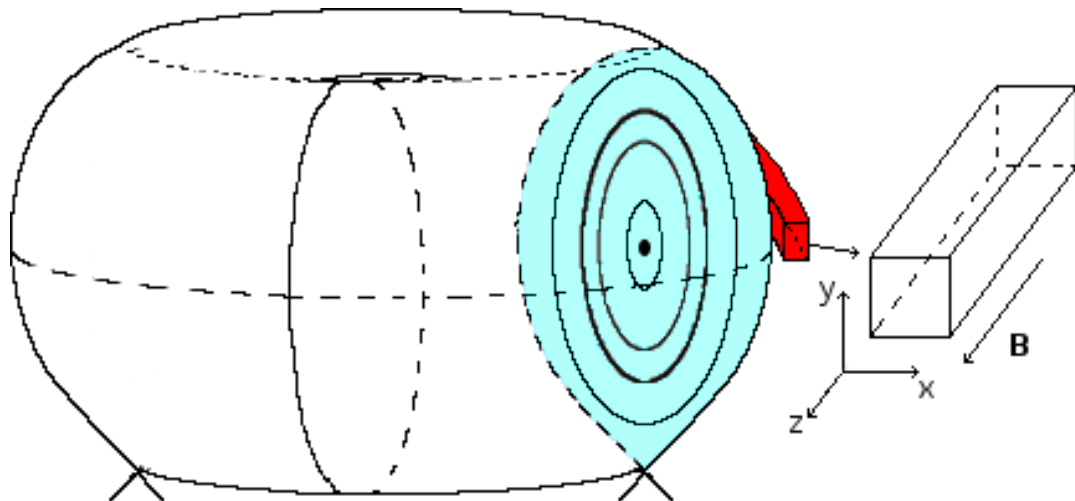

Figure 2.1: An illustration of the slab geometry used in this project. The slab is located just outside the region of closed field lines in the SOL at the out board mid-plane and follows the magnetic field lines from divertor to divertor. The coordinate system is as illustrated in the bottom right corner, and the magnetic field points in the positive z-direction.

located just outside the region of closed field lines. The slab follows the magnetic field from divertor to divertor with the coordinates as illustrated in the figure.

2.2 The two-fluid equations

With a coordinate system defined, we now move on to derive a simple set of equations to be used for investigating the propagation of a blob in three dimensions. We initially look at the so-called two-fluid equations[26], given by the continuity equation

$$\frac{\partial}{\partial t} n_\sigma + \nabla \cdot (n_\sigma \mathbf{u}_\sigma) = S_n, \tag{2.1}$$

and the momentum equation

$$n_\sigma m_\sigma \left(\frac{\partial}{\partial t} + \mathbf{u}_\sigma \cdot \nabla \right) \mathbf{u}_\sigma = n_\sigma q_\sigma \left(\mathbf{E} + \mathbf{u}_\sigma \times \mathbf{B} \right) - \nabla \cdot \overline{\overline{\mathbf{P}}}_\sigma - \mathbf{R}_{\sigma\alpha} - m_\sigma \mathbf{u}_\sigma S_n. \tag{2.2}$$

Here the subscript σ denotes a species, n_σ denotes the density, $\mathbf{u}_\sigma$ denotes the average velocity, m_σ denotes the mass, $\mathbf{E}$ is the electric field, $\mathbf{B}$ is the magnetic field and S_n denotes a particle source. The term $\overline{\overline{\mathbf{P}}}_\sigma$ is the pressure tensor. Following the approach in ref. [27], this can be divided into an isotropic part, $p_\sigma \overline{\overline{\mathbf{I}}}$, where $\overline{\overline{\mathbf{I}}}$ is the identity tensor, and an anisotropic part $\overline{\overline{\mathbf{\Pi}}}_\sigma$. The pressure tensor can then be expressed as

$$\overline{\overline{\mathbf{P}}}_\sigma = p_\sigma \overline{\overline{\mathbf{I}}} + \overline{\overline{\mathbf{\Pi}}}_\sigma, \tag{2.3}$$

where the isotropic pressure is given by the equation of state $p_\sigma = n_\sigma T_\sigma$ and T_σ is the temperature of species σ.

Finally $\mathbf{R}_{\sigma\alpha}$ is a momentum transfer term from species σ to species α, which consists of a part due to friction $\mathbf{R}_{u\sigma\alpha}$ and a part due to thermal forces $\mathbf{R}_{T\sigma\alpha}$ given by[27]

$$\mathbf{R}_{\sigma\alpha} = -\mathbf{R}_{\alpha\sigma} = \mathbf{R}_{u\sigma\alpha} + \mathbf{R}_{T\sigma\alpha}, \tag{2.4}$$

For charge number $Z = 1$ the friction force is given by[27]

$$\mathbf{R}_{u\sigma\alpha} = \nu_{\sigma\alpha} m_\sigma n_\sigma \left(0.51 \left(\mathbf{u}_{\sigma\parallel} - \mathbf{u}_{\alpha\parallel} \right) + \left(\mathbf{u}_{\sigma\perp} - \mathbf{u}_{\alpha\perp} \right) \right), \tag{2.5}$$

and the thermal force is given by[27]

$$\mathbf{R}_{T\sigma\alpha} = 0.71 n_\sigma \nabla_\parallel T_\sigma + \frac{3}{2} \frac{n_\sigma \nu_{\sigma\alpha}}{\omega_{c\sigma B}} \mathbf{b} \times \nabla T_\sigma, \tag{2.6}$$

where $\nu_{\sigma\alpha}$ is the collision frequency between species σ and α and $\omega_{c\sigma B} = |q_\sigma B / m_\sigma|$ is the species gyrofrequency, where B is the magnetic field. For simplicity we keep the notation $\mathbf{R}_{\sigma\alpha}$ and $\overline{\overline{\mathbf{P}}}_\sigma$ for now.

Due to the Lorentz force confining charged particles to magnetic field lines, the motion of charged particles is very different in the direction perpendicular and in the direction parallel to the applied magnetic field. It is therefore fruitful to split the velocity vector, the gradient operator and the electric field into components parallel and perpendicular

to the magnetic field, so $\mathbf{u}_\sigma = \mathbf{u}_{\sigma\perp} + \mathbf{u}_{\sigma\parallel}$, $\nabla = \nabla_\perp + \nabla_\parallel$ and $\mathbf{E} = \mathbf{E}_\perp + \mathbf{E}_\parallel$. Inserting this in the momentum equation, eq. (2.2), and splitting $\nabla \cdot \overline{\overline{\mathbf{P}}}_\sigma$ and $\mathbf{R}_{\sigma\alpha}$ we get

$$\left(\frac{\partial}{\partial t} + \left(\mathbf{u}_{\sigma\perp} + \mathbf{u}_{\sigma\parallel}\right) \cdot \left(\nabla_\perp + \nabla_\parallel\right)\right)\left(\mathbf{u}_{\sigma\perp} + \mathbf{u}_{\sigma\parallel}\right) = \frac{q_\sigma}{m_\sigma}\left(\mathbf{E}_\parallel + \mathbf{E}_\perp + \mathbf{u}_{\sigma\perp} \times \mathbf{B}\right)$$

$$- \frac{\left(\nabla \cdot \overline{\overline{\mathbf{P}}}_\sigma\right)_\perp}{n_\sigma m_\sigma} - \frac{\left(\nabla \cdot \overline{\overline{\mathbf{P}}}_\sigma\right)_\parallel}{n_\sigma m_\sigma} - \frac{\mathbf{R}_{\sigma\alpha\perp}}{n_\sigma m_\sigma}$$

$$- \frac{\mathbf{R}_{\sigma\alpha\parallel}}{n_\sigma m_\sigma} - \frac{\mathbf{u}_{\sigma\parallel}S_n}{n_\sigma} - \frac{\mathbf{u}_{\sigma\perp}S_n}{n_\sigma}. \qquad (2.7)$$

This equation can now be split into a parallel and perpendicular part by operator splitting. Assuming that the magnetic field direction does not vary, we get the perpendicular equation

$$\frac{\partial}{\partial t}\mathbf{u}_{\sigma\perp} + \left(\mathbf{u}_{\sigma\perp} \cdot \nabla_\perp\right)\mathbf{u}_{\sigma\perp} + \left(\mathbf{u}_{\sigma\parallel} \cdot \nabla_\parallel\right)\mathbf{u}_{\sigma\perp} = \frac{q_\sigma}{m_\sigma}\left(\mathbf{E}_\perp + \mathbf{u}_{\sigma\perp} \times \mathbf{B}\right) - \frac{\left(\nabla \cdot \overline{\overline{\mathbf{P}}}_\sigma\right)_\perp}{n_\sigma m_\sigma}$$

$$- \frac{\mathbf{R}_{\perp\sigma\alpha}}{n_\sigma m_\sigma} - \frac{\mathbf{u}_{\sigma\perp}S_n}{n_\sigma}, \qquad (2.8)$$

and the parallel equation

$$\frac{\partial}{\partial t}\mathbf{u}_{\sigma\parallel} + \left(\mathbf{u}_{\sigma\perp} \cdot \nabla_\perp\right)\mathbf{u}_{\sigma\parallel} + \left(\mathbf{u}_{\sigma\parallel} \cdot \nabla_\parallel\right)\mathbf{u}_{\sigma\parallel} = \frac{q_\sigma}{m_\sigma}\mathbf{E}_\parallel - \frac{\left(\nabla \cdot \overline{\overline{\mathbf{P}}}_\sigma\right)_\parallel}{n_\sigma m_\sigma} - \frac{\mathbf{R}_{\parallel\sigma\alpha}}{n_\sigma m_\sigma} - \frac{\mathbf{u}_{\sigma\parallel}S_n}{n_\sigma}. \qquad (2.9)$$

2.3 Drift ordering

The perpendicular velocity is difficult to interpret in terms of typical measurable plasma parameters and it is therefore fruitful to express the velocity in terms of known parameters. With this in mind, we expand $\mathbf{u}_{\sigma\perp}$. Before we do this, however, we emphasise that throughout this thesis, only hydrogen isotopes are considered, so the charge number is $Z = 1$.

In order to expand of $\mathbf{u}_\sigma$ we employ the so-called drift ordering[28, 29]. This ordering relies on assumptions about the orders of magnitude for the terms in the perpendicular equations. We therefore need some assumptions on the scales of time and length of the plasma. In this respect, we define a small parameter ϵ.

The first assumption is that we look at low frequency oscillations. Typical frequencies are thus

$$\frac{\partial}{\partial t} \propto \epsilon \ll \omega_{ci}, \qquad (2.10)$$

where $\omega_{ci} = eB_0/m_i$ is the ion gyrofrequency at constant magnetic field, e is the elementary charge, B_0 is the magnetic field at the out-board mid-plane and m_i is the ion mass. Next we assume that the plasma is weakly collisional, i.e.,

$$|\mathbf{R}_{\perp\sigma\alpha}| \propto \epsilon. \qquad (2.11)$$

We assume that the source is on the same order of magnitude as the perpendicular collisions, and we assume that the typical parallel and perpendicular gradient length scales, $1/L$, are of order ϵ,

$$S_n \propto \epsilon, \qquad \nabla_\perp \cdot \mathbf{u}_{\sigma\perp} \propto 1/L \propto \epsilon, \qquad \nabla_\parallel \cdot \mathbf{u}_{\sigma\perp} \propto 1/L \propto \epsilon. \tag{2.12}$$

Finally we assume that the source is located at the upper and lower boundaries in the parallel direction, which means that $\nabla_\perp S_n = 0$. Looking at eq. (2.3) and following the analysis conducted in ref. [27], we have that the isotropic part of the pressure tensor is of order $\epsilon^0 = 1$ and that the anisotropic viscosity tensor is of order ϵ

$$p_\sigma \bar{\bar{\mathbf{I}}} \propto 1, \qquad \bar{\bar{\mathbf{\Pi}}}_\sigma \propto \epsilon. \tag{2.13}$$

With this, we can now expand the perpendicular velocity using perturbation theory

$$\mathbf{u}_{\sigma\perp} = \mathbf{u}_{\sigma\perp 0} + \mathbf{u}_{\sigma\perp 1} + \mathbf{u}_{\sigma\perp 2} + ..., \tag{2.14}$$

where $\mathbf{u}_{\sigma\perp 0} \propto 1$, $\mathbf{u}_{\sigma\perp 1} \propto \epsilon$ and $\mathbf{u}_{\sigma\perp 2} \propto \epsilon^2$ and so on. We now derive expressions of order 1 and ϵ and neglect all higher order terms. This gives us the expressions[1]

$$\mathbf{u}_{\sigma\perp 0} = \mathbf{u}_E + \mathbf{u}_{d\sigma} \tag{2.15}$$

and

$$\mathbf{u}_{\sigma\perp 1} = \mathbf{u}_{p\sigma} + \mathbf{u}_{\mathbf{\Pi}\sigma} + \mathbf{u}_{\nabla_\parallel \sigma} + \mathbf{u}_{S_n\sigma} + \mathbf{u}_{\mathbf{R}_{\sigma\alpha}}, \tag{2.16}$$

where we have defined the seven contributions to the perpendicular velocity in terms of measurable parameters:

$$\mathbf{u}_E = \frac{\mathbf{E}_\perp \times \mathbf{b}}{B} \tag{2.17}$$

$$\mathbf{u}_{d\sigma} = -\frac{\nabla_\perp p_\sigma \times \mathbf{b}}{q_\sigma n_\sigma B} \tag{2.18}$$

$$\mathbf{u}_{p\sigma} = \left(\frac{\partial}{\partial t} + \left[-\frac{\nabla_\perp p_\sigma \times \mathbf{B}}{q_\sigma n_\sigma B^2} + \frac{\mathbf{E}_\perp \times \mathbf{b}}{B} \right] \cdot \nabla_\perp \right) \left(-\frac{m_\sigma \nabla_\perp p_\sigma}{q_\sigma^2 n_\sigma B^2} + \frac{m_\sigma \mathbf{E}_\perp}{q_\sigma B^2} \right) \tag{2.19}$$

$$\mathbf{u}_{\mathbf{\Pi}\sigma} = -\frac{\left(\nabla \cdot \bar{\bar{\mathbf{\Pi}}}_\sigma \right)_\perp \times \mathbf{b}}{n_\sigma q_\sigma B} \tag{2.20}$$

$$\mathbf{u}_{\nabla_\parallel \sigma} = \left(\mathbf{u}_{\sigma\parallel} \cdot \nabla_\parallel \right) \left(-\frac{m_\sigma \nabla_\perp p_\sigma}{q_\sigma^2 n_\sigma B^2} + \frac{m_\sigma \mathbf{E}_\perp}{q_\sigma B^2} \right) \tag{2.21}$$

$$\mathbf{u}_{S_n\sigma} = \frac{S_n}{n_\sigma} \left(-\frac{m_\sigma \nabla_\perp p_\sigma}{q_\sigma^2 n_\sigma B^2} + \frac{m_\sigma \mathbf{E}_\perp}{q_\sigma B^2} \right) \tag{2.22}$$

$$\mathbf{u}_{\mathbf{R}_{\sigma\alpha}} = -\frac{\mathbf{R}_{\perp \sigma\alpha} \times \mathbf{b}}{n_\sigma q_\sigma B}. \tag{2.23}$$

In the above expressions we have defined the unit vector in the direction of the magnetic field $\mathbf{b} = \mathbf{B}/B$. The seven drifts are the $\mathbf{E} \times \mathbf{B}$ drift $\mathbf{u}_E$, the diamagnetic drift $\mathbf{u}_{d\sigma}$, the polarisation drift $\mathbf{u}_{p\sigma}$, the viscosity drift $\mathbf{u}_{\mathbf{\Pi}\sigma}$, the parallel gradient drift $\mathbf{u}_{\nabla_\parallel \sigma}$, the source

---

[1]see Appendix A.1 for the derivation

drift $\mathbf{u}_{S_n\sigma}$, and the resistive drift $\mathbf{u}_{R_{\sigma\alpha}}$. The perpendicular velocity to first order can then be expressed as

$$\mathbf{u}_{\sigma\perp} = \mathbf{u}_E + \mathbf{u}_{d\sigma} + \mathbf{u}_{p\sigma} + \mathbf{u}_{\mathbf{\Pi}\sigma} + \mathbf{u}_{\nabla_\parallel\sigma} + \mathbf{u}_{S_n\sigma} + \mathbf{u}_{\mathbf{R}_{\sigma\alpha}}. \tag{2.24}$$

This can be inserted in the continuity equation to get an expression for the evolution of the density in terms of measurable parameters. In eqs. (2.17) to (2.23), all expressions are expanded in terms of measurable parameters except for $\mathbf{u}_{\mathbf{R}\sigma\alpha}$ and $\mathbf{u}_{\mathbf{\Pi}\sigma}$. $\mathbf{u}_{\mathbf{R}\sigma\alpha}$ is evaluated in App. A.3.2 and, since the derivation of $\mathbf{u}_{\mathbf{\Pi}\sigma}$ is rather lengthy, this term is evaluated separately in App. A.2.

The drifts expressed above along with the parallel electron and ion velocities leave us with seven unknown parameters, assuming that the magnetic field is applied and known. There is n_σ, T_σ and $\mathbf{u}_{\sigma\parallel}$ for each species (ions and electrons), and there is the electric field, $\mathbf{E}$. This means that in order to solve the system, we need seven equations.

2.4 Perpendicular dynamics

To derive the model equations for the perpendicular components of the 3D system described in sec. 2.1, we now turn to the electron and ion continuity equations, starting at eq. (2.1).

2.4.1 Electron continuity equation

We start by looking at the electron continuity equation. Since the electron mass is very small compared to the ion mass, all terms involving m_e can be neglected. This means that we can express the perpendicular electron velocity to first order as

$$\mathbf{u}_{e\perp} = \mathbf{u}_E + \mathbf{u}_{de} + \mathbf{u}_{\mathbf{\Pi}e} + \mathbf{u}_{\mathbf{R}_{ei}}, \tag{2.25}$$

where we have assumed that the plasma is fully ionised, so only electron-ion collisions contribute to the drifts. This gives the electron continuity equation

$$\frac{\partial}{\partial t}n_e + \nabla_\parallel \cdot \left(n_e\mathbf{u}_{e\parallel}\right) + \nabla_\perp \cdot \left(n_e\left(\mathbf{u}_E + \mathbf{u}_{de} + \mathbf{u}_{\mathbf{\Pi}e} + \mathbf{u}_{\mathbf{R}ei}\right)\right) = S_n. \tag{2.26}$$

Assuming an electrostatic $\mathbf{E}$-field, $\mathbf{E} = -\nabla\phi$, we get[2].

$$\frac{\partial}{\partial t}n_e + \nabla_\parallel \cdot \left(n_e\mathbf{u}_{e\parallel}\right) + \mathbf{u}_E \cdot \nabla_\perp n_e + n_e\mathcal{K}(\phi) + \frac{\mathcal{K}(p_e)}{e}$$
$$= \frac{1}{m_e}\nabla_\perp \cdot \left(\frac{\nu_{ei}}{\omega_{ceB}^2}n_e\left(\frac{\nabla_\perp p_e}{n_e} + \frac{\nabla_\perp p_i}{n_i}\right) - \frac{3}{2}\frac{\nu_{ei}}{\omega_{ceB}^2}n_e\nabla_\perp T_e\right) + S_n. \tag{2.27}$$

where

$$\left(\nabla \times \frac{\mathbf{b}}{B}\right) \cdot \nabla_\perp f \equiv \mathcal{K}(f) \tag{2.28}$$

is the curvature operator, $\omega_{ceB} = eB/m_e$ is the electron gyrofrequency and m_e is the electron mass. However, the inclusion of electron temperature dynamics requires an

---

[2]See Appendix A.3 for the derivation

equation to solve for T_e, so to simplify the system for computational expediency we assume isothermal electrons. This means that we assume $T_e \equiv T_{e0}$ and $\nabla T_{e0} = \mathbf{0}$. With this assumption, defining the convective derivative $\partial/\partial t + \mathbf{u}_E \cdot \nabla \equiv \mathrm{d}/\mathrm{d}t$ and assuming that the collision frequencies are constant, $\nu_{ei} = \nu_{ei0}$ and $\nu_{ii} = \nu_{ii0}$, we get the electron continuity equation

$$
\frac{\mathrm{d}}{\mathrm{d}t}n_e + \nabla_\parallel \cdot \left(n_e \mathbf{u}_{e\parallel}\right) + n_e \mathcal{K}(\phi) + \frac{T_{e0}\mathcal{K}(n_e)}{e}
$$
$$
= \frac{\nu_{ei0}}{m_e}\nabla_\perp \cdot \left(\frac{1}{\omega_{ceB}^2}n_e \left(\frac{T_{e0}\nabla_\perp n_e}{n_e} + \frac{\nabla_\perp p_i}{n_i}\right)\right) + S_n, \tag{2.29}
$$

where we have used the equation of state $p_\sigma = n_\sigma T_\sigma$. Finally we note that the typical length scales of B in a tokamak is on the order of the major radius, R_0, which is usually on the order of a meter. The typical length scale of the ion and electron temperatures, the density and the potential, L, is smaller than the width of the SOL, which in conventional tokamaks is usually on the order of a few centimetres. This means that $|\nabla B| \ll 1/L$ and in turn $|\nabla B| \ll \epsilon$ and $|\nabla \omega_{ceB}| \ll \epsilon$. This means that we can neglect ∇B and $\nabla \omega_{ceB}$ and assume $\omega_{ceB} \approx \omega_{ce} = eB_0/m_e$. Inserting this and defining the electron gyroradius $\rho_{e0}^2 = \sqrt{T_{e0}/(m_e \omega_{ce^2})}$ we get the electron continuity equation

$$
\frac{\mathrm{d}^0}{\mathrm{d}t}n_e + \nabla_\parallel \cdot \left(n_e \mathbf{u}_{e\parallel}\right) + n_e \mathcal{K}(\phi) + \frac{T_{e0}\mathcal{K}(n_e)}{e}
$$
$$
= \frac{\nu_{ei0}\rho_{e0}^2}{T_{e0}}\nabla_\perp \cdot \left(n_e \left(\frac{T_{e0}\nabla_\perp n_e}{n_e} + \frac{\nabla_\perp p_i}{n_i}\right)\right) + S_n, \tag{2.30}
$$

where $\mathrm{d}^0/\mathrm{d}t = \partial/\partial t + \mathbf{u}_E^0 \cdot \nabla$ and $\mathbf{u}_E^0$ is the $\mathbf{E} \times \mathbf{B}$ velocity evaluated at $B = B_0$.

2.4.2 Ion continuity equation

For the ions we include all perpendicular drifts. The perpendicular ion velocity is then given by

$$
\mathbf{u}_{i\perp} = \mathbf{u}_E + \mathbf{u}_{di} + \mathbf{u}_{pi} + \mathbf{u}_{\Pi i} + \mathbf{u}_{\nabla_\parallel i} + \mathbf{u}_{S_n i} + \mathbf{u}_{\mathbf{R}ie}. \tag{2.31}
$$

This gives the ion continuity equation

$$
\frac{\partial}{\partial t}n_i + \nabla_\parallel \cdot \left(n_i \mathbf{u}_{i\parallel}\right) + \nabla_\perp \cdot \left(n_i \left(\mathbf{u}_E + \mathbf{u}_{di} + \mathbf{u}_{pi} + \mathbf{u}_{\Pi i} + \mathbf{u}_{\nabla_\parallel i} + \mathbf{u}_{S_n i} + \mathbf{u}_{\mathbf{R}ie}\right)\right) = S_n. \tag{2.32}
$$

Using the assumptions stated in the derivation of the electron continuity equation, we can get an expression for the ion continuity equation in terms of the parameters we wish

to model[3]

$$\frac{d^0}{dt}n_i + \nabla_\parallel \cdot (n_i \mathbf{u}_{i\parallel}) + n_i \mathcal{K}(\phi) + \frac{\mathcal{K}(p_i)}{e} - \frac{S_n}{\omega_{ci}B}\nabla_\perp \cdot \left(\frac{\nabla_\perp p_i}{en_i} + \nabla_\perp \phi\right)$$

$$- \frac{\rho_{e0}^2 \nu_{ei0}}{T_{e0}}\nabla_\perp \cdot \left(n_e \left(\frac{T_{e0}\nabla_\perp n_e}{n_e} + \frac{\nabla_\perp p_i}{n_i}\right)\right)$$

$$- \frac{1}{\omega_{ci}B}\nabla_\perp \cdot \left(n_i \left(\mathbf{u}_{i\parallel} \cdot \nabla_\parallel\right)\left(\frac{\nabla_\perp p_i}{en_i} + \nabla_\perp \phi\right)\right) - \frac{\mathcal{K}(p_i)}{e\omega_{ci}B}\nabla_\perp \cdot \left(\frac{\nabla_\perp p_i}{en_i} + \nabla_\perp \phi\right)$$

$$- \frac{1}{\omega_{ci}B}\nabla_\perp \cdot \left(n_i \left(\partial_t + \mathbf{u}_E^0 \cdot \nabla_\perp\right)\left(\frac{\nabla_\perp p_i}{en_i} + \nabla_\perp \phi\right)\right)$$

$$+ \nabla_\perp \cdot (n_i (\mathbf{u}_{pid} + \mathbf{u}_{\Pi iFLR})) + \nabla_\perp \cdot (n_i \mathbf{u}_{\Pi i\nu}) = S_n, \tag{2.33}$$

where the last two terms are defined in eq. (A.19) and (A.15), respectively. This is a rather lengthy equation and in order to simplify it for future calculations we make further assumptions.

The next assumption we make is also mainly done for computational expediency. We assume that the ions are cold, so $T_i = 0$, which is usually not the case in a tokamak SOL, where T_i is usually greater than T_e[30, 31]. However, this assumption significantly simplifies the calculations and still allows us to investigate the effects of parallel dynamics on filament evolution. The assumption leaves us with the ion continuity equation

$$\frac{d^0}{dt}n_i + \nabla_\parallel \cdot (n_i \mathbf{u}_{i\parallel}) + n_i \mathcal{K}(\phi) - \frac{S_n}{\omega_{ci}B}\nabla_\perp^2 \phi - \rho_{e0}^2 \nu_{ei0}\nabla_\perp^2 n_e$$

$$- \frac{1}{\omega_{ci}B}\nabla_\perp \cdot \left(n_i \left(\partial_t + \mathbf{u}_E^0 \cdot \nabla_\perp\right)\nabla_\perp \phi\right) - \frac{1}{\omega_{ci}B}\nabla_\perp \cdot \left(n_i \left(\mathbf{u}_{i\parallel} \cdot \nabla_\parallel\right)\nabla_\perp \phi\right) = S_n. \tag{2.34}$$

With the ion and electron continuity equations, we have two equations, where seven were initially required. However, with the assumptions of isothermal electrons and cold ions only five equations are now needed to solve for the unknown parameters n_i, n_e, $\mathbf{u}_{e\parallel}$, $\mathbf{u}_{i\parallel}$ and ϕ.

2.4.3 Vorticity equation

With expressions for the evolution of n_i and n_e at hand, we now turn to obtain an expression for ϕ. In a plasma we have that $n_i = n_e \equiv n$ on length scales larger than the Debye length $\lambda_D = \sqrt{\epsilon_0 T_{e0}/en}$[32], where ϵ_0 is the vacuum permittivity. In a tokamak plasma, λ_D is usually on the order of 10^{-4} m, which is much smaller than the length scales we wish to model. This means that we can assume $n_i = n_e \equiv n$ and subtract the ion continuity equation from the electron continuity equation;

$$\nabla_\parallel \cdot \left(n(\mathbf{u}_{e\parallel} - \mathbf{u}_{i\parallel})\right) - T_{e0}\frac{\mathcal{K}(n)}{e} + \frac{S_n}{\omega_{c_i}B}\nabla_\perp^2 \phi - \frac{1}{\omega_{ci}B}\nabla_\perp \cdot \left(n \left(\partial_t + \mathbf{u}_E^0 \cdot \nabla_\perp\right)\nabla_\perp \phi\right)$$

$$- \frac{1}{\omega_{ci}B}\nabla_\perp \cdot \left(n \left(\mathbf{u}_{i\parallel} \cdot \nabla_\parallel\right)\nabla_\perp \phi\right) = 0. \tag{2.35}$$

---

[3]See Appendix A.4 for the derivation

In principle this expression gives us an equation for ϕ. However, it is difficult to solve for ϕ in this equation, so to simplify the equations even further, we again use an assumption that may not be justified in tokamak plasmas, but significantly reduces the computation times needed to solve the system. The assumption is the so-called thin-layer approximation[24], where it is assumed that $|\nabla_\perp n| \ll 1/L$. This is generally not the case in tokamak plasmas, and the assumption is rather unjustified, but is used for computational expediency. Although the use of the local approximation has been shown to influence the plasma dynamics[33, 34], the differences were not catastrophic and the model derived here can still shed light on the dynamics of coherent plasma filaments. Neglecting terms of $\nabla_\perp n$ we get the so-called vorticity equation

$$\frac{\mathrm{d}^0}{\mathrm{d}t}\nabla_\perp^2\phi = -\left(\mathbf{u}_{i\parallel}\cdot\nabla_\parallel\right)\nabla_\perp^2\phi + \frac{\omega_{ci}B}{n}\nabla_\parallel\cdot\left(n\left(\mathbf{u}_{i\parallel}-\mathbf{u}_{e\parallel}\right)\right) + T_{e0}\frac{\omega_{ci}B}{n}\frac{\mathcal{K}(n)}{e}$$
$$- \frac{S_n}{n}\nabla_\perp^2\phi - \left(\nabla_\perp\left(\mathbf{u}_{i\parallel}\cdot\nabla_\parallel\right)\right)\cdot\nabla_\perp\phi. \tag{2.36}$$

Finally we assume that all cross-terms, i.e., terms of the form $\partial_x f \partial_z g$, are small, which leads to the vorticity equation

$$\frac{\mathrm{d}}{\mathrm{d}t}\nabla_\perp^2\phi = -\left(\mathbf{u}_{i\parallel}\cdot\nabla_\parallel\right)\nabla_\perp^2\phi + \frac{\omega_{ci}B}{n}\nabla_\parallel\cdot\left(n\left(\mathbf{u}_{i\parallel}-\mathbf{u}_{e\parallel}\right)\right) + T_{e0}\frac{\omega_{ci}B}{n}\frac{\mathcal{K}(n)}{e} - \frac{S_n}{n}\nabla_\perp^2\phi. \tag{2.37}$$

With an equation for the electron density and an equation for the potential we now have two equations, one for n and one for ϕ. However, the assumption of quasineutrality has left us with only four unknown parameters, n, ϕ, $\mathbf{u}_{e\parallel}$ and $\mathbf{u}_{i\parallel}$. This means that we still need to determine equations for $\mathbf{u}_{e\parallel}$ and $\mathbf{u}_{i\parallel}$, but before moving on to determine equations for the parallel dynamics of the system, we normalise the density and vorticity equations.

2.4.4 Normalisation

In normal tokamak plasmas all fields are on very different scales, so in order to get values close to unity to be able to solve the system numerically, we normalise the equations with a typical reference value. In this regard we invoke the so-called gyro-Bohm normalisation[24];

$$\omega_{ci}t = \tilde{t}, \qquad \frac{\mathbf{x}}{\rho_s} = \tilde{\mathbf{x}}, \qquad \frac{e\phi}{T_{e0}} = \varphi, \qquad \frac{n}{n_0} = \tilde{n}, \qquad \frac{\mathbf{u}_{i\parallel}}{c_{s0}} = \tilde{\mathbf{u}}_{i\parallel}, \qquad \frac{\mathbf{u}_{e\parallel}}{c_{s0}} = \tilde{\mathbf{u}}_{e\parallel}, \quad (2.38)$$

where $\omega_{ci} = eB_0/m_i$ is the ion gyrofrequency at constant magnetic field, $c_{s0} = \sqrt{T_{e0}/m_i}$ is the cold ion sound speed at reference electron temperature, $\rho_s = c_{s0}/\omega_{ci}$ is the ion gyroradius at reference electron temperature, and n_0 is a reference particle density.

Inserting the normalised parameters and using the assumptions stated in sec. 2.4.2 and 2.4.3 in the electron continuity equation, eq. (2.26), gives

$$n_0\omega_{ci}\frac{\mathrm{d}}{\mathrm{d}\tilde{t}}\tilde{n} + \frac{n_0 c_{s0}}{\rho_s}\tilde{\nabla}\cdot\left(\tilde{n}\tilde{\mathbf{u}}_{e\parallel}\right) + \frac{n_0 T_{e0}}{eB_0\rho_s^2}\tilde{n}\tilde{\mathcal{K}}\left(\varphi\right) - \frac{n_0 T_{e0}\tilde{\mathcal{K}}(\tilde{n})}{eB_0\rho_s^2} = \frac{n_0\nu_{ei0}\rho_{e0}^2}{\rho_s^2}\tilde{\nabla}_\perp^2\tilde{n} + S_n$$

$$\Rightarrow \omega_{ci}\frac{\mathrm{d}}{\mathrm{d}\tilde{t}}\tilde{n} + \omega_{ci}\tilde{\nabla}\cdot\left(\tilde{n}\tilde{\mathbf{u}}_{e\parallel}\right) + \frac{T_{e0}\omega_{ci}}{eB_0\rho_s^2}\tilde{n}\tilde{\mathcal{K}}\left(\varphi\right) - \frac{T_{e0}\omega_{ci}}{eB_0\rho_s^2}\omega_{ci}\tilde{\mathcal{K}}(\tilde{n}) = \frac{\nu_{ei0}\rho_{e0}^2}{\rho_s^2}\tilde{\nabla}_\perp^2\tilde{n} + \frac{S_n}{n_0}$$

$$\Rightarrow \frac{\mathrm{d}}{\mathrm{d}\tilde{t}}\tilde{n} + \tilde{\nabla}\cdot\left(\tilde{n}\tilde{\mathbf{u}}_{e\parallel}\right) + \tilde{n}\tilde{\mathcal{K}}\left(\varphi\right) - \tilde{\mathcal{K}}(\tilde{n}) = \frac{\nu_{ei0}\rho_{e0}^2}{\omega_{ci}\rho_s^2}\tilde{\nabla}_\perp^2\tilde{n} + \frac{S_n}{\omega_{ci}n_0}.$$

We now define the normalised diffusion coefficient,

$$D_n = \frac{\nu_{ei0}\rho_{e0}^2}{\omega_{ci}\rho_s^2}, \tag{2.39}$$

and the normalised source term

$$\tilde{S}_n = \frac{S_n}{\omega_{ci}n_0} \tag{2.40}$$

for future use. Finally, assuming that we have a magnetic field that only varies in the radial direction, given by $\mathbf{B} = (B_0 R_0/R)\mathbf{b}$, where $R = R_0 + a + x$ with R_0 being the major radius, a being the distance from R_0 to the LCFS and x being the distance from the LCFS to a given point in the SOL, we have

$$\mathcal{K}(f) = \left(\nabla \times \frac{\mathbf{b}}{B}\right) \cdot \nabla_\perp f = -\left(\frac{\partial}{\partial x}\frac{1}{B}\right)\frac{\partial}{\partial y}f = -\frac{1}{R_0 B_0}\frac{\partial}{\partial y}f, \tag{2.41}$$

which finally leads to the normalised electron continuity equation

$$\frac{\mathrm{d}}{\mathrm{d}\tilde{t}}\tilde{n} + \tilde{\nabla}\cdot\left(\tilde{n}\tilde{\mathbf{u}}_{e\parallel}\right) - \frac{\rho_s}{R_0}\tilde{n}\frac{\partial}{\partial\tilde{y}}\varphi + \frac{\rho_s}{R_0}\frac{\partial}{\partial\tilde{y}}\tilde{n} = D_n\tilde{\nabla}_\perp^2\tilde{n} + \tilde{S}_n. \tag{2.42}$$

Next we normalise the vorticity equation, eq. (2.37),

$$\frac{\omega_{ci}T_{e0}}{e\rho_s^2}\frac{\mathrm{d}}{\mathrm{d}\tilde{t}}\tilde{\nabla}_\perp^2\varphi = -\frac{c_{s0}T_{e0}}{e\rho_s^3}\left(\tilde{\mathbf{u}}_{i\parallel}\cdot\tilde{\nabla}_\parallel\right)\tilde{\nabla}_\perp^2\varphi + \frac{c_{s0}\omega_{ci}\tilde{B}B_0}{\rho_s\tilde{n}}\tilde{\nabla}_\parallel\cdot\left(\tilde{n}\left(\tilde{\mathbf{u}}_{i\parallel} - \tilde{\mathbf{u}}_{e\parallel}\right)\right)$$

$$+ \frac{T_{e0}\omega_{ci}\tilde{B}B_0}{B_0\rho_s^2\tilde{n}}\frac{\tilde{\mathcal{K}}(\tilde{n})}{e} - \frac{T_{e0}S_n}{en_0\rho_s^2\tilde{n}}\tilde{\nabla}_\perp^2\varphi$$

$$\Rightarrow \frac{\mathrm{d}}{\mathrm{d}\tilde{t}}\tilde{\nabla}_\perp^2\varphi = -\left(\tilde{\mathbf{u}}_{i\parallel}\cdot\tilde{\nabla}_\parallel\right)\tilde{\nabla}_\perp^2\varphi + \frac{\tilde{B}}{\tilde{n}}\tilde{\nabla}_\parallel\cdot\left(\tilde{n}\left(\tilde{\mathbf{u}}_{i\parallel} - \tilde{\mathbf{u}}_{e\parallel}\right)\right) + \frac{B_0\tilde{B}}{\tilde{n}}\tilde{\mathcal{K}}(\tilde{n}) - \frac{S_n}{\omega_{ci}n_0\tilde{n}}\tilde{\nabla}_\perp^2\varphi$$

$$\Rightarrow \frac{\mathrm{d}}{\mathrm{d}\tilde{t}}\tilde{\nabla}_\perp^2\varphi = -\left(\tilde{\mathbf{u}}_{i\parallel}\cdot\tilde{\nabla}_\parallel\right)\tilde{\nabla}_\perp^2\varphi + \frac{\tilde{B}}{\tilde{n}}\tilde{\nabla}_\parallel\cdot\left(\tilde{n}\left(\tilde{\mathbf{u}}_{i\parallel} - \tilde{\mathbf{u}}_{e\parallel}\right)\right) - \frac{\rho_s\tilde{B}}{R_0\tilde{n}}\frac{\partial}{\partial\tilde{y}}\tilde{n} - \frac{S_n}{\omega_{ci}n_0\tilde{n}}\tilde{\nabla}_\perp^2\varphi, \tag{2.43}$$

where $\tilde{B} \equiv B/B_0$. Since we have already assumed $\nabla B \ll 1$, we can assume that $\tilde{B} \approx 1$. Defining the vorticity as $\tilde{\nabla}_\perp^2\varphi \equiv \omega$ we get the normalised vorticity equation

$$\frac{\mathrm{d}^0}{\mathrm{d}\tilde{t}}\omega = -\left(\tilde{\mathbf{u}}_{i\parallel}\cdot\nabla_\parallel\right)\omega + \frac{1}{\tilde{n}}\nabla\cdot\left(\tilde{n}\left(\tilde{\mathbf{u}}_{i\parallel} - \tilde{\mathbf{u}}_{e\parallel}\right)\right) - \frac{\rho_s}{R_0 n}\frac{\partial}{\partial\tilde{y}}\tilde{n} - \frac{\tilde{S}_n}{\tilde{n}}\omega, \tag{2.44}$$

where $\mathrm{d}^0/\mathrm{d}\tilde{t}$ is the convective derivative at constant $B = B_0$.

2.5 Parallel dynamics

With the normalised equations for the perpendicular dynamics of the system described in sec. 2.1 at hand, we move on to look at the parallel dynamics. In order to model the parallel dynamics, we turn to the parallel continuity equation, eq. (2.9).

We start by looking at the parallel electron equation, where we only include lowest order perpendicular dynamics and use the same assumptions as those stated in the previous sections[4];

$$\frac{\mathrm{d}^0}{\mathrm{d}t}\mathbf{u}_{e\parallel} = -\left(\mathbf{u}_{e\parallel}\cdot\nabla_\parallel\right)\mathbf{u}_{e\parallel} + \frac{e}{m_e}\nabla_\parallel\phi - \frac{T_{e0}\nabla_\parallel n}{nm_e} + 0.51\nu_{ei0}\left(\mathbf{u}_{e\parallel}-\mathbf{u}_{i\parallel}\right) - \frac{\mathbf{u}_{e\parallel}S_n}{n}$$
$$+ \frac{2.92T_{e0}}{3m_e\nu_{ei0}}\nabla_\parallel^2\mathbf{u}_{e\parallel}.$$

This can now be normalised using eq. (2.38), which leads to the normalised electron continuity equation[5]

$$\frac{\mathrm{d}^0}{\mathrm{d}\tilde{t}}\tilde{\mathbf{u}}_{e\parallel} = -\left(\tilde{\mathbf{u}}_{e\parallel}\cdot\tilde{\nabla}_\parallel\right)\tilde{\mathbf{u}}_{e\parallel} + \mu\tilde{\nabla}_\parallel\varphi - \mu\frac{\tilde{\nabla}_\parallel\tilde{n}}{\tilde{n}} + \nu_\parallel\left(\tilde{\mathbf{u}}_{i\parallel}-\tilde{\mathbf{u}}_{e\parallel}\right) - \frac{\tilde{\mathbf{u}}_{e\parallel}\tilde{S}_n}{\tilde{n}} + \mu\nu_{e\parallel}^{-1}\tilde{\nabla}_\parallel^2\tilde{\mathbf{u}}_{e\parallel},$$

(2.45)

where we have defined $\nu_\parallel \equiv 0.51\nu_{ei}/\omega_{ci}$, $\nu_{e\parallel}^{-1} \equiv 2.92\rho_{e0}^2\omega_{ce}/(3\rho_s^2\nu_{ei0})$ and $\mu \equiv m_i/m_e$.

The approach for deriving and normalising the parallel ion equation is similar to that of the parallel electron equation, and using the assumption that $T_i = 0$ as we did in sec. 2.4.2, we get the normalised parallel ion velocity equation[6]

$$\frac{\mathrm{d}^0}{\mathrm{d}\tilde{t}}\tilde{\mathbf{u}}_{i\parallel} = -\left(\tilde{\mathbf{u}}_{i\parallel}\cdot\tilde{\nabla}_\parallel\right)\tilde{\mathbf{u}}_{i\parallel} - \tilde{\nabla}_\parallel\varphi - \frac{\nu_\parallel}{\mu}\left(\tilde{\mathbf{u}}_{i\parallel}-\tilde{\mathbf{u}}_{e\parallel}\right) - \frac{\tilde{\mathbf{u}}_{i\parallel}\tilde{S}_n}{\tilde{n}}.$$

(2.46)

2.6   Summary of the 3D model

We now have the full set of normalised equations for the three-dimensional model at hand, so to give the reader a better overview, we dedicate this section to a recap of the equations and assumptions used to reach them. The assumptions for the derivation of the equations have been spread out throughout the chapter. This was done so one does not have to start from scratch with the derivations in case it turns out that an assumption is not valid and has to be omitted, but instead one can start from the equation just before the assumption was made. However, this may cause difficulties keeping track of all the assumptions used, so for clarity, they are summarised here in the order they were introduced in;

- Constant magnetic field direction.

- Only hydrogen isotopes are considered, $Z = 1$.

- Low frequency oscillations, $\partial/\partial t \propto \epsilon \ll \omega_{ci}$.

- Weakly collisional plasma, $\mathbf{R}_{\perp\sigma\alpha} \propto \epsilon$.

- Weak source $S_n \propto \epsilon$.

---

[4]See Appendix B.1 for the derivation.
[5]See Appendix B.1 for the derivation.
[6]See Appendix B.2 for the derivation

- Long gradient length scales on the parallel and perpendicular velocities $\nabla \cdot \mathbf{u}_\sigma \propto \epsilon$.

- Small anisotropic viscosity tensor $\overline{\overline{\mathbf{\Pi}}}_\sigma \propto \epsilon$.

- Fully ionised plasma, so only electron-ion collisions contribute to $\mathbf{R}_{\sigma\alpha}$.

- Electrostatic electric field $\mathbf{E} = -\nabla\phi$.

- Isothermal electrons $T_e = T_{e0}$ and $\nabla T_{e0} = \mathbf{0}$.

- Collision frequencies only depend on the reference parameters, $\nu_{e(i)i} = \nu_{e(i)i0}$.

- Long length scales on the gradient of the magnetic field $|\nabla B| \ll \epsilon$.

- Cold ions $T_i = 0$.

- Quasineutrality, $n_i = n_e \equiv n$.

- The perpendicular gradient length-scales are much smaller than typical gradient length scales $|\nabla_\perp n| \ll \epsilon$.

- Cross terms are small, $\partial_x f \partial_z g \propto \epsilon$.

- A magnetic field varying only in the radial direction, $B = B_0 R_0/R$ with $R = R_0 + a + x$.

- Small variation in the magnetic field $B \approx B_0$.

With these assumptions, we have derived a set of normalised equations given by

$$\frac{\mathrm{d}^0}{\mathrm{d}t}\omega = -\left(\mathbf{u}_{i\parallel} \cdot \nabla_\parallel\right)\omega + \frac{1}{n}\nabla_\parallel \cdot \left(n\left(\mathbf{u}_{i\parallel} - \mathbf{u}_{e\parallel}\right)\right) - \frac{\rho_s}{R_0 n}\frac{\partial}{\partial y}n - \frac{S_n}{n}\omega \tag{2.47}$$

$$\frac{\mathrm{d}^0}{\mathrm{d}t}n = -\nabla_\parallel \cdot \left(n\mathbf{u}_{e\parallel}\right) + \frac{\rho_s}{R_0}n\frac{\partial}{\partial y}\varphi - \frac{\rho_s}{R_0}\frac{\partial}{\partial y}n + D_n\nabla_\perp^2 n + S_n \tag{2.48}$$

$$\frac{\mathrm{d}^0}{\mathrm{d}t}\mathbf{u}_{e\parallel} = -\left(\mathbf{u}_{e\parallel} \cdot \nabla_\parallel\right)\mathbf{u}_{e\parallel} + \mu\nabla_\parallel\varphi - \frac{\mu\nabla_\parallel n}{n} + \nu_\parallel\left(\mathbf{u}_{i\parallel} - \mathbf{u}_{e\parallel}\right) - \frac{\mathbf{u}_{e\parallel}S_n}{n} + \mu\nu_{e\parallel}^{-1}\nabla_\parallel^2\mathbf{u}_{e\parallel} \tag{2.49}$$

$$\frac{\mathrm{d}^0}{\mathrm{d}t}\mathbf{u}_{i\parallel} = -\left(\mathbf{u}_{i\parallel} \cdot \nabla_\parallel\right)\mathbf{u}_{i\parallel} - \nabla_\parallel\varphi - \frac{\nu_\parallel}{\mu}\left(\mathbf{u}_{i\parallel} - \mathbf{u}_{e\parallel}\right) - \frac{\mathbf{u}_{i\parallel}S_n}{n}, \tag{2.50}$$

where we have omitted tilde for brevity. The parameters are given by $\mu = m_i/m_e$, $D_n = \rho_e^2\nu_{ei0}/(\rho_s^2\omega_{ci})$, $\nu_\parallel = 0.51\nu_{ei0}/\omega_{ci}$ and $\nu_{e\parallel}^{-1} = 2.92\rho_{e0}^2\omega_{ce}/(3\rho_s^2\nu_{ei0})$. The convective derivative is given by $\mathrm{d}^0/\mathrm{d}t = \partial/\partial t + \mathbf{u}_E^0 \cdot \nabla_\perp$ where $\mathbf{u}_E^0$ is the $\mathbf{E} \times \mathbf{B}$-velocity evaluated at constant $B = B_0$.

2.7 The HESEL 2D fluid model

The model derived in the previous sections is used for simulations of blobs with 3D dynamics. However, most of the thesis revolves around studying blobs in a two-dimensional geometry. For these simulations the HESEL model[24] has been used, which we briefly

describe in this section. The derivation of the HESEL model equations is very similar to the approach used to derive the model in sec. 2.6, however, HESEL does not assume cold ions and does not use the assumption of isothermal temperatures. The derivation of the model can be found in ref. [24].

HESEL is a two-dimensional four-field model based on the drift reduced Braginskii equations. All equations are normalised following the gyro-Bohm normalisation given in eq. (2.38). It solves the equations for the four normalised fields; density, n, generalised vorticity, $\omega^* = \nabla_\perp^2 \varphi + \nabla_\perp^2 p_i$, electron pressure, p_e, and ion pressure, p_i. The equations being solved are given by

$$\frac{\mathrm{d}}{\mathrm{d}t} n + n\mathcal{K}(\varphi) - \mathcal{K}(p_e) = \Lambda_n, \tag{2.51}$$

$$\nabla \cdot \left(\frac{\mathrm{d}^0}{\mathrm{d}t} \nabla_\perp \varphi^* \right) - \mathcal{K}(p_e + p_i) = \Lambda_{\omega^*}, \tag{2.52}$$

$$\frac{3}{2} \frac{\mathrm{d}}{\mathrm{d}t} p_e + \frac{5}{2} p_e \mathcal{K}(\varphi) - \frac{5}{2} \mathcal{K}\left(\frac{p_e^2}{n} \right) = \Lambda_{p_e}, \tag{2.53}$$

$$\frac{3}{2} \frac{\mathrm{d}}{\mathrm{d}t} p_i + \frac{5}{2} p_i \mathcal{K}(\varphi) + \frac{5}{2} \mathcal{K}\left(\frac{p_i^2}{n} \right) - p_i \mathcal{K}(p_e + p_i) = \Lambda_{p_i}, \tag{2.54}$$

where the convective derivative is defined as

$$\frac{\mathrm{d}}{\mathrm{d}t} f = \frac{\partial}{\partial t} f + B^{-1} \{\varphi, f\}, \qquad \text{and} \qquad \frac{\mathrm{d}^0}{\mathrm{d}t} f = \frac{\partial}{\partial t} f + \{\varphi, f\}, \tag{2.55}$$

with B being the magnitude of the magnetic field and with the $\mathbf{E} \times \mathbf{B}$ advection written as Poisson brackets

$$\{\varphi, f\} = \frac{\partial \varphi}{\partial x} \frac{\partial f}{\partial y} - \frac{\partial f}{\partial x} \frac{\partial \varphi}{\partial y}. \tag{2.56}$$

The curvature operator is defined as

$$\mathcal{K}(f) = -\frac{\rho_s}{R_0} \frac{\partial}{\partial y} f, \tag{2.57}$$

while the generalised potential reads $\varphi^* = \varphi + p_i$. The right-hand sides of eqs. (2.51)-(2.54) denote losses due to diffusion and parallel damping and are given by

$$\Lambda_n = D_e (1 + \tau) \nabla_\perp^2 n - \sigma(x) \frac{n}{\tau_d}, \tag{2.58}$$

$$\Lambda_{\omega^*} = \frac{3}{10} D_{\omega^*} \nabla_\perp^2 \omega^* - \sigma(x) \frac{\omega^*}{\tau_d} + \sigma(x)\mathcal{S}, \tag{2.59}$$

$$\Lambda_{p_e} = D_e (1 + \tau) \nabla \cdot (T_e \nabla_\perp n) + D_e \frac{11}{12} \nabla \cdot (n \nabla_\perp T_e) + D_e (1 + \tau) \nabla_\perp \ln n \cdot \nabla_\perp p_i$$
$$- \frac{3m_e}{m_i} \nu_{ei0} (p_e - p_i) - \sigma(x) \left[\frac{9}{2} \frac{p_e}{\tau_n} + \frac{T_e^{7/2}}{\tau_{SH,e}} \right], \tag{2.60}$$

$$\Lambda_{p_i} = \frac{5}{2} D_e (1 + \tau) \nabla \cdot (T_i \nabla_\perp n) - D_e (1 + \tau) \nabla_\perp \ln n \cdot \nabla_\perp p_i + 2D_i \nabla \cdot (n \nabla_\perp T_i)$$
$$+ \frac{3}{10} D_i \left[\left(\partial_{xx}^2 \varphi^* - \partial_{yy}^2 \varphi^* \right)^2 + 4 \left(\partial_{xy}^2 \varphi^* \right)^2 \right]$$
$$+ \frac{3m_e}{m_i} \nu_{ei0} (p_e - p_i) + \sigma(x) \left(p_i \mathcal{S} - \frac{9}{2} \frac{p_i}{\tau_d} \right), \tag{2.61}$$

21

where $\tau = T_{i0}/T_{e0}$ and $\sigma(x)$ indicates a smooth transition from closed to open field lines given by

$$\sigma(x) = \frac{\sigma_s}{2}\left[1 + \tanh\left(\frac{x - x_s}{\delta_s}\right)\right], \tag{2.62}$$

where x is the radial position, x_s is the location of the LCFS, δ_s is the width of the transition region and σ_s is an amplitude, normally $\sigma_s = 1$. The normalised diffusion coefficients are given by

$$D_e = \left(1 + \frac{R_0}{a}q^2\right)\frac{\rho_{e0}^2 \nu_{ei0}}{\rho_s^2 \omega_{ci}}, \qquad D_{\omega^*} = \left(1 + \frac{R_0}{a}q^2\right)\frac{\rho_{i0}^2 \nu_{ii0}}{\rho_s^2 \omega_{ci}}, \tag{2.63}$$

where q is the safety factor, R_0 is the device major radius, a is the minor radius, ρ_{e0} is the electron gyroradius at reference electron temperature, ν_{ei0} is the electron-ion collision frequency at reference temperature, $\rho_s = \sqrt{T_{e0}/(m_i\omega_{ci}^2)}$ is the ion gyroradius at electron temperature, $\omega_{ci} = eB_0/m_i$ is the ion gyrofrequency at constant magnetic field, ν_{ii0} is the ion-ion collision frequency at reference temperature and B_0 is the magnetic field magnitude at the outboard mid-plane. The parallel losses are parametrised with the parallel advection and the parallel Spitzer-Härm conduction given by

$$\tau_d = \frac{qR_0}{2M\sqrt{(T_e + T_i)/m_i}}, \qquad \tau_{SH,e} = \frac{m_e \nu_{ei0} T_{e0}^{3/2} L_\parallel}{3.16 n_0}, \tag{2.64}$$

both normalised with ω_{ci}^{-1} in the equations. Here n_0 is a reference density, $L_\parallel$ is the parallel connection length and M is the Mach number. Finally the connection to the sheath is parametrised with a vorticity sink given by

$$\mathcal{S} = \frac{en_0 \langle c_s \rangle_y}{L_\parallel}\left[1 - \exp\left(\Lambda - \frac{e\langle \varphi \rangle_y}{\langle T_e \rangle_y}\right)\right], \tag{2.65}$$

normalised by $en_0\omega_{ci}$ in the equations. Here $\langle \cdot \rangle_y$ denotes a poloidal average and Λ is the Bohm potential.

Chapter 3

Numerics

With the theoretical models for describing plasma dynamics at hand, we now need to be able to solve them in order to investigate the evolution of plasma filaments. The equations cannot be solved analytically, so instead we seek out approximate numerical solutions. The numerical implementation of the model equations in sec. 2.6 are implemented using the BOUT++ framework[35] developed at the university of York. HESEL, on the other hand, is not yet implemented in BOUT++. The current version of HESEL is implemented in C.

This chapter is therefore dedicated to describing the numerical implementation of both models and is split into two sections; first the BOUT++ framework is described, then the numerical implementation of HESEL is briefly discussed.

3.1   The BOUT++ framework

The BOUT++ framework is developed at the university of York and is primarily written in C++. The framework is designed for solving plasma fluid models with an arbitrary number of equations in curvilinear coordinates. The idea behind the framework is to allow the user to implement the equations to be solved using simple commands and leave the error prone features such as parallel communication and spatial discretisation to be handled by the underlying framework, which has been verified. BOUT++ is open source and is available at `http://boutproject.github.io`, where the newest version and all related documentation can be found.

BOUT++ is designed to solve problems in plasma physics, and since most problems in plasma physics rely on solving partial differential equations (PDEs), the framework provides methods for solving these. The way the model is kept general is by treating the temporal and spatial operators separately using the so-called method of lines (MOL)[36]. The method discretises spatial derivatives using, e.g., finite difference schemes, which reduces the problem at hand to a set of ordinary differential equations (ODE), for which a series of solvers are readily available.

The documentation for BOUT++ can be found at
`http://bout-dev.readthedocs.io/en/latest/`, but for completeness, the methods rel-

evant for solving the system of equations in sec. 2.6 are listed and briefly explained in the following subsections.

The outline is as follows; in sec. 3.1.1 we describe the spatial discretisation available in BOUT++, in sec. 3.1.2 we describe the temporal solver used in this project, in sec. (3.1.3) we discuss Laplace inversion, in sec. 3.1.4 we briefly discuss staggered grids and finally in sec. 3.1.5 we discuss the boundary conditions available in BOUT++.

3.1.1 Spatial discretisation

We start by discussing the spatial discretisation used in BOUT++. There are a variety of spatial discretisations available, and they each serve a different purpose. It is important to note that BOUT++ distinguishes between differencing methods and differential operators. Differencing methods refer to the method used to discretise a spatial derivative, e.g., finite differencing, where differential operators, such as $\nabla_\parallel$, take the geometry of the system into account when applying the specified differencing method. Before moving on to discuss the differencing methods available in BOUT++, we need to state the coordinate system of the framework, since it are different from the coordinate system discussed in sec. 2.1. In BOUT++, x is the radial direction, z is the axisymmetric direction and y is aligned with the magnetic field.

Differencing methods

The differencing methods available in BOUT++ are designed to model three terms that typically arise in plasma physics, namely diffusive terms of the form $\partial_x f$ and $\partial_x^2 f$, advective terms of the form $v_x \partial_x f$ and a method for flux conserving and limiting terms of the form $\partial_x(v_x f)$, where x is an arbitrary coordinate.

We start by looking at the methods meant to model the diffusive terms. These are;

C2: 2nd order centred finite difference;

$$\partial_x f_n = \frac{f_{n+1} - f_{n-1}}{2h}, \tag{3.1}$$

$$\partial_x^2 f_n = \frac{f_{n-1} - 2f_n + f_{n+1}}{h^2}, \tag{3.2}$$

where f_n is the function f at grid point n and h is the distance between grid-points.

C4: 4th order centred finite difference given by

$$\partial_x f_n = \frac{8f_{n+1} - 8f_{n-1} - f_{n+2} + f_{n-2}}{12h}, \tag{3.3}$$

$$\partial_x^2 f_n = \frac{-f_{n+2} + 16f_{n+1} - 30f_n + 16f_{n-1} - f_{n-2}}{12h^2}. \tag{3.4}$$

W2: 2nd order centred essentially non-oscillatory (CWENO) reconstruction polynomial scheme (see, e.g., ref. [37] for a description of this method).

W3: 3rd order centred essentially non-oscillatory (CWENO) reconstruction polynomial scheme (see, e.g., ref. [37] for a description of this method).

FFT: Fast Fourier transform method, which is implemented using the `fftw`-package[38]. Note that this method is only available in the axisymmetric direction (the z-direction in BOUT++ coordinates).

Next we look at the methods intended for advective terms. Since there is an inherent asymmetry in the advection equations due to the v_x term (if $v_x > 0$ the solution moves to the right and if $v_x < 0$, the solution moves to the left), it is preferred to use asymmetric differencing methods[36]. The available methods are:

U1: 1st order upwinding scheme given by

$$v_x \partial_x f_n = v_x \frac{f_n - f_{n-1}}{h}, \qquad \text{for } v_x > 0, \tag{3.5}$$

$$v_x \partial_x f_n = v_x \frac{f_{n+1} - f_n}{h} \qquad \text{for } v_x < 0. \tag{3.6}$$

U4: 4th order upwinding scheme given by

$$v_x \partial_x f_n = v_x \frac{4f_{n+1} - 12f_{n-1} + 2f_{n-2} + 6f_n}{12h}, \qquad \text{for } v_x > 0, \tag{3.7}$$

$$v_x \partial_x f_n = v_x \frac{-4f_{n-1} + 12f_{n+1} - 2f_{n+2} - 6f_n}{12h}, \qquad \text{for } v_x < 0. \tag{3.8}$$

W3: 3rd order centred essentially non-oscillatory (CWENO) reconstruction polynomial scheme (see, e.g., ref. [37] for a description of this method).

Finally there are two methods available, meant to tackle terms of the form $\partial_x(v_x f)$ while remaining flux conserving. These are:

SPLIT: A method where $\partial_x(v_x f)$ is split into an upwind term and a central differencing term as $v_x \partial_x f + f \partial_x v_x$, where the first part uses the upwind scheme and the second part uses central differencing, both specified by the user.

NND: Non-oscillatory, containing No free parameters and Dissipative (NND) scheme. See ref. [39] for a description.

All these differencing schemes are available for all three spatial dimensions with the exception of `FFT`, which is only available in the axisymmetric direction. All of the schemes stated above also support non-uniform meshes when the flag `non_uniform=true` is set in the input file. When the flag is set, the corrections

$$\frac{\partial}{\partial x} f \approx \frac{1}{\Delta x} \frac{\partial}{\partial i} f, \tag{3.9}$$

$$\frac{\partial^2}{\partial x^2} f \approx \frac{1}{\Delta x^2} \frac{\partial^2}{\partial i^2} f + \frac{1}{\Delta x} \frac{\partial}{\partial x} f \cdot \frac{\partial}{\partial i} \frac{1}{\Delta x}, \tag{3.10}$$

are made, where i is the cell index number, Δx is the local distance between grid-points, and $\partial_i(1/\Delta x)$ is a correction factor that can either be calculated automatically or be specified in the grid file. However, care should be taken when using non-uniform meshes, since non-uniform meshes have a separate switch for doing Laplace inversion, which is not automatically set with the flag mentioned above.

All of these differencing schemes can be used directly using the corresponding function calls in the framework, e.g., by using `DDX(f)` for a single derivative in the radial direction.

However, these finite difference methods do not take the geometry of the problem at hand into account. In order to account for a given geometry, it is necessary to use the general differential operators implemented in BOUT++, which use the differencing schemes stated above along with a user specified geometry to evaluate the equations to be solved.

General operators

The general operators take an input from the input file (`BOUT.inp` per default), specifying which differencing scheme to use. The operators implemented in BOUT++ for a general coordinate system are listed in the following;

`Grad(Field)`: The gradient of a field resulting in a vector, $\mathbf{v} = \nabla f$, which is implemented as

$$\nabla f = \frac{\partial f}{\partial u^i} \nabla u^i \rightarrow (\nabla f)_i = \frac{\partial}{\partial u^i} f, \tag{3.11}$$

where i denotes a cell index number, u^i is a unit change at i, superscripts indicate a contravariant vector and subscripts indicate a covariant vector[40].

`Div(Vector)`: The divergence of a vector resulting in a field, $f = \nabla \cdot \mathbf{v}$, given by

$$\nabla \cdot \mathbf{v} = \frac{1}{J} \frac{\partial}{\partial u^i} \left(J g^{ij} v_j \right), \tag{3.12}$$

where J is the Jacobian matrix and g is the metric tensor, with g^{ij} being the i, j^{th} component.

`Curl(Vector)`: The curl of a vector resulting in a vector, $\mathbf{v} = \nabla \times \mathbf{a}$, given by

$$\nabla \times \mathbf{a} = \frac{1}{\sqrt{g}} \sum_k \left(\frac{\partial a_j}{\partial u_i} - \frac{\partial a_i}{\partial u_j} \right) \mathbf{e}_k, \qquad i, j, k \text{ cyc } x, y, z, \tag{3.13}$$

where $\mathbf{e}_k$ is a unit vector in the direction k.

`V_dot_Grad(Vector,Field)`: The dot product between a vector and a gradient of a field, i.e. an advection term, resulting in a field, $l = \mathbf{v} \cdot \nabla f$, given by

$$\mathbf{v} \cdot \nabla f = v_x \partial_x f_n + v_y \partial_y f_n + v_z \partial_z f_n, \tag{3.14}$$

using the scheme specified for advective terms.

`V_dot_Grad(Vector,Vector)`: The product between a vector and a divergence of a vector, resulting in a vector, $\mathbf{v} = (\mathbf{a} \cdot \nabla)\mathbf{b}$. Although the command is the same as for the dot-product between a vector and a field, the evaluation is different. The method depends on whether the vector being advected is covariant or contravariant. Since this method is not used in the implementation of the 3D model derived in sec. 2.6, the reader is referred to the file for operators on vector objects in the BOUT++ source code for details on the implementation.

`Laplace(Field)`: The Laplacian of a field resulting in a field, $l = \nabla^2 f$, which is incorporated as

$$\nabla^2 f = \frac{1}{J} \frac{\partial}{\partial u^i} \left(J g^{ij} \right) \frac{\partial}{\partial u^i} f + g^{ij} \frac{\partial^2 f}{\partial u^i \partial u^j}. \tag{3.15}$$

There are also a range of operators that require the magnetic field to be in Clebsch form, which means that the magnetic field must be on the form

$$\mathbf{B} = \nabla z \times \nabla x, \qquad \mathbf{B} = \|\mathbf{B}\|\mathbf{b} = B\mathbf{b} \qquad \text{and} \qquad B = \frac{\sqrt{g_{yy}}}{J} \tag{3.16}$$

where x is the radial direction and z is the axisymmetric direction, J is the Jacobian, g_{yy} is the yy component of the metric tensor and $\mathbf{B}$ is the equilibrium magnetic field. If this is fulfilled in the geometry used, a series of operators are available. These are

`Grad_par`: The parallel gradient given by

$$\partial_\| f = \mathbf{b} \cdot \nabla f = \frac{1}{\sqrt{g_{yy}}} \frac{\partial}{\partial y} f \tag{3.17}$$

`Div_par`: The parallel divergence given by

$$\nabla_\| \cdot \mathbf{v} = \mathbf{B} \cdot (\mathbf{b} \cdot \nabla) \frac{\mathbf{v}}{B} = \mathbf{B} \cdot \frac{1}{\sqrt{g_{yy}}} \frac{\partial}{\partial y} \frac{\mathbf{v}}{B} \tag{3.18}$$

`Grad2_par2`: The second order gradient in the y-direction given by

$$\partial_\|^2 f = \partial_\| \left(\partial_\| f\right) = \frac{1}{\sqrt{g_{yy}}} \frac{\partial}{\partial y} \left(\frac{1}{\sqrt{g_{yy}}}\right) \frac{\partial}{\partial y} f + \frac{1}{g_{yy}} \frac{\partial^2}{\partial y^2} f. \tag{3.19}$$

`Laplace_par`: The parallel Laplacian given by

$$\nabla_\|^2 f = \nabla \cdot \mathbf{b}\mathbf{b} \cdot \nabla f = \frac{1}{J} \frac{\partial}{\partial y} \left(\frac{J}{g_{yy}} \frac{\partial}{\partial y} f\right), \tag{3.20}$$

`Laplace_perp`: The perpendicular Laplacian given by

$$\nabla_\perp^2 f = (\nabla^2 - \nabla_\|^2) f, \tag{3.21}$$

`Delp2`: The perpendicular Laplacian, where all y-derivatives, ∂_y, are neglected, given by

$$\nabla_\perp^2 f = \left(g^{xx} \frac{\partial^2}{\partial x^2}\right) f + G^x \frac{\partial}{\partial x} f + \left(g^{zz} \frac{\partial^2}{\partial z^2}\right) f + G^z \frac{\partial}{\partial z} f + 2 \left(g^{xz} \frac{\partial}{\partial x} \frac{\partial}{\partial z}\right) f, \tag{3.22}$$

where

$$G^i = \frac{1}{J} \left(\frac{\partial}{\partial x} \left[J g^{xi}\right] + \frac{\partial}{\partial z} \left[J g^{zi}\right]\right), \tag{3.23}$$

Finally since the term

$$-\frac{\nabla\varphi \times \mathbf{b}}{B} \cdot \nabla f, \tag{3.24}$$

is commonly occurring in plasma physics there are different ways to solve this expression incorporated in BOUT++. Eq. (3.24) can be written as a Poisson bracket given by

$$-\frac{\nabla\varphi \times \mathbf{b}}{B} \cdot \nabla f = -\frac{1}{B} \left(\frac{\partial\varphi}{\partial x} \frac{\partial f}{\partial z} - \frac{\partial f}{\partial x} \frac{\partial\varphi}{\partial z}\right) = -\frac{1}{B} \{\varphi, f\}, \tag{3.25}$$

when $\mathbf{b}$ is along the y-direction. A series of bracket evaluation operators are available in BOUT++, which are set in the input file or in the main code as `brackets(phi, f, method)`, where the most commonly used method, and the one used in this thesis is Arakawa's stencil.

Arakawa's stencil

Arakawa's stencil[41] was developed in 1966 by A. Arakawa to solve a problem in computational fluid dynamics. Finite difference methods caused instabilities, where vorticity and energy were artificially created from the numerical schemes when used on the vorticity equation in an incompressible fluid[42]

$$\frac{\partial}{\partial t}\zeta + \mathbf{v} \cdot \nabla\zeta = 0. \tag{3.26}$$

Here $\mathbf{v} = \mathbf{k} \times \nabla\psi$, $\zeta = \nabla^2\psi$, ψ is a streaming function, ∇ is the two-dimensional gradient operator in the plane of motion and $\mathbf{k}$ is a unit vector in a direction normal to the plane of motion. As is seen from eq. (3.26), the last term on the left-hand side strongly resembles the term in eq. (3.24). The method derived by Arakawa is vorticity and energy conserving for a curvilinear coordinate system on Clebsch form and the numerical implementation can be found in his original paper[41]. However, it should be noted that in the implementation of Arakawa's stencil in BOUT++, gradients in the direction parallel to the magnetic field are neglected. When the Arakawa bracket is used in BOUT++

$$-\frac{\nabla\varphi \times \mathbf{b}}{B} \cdot \nabla f \approx \frac{1}{g_{yy}}\left(g_{yy}\left\{\varphi, f\right\}_{z,x}\right) = \frac{\partial}{\partial z}\varphi\frac{\partial}{\partial x}f - \frac{\partial}{\partial x}\varphi\frac{\partial}{\partial z}f \tag{3.27}$$

is returned, i.e., off-diagonal terms in the metric tensor are not evaluated.

3.1.2 Temporal solver

Since the BOUT++ framework uses MOL to discretise the set of equations used to model the plasma dynamics, the set of coupled partial differential equations are converted into a series of ordinary differential equations. Several different solvers for ODEs already exist for C and C++. The default solver and the one used in this project is PVODE[43], so in the following section we give a brief introduction to PVODE. A full description of the solver can be found in ref. [43].

PVODE is a general purpose solver for initial value problem (IVP) ODEs, designed to solve both stiff and non-stiff problems. It is written in ANSCI standard C and uses the message passing interface (MPI) to parallelise the solving vectors in user specified segments. For stiff cases (which plasma physics problems usually are[44]), i.e., if the problem at hand contains time scales much faster than those we wish to compute it uses backward differentiation with a preconditioned generalised minimal residual method (PGMRES) iteration[43].

Two different methods are available for solving IVP ODEs in PVODE which are designed to tackle either stiff or non-stiff problems. A backward differentiation formula (BDF) is used for stiff problems, while the so-called Adams-Moulton formula is used for non-stiff problems. The solver uses both variable step-size and variable-order form to ensure the desired accuracy while minimising the number of steps used to solve the equation.

The formulas used to solve the ODEs (BDF and Adams-Moulton) can both be represented by the linear multistep formula[43]

$$\sum_{i=0}^{K_1} \alpha_{n,i} y_{n-i} + h_n \sum_{i=0}^{K_2} \beta_{n,i} \dot{y}_{n-i} = 0, \tag{3.28}$$

where the vector y_n is computed to approximate $y(t_n)$, which is the exact solution at t_n, $\dot{y}_{n-1} = \mathrm{d}/\mathrm{d}t(y_{n-1})$, $\alpha_{n,i}$ and $\beta_{n,i}$ are uniquely determined by the method, the history of the step-size and the normalisation $\alpha_{n,0} = -1$ and $h_n = t_n - t_{n-1}$ is the step size.

For non-stiff problems, the Adams-Moulton formula is preferred[43], which is given by eq. (3.28) for $K_1 = 1$ and $K_2 = q - 1$, where q is the order of the system. For stiff problems, BDF should be used, where $K_1 = q$ and $K_2 = 0$. For Adams-Moulton, q can be from 1-12 and for BDF q can be 1-5. PVODE starts with $q = 1$ and then varies it dynamically to get the desired accuracy with minimal amount of iterations.

For both Adams-Moulton and BDF we have that $\dot{y}_n = f(t_n, y_n)$, where $f(t_n, y_n)$ is the right-hand side of the ODE to be solved. This means that eq. (3.28) becomes an implicit formula with the nonlinear equation

$$G(y_n) \equiv y_n - h_n \beta_{n,0} f(t_n, y_n) - a_n = 0, \tag{3.29}$$

where

$$a_n \equiv \sum_{i>0} \left(\alpha_{n,i} y_{n-i} + h_n \beta_{n,i} \dot{y}_{n-i} \right). \tag{3.30}$$

This needs for be solved for y_n at each time-step. For non-stiff problems the solution can be determined through iterations and there is no need to solve the linear system of equations. For stiff problems, Newton iteration is used, and the underlying system must be solved for each iteration, which means solving the linear system of equations given by

$$M \left[y_{n(m+1)} - y_{n(m)} \right] = -G \left(y_{n(m)} \right), \tag{3.31}$$

where $y_{n(m)}$ is the mth approximation to y_n, and M approximates $\partial/\partial_y(G)$ as

$$M \approx 1 - \gamma J, \qquad J = \frac{\partial f}{\partial y}, \qquad \gamma = h_n \beta_{n,0}. \tag{3.32}$$

This is solved using the iterative method SPGMR (scaled, preconditioned GMRES), a Krylov subspace method[43]. PVODE can take a preconditioner on either the left, the right or both sides of eq. (3.31). It can also run without any preconditioner, however, it is usually more efficient to include one[43]. The integrator then computes an estimate, E_n, of the local error at each timestep. PVODE tries to ensure that

$$\|E_n\|_{rms,w} \equiv \left[\sum_{i=1}^{N_f} \frac{1}{N_f} \left(w_i, E_{n,i} \right)^2 \right]^{1/2} < 1, \tag{3.33}$$

where $E_{n,i}$ denotes the ith component of E_n, N_f is the number of coupled ODEs being solved and w_i is the ith component of the weight vector,

$$w_i = \frac{1}{\text{rtol}|y_i| + \text{atol}_i}. \tag{3.34}$$

Here the relative tolerance rtol, which indicates the relative accuracy for a single time step, is a scalar specified by the user, and the absolute tolerance, atol_i, which can be thought of as the noise level, can be a vector of length N_f. PVODE varies the timestep h_n, and order, q, to try to get the least amount of iterations while still fulfilling eq. (3.33).

3.1.3 Laplace inversion

The next part of the BOUT++ framework we describe is used to get an expression for the normalised potential in the equations derived in sec. 2. In order to evaluate φ it is necessary to invert the expression for the vorticity, $\nabla_\perp^2 \varphi = \omega$, since the vorticity is the field being solved for in the set of equations. Now, since equations of the form

$$d\nabla_\perp^2 f + \frac{1}{c_1}\left(\nabla_\perp c_2\right) \cdot \nabla_\perp f + af = b, \tag{3.35}$$

where a, b, c and d are constants, are often occurring in plasma physics, standard ways to solve equations of this type have been implemented in BOUT++. There are a series of different algorithms and parallelisations schemes available to choose from. In general the solvers use one of two methods to solve the inversion problem, namely a fast Fourier transform (FFT) in the axisymmetric direction or solving the full 2D problem by inverting the full evolution matrix. One thing to note when using BOUT++ is that even if g_{xy} and g_{yz} are non-zero, they are neglected when using the `Laplacian` and `LaplaceXZ` options. This approach allows the inversion problem to be solved independently for each y-plane, which significantly speeds up the computation.

For the geometry used in this thesis (see sec. 2.1), the standard Laplace solver is sufficient. This method uses the FFT inversion solving a tri-diagonal system (using the default `serial_tri` option in the input). This method is very efficient and scales with $\mathcal{O}(n_x)$, where n_x is the number of grid-points in the radial direction, using the so-called Thomas algorithm. When using tri-diagonal solvers, $c_1 = c_2 \equiv c$ in eq. (3.35). Since g_{xy} and g_{yz} are neglected, even if they are non-zero, eq. (3.35) can be rewritten as

$$d\left(g^{xx}\frac{\partial^2}{\partial x^2} + G^x\frac{\partial}{\partial x} + g^{zz}\frac{\partial^2}{\partial z^2} + G^z\frac{\partial}{\partial z} + 2g^{xz}\frac{\partial}{\partial x}\frac{\partial}{\partial z}\right)f$$
$$+ \frac{1}{c}\left(\mathbf{e}^x\frac{\partial}{\partial x} + \mathbf{e}^z\frac{\partial}{\partial z}\right)c \cdot \left(\mathbf{e}^x\frac{\partial}{\partial x} + \mathbf{e}^z\frac{\partial}{\partial z}\right)f + af = b, \tag{3.36}$$

where $\mathbf{e}^{x(z)}$ is a unit vector in the radial (axisymmetric) direction and g is the metric tensor. Now a discrete fourier transform is made in the axisymmetric direction

$$F(x,y)_k = \frac{1}{n_z}\sum_{z=0}^{n_z-1} f(x,y)_z \exp\left(\frac{-2\pi ikz}{n_z}\right), \tag{3.37}$$

where n_z is the number of axisymmetric grid-points. Since the desire is to decouple the different Fourier modes, a, c and d cannot be functions of z, which means that $\partial_z c = 0$. Using the discrete Fourier transform on eq. (3.36) gives

$$d\left(g^{xx}\frac{\partial^2}{\partial x^2} + G^x\frac{\partial}{\partial x} - k^2 g^{zz} + ikG^z + ik2g^{xz}\frac{\partial}{\partial x}\right)F_z + \frac{g^{xx}}{c}\left(\frac{\partial}{\partial x}c\right)\frac{\partial}{\partial x}F_z + aF_z = B_z. \tag{3.38}$$

The x-derivatives can now be evaluated using the 2$^{\text{nd}}$ order finite difference schemes, eqs.

(3.1) and (3.2), and the different Fourier modes are decoupled which gives

$$
d\left(g^{xx}\frac{F_{z,n-1}-2F_{z,n}+F_{z,n+1}}{dx^2}+G^x\frac{F_{z,n+1}-F_{z,n-1}}{2dx}-k^2g^{zz}F_{z,n}+ikG^zF_{z,n}\right.
$$
$$
\left.+ik2g^{xz}\frac{F_{z,n+1}-F_{z,n-1}}{2dx}\right)+\frac{g^{xx}}{c_n}\left(\frac{c_{n+1}-c_{n-1}}{2dx}\right)\frac{F_{z,n+1}-F_{z,n-1}}{2dx}+aF_{z,n}=B_{z,n}.
$$
$$\text{(3.39)}$$

Finally terms of $F_{z,n-1}, F_{z,n}$ and $F_{z,n+1}$ can be collected and introducing

$$
\gamma_1=\frac{dg^{xx}}{dx^2},\quad \gamma_2=dg^{zz},\quad \gamma_3=\frac{dg^{xz}}{dx},\quad \gamma_4=\frac{dG^x+g^{xx}\frac{c_{n+1}-c_{n-1}}{2c_ndx}}{2dx},\quad \gamma_5=dG^z,\quad \text{(3.40)}
$$

gives the expression

$$
\left(\gamma_1-\gamma_4-ik\gamma_3\right)F_{z,n-1}+\left(-2\gamma_1-k^2\gamma_2+ik\gamma_5+a\right)F_{z,n}+\left(c_1+c_4+ikc_3\right)F_{z,n+1}=B_{z,n},
$$
$$\text{(3.41)}$$

which can be rewritten as the matrix equation

$$
AF_z=B_z, \tag{3.42}
$$

where A is a tri-diagonal matrix. The boundary conditions are then set in the first and last rows of A and B_z, and the matrix inversion is done to solve for F_z.

This procedure is much faster than doing the full 2D-inversion, however it can only be used when the local approximation, stated in sec. 2.4.3, is used.

3.1.4 Staggered grids

The next option we discuss regarding the BOUT++ framework is regarding the grids used. By default, all grids in BOUT++ are cell-centred. However, for numerical stability, it is sometimes useful to use staggered grids, where some fields are shifted down or up with respect to the other fields. This is enabled in BOUT++ in the input file, where the flag `StaggerGrids = true` needs to be set. If BOUT++ is not configured with checks and the `StaggerGrids` flag is not set in the input file, but the staggered grids are still used in the code, then all fields will be set to be cell centred without any warning, so one needs to be careful when using this option.

In order to set the location of the individual fields, `Field3D::setLocation()` needs to be set in the initialisation of the fields with one of the options `CELL_CENTRE`, `CELL_XLOW`, `CELL_YLOW` or `CELL_ZLOW`. Operations involving two different fields can only be performed if the fields are defined at the same location. This means that in order to perform an operation between fields defined at different locations, interpolation needs to be done. This can be achieved by including `interpolation.hxx` from the BOUT++ library and using `interp_to(field,location,region)`. The option `region` can be set to `RGN_ALL`, which sets the communication between processors to be done before returning the result from `interp_to`, or `RGN_NOBNDRY`, where no communication is performed. Differential operators are by default set at the location of the input field, while advection operators, which take two inputs, are defined at the location of the field being advected. For example when using `Vpar_Grad_par(v,f)`, the term $v\nabla_\parallel f$ is being calculated and the output is at the location of the field f.
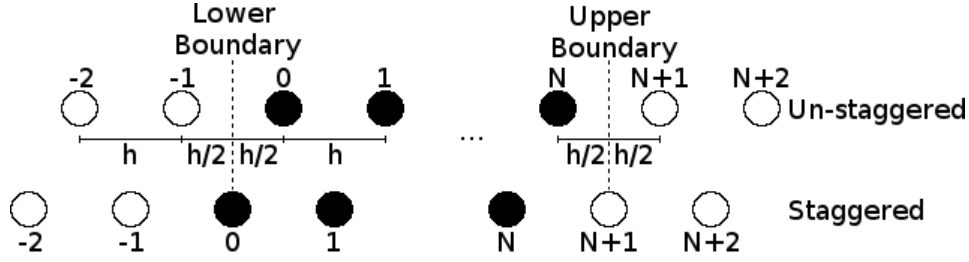
Figure 3.1: The position of the boundaries and the numbering of the grid points for staggered and un-staggered grids in BOUT++.

3.1.5 Boundary conditions

Finally we need to discuss the boundary conditions used in BOUT++. The implementation of the boundaries varies depending on whether or not a staggered grid is used, and of what order the boundary conditions need to be. There are typically three kinds of boundary conditions used. There is the Dirichlet boundary, $f|_{j=L_{lbnd},L_{ubnd}} = a$, where j is the location of the field f, L_{lbnd} is the location of the lower domain boundary, L_{ubnd} is the location of the upper domain boundary and a is a constant value (which can also be a vector spanning the remaining spatial dimensions). There is the Neumann boundary, where $\partial_j f|_{j=L_{lbnd},L_{ubnd}} = a$, and there is the free boundary condition, where the inner points are extrapolated to the ghost-points at each time-step to emulate the scenario where no boundary conditions are set.

It should be noted here that, by default, BOUT++ is cell centred so the boundary is located between the last grid point and the first ghost-point unless a staggered grid is used in which case the first interior point is located at the lower boundary and the first upper ghost point is located at the upper boundary as illustrated in fig. 3.1.

The definitions of the boundary conditions used are stated in tabs. 3.1 to 3.3. It should be noted that these boundary conditions can be set in the input file using `dirichlet_o3(a.)`, `neumann_o2(a.)` or `free_o3`. Here one needs to be careful since the `o3` in the dirichlet and free boundary conditions refers to the order with which the ghost-points are evaluated, whereas the `o2` for the neumann boundary condition refers to the order of the boundary condition itself, which means that all three of these boundary conditions are $\mathcal{O}(h^2)$, where h is the step-size[45]. The actual boundaries implemented in BOUT++ can be found, e.g., in ref. [45], and are stated here in tab. 3.1 for the Dirichlet boundary, tab. 3.2 for the Neumann boundary and tab. 3.3 for the free boundary condition. The definitions of the grid point positions can be seen in fig. 3.1.

3.2 Numerical implementation of HESEL

At the time of writing, HESEL is not yet fully implemented in the BOUT++ framework, and the simulations using HESEL are carried out using a numerical implementation in C. The implementation along with the boundary conditions used is briefly stated in this section. A full description of the numerical methods used can be found in ref. [46].

The implementation of the spatial derivatives in HESEL is done using a 2$^\text{nd}$ order finite

Table 3.1: Implementation of the Dirichlet boundary condition of order $\mathcal{O}(h^2)$ in BOUT++[45].

Boundary	Grid	Implementation
Lower	Un-staggered	$f_{-1} = (8a - 6f_0 + f_1)/3$ $f_{-2} = 3f_{-1} - 3f_0 + f_1$
Lower	Staggered	$f_0 = a$ $f_{-1} = 3f_0 - 3f_1 + f_2$ $f_{-2} = 3f_{-1} - 3f_0 + f_1$
Upper	Un-staggered	$f_{N+1} = (8a - 6f_N + f_{N-1})/3$ $f_{N+2} = 3f_{N+1} - 3f_N + f_{N-1}$
Upper	Staggered	$f_{N+1} = a$ $f_{N+2} = 3f_{N+1} - 3f_N + f_{N-1}$

Table 3.2: Implementation of the Neumann boundary condition of order $\mathcal{O}(h^2)$ in BOUT++[45].

Boundary	Grid	Implementation
Lower	Un-staggered	$f_{-1} = f_0 - ah$ $f_{-2} = f_1 - 3ah$
Lower	Staggered	$f_0 = (4f_1 - f_2 - 2ah)/3$ $f_{-1} = f_1 - 2ah$ $f_{-2} = f_2 - 4ah$
Upper	Un-staggered	$f_{N+1} = f_N + ah$ $f_{N+2} = f_{N-1} + 3ah$
Upper	Staggered	$f_{N+1} = (4f_N - f_{N-1} + 2ah)/3$ $f_{N+2} = f_N + 2ah$

Table 3.3: Implementation of the free boundary condition of order $\mathcal{O}(h^2)$ in BOUT++[45].

Boundary	Grid	Implementation
Lower	Un-staggered	$f_{-1} = 3f_0 - 3f_1 + f_2$ $f_{-2} = 3f_{-1} - 3f_0 + f_1$
Lower	Staggered	$f_0 = 3f_1 - 3f_2 + f_3$ $f_{-1} = 3f_0 - 3f_1 + f_2$ $f_{-2} = 3f_{-1} - 3f_0 + f_1$
Upper	Un-staggered	$f_{N+1} = 3f_N - 3f_{N-1} + f_{N-2}$ $f_{N+2} = 3f_{N+1} - 3f_N + f_{N-1}$
Upper	Staggered	$f_{N+1} = 3f_N - 3f_{N-1} + f_{N-2}$ $f_{N+2} = 3f_{N+1} - 3f_N + f_{N-1}$

difference scheme with derivatives defined as in eqs. (3.1) and (3.2) and with the boundary located between grid-points. The advective terms employ an Arakawa stencil, while the temporal derivative uses an explicit stiffly stable 3rd order scheme with diffusive terms treated implicitly using operator splitting. The inversion of the Laplacian terms is done by means of Fourier modes in the axisymmetric direction and a 2nd order finite difference scheme in the radial direction, which results in a tri-diagonal matrix. Each Fourier mode is then solved using pivoted Gaussian elimination.

HESEL solves a small domain at the outboard midplane of a tokamak with periodic

boundary conditions employed in the axisymmetric direction, y, in HESEL. Fixed profiles of n, p_e and p_i at the inner radial boundary, maintained with a characteristic time, τ_p, act as particle and energy sources. The remaining boundaries are as follows; for $n, \varphi, \omega^*, p_e$ and p_i the outer radial boundary is a Neumann boundary with zero gradient enforced, while the inner radial boundaries are all Dirichlet where n, p_e and p_i are the prescribed profiles, ω^* is set to zero and φ is set so that $\nabla_\perp^2 \varphi + \nabla_\perp^2 p_i = 0$ at the inner radial boundary.

With these numerical implementations of the two models described in sec. 2 at hand, we can now move on to conduct simulations investigating coherent plasma filaments in magnetically confined plasmas.

Chapter 4

Two dimensional seeded blobs

With the models and methods used to investigate propagation of isolated plasma filaments at hand we can now move on to study these filaments. We start by investigating how isolated filaments propagate when three-dimensional effects are parametrised or completely neglected, which is what this chapter is dedicated to. First, two code validation exercises are described, where HESEL was compared to other numerical models and experimental results. Then the propagation of isolated filaments and the effects of temperature dynamics is studied as well as how the velocity of these filaments scales with different parameters.

4.1 Multi-code validations

In order to investigate how well results from different numerical models compared to experiments, two validation exercises were conducted, where the different participating models were held up against experimental data from the TORPEX experiment and the MAST tokamak.

4.1.1 Blob dynamics in the TORPEX experiment: a multi-code validation

The first code validation exercise was published in 2016 and is a multi-code validation based on the TORPEX experiment in Lausanne[47]. It features the five numerical models; HESEL, GBS, TOKAM3X and the STORM2D and STORM3D modules in BOUT++. Seeded blobs were initialised based on experimental results gathered using Langmuir probes. All results presented in this section are published in ref. [48]. Part of the work for the publication was done in my master thesis [49], while the results were finalised during this project. Our contribution to the publication was the numerical results concerning HESEL.

We start this section by briefly describing the TORPEX experiment. We then move on to discuss the five numerical models used in this study and finally we describe the results obtained from the comparison between the models and the experiment.

The TORPEX experiment

The TORPEX experiment is a small toroidal device with a major radius of $R_0 = 1$ m, a minor radius of $a = 0.2$ m and it features a simple magnetised toroidal geometry. It has a toroidal magnetic field of $B_T = 76$ mT on axis and a poloidal magnetic field of $B_p = 1.6$ mT, which results in helical field lines. The helical magnetic field lines intercept the lower and upper wall at the HFS and are interrupted by a poloidal limiter at the LFS. This results in an almost constant connection length of $L_\parallel \approx 2\pi R_0$.

The plasma is produced using hydrogen and is heated by electron cyclotron resonance heating (ECRH) with typical plasma parameters of $n_0 \approx 10^{16}$ m^{-3} and $T_{e0} \approx 5$ eV in the source region. Furthermore, ions are typically much colder than the electrons. This means that the plasma is only weakly ionised with a degree of ionisation of only around 5%.

The data is collected using a linear array of Langmuir probes with a distance between the tips of 1.8 cm, as well as a single Langmuir probe located 3 cm from the limiter. The sampling of the blobs was done using conditional averaging over several blob events, and the coordinates were defined to be the same as in sec. 2.1.

The numerical models

The simulations modelling the experimental data were carried out using seeded blob simulations in five different numerical models, all based on drift-ordering (see for example[50]) using the Braginskii equations[27]. All five models employ the so-called local approximation[24] and use the electrostatic assumption, so $\mathbf{E} = -\nabla\varphi$, where φ is the normalised electrostatic potential. However, different assumptions and parametrisations have been used in the equations, where the full effects of these assumptions on seeded blob dynamics are not yet fully known. The five models are all normalised following Bohm normalisation, eq. (2.38) and are given as follows:

STORM3D:
The model equations solved in the STORM3D module[51] assume cold ions and isothermal electrons and solves the four fields; particle density, n, vorticity, $\omega = \nabla_\perp^2 \varphi$, parallel ion velocity, $v_{\parallel i}$, and parallel electron velocity, $v_{\parallel e}$, which are given by

$$\frac{\mathrm{d}^0}{\mathrm{d}t}n + n\hat{\mathcal{K}}(\varphi) - \hat{\mathcal{K}}(n) = -\nabla_\parallel\left(nv_{\parallel e}\right) + D_e\nabla_\perp^2 n + S_n \tag{4.1}$$

$$\frac{\mathrm{d}^0}{\mathrm{d}t}\omega - \frac{\hat{\mathcal{K}}(n)}{n} = -\nu_{\parallel i}\nabla_\parallel\omega + \frac{\nabla_\parallel j_\parallel}{n} + D_\omega\nabla_\perp^2\omega \tag{4.2}$$

$$\frac{\mathrm{d}^0}{\mathrm{d}t}v_{\parallel i} = -v_{\parallel i}\nabla_\parallel v_{\parallel i} - \nabla_\parallel\phi - \eta_\parallel j_\parallel - \frac{S_n v_{\parallel i}}{n} \tag{4.3}$$

$$\frac{\mathrm{d}^0}{\mathrm{d}t}v_{\parallel e} = -v_{\parallel e}\nabla_\parallel v_{\parallel e} + \frac{m_i}{m_e}\left(\nabla_\parallel\phi - \frac{\nabla_\parallel n}{n} + \eta_\parallel j_\parallel\right) - \frac{S_n v_{\parallel e}}{n}, \tag{4.4}$$

where $\mathrm{d}^0 f/\mathrm{d}t = \partial f/\partial t + \mathbf{b}\cdot(\nabla\varphi\times\nabla f)$ is a convective derivative with $\mathbf{b}$ being the unit vector along the magnetic field. $\hat{\mathcal{K}}(f) = -\hat{g}\partial f/\partial y$ is the curvature operator, $\hat{g} = 2\rho_s/R_0$ is the strength of the ∇B and curvature drifts and S_n is a particle source (defined in eq.

(4.21)). The parallel current is defined as $j_\parallel = n\left(v_{\parallel i} - v_{\parallel e}\right)$, $D_e = 2m_e\nu_{ei0}/(m_i\omega_{ci})$ is the normalised perpendicular density diffusion coefficient, $D_\omega = 3\nu_{ei0}\sqrt{m_e/m_i}/(4\omega_{ci})$ is the normalised perpendicular ion viscosity, $\nu_{ei0} = n_0 e^4 \ln\Lambda/(3me^{1/2}\epsilon_0(2\pi T_{e0})^{3/2})$ is the electron-ion collision frequency and $\eta_\parallel = m_e\nu_{ei0}/(1.96m_i\omega_{ci})$ is the normalised parallel resistivity.

For the upper parallel boundary, sheath boundary conditions were used; $v_{\parallel i}|_{z=\tilde{L}_\parallel} = 1$ and $v_{\parallel e}|_{z=\tilde{L}_\parallel} = \exp(-\varphi|_{z=\tilde{L}_\parallel})$, where $\tilde{L}_\parallel = 2\pi R_0/\rho_s$ is the normalised parallel connection length. At the lower parallel boundary symmetry boundary conditions were applied.

STORM2D:
The STORM2D model[51] uses the same assumptions as STORM3D, but assumes no variation in the density and electrostatic potential in the parallel direction. Linearising the sheath boundary conditions and integrating the parallel direction gives a much simpler system;

$$\frac{d^0}{dt}n + n\hat{\mathcal{K}}(\varphi) - \hat{\mathcal{K}}(n) = -2\frac{n(1-\varphi)}{\tilde{L}_\parallel} + D_e\nabla_\perp^2 n + S_n \tag{4.5}$$

$$\frac{d^0}{dt}\omega - \frac{\hat{\mathcal{K}}(n)}{n} = 2\frac{\varphi}{\tilde{L}_\parallel} + D_\omega\nabla_\perp^2\omega, \tag{4.6}$$

where the source term is given by $S_n = 2\tilde{n}_{bg}/\tilde{L}_\parallel$, with $\tilde{n}_{bg}$ being the normalised background density profile.

GBS:
The global braginskii solver (GBS)[52] is developed at the Swiss Plasma Center at EPFL in Lausanne. It assumes cold ions but does not, unlike STORM, assume isothermal electrons, which means that it solves the five fields; particle density, n, vorticity, ω, the parallel ion velocity, $v_{\parallel i}$, the parallel electron velocity, $v_{\parallel e}$, and the electron temperature, T_e. This leads to the model

$$\frac{d^0}{dt}n + n\hat{\mathcal{K}}(\varphi) - \hat{\mathcal{K}}(p_e) = -\nabla_\parallel\left(nv_{\parallel e}\right) + \hat{D}_n\nabla_\perp^2 n + S_n \tag{4.7}$$

$$\frac{d^0}{dt}\omega - \frac{\hat{\mathcal{K}}(p_e)}{n} = -v_{\parallel i}\nabla_\parallel\omega + \frac{\nabla_\parallel j_\parallel}{n} + \hat{D}_\omega\nabla_\perp^2\omega + \frac{\hat{\mathcal{K}}(G_i)}{3n} \tag{4.8}$$

$$\frac{d^0}{dt}v_{\parallel i} = -v_{\parallel i}\nabla_\parallel v_{\parallel i} - \frac{\nabla_\parallel p_e}{n} - \hat{\nu}_{in}v_{\parallel i} + \hat{D}_{v_{\parallel i}}\nabla_\perp^2 v_{\parallel i} - \frac{2\nabla_\parallel G_i}{3n} \tag{4.9}$$

$$\frac{d^0}{dt}v_{\parallel e} = -v_{\parallel e}\nabla_\parallel v_{\parallel e} - \hat{\nu}_{en}v_{\parallel e} + \hat{D}_{v_{\parallel e}}\nabla_\perp^2 v_{\parallel e}$$
$$+ \frac{m_i}{m_e}\left(\nabla_\parallel\varphi - \frac{\nabla_\parallel p_e}{n} - 0.71n\nabla_\parallel T_e + \eta_\parallel j_\parallel - \frac{2\nabla_\parallel G_e}{3n}\right) \tag{4.10}$$

and

$$\frac{d^0}{dt}T_e + \frac{2}{3}\left(\hat{\mathcal{K}}(\varphi) - \frac{5}{2}\hat{\mathcal{K}}(T_e) - \frac{\hat{\mathcal{K}}(p_e)}{n}\right) = -v_{\parallel e}\nabla_\parallel T_e + \frac{2}{3}T_e\left(0.71\frac{\nabla_\parallel j_\parallel}{n} - \nabla_\parallel v_{\parallel e}\right)$$
$$+ \hat{D}_{T_e}\nabla_\perp^2 T_e + S_{T_e}. \tag{4.11}$$

Here $\hat{\nu}_{en}$ and $\hat{\nu}_{in}$ are the normalised electron-neutral and ion-neutral collision frequencies introduced to account for the weak ionisation of TORPEX. S_n and S_{T_e} are source terms for the particle density and electron temperature, respectively. The diffusion coefficients, $\hat{D}_a$, for a field a, are set to be constants and are mainly introduced for numerical stability. To account for gyroviscous effects, the operators $G_i = -\eta_{0i} \left(2\nabla_{\parallel} v_{\parallel i} + \hat{\mathcal{K}}(\varphi) \right)$ and $G_e = -\eta_{0e} \left(2\nabla_{\parallel} v_{\parallel e} - \hat{\mathcal{K}}(p_e)/n + \hat{\mathcal{K}}(\varphi) \right)$ are introduced, where $\eta_{0i} = 0.96 p_i / \nu_{ii0}$ and $\eta_{0e} = 0.76 p_e / \nu_{ei0}$, where ν_{ii0} and ν_{ei0} are the collision frequencies evaluated at reference temperature.

At the upper and lower parallel boundaries, sheath boundary conditions are applied $v_{\parallel i}|_{z=\pm \tilde{L}_{\parallel}} = \pm \sqrt{T_e|_{z=\pm \tilde{L}_{\parallel}}}$ and $v_{\parallel e}|_{z=\pm \tilde{L}_{\parallel}} = \pm \sqrt{T_e|_{z=\pm \tilde{L}_{\parallel}}} \exp \left(\Lambda - \varphi|_{z=\pm \tilde{L}_{\parallel}} / T_e|_{z=\pm \tilde{L}_{\parallel}} \right)$, where $\sqrt{T_e|_{z=\pm \tilde{L}_{\parallel}}}$ is to account for the temperature dependence of the sound speed, c_s, and $\Lambda = 2.8$ is the Bohm potential in hydrogen.

HESEL:
The HESEL model has already been treated in section 2.7, but due to the substantially different conditions in TORPEX compared to the plasmas HESEL is designed to model, significant revisions were made to the equations to account for the weakly ionised plasma and the low ion temperatures. Electron-ion collisions were neglected and instead collisions with neutrals were introduced, since these dominate in weakly ionised plasmas like those in TORPEX. Furthermore, ion temperature dynamics were neglected, so the set of equations solved was given by

$$\frac{\mathrm{d}}{\mathrm{d}t} n + n\mathcal{K}(\varphi) - \mathcal{K}(p_e) = -\frac{n}{\tau_n} + \hat{\nu}_{en} \nabla_{\perp}^2 (n - \varphi) \tag{4.12}$$

$$\frac{\mathrm{d}^0}{\mathrm{d}t} \omega - \mathcal{K}(p_e) = D_{\omega} \nabla_{\perp}^2 \omega - \hat{\nu}_{in} \omega + \frac{2\rho_s}{L_{\parallel}} \left[1 - \exp \left(\Lambda - \frac{\langle \varphi \rangle_y}{\langle T_e \rangle_y} \right) \right] \tag{4.13}$$

$$\frac{3}{2} \frac{\mathrm{d}}{\mathrm{d}t} p_e + \frac{5}{2} p_e \mathcal{K}(\varphi) - \frac{5}{2} \mathcal{K} \left(\frac{p_e^2}{n} \right) = -\frac{p_e}{\tau_{p_e} n} + \frac{3}{2} \hat{\nu}_{en} (p_e - \varphi), \tag{4.14}$$

where $\mathrm{d}/\mathrm{d}t = \partial/\partial_t f + \mathbf{b}/B \cdot (\nabla \varphi \times \nabla f)$ is the convective derivative, $\mathcal{K}(f) = -g\partial_y f$ is the curvature operator with $g = \rho_s / R_0$. The normalised diffusion coefficients are given by $\hat{\nu}_{en} = \rho_{e0}^2 \nu_{en} / (\rho_s^2 \omega_{ci})$, where ρ_{e0} is the electron gyroradius at reference electron temperature and ν_{en} is the electron-neutral collision frequency. $\hat{\nu}_{in} = \rho_{i0}^2 \nu_{in} / (\rho_s^2 \omega_{ci})$ is the normalised ion-neutral collision frequency and $D_{\omega} = \rho_{i0}^2 \nu_{ii0} / (\rho_s^2 \omega_{ci})$ is the ion viscosity, where ρ_{i0} is the ion gyroradius at reference ion temperature (since ion temperature effects were neglected, but ρ_{i0} depends on T_{i0}, T_{i0} was set to room temperature) and ν_{ii0} is the ion-ion collision frequency at reference temperature. The parallel dynamics are parametrised using the normalised characteristic parallel loss-times $\tau_n = \omega_{ci} L_{\parallel} / (2c_s)$ and $\tau_{p_e} = 15 \omega_{ci} L_{\parallel}^2 \nu_{en} (1 + 4/\nu_{es}) / (128 v_e^2)$, where $\nu_{es} = L_{\parallel} \nu_{en} / (2v_e)$, and v_e is the electron thermal velocity. Finally the sheath connection is parametrised by the last expression in the vorticity equation, eq. (4.13), where $\Lambda = 2.8$ for a hydrogen plasma and $\langle \cdot \rangle_y$ denotes a poloidal average.

TOKAM3X:

The final model considered in the paper was TOKAM3X[53], developed at CEA in Cadarache. This model also assumes cold ions and isothermal electrons, but takes a different approach from STORM3D and GBS to modelling the parallel dynamics. It uses the parallel ion momentum and the parallel generalised Ohm's law instead of the electron and ion velocities. The set of equations being solved is given by

$$\frac{\mathrm{d}}{\mathrm{d}t}n + n\hat{\mathcal{K}}(\varphi) - \hat{\mathcal{K}}(n) = -\nabla \cdot \left[\left(\Gamma - j_{\parallel}\right)\mathbf{b}\right] + \hat{D}_n\nabla_{\perp}^2 n + S_n \qquad (4.15)$$

$$\frac{\mathrm{d}}{\mathrm{d}t}\Omega + \Omega\hat{\mathcal{K}}(\varphi) - 2\hat{\mathcal{K}}(n) = \nabla \cdot \left[\left(j_{\parallel} - \Omega\frac{\Gamma}{n}\right)\mathbf{b}\right] + \hat{D}_{\Omega}\nabla_{\perp}^2 \Omega \qquad (4.16)$$

$$\frac{\mathrm{d}}{\mathrm{d}t}\Gamma + \Gamma\hat{\mathcal{K}}(\varphi) + \hat{\mathcal{K}}(\Gamma) = -\nabla \cdot \left(\Gamma\frac{\Gamma}{n}\mathbf{b}\right) - 2\nabla_{\parallel}n + \hat{D}_{\Gamma}\nabla_{\perp}^2\Gamma \qquad (4.17)$$

$$n\nabla_{\parallel}\varphi - \nabla_{\parallel}n + \eta_{\parallel}nj_{\parallel} = 0, \qquad (4.18)$$

where $\Gamma = nv_{\parallel i}$ is the parallel ion momentum and $\Omega = \nabla \cdot (\nabla_{\perp}\varphi/B^2)$ is the vorticity accounting for magnetic field variations. The diffusion coefficients $\hat{D}_a$ for fields a are assumed constant and are introduced for numerical stability.

At the upper and lower parallel boundaries, linearised sheath conditions are applied, which means $\Gamma|_{z=\pm\tilde{L}_{\parallel}} = \pm n|_{z=\pm\tilde{L}_{\parallel}}$ and $j_{\parallel}|_{z=\pm\tilde{L}_{\parallel}} = \pm n|_{z=\pm\tilde{L}_{\parallel}}(\varphi|_{z=\pm\tilde{L}_{\parallel}} - \Lambda)$.

Comparison of the models:
Despite the similarities between the models, there are a few notable differences;

Full 3D effects are included in STORM3D, GBS and TOKAM3X, where the 3D dynamics are parametrised in the 2D models HESEL and STORM2D. In HESEL the parallel closures used are based on the approximation $v_{\parallel i}\nabla_{\parallel} = v_{\parallel e}\nabla_{\parallel} \approx c_s/L_{\parallel}$ and $j_{\parallel} = 0$ using the so-called vorticity advection closure, whereas STORM2D assumes no variation in φ and n along the parallel direction and analytically integrates and averages using the so-called sheath dissipation closure.

Different sheath boundary conditions are used in the models. Where GBS and STORM3D use the full sheath boundary conditions, STORM2D and TOKAM3X use linearised sheath boundary conditions. HESEL uses the full sheath boundary, but on poloidally averaged fields assuming a weak sheath coupling.

Electron temperature dynamics are included in HESEL and GBS, where separate equations for T_e are solved. The electron temperature dynamics are neglected in STORM3D, STORM2D and TOKAM3X, where isothermal electrons are assumed.

The magnetic field equilibria are different in the different models. While STORM3D, STORM2D and GBS ignore the effects of a varying magnetic field in the convective derivative, it is retained in HESEL and TOKAM3X. On top of this, the variation in the magnetic field is retained in the expression for the vorticity in TOKAM3X but is neglected in all the other models. Furthermore, the curvature operator in HESEL is only half that of the other models, which means that the interchange term will only be half as strong.

In the 3D models, electron inertia is included to varying degree. In STORM3D it is included both in the parallel electron and ion velocity equations, in GBS it is only retained in the electron velocity equation and in TOKAM3X it is neglected all together.

Finally there is a difference in how the dissipative terms are included. In STORM3D and STORM2D, the perpendicular dissipation is calculated using collision frequencies based on the electron-ion and ion-ion collisions, while HESEL uses the electron-neutral and ion-neutral collisions, both calculated using the method described in ref. [54]. In GBS and TOKAM3X the collision frequencies are taken to be constant terms, mainly introduced for numerical reasons.

Seeded blob simulations

The simulations carried out using the five models described above were conducted using seeded blobs initialised based on experimental parameters. Three different cases were examined, each with a different set of initial conditions, chosen to get three different amplitudes of the blobs for each case. They were chosen based on peak events from intervals in the ion saturation current and dubbed case 1, 2 and 3. Case 1 was for peak events in the interval $I_{sat} \in [2.0\sigma, 2.75\sigma]$, where σ was the standard deviation of the reference signal, case 2 was for the interval $I_{sat} \in [2.75\sigma, 3.5\sigma]$ and case 3 was for the interval $I_{sat} \in [3.5\sigma, 4.25\sigma]$. This resulted in blobs with different amplitudes with respect to the background, where case 1 had $n_0/n_{bg} \approx 0.85$, case 2 had $n_0/n_{bg} \approx 1.0$ and case 3 had $n_0/n_{bg} \approx 1.9$, where n_{bg} is the background density. The background density and electron temperatures were evaluated using the median values found based on the Langmuir probe I-V characteristics. The background values in the experiments were found to only be weakly dependent on the poloidal position. They were therefore implemented in the models with only a radial variation, given by

$$n_{bg} = \alpha(\beta x)^\gamma + \delta \tag{4.19}$$
$$T_{e,bg} = \epsilon \cdot \exp(\zeta x), \tag{4.20}$$

where $\alpha = -4.2 \cdot 10^{17}$ m^3, $\beta = 1$ m^{-1}, $\gamma = 2.9$, $\delta = 2.5 \cdot 10^{15}$ m^{-3}, $\epsilon = 2.8$ eV, and $\zeta = -5.9$ m^{-1}. In TOKAM3X and STORM3D a background source is needed, and despite no measurements being available in the direction parallel to the magnetic field, a source localised at the limiter was estimated to be

$$S_n(x, z) = n_{bg}(x) \cdot \frac{10 \exp(10|z - \pi|/\pi)}{\pi [\exp(10) - 1]}, \tag{4.21}$$

based on earlier measurements[55]. This source was needed to keep the background profiles sustained in STORM3D and TOKAM3X, while STORM2D used a source given by $S_n(x) = n_{bg}(x)/\pi$, GBS kept the background profiles fixed, and HESEL initialised the background profiles and assumed them to be constant on the time scale of blob motion.

The actual blobs were initialised as perturbations on top of the background stated above with a density perturbation and a temperature perturbation in the models with electron temperature dynamics and with only a density perturbation in the isothermal models, assuming $T_{e,bl} = 0$. A dipole electrostatic potential was also used to initialise the blobs,

Table 4.1: Input values used in the blob initialisation in the TORPEX experiment.

	Case 1	Case 2	Case 3
n_0 [10^{15} m^{-3}]	1.975 ± 0.135	2.335 ± 0.325	4.395 ± 0.855
$\sigma_{n,x}$ [cm]	2.20 ± 0.20	2.40 ± 0.30	1.65 ± 0.45
$\sigma_{n,y}$ [cm]	2.40 ± 0.20	2.10 ± 0.20	1.75 ± 0.25
$T_{e,0}$ [eV]	0.345 ± 0.065	0.960 ± 0.250	1.730 ± 0.280
$\sigma_{T_e,x}$ [cm]	1.05 ± 0.15	1.05 ± 0.25	0.80 ± 0.20
$\sigma_{T_e,y}$ [cm]	3.65 ± 1.05	1.45 ± 0.25	2.85 ± 0.95
ϕ_1 [V]	2.33 ± 0.17	4.60 ± 0.74	4.72 ± 0.41
$\sigma_{\phi,x,1}$ [cm]	3.55 ± 0.25	3.25 ± 0.25	4.95 ± 0.35
y_1 [cm]	2.55 ± 0.25	2.60 ± 0.20	1.15 ± 0.35
$\sigma_{\phi,y,1}$ [cm]	2.95 ± 0.05	3.10 ± 0.20	4.90 ± 0.60
ϕ_2 [V]	-1.54 ± 0.14	-2.35 ± 0.55	-6.16 ± 0.97
$\sigma_{\phi,x,2}$ [cm]	3.10 ± 0.20	2.75 ± 0.35	2.95 ± 0.45
y_2 [cm]	-2.10 ± 0.40	-0.50 ± 0.80	-2.45 ± 0.15
$\sigma_{\phi,y,2}$ [cm]	4.00 ± 0.30	4.75 ± 0.45	2.50 ± 0.30

so the full blob initialisation profiles were

$$n_{bl}(x,y) = n_0 \cdot \exp\left[-\left(\frac{x-x_0}{\sigma_{n,x}}\right)^2 - \left(\frac{y}{\sigma_{n,y}}\right)^2\right] \tag{4.22}$$

$$T_{e,bl}(x,y) = T_{e,0} \cdot \exp\left[-\left(\frac{x-x_0}{\sigma_{T_e,x}}\right)^2 - \left(\frac{y}{\sigma_{T_e,y}}\right)^2\right] \tag{4.23}$$

$$\phi_{fl,bl}(x,y) = \phi_1 \cdot \exp\left[-\left(\frac{x-x_0}{\sigma_{\phi,x,1}}\right)^2 - \left(\frac{y-y_1}{\sigma_{\phi,y,1}}\right)^2\right]$$
$$+ \phi_2 \cdot \exp\left[-\left(\frac{x-x_0}{\sigma_{\phi,x,2}}\right)^2 - \left(\frac{y-y_2}{\sigma_{\phi,y,2}}\right)^2\right], \tag{4.24}$$

where $x_0 = 0.07$ m and the rest of the parameters are defined in tab. 4.1.

Finally, in order to compare the simulation results with the experimentally found values, a measure for the blob position was required. In this regard, the blob saturation current density was defined in the simulation as

$$j_{bl}(x,y,t) = \frac{n(x,x,t)}{2}\sqrt{T_e(x,y,t)} - \frac{n_{bg}(x)}{2}\sqrt{T_{e,bg}(x)},$$

where $n(x,y,t) = n_{bg}(x) + n_{bl}(x,y,t)$ and $T_e(x,y,t) = T_{e,bg}(x) + T_{e,bl}(x,y,t)$, while it was found as

$$j_{bl}(x,y,t) = \frac{I_{sat}(x,y,t) - \langle I_{sat}(x,y,t)\rangle_t}{A}$$

in the experiments. Here $I_{sat}(x,y,t)$ denotes the ion saturation current measured by the Langmuir probes, $\langle.\rangle_t$ denotes the median of the temporal signal and A is the probe collection area. Next a surface was defined, where $\langle j_{bl}(x,y,t)\rangle_{S(t)} = 0.2 j_{bl}(t)$ and $j_{bl}(t) = \langle j_{bl}(x,y,t)\rangle_{x,y}$ with $\langle\cdot\rangle_{x,y}$ being the spatial average in the domain perpendicular to the

magnetic field. This means that the surface $S(t)$ only encompassed values larger than 20% of the mean value, effectively filtering out noise. The position of the blob was then defined as

$$x_{bl} = \frac{\int \int_{S(t)} x dx dy}{\int \int_{S(t)} dx dy} \tag{4.25}$$

$$y_{bl} = \frac{\int \int_{S(t)} y dx dy}{\int \int_{S(t)} dx dy}, \tag{4.26}$$

while the velocities were defined as

$$v_x(t) = \frac{\mathrm{d}}{\mathrm{d}t} x_{bl}(t) \tag{4.27}$$

$$v_y(t) = \frac{\mathrm{d}}{\mathrm{d}t} y_{bl}(t). \tag{4.28}$$

Results

The results for this validation study were split into two parts. The first part concerned sensitivity studies and was carried out using a variety of input parameters. This was done to investigate how robust the simulations were to the assumption of isothermal electrons as well as how sensitive the simulations were to the uncertainties in the input parameters and the different diffusivity coefficients used in the models.

In order to test the effect of isothermal electrons, two simulations were carried out for each of the isothermal models. One with a constant background temperature of $T_{e,bg} = 2.8$ eV and one with a constant background temperature of $T_{e,bg} = 1.85$ eV. Two simulations meant to investigate the effect of a temperature background were also done in GBS. One with a constant background temperature of $T_{e,bg} = 2.8$ eV and one with a background temperature given by equation (4.19). It was found that the background electron temperature has a large influence on the blob dynamics. Larger background temperatures caused the blobs to propagate faster in the radial direction. Furthermore, using a constant electron temperature background, opposed to the profile in eq. (4.19), caused the blobs to propagate much faster. It was also tested in GBS, whether the initialisation of an electron temperature profile had an effect. This was done by making three simulations. One where the electron temperature was not evolved and was initialised without a perturbation, one where the electron temperature was evolved, but was initialised without a perturbation, and finally one where the electron temperature was evolved and initialised with the perturbation given by eq. (4.23). The results showed no significant influence of a temperature perturbation on the radial propagation. The blob initialised with an initial perturbation was slightly faster than the blob initialised without a perturbation, which again was slightly faster than the blob where the temperature was not evolved, but these differences were minor.

The sensitivity to the input parameters was investigated by making five simulations for each of the five models used. One simulation with the mean value stated in tab. 4.1, two simulations using the minimum and maximum blob size within the uncertainties

given and two simulations using the minimum and maximum peak to peak value in the potential dipole. It was found that within the interval given by the uncertainties in tab. 4.1, none of the five models varied significantly, leading to the conclusion that the input parameters did not significantly influence the simulations.

Finally, the effect of the artificial diffusion coefficients used in GBS and TOKAM3X was investigated by scanning a range of diffusion coefficients relevant to the TORPEX experiment, and the results showed that the diffusion coefficients used in the simulations had no major influence on the blob propagation.

The second part of the results were focused on discussing the qualitative aspects of the blob propagation and on comparing the velocity profiles obtained using eqs. (4.27) and (4.28) in the experiments with the numerical results from the five codes. The qualitative analysis was based on a background temperature of $T_{e,bg} = 2.8$ eV for the isothermal models, while GBS and HESEL used the background profile given in eq. (4.20).

First it was noted that there was a significant difference between the three cases listed in tab. 4.1. Case 3 was smaller and had a much higher amplitude with respect to the background than case 1 and case 2. This caused case 3 to develop steeper gradients which lead to more secondary instability effects breaking up the blob. An effect which was observed in all five models.

It was seen that all three isothermal models, STORM2D, STORM3D and TOKAM3X showed very similar evolution with a propagation mainly in the radial direction, whereas GBS and HESEL also showed a propagation in the poloidal direction on top of the radial displacement. This was attributed to the use of a background electron temperature profile. All 3D models and STORM2D showed very similar coherent blobs, whereas the HESEL blobs generated a more mushroom-like structure, which was attributed to the weak vorticity advection closure used to parametrise the sheath physics in HESEL.

Finally a qualitative analysis was conducted based on the velocity profiles given by eqs. (4.27) and (4.28). The simulation results were compared with the experimental results, both with respect to the velocity profiles and using the average velocities.

In the experiments the radial velocity peaked early and then gradually decreased for all three cases. For case 1 and case 2 in STORM2D, STORM3D and TOKAM3X, the radial velocity remained roughly constant, while it slightly decreased in GBS and steadily increased in HESEL. This meant that none of the models captured the full evolution of the blob in cases 1 or 2, although GBS captured the overall trends best. The fact that HESEL showed trends opposite of what was observed in the experiments was attributed to the parametrisation of the sheath. From the comparison with the 3D models it was concluded that the sheath parametrisation used in HESEL did not describe the conditions in TORPEX well. The constant velocities in STORM2D, STORM3D and TOKAM3X were likely due to the constant background temperature used in the simulations. For case 3, all five models showed a decelerating blob, but none of the models captured the velocity profile found in the experiments. This was likely due to the blobs in the simulations breaking up due to the large secondary instabilities, such as the Kelvin-Helmholtz instability, causing the blob to stay less coherent. The same observations, with none of the models capturing the experimental trends in any of the experimental cases, were seen for the poloidal velocity profiles. HESEL blobs accelerated for case 1 and case 2, while STORM2D, STORM3D and TOKAM3X remained roughly constant at

$v_y \approx 0$. GBS blobs initially accelerated and then decelerated in a manner similar to what was observed in the experiments.

The results based on the average velocities showed that the isothermal models gave very similar radial velocities for case 1 and case 2, which compared well with the experimental values. However, this was due to a coincidence, where the velocities were underestimated compared to the experimental results in the beginning of the simulation and at the end of the simulations the velocities were overestimated. This over- and underestimation of the experimental velocity ended up cancelling out, leading to an average velocity close to that of the experiments in the isothermal models. HESEL grossly overestimated the velocities, again attributed to the parametrisation used for the sheath connection, which was not suitable for TORPEX. Finally, for case 3, the average velocity was underestimated by HESEL, while it was overestimated by the four other models. The slower propagation of the experimental blob for case 3 compared to the four other numerical models was expected to be due to the blob in the experiment losing coherence due to the steep gradients in the density and temperature profiles.

Conclusions

The main messages from the paper were that none of the models described TORPEX well. This was likely due to none of the models being designed for the parameter range present in TORPEX. Also the diagnostic used to determine the position, size and amplitude of the blobs was based on conditional averaging, i.e., an ensemble of blobs, which may provide different results from the single seeded blob used in the simulations. However, the comparison between the different models used in this paper did provide useful results. It was shown that a background profile has a large influence on how blobs propagate and that if full 3D fields are not included, the parametrisation of the parallel dynamics needs to be done with care. The sheath dissipation closure used in HESEL did not capture the conditions in TORPEX, which lead to results very different from all the other models, underlining the importance of using a correct sheath parametrisation.

4.1.2 Multi-code analysis of scrape-off layer filament dynamics in MAST

The second validation exercise performed was also published in 2016 and was done with data from a tokamak with parameters closer to the range for which the numerical models were designed, namely the MAST tokamak in Culham. The same models used in section 4.1.1 were applied to this validation study with the exception of STORM2D, which was omitted. However, due to the higher temperatures in MAST compared to TORPEX and thus the higher degree of ionisation, the models were altered compared to the previously listed ones. We start this section by describing the MAST tokamak and then move on to list the changes in the numerical models stated in eqs. (4.1) to (4.18). Again our contribution to the publication are the simulations conducted using HESEL. The results of this validation study are published in ref. [56].

The MAST tokamak

MAST is a tight aspect ratio tokamak with a major radius of $R_0 = 0.85$ m and a minor radius of $a = 0.59$ m. The discharge considered for the analysis of this validation exercise featured a toroidal magnetic field of $B_T = 0.39$ T at $R = 0.66$ m, which decreased by 0.19 T at the outboard mid-plane, where the simulations were conducted. The poloidal magnetic field at $R = 0.66$ m was $B_p \approx 0.12$ T and the plasma current was $I_p \approx 0.56$ MA, which results in a safety factor of $q = 4.8$. Finally, the discharge was performed in a deuterium plasma in double null L-mode with a separatrix electron temperature of $T_{e,sep} = 35$ eV and a separatrix density of $n_{sep} = 1.2 \times 10^{19}$ m^{-3}. Measurements of the ion temperature were not available, so based on earlier L-mode discharges[57], the ion temperature was assumed to be $T_i = 2T_e$. Finally, the parallel connection length from midplane to divertor in the SOL for the discharge considered was found to be $L_\parallel = 7$ m.

Numerical models

Since the same models were used for this validation exercise as those stated in sec. 4.1.1, only the differences between the version of the models used for this validation study and the previously stated models will be listed here.

STORM3D implemented dynamic electrons, which means that a fifth equation was added to the model in order to evolve the electron temperature, as well as additional terms for the electron temperature gradients in the existing equations. Finally a modification to the electron sheath boundary condition was made since it depends on the electron temperature through the sound speed. The full model can be found in ref. [58].

GBS included dynamic ion temperature effects and neglected neutral effects due to the fully ionised plasma in MAST. Furthermore, the constant background used in TORPEX was replaced here by a steady-state (flat) background, generated using sources to be specified later. The full model used can be found in ref. [59].

HESEL was significantly altered for the TORPEX validation exercise due to the low ion temperatures and the low degree of ionisation. For the MAST simulations the full model described in section 2.7 was used. Furthermore, to be able to compare HESEL with the other models, the curvature operator was changed from the standard HESEL $g = \rho_s/R_0$ to the one used in the other codes, $\hat{g} = 2\rho_s/R_0$ in the code comparisons, while $g = \rho_s/R_0$ was used when comparing with experiments.

TOKAM3X did not implement any major revisions for the MAST simulations and merely changed the input parameters to fit the experimental data. The full model can be found in ref. [53].

Seeded blob simulations

Unlike in the case for TORPEX, the diffusivities used in this validation study were based on the neoclassical coefficients stated in sec. 2.7, which lead to a perpendicular density diffusion coefficient at the background values given by $D_e = 0.63$ m^{2}s^{-1} and a perpendicular viscosity at the background values of $D_\omega = 8.3$ m^{2}s^{-1}, both Bohm normalised with $D_b = 62$ m^{2}s^{-1} in all models. The diffusion coefficients were based on

Table 4.2: A table of the parameters used to initialise the MAST simulations.

Blob 1	Case 1	Case 2	Case 3
A_n [10^{19} m^{-3}]	4.23	2.26	0.96
$\sigma_{n,x}$ [cm]	1.11	1.11	1.11
$\sigma_{n,y}$ [cm]	1.18	1.18	1.18
A_{T_e} [eV]	0.00	0.55	4.00
$\sigma_{T_e,x}$ [cm]	1.11	1.11	1.11
$\sigma_{T_e,y}$ [cm]	1.18	1.18	1.18
Blob 2	Case 1	Case 2	Case 3
A_n [10^{19} m^{-3}]	3.98	2.37	0.88
$\sigma_{n,x}$ [cm]	0.95	0.95	0.95
$\sigma_{n,y}$ [cm]	0.91	0.91	0.91
A_{T_e} [eV]	0.00	0.41	4.00
$\sigma_{T_e,x}$ [cm]	0.95	0.95	0.95
$\sigma_{T_e,y}$ [cm]	0.91	0.91	0.91

background values of n_0 and T_{e0} in GBS, HESEL and TOKAM3X, while were set to account for the perturbation imposed by the blob in STORM3D.

Similar to the TORPEX validation, the experimental data of the blobs were gathered using conditional averaging. Instead of determining the blob dimensions and parameters by Langmuir probes as was done in TORPEX, the data was gathered using the D_α diagnostic along with a blob detection algorithm to trace individual filaments. However, since D_α was used, it was not possible to separate the particle density and the electron temperature in the experimental data, so the output was given in terms of a function of the two. Using the blob detection algorithm, two separate filaments were identified and different ratios of electron temperature to particle density were chosen. The filaments were initialised as

$$n_{bl} - n_{bg} = \frac{A_n}{2} \exp\left[-\left(\frac{x - x_0}{\sigma_{n,x}}\right)^2 - \left(\frac{y}{\sigma_{n,y}}\right)^2 \right] \left[1 - \tanh\left(\frac{z - L_\parallel/2}{\sigma_{n,z}}\right) \right] \quad (4.29)$$

$$T_{e,bl} - T_{e,bg} = \frac{A_{T_e}}{2} \exp\left[-\left(\frac{x - x_0}{\sigma_{T_e,x}}\right)^2 - \left(\frac{y}{\sigma_{T_e,y}}\right)^2 \right] \left[1 - \tanh\left(\frac{z - L_\parallel/2}{\sigma_{T_e,z}}\right) \right], \quad (4.30)$$

where $\tanh\left(\frac{z - L_\parallel/2}{\sigma_{T_e,z}}\right) = 0$ was used in HESEL, while $\sigma_{T_e,z} = 0.1 L_\parallel$ was used in the 3D models. Since the background was assumed flat, x_0 was simply set to be 1/3 of the total domain size to avoid noise from the radial boundaries. The remaining parameters used in the simulations are listed in tab. 4.2. Here it is worth noting, that in contrast to TORPEX, no uncertainties are given in the input parameters and more importantly, the blobs are initialised without any potential perturbation. This may cause the simulations to differ significantly from the experimental results, since a potential dipole needs to built up in the simulations before the blobs start moving, whereas it is already in motion in the experimental observations. In the 3D models, source terms are needed and these were

defined as

$$S_n(z) = C_1 \frac{10 \exp\left(10z/L_\parallel\right)}{L_\parallel\left(\exp(10) - 1\right)} \tag{4.31}$$

$$S_E(z) = C_2 \frac{\exp\left(-5z/L_\parallel\right)}{L_\parallel}, \tag{4.32}$$

where $S_E(z)$ is an energy source, and where C_1 and C_2 were adjusted so that the midpoint values of the corresponding normalised fields (n and T_e) were 1, which meant $C_1 = 0.71$ and $C_2 = 14.06$. Finally, the position and the velocity of the blobs were determined based on a synthetic D_α diagnostic, which meant that the same tracing algorithms used for the experiment could be used for the simulation data.

Results

Before the simulation results were compared with the experiments, a cross-comparison between the four models was made. The comparison was made with $T_i = 0$ to eliminate differences in the interchange drives between the four models. All three 3D models generated a slight mushroom-like structure with the parameters used. HESEL on the other hand remained more rounded, retaining more of the initial shape, likely due to the sheath parametrisation employed. Despite the slight mushroom-like structures in the 3D models, the blobs remained mostly coherent. This coherence of the blobs was attributed to the large collisionality used in the simulations for parameters relevant to MAST, which smears out small-scale fluctuations. It was also observed that the radial propagation of the blobs in TOKAM3X was slower than in the other three models in the initial stages of propagation. This was attributed to the lack of electron inertia in the parallel dynamics in TOKAM3X, which lead to an instantaneous current to the sheath, effectively damping the dipole generated.

To investigate the effects of ion temperature dynamics and the different sheath closures used, HESEL was applied for blob 1 case 1 with cold ions, $T_i = 0$ and warm ions, $T_i = 2T_e$ and with two different sheath closures. One with the vorticity sink on the full profiles given by

$$\Lambda_{s,1,\omega} = \frac{2\rho_s}{L_\parallel}\left[1 - \exp\left(\Lambda - \frac{\varphi}{T_e}\right)\right], \tag{4.33}$$

and one with the vorticity sink on the poloidally averaged profiles given by

$$\Lambda_{s,2,\omega} = \frac{2\rho_s}{L_\parallel}\left[1 - \exp\left(\Lambda - \frac{\langle\varphi\rangle_y}{\langle T_e\rangle_y}\right)\right]. \tag{4.34}$$

The outcome of these simulations are seen in fig. 4.1. We observe that for the cold ion case, the blob remains less coherent, while it generates the mushroom-like shape seen in previous papers for simple blobs (see for example ref. [60]). Including ion temperature effects causes the blob to stay more coherent and to also propagate in the poloidal direction on top of the radial displacement. What is also seen in fig. 4.1 is that the sheath closure has a large influence on how the blob propagates. In the middle row the sheath damping on the vorticity is given by eq. (4.33). For this case we observe a smaller velocity, a more
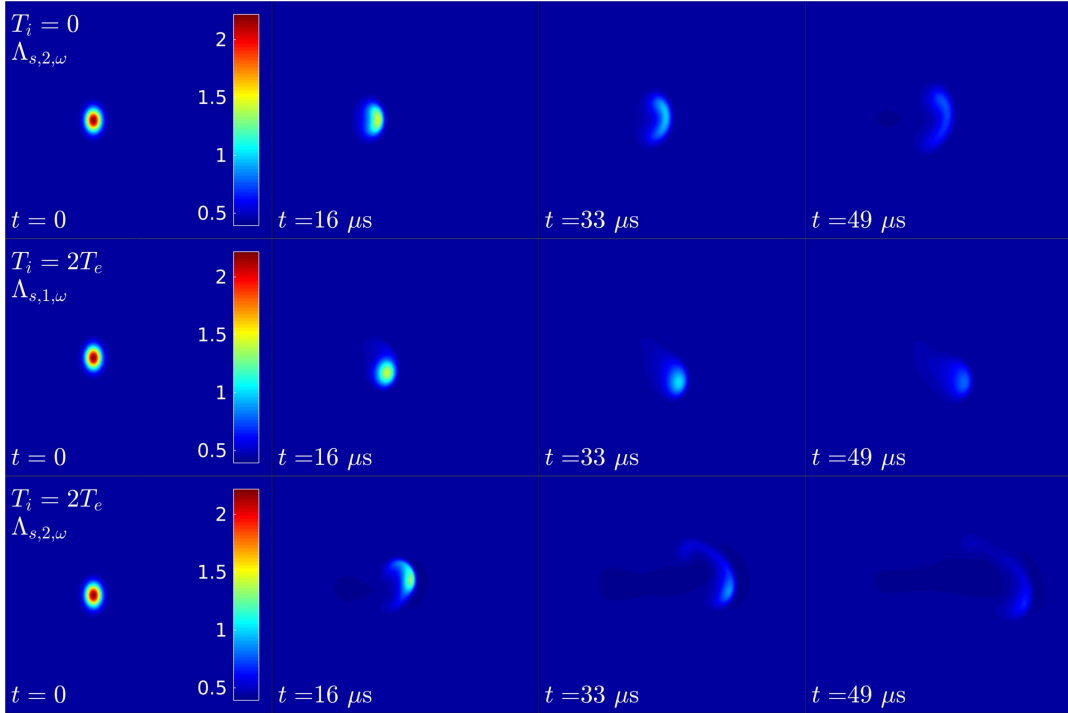
Figure 4.1: Propagation of blob 1 case 1 in three different scenarios in the HESEL simulations. The top row is for a simulation where ion temperature dynamics are switched off with a sheath closure based on the poloidally averaged electron temperature and potential. The middle row is for a simulation with $T_i = 2T_e$ and a sheath closure based on the full electron temperature and potential. The bottom row is for a simulation with $T_i = 2T_e$ and with a sheath clousure based on the averaged electron temperature and potential. The size of the domain is 40 cm in the radial direction and 25 cm in the poloidal direction.

coherent blob and a propagation in the opposite poloidal direction compared to the blob propagation observed in the last row in fig. 4.1, where the sheath dissipation closure is given by eq. (4.34). The differences are substantial, indicating that the sheath parametrisation needs to be used with care and the regime in which the blob propagates needs to be known before a comparison can be made between experiments and simulations. In the rest of the paper, the sheath parametrisation stated in eq. (4.34) was used for HESEL.

The remainder of the paper considered the experimental data where the comparison with the numerical simulations were based on the synthetic D_α diagnostic. For blob 1 in both case 1 and case 2, STORM3D and GBS produced results close to the experimentally found value, which lead to the conclusion that the temperature of the blob was roughly equal to the background temperature. TOKAM3X underestimated the filament velocity, explained by the lack of electron inertia, and HESEL greatly overestimated the velocity of blob 1 for all three cases, likely due to the ion temperature dynamics included in the model. The ion temperature dynamics lead to a larger interchange drive resulting in a much faster blob propagation than what was observed in the other models.

Case 3 was found to fit well for GBS and STORM3D for blob 2. TOKAM3X underestimated the blob position for this case and HESEL again estimated a velocity much faster than the other models. The conclusion based on STORM3D and GBS was that for blob 2, the temperature of the blob was much higher than the background.

The fact that HESEL consistently estimated a velocity much larger than the other models, due to the contribution from the ion temperature to the interchange drive, lead us to conclude that $T_i < 2T_e$ in the blobs considered in this validation exercise.

Regarding the poloidal motion, the same trends were seen as for the radial motion. TOKAM3X systematically underestimated the poloidal propagation, GBS and STORM3D fit well in case 1 and case 2 for blob 1 and in case 3 for blob 2, except for in the later stages of propagation. The discrepancy in the later stages of propagation in case 3 blob 2 for GBS and STORM3D was attributed to the experimental blob experiencing internal reconstruction. HESEL on the other hand showed trends opposite of what was seen in the experiments for all cases of both blobs, which was linked to the fact that the poloidal displacement and rotation is an attribute of ion temperature dynamics[61] and 3D effects[51], where the 3D effects are parametrised in HESEL and are thus not expected to be fully captured by the model.

Conclusions

The conclusions from this validation exercise were again mostly based on the comparison between the four numerical models, since the diagnostics to determine the filament parameters were lacking. This meant that the background was initialised as being flat, where the conclusion for the TORPEX validation exercise was that a background profile has a large influence on the blob propagation. Furthermore ion temperatures were not measured and the blobs were initialised without a potential perturbation which means that a potential field has to build up before the blob propagates, unlike in the experiment where it is already moving. However, we did learn some key points from comparing the numerical models. First, ion temperature dynamics greatly influence blob propagation, breaking the poloidal symmetry of the blob and causing it to propagate faster. We also learned that blob propagation greatly depends on the sheath parametrisation used. If poloidally averaged potential and temperature fields are used, the connection to the sheath is weak and the blob will propagate faster and remain less coherent compared to when the full fields are taken into account in the parametrisation.

4.2 Temperature dynamics and velocity scaling laws for interchange driven, warm ion plasma filaments

The two validation exercises performed in section 4.1 did not fully capture the dynamics of the experimentally observed blobs. However, the conditions in TORPEX were different from what the models are designed for and the diagnostics in MAST were lacking. Furthermore, several interesting results were gathered from the code validation exercises, where it was found that background profiles, 3D parametrisations and electron and ion temperature dynamics greatly influence the dynamics of blobs. We therefore move on to investigate how different parameters influence blob propagation. Specifically we wish to investigate how temperature dynamics influence seeded blobs.

4.2.1 Introduction

In order to investigate how temperature dynamics influences blob propagation, we performed a separate study with seeded blobs using the HESEL model. To isolate the effects of temperature dynamics, the blobs were initialised on a flat background and all parallel dynamics were completely removed from the HESEL equations. Since the driving mechanism for blobs in the far SOL region is believed to be the so-called interchange drive[62, 63], which is captured well by the HESEL model, we believe that this study can shed light on the propagation of blobs in the SOL.

The study is published in *Plasma Phys. Contr. Fusion* (vol. 58 issue 4) on the 22$^{\text{nd}}$ February 2016[64] and is republished here with the permission of IOP publishing.

In the paper we describe the influence of temperature dynamics on cross-field blob convection and investigate how the radial velocity of blobs scales with the blob size, σ, the blob amplitude, Δn, and ion to electron temperature ratio, $\tau = T_{i0}/T_{e0}$. First we qualitatively describe the effects of including temperature evolution and perturbations on the dynamics of seeded blobs by comparing simulations with different degrees of temperature effects included. We then move on to investigate the effects of different initial parameters on blob dynamics using full temperature dynamics and initial temperature perturbations. Finally, we investigate the validity of two existing blob velocity scalings with different initial parameters.

Temperature dynamics and velocity scaling laws for interchange driven, warm ion plasma filaments

Jeppe Olsen, Jens Madsen, Anders Henry Nielsen, Jens Juul Rasmussen and Volker Naulin

PPFE, Department of Physics, Technical University of Denmark, Building 309, 2800 Kgs. Lyngby, Denmark

E-mail: jmbols@fysik.dtu.dk, jmad@fysik.dtu.dk, ahnie@fysik.dtu.dk, jjra@fysik.dtu.dk and vona@fysik.dtu.dk

CrossMark

Abstract

The influence of electron and ion temperature dynamics on the radial convection of isolated structures in magnetically confined plasmas is investigated by means of numerical simulations. It is demonstrated that the maximum radial velocity of these plasma blobs roughly follows the inertial velocity scaling, which is proportional to the ion acoustic speed times the square root of the filament particle density times the sum of the electron and ion temperature perturbations. Only for small blobs the cross field convection does not follow this scaling. The influence of finite Larmor radius effects on the cross-field blob convection is shown not to depend strongly on the dynamical ion temperature field. The blob dynamics of constant finite and dynamical ion temperature blobs is similar. When the blob size is on the order of 10 times the ion Larmor radius the blobs stay coherent and decelerate slowly compared to larger blobs which dissipate faster due to fragmentation and turbulent mixing.

Keywords: velocity scaling, warm ions, scrape-off layer transport, blob dynamics

(Some figures may appear in colour only in the online journal)

1. Introduction

The radial transport of particles and heat out of the confining region of magnetically confined toroidal plasmas and into the region of open magnetic field-lines, known as the scrape-off layer (SOL), is an ongoing topic of investigation in fusion research. Whether the transport is turbulent or due to neo-classical drift-orbit effects is largely debated in the community [1, 2]. It is, however, well established that the radial transport in the far SOL is predominantly turbulent [3, 4]. The turbulence in the far SOL region is known to be strongly intermittent resulting in broadened particle density and temperature probability distribution functions (PDFs) skewed with a broad tail toward positive perturbations. The intermittent transport is carried in the form of filamentary structures aligned along the magnetic field. The filaments propagate perpendicular to the magnetic field at a significant fraction of the acoustic speed

[5–8]. These filamentary structures are known as blobs in low confinement (L-mode) [9–14] and edge localised mode (ELM) filaments in high confinement (H-mode) [15–18]. Although the generation mechanisms for blobs and ELMs are different, the mechanism driving both types of filaments towards the wall is believed to be the interchange drive [15, 19–21]. The blobs give rise to problems such as erosion of the main chamber walls where the resulting impurities influence operation parameters such as the density disruption limit [21, 22]. The blobs result in peak heat loads at plasma facing components much higher than predicted by classical theory. Predictions of the peak heat loads thus require a thorough understanding of the blob temperature dynamics. In particular, since the ion temperature typically exceeds the electron temperature in a tokamak SOL [23, 24], a proper description requires models which include the temperature dynamics of both electrons and ions. Temperature dynamics is also a necessity for describing

the interaction of blobs with neutral particles, e.g. T_e for electron impact ionization and T_i for charge exchange, which, in general, have very strong dependencies on temperature [25]. The blob-neutral interactions define a non-negligible particle source and imply energy and momentum losses and are therefore essential when describing plasma dynamics in fusion relevant experiments.

Extensive numerical studies of the dynamics of seeded blobs have been made in previous studies [14, 26–29] which have aimed at deducing scaling laws for the radial velocity of blobs. However, most models did not include temperature dynamics and assumed cold ions. Although these simplifications are reasonable in the description of most basic plasma physics experiments [30–32], it is generally not the case in a tokamak SOL. Recent studies [33–37] have shown that finite ion temperature effects alter the cross field blob transport. Blobs stay coherent and decelerate at a slower rate than cold ion blobs. Furthermore, the observed structures in gas-puff imaging (GPI) observations [38] and finite ion temperature simulations show very similar dynamics. However, the finite ion temperature studies have not included ion temperature dynamics and collisional effects are treated in an ad-hoc manner. Collisional effects influence the cross-field transport blob transport [39] and play an important role in the SOL region profile broadening in the high density limit and in divertor detachment [40]. A consistent model for collisional effects is therefore important for any effort modelling blob transport in the high density limit.

In this paper we investigate the dynamics of blobs in the SOL region by means of numerical simulations. Specifically, we describe the influence of temperature dynamics on the cross-field blob convection and investigate how the radial blob velocity scales with blob size, amplitude, and ion to electron temperature ratio. Furthermore, we investigate the validity of two scaling laws for the maximum radial blob velocity. We apply a four-field drift fluid model, HESEL (Hot Edge-Sol ELectrostatic turbulence), based on the Braginskii equations, describing the evolution of the particle density, generalised vorticity and electron and ion pressure. Collisional transport is described by a partly linearized model derived from the Braginskii equations.

The article is outlined as follows: in section 2 we describe the HESEL model used in the simulations. In section 3 we qualitatively describe the effects of including temperature evolution and perturbations on the dynamics of seeded blobs by comparing simulations with different degrees of temperature effects. In section 4 we investigate the effect of different initial parameters on blob dynamics with full temperature evolution and initial perturbations. In section 5 we test the validity of existing blob velocity scalings with different initial parameters. Finally in section 6 we summarise and conclude our results.

2. The HESEL model

The investigations have been carried out using the HESEL model [41–43]. HESEL is an energy conserving 2D drift fluid model derived from the Braginskii equations using slab

geometry, which describes the evolution of four fields: The particle density, n, the generalised vorticity, ω, the electron pressure, p_e, and the ion pressure, p_i. The governing equations are Bohm normalised according to (see for example [44]),

$$\omega_{ci} t \to t, \quad \frac{\mathbf{x}}{\rho_s} \to \mathbf{x}, \quad \frac{e\phi}{T_{e0}} \to \varphi, \quad \frac{n}{n_0} \to n, \quad \frac{T_e}{T_{e0}} \to T_e, \quad \frac{T_i}{T_{e0}} \to T_i, \tag{1}$$

where $\omega_{ci} = eB_0/m_i$ is the ion cyclotron frequency, $\rho_s = c_s/\omega_{ci}$ is the ion gyroradius at background electron temperature, e is the electron charge, T_{e0} is the background electron temperature, n_0 is the background particle density, B_0 is the magnetic field at major radius R_0, m_i is the ion mass, $c_s = (T_{e0}/m_i)^{1/2}$ is the sound speed and $T_{e(i)}$ is the electron (ion) temperature. With this normalisation the equations are given as

$$\frac{d}{dt} n + n\mathcal{K}(\varphi) - \mathcal{K}(p_e) = \Lambda_n, \tag{2}$$

$$\frac{d^0}{dt} \omega + \{\nabla\varphi, \nabla p_i\} - \mathcal{K}(p_e + p_i) = \Lambda_\omega, \tag{3}$$

$$\frac{3}{2}\frac{d}{dt} p_e + \frac{5}{2} p_e \mathcal{K}(\varphi) - \frac{5}{2}\mathcal{K}\left(\frac{p_e^2}{n}\right) = \Lambda_{p_e}, \tag{4}$$

$$\frac{3}{2}\frac{d}{dt} p_i + \frac{5}{2} p_i \mathcal{K}(\varphi) + \frac{5}{2}\mathcal{K}\left(\frac{p_i^2}{n}\right) - p_i\mathcal{K}(p_e + p_i) = \Lambda_{p_i}. \tag{5}$$

Here, $d/dt = \partial/\partial t + B^{-1}\{\varphi, \cdot\}$ denotes the convective derivative with the compressible magnetic field, $B(x)\hat{\mathbf{z}} = (B_0 R_0) / (R_0 + r_0 + x)\hat{\mathbf{z}}$, where x is the radial position, R_0 and r_0 denote the major and minor radius, respectively, and $\hat{\mathbf{z}}$ is a unit vector parallel to the magnetic field. $d^0/dt = \partial/\partial t + B_0^{-1}\{\varphi, \cdot\}$ denotes the convective derivative with constant magnetic field B_0 and $\mathcal{K}$ is the curvature operator defined as

$$\mathcal{K}(f) = -\frac{\rho_s}{R_0}\frac{\partial}{\partial y} f. \tag{6}$$

The $\mathbf{E} \times \mathbf{B}$ advection is written in the terms of a Poisson bracket defined as

$$\{\varphi, f\} = \frac{\partial\varphi}{\partial x}\frac{\partial f}{\partial y} - \frac{\partial f}{\partial x}\frac{\partial\varphi}{\partial y}. \tag{7}$$

$\omega = \nabla^2(\varphi + p_i)$ is the generalised vorticity, which contains the magnetic field aligned components of the $\mathbf{E} \times \mathbf{B}$ vorticity, $\nabla^2\varphi$, and the ion diamagnetic contribution, $\nabla^2 p_i$. Finite Larmor radius (FLR) effects are thus only included to lowest order, which means that $k_\perp^3 \rho_i^3 \ll 1$ is assumed, where $k_\perp$ is the characteristic perpendicular inverse length scale, $\rho_i = (T_{i0}/m_i)^{1/2}\omega_{ci}^{-1}$ is the thermal ion gyroradius and T_{i0} is the background ion temperature (see [33] and [45] for a thorough description of FLR effects in drift fluid models). Furthermore we note that the thin-layer approximation [46], which resembles the Boussinesq approximation, is invoked in the vorticity equation (equation (3)). The central assumptions of the thin-layer

approximation are small perturbation amplitudes and gradients in the particle density field. Although this is not fulfilled in the case of blobs, previous studies [34] have shown that the approximation does not significantly alter the evolution of blobs in the early stages of propagation. Since we wish to investigate the effects of dynamic temperatures as well as blob transport through the maximum centre of mass velocity, which occurs early in the propagation of the blob, we have invoked the thin-layer approximation for computational expediency.

The terms on the right-hand sides are the dissipative terms defined as

$$\Lambda_n = D_n(1 + \tau)\nabla^2 n \tag{8}$$

$$\Lambda_\omega = D_i\nabla^2\omega \tag{9}$$

$$\Lambda_{p_e} = D_n\left[\frac{5}{2}(1 + \tau)\nabla^2 p_e + \left(\frac{13}{6} - \frac{5}{2}\tau\right)\nabla \cdot (n\nabla T_e)\right.$$
$$\left. + (1 + \tau)\nabla \ln n \cdot \nabla p_i\right] - \frac{3m_e}{m_i}\nu_{ei}(p_e - p_i) \tag{10}$$

$$\Lambda_{p_i} = \left[\frac{5}{2}D_n(1 + \tau)\nabla \cdot (T_i\nabla n) - D_n(1 + \tau)\nabla \ln n \cdot \nabla p_i\right.$$
$$\left. + D_i(\nabla^2 p_i - p_i\nabla^2 \ln n - \nabla \ln n \cdot \nabla p_i)\right]$$
$$+ \frac{3m_e}{m_i}\nu_{ei}(p_e - p_i) + p_i\Lambda_\omega, \tag{11}$$

where $\tau = T_{i0}/T_{e0}$. The temperatures are defined as $T_{e(i)}(x, y, t) = p_{e(i)}(x, y, t)/n(x, y, t)$. Note that all parallel effects, including sheath dissipation, have been neglected. The dissipative terms account for friction, electron heat fluxes, and energy exchange due to electron-ion collisions and viscosity and ion heat fluxes due to ion-ion collisions. These collisional terms are written in terms of the diffusion coefficients

$$D_n = (1 + 1.6q^2)\rho_e^2\nu_{ei}, \tag{12}$$

$$D_i = (1 + 1.6q^2)\rho_i^2\nu_{ii}, \tag{13}$$

where ν_{ii} and ν_{ei} are the normalized ion-ion and electron-ion collision frequencies, respectively, $\rho_{e(i)} = \omega_{ce(i)}^{-1}(T_{e(i)0}/m_{e(i)})^{1/2}$ is the electron (ion) thermal gyroradius and $\omega_{ce(i)} = eB_0/m_{e(i)}$ is the electron (ion) cyclotron frequencies. The diffusion coefficients are evaluated using the background values n_0, T_{e0} and T_{i0}. The 1.6 q^2 factor is the neo-classical Pfirsch–Schlüter correction to the diffusion coefficients, where q denotes the safety factor at the last closed flux surface (LCFS) (see [47] for a thorough description of these diffusive terms).

Previous studies [14, 28, 39] have shown that the maximum radial velocity of interchange driven blobs is captured well by the inertial scaling

$$V_{iner} = \gamma\sigma = c_s\left(\frac{\sigma\Delta\Theta}{R\Theta_0}\right)^{1/2}. \tag{14}$$

Here, $\gamma = V/\sigma$ denotes the interchange rate and σ is the characteristic blob size. Θ is a thermodynamic quantity (e.g. n, p_e, p_i) and Θ_0 is a uniform background. In order to eliminate

effects already described by the inertial scaling, we use this normalisation to investigate the differences in blob dynamics.

In order to describe the blob motion, we define the blob centre of mass position

$$\mathbf{x}_{CoM}(t) \equiv \frac{1}{\int (n(x, y, t) - n_0)\mathrm{d}\mathbf{x}} \int (n(x, y, t) - n_0)\mathbf{x}\mathrm{d}\mathbf{x} \tag{15}$$

where the integration is over the entire domain and where $\mathbf{x} = (x, y)$ is used to define the position of the blob. We consider a deuterium plasma with parameters typical for ASDEX Upgrade (AUG)

$$T_{e0} = 40 \text{ eV}, \ n_0 = 1 \times 10^{19} \text{ m}^{-3}, \ B_0 = 1.86 \text{ T} \tag{16}$$

$$R_0 = 1.65 \text{ m, and } r_0 = 0.5 \text{ m.} \tag{17}$$

3. Effect of temperature dynamics

In the following we will describe the effects of including initial temperature perturbations and temperature dynamics on the evolution of seeded blobs. The blobs are initialised as Gaussian perturbations on constant backgrounds

$$n(x, y, 0) = n_0 + \Delta n \exp\left(-\frac{(x - x_0)^2 + (y - y_0)^2}{2\sigma^2}\right), \tag{18}$$

$$T_e(x, y, 0) = T_{e0} + \Delta T_e \exp\left(-\frac{(x - x_0)^2 + (y - y_0)^2}{2\sigma^2}\right), \tag{19}$$

$$T_i(x, y, 0) = T_{i0} + \Delta T_i \exp\left(-\frac{(x - x_0)^2 + (y - y_0)^2}{2\sigma^2}\right), \tag{20}$$

where (x_0, y_0) is the initial blob position, Δn is the initial particle density perturbation amplitude, σ is the initial blob radius, and $\Delta T_{e(i)}$ is the initial electron (ion) temperature perturbation amplitude. The potential, φ, and generalised vorticity, ω, are both initialised to 0. The magnetic field is set to point out of the plane, and the simulations are carried out in a square box with a side length of $L = 40\sigma$. We invoke periodic boundary conditions in the y-direction and apply Dirichlet boundary conditions

$$\phi = 0, \quad \omega = 0, \quad n = n_0, \quad T_e = T_{e0}, \quad T_i = T_{i0} \tag{21}$$

at both radial boundaries $x = 0$ and $x = L_x$. The spatial resolution is $\sigma/dx = 50$, where dx is the numerical grid resolution, to ensure that the simulations converge with respect to the size of the simulation domain.

We have investigated the evolution of seeded blobs for four different cases with varying degrees of temperature dynamics included in the governing model equations: 1; ions are cold except in calculations of the ion diffusion coefficient, D_i, and electron and ion temperature dynamics is neglected. This means that we only solve equations (2) and (3) and neglect all contributions from finite ion temperature effects in the vorticity equation, equation (3). 2; Electron temperature dynamics has been included but the ions are cold, which means that we

Table 1. Detail of temperature dynamics for the four different cases.

Case	Electron temperature	Ion temperature	ΔT_e	ΔT_i
1	$T_{e0} = $ const.	0	0	0
2	$T_e(x, y, t)$	0	$T_{e0}\Delta n/n_0$	0
3	$T_e(x, y, t)$	$T_{i0} = $ const.	$T_{e0}\Delta n/n_0$	0
4	$T_e(x, y, t)$	$T_i(x, y, t)$	$T_{e0}\Delta n/n_0$	$T_{i0}\Delta n/n_0$

are solving equations (2)–(4), but where the finite ion temperature effects are removed in the same way as in case 1. (3) Electron temperature dynamics is included and the ions are warm. Finite ion temperature effects are included by setting $p_i(x, y, t) = T_{i0}n(x, y, t)$ at each time step and then solving equations (2)–(4). (4) Both electron and ion temperature dynamics are included by solving the full set of HESEL equations, equations (2)–(5). The four cases are summarised in table 1.

In figure 1 we have plotted the density, vorticity, electron and ion temperatures at $t = 20\gamma^{-1}$ for simulations of all four cases. At $t = 20\gamma^{-1}$ the blobs have moved approximately 5 times their initial size, σ, and differences in the blob convection in the different simulations are perceptible at this time. For the initial blob size used in this section, $\sigma = 10$, the blobs have moved 5 cm, which is less than the typical SOL region width in AUG. The parameters used for all four simulations are $\Delta n = 0.5n_0$ and $\tau = 1$. Upon comparing case 2 with case 1, we see that the inclusion of electron temperature dynamics causes the blob to spread out more and the lobes behind the front to curl up, but otherwise no big differences are observed. The electron temperature in case 2 is seen to closely resemble the particle density, but due to stronger diffusion, the electron temperature is less localised.

Looking at case 3 in the third row in figure 1, it is seen that the most prominent difference between the cold ion simulations and the inclusion of finite ion temperatures is in the vorticity where the up-down symmetry is broken, and the vorticity is elongated along the blob. As a result we see that the up-down symmetry of the blob particle density is broken and the blob stays more coherent, as was also observed in previous works (see for example [33]). As shown in the next section the influence of finite ion temperatures is stronger when the ratio of the ion gyroradius to the blob size increases. The bottom plot shows the blob when both electron and ion temperature dynamics are included solving the full set of HESEL equations (case 4). Here, we observe that the symmetry breaking is more profound than in the constant ion temperature case and the blob propagates further downwards. As for the case with no ion temperature effects and electron temperature dynamics, the blob is more spread out. These effects increase with ion to electron temperature ratio. The ion temperature is observed to be less localised than both the electron temperature and the particle density, but it still closely resembles both. This is due to the much stronger diffusion on the ions compared to the electrons (a factor of 10^2). Overall, however, we do not observe significantly different blob dynamics with the inclusion of a dynamic ion temperature compared to the finite ion temperature case.

4. Velocity dependence on blob size, amplitude, and ion temperature

We now move on to examine the effects of different initial parameters on the dynamics of the blobs. Throughout the rest of the paper, the simulations are carried out using the full HESEL model including both electron and ion temperature dynamics. The blobs are initialised according to equations (18)–(20) using case 4 in table 1, where we vary the initial blob width, σ, the ion to electron temperature ratio, τ, and the initial blob particle density perturbation, Δn. Figure 2 shows the evolution of four different blobs with different initial parameters which capture the general trends of the simulations. For low values of τ, illustrated in the first row, the blob generates the typical mushroom shape seen in for example [26]. For the high ion temperature blobs, otherwise with the same parameters (second row in figure 2), the up-down symmetry is broken due to the increased contribution of the ion pressure in the vorticity equation. The high ion temperature blob seen in row 2 propagates in the $\mathbf{B} \times \nabla B$ direction as was also observed in [33] leaving behind part of the initial mass and propagating as a smaller more coherent structure. The symmetry breaking is not observed for low amplitude blobs as illustrated in the third row of figure 2. The blob dissipates fast due to collisional diffusion and generates the typical mushroom shape, also seen for low ion temperatures, due to the smaller contribution of the ion pressure to the generalised vorticity. Finally, comparing rows 2 and 4 in figure 2, it is seen that larger blobs leave behind more of the initial mass and the curl-up of the lobes is more profound than for smaller blobs.

The curling up of the lobes is, as described in [33], a consequence of poloidal gradients in the radial component of the advecting $\mathbf{E} \times \mathbf{B}$ velocity field which peaks at $y = 0$. This means that the blob centre is advected faster than the blob sides, which generates the typical mushroom-like shape. As seen in section 3 the blob centre consists of two layers of oppositely signed vorticity. This creates a shear flow which gives rise to the Kelvin–Helmholtz instability [48] resulting in a curling up of the lobes, seen, e.g. in row 4 in figure 2. The sheared flow is stabilised when FLR effects become significant with increasing $k_\perp\rho_i$, where $k_\perp^{-1}$ is the characteristic length-scale. This reduces the curling up of the lobes and causes the blob to stay more coherent [33].

In figure 3 we have plotted the evolution of the radial centre of mass velocity, $V = \mathrm{d}/\mathrm{d}t(x_{\mathrm{com}})$, as a function of time for the four cases displayed in figure 2. We see that all blobs initially accelerate, reach a maximum velocity and then decelerate due to sheared flows and collisional diffusion. Upon comparing the black (dash-dot) and the blue (dashed) curve we observe that the velocity of blobs subjected to strong FLR effects flattens at late stages. This flattening can be attributed to the blobs slowing down in the poloidal direction which leads to a reversal of the poloidal propagation. This reversal in the direction of the poloidal propagation results in a slight radial acceleration seen as the flattening in the blue (dashed) curve in figure 3.
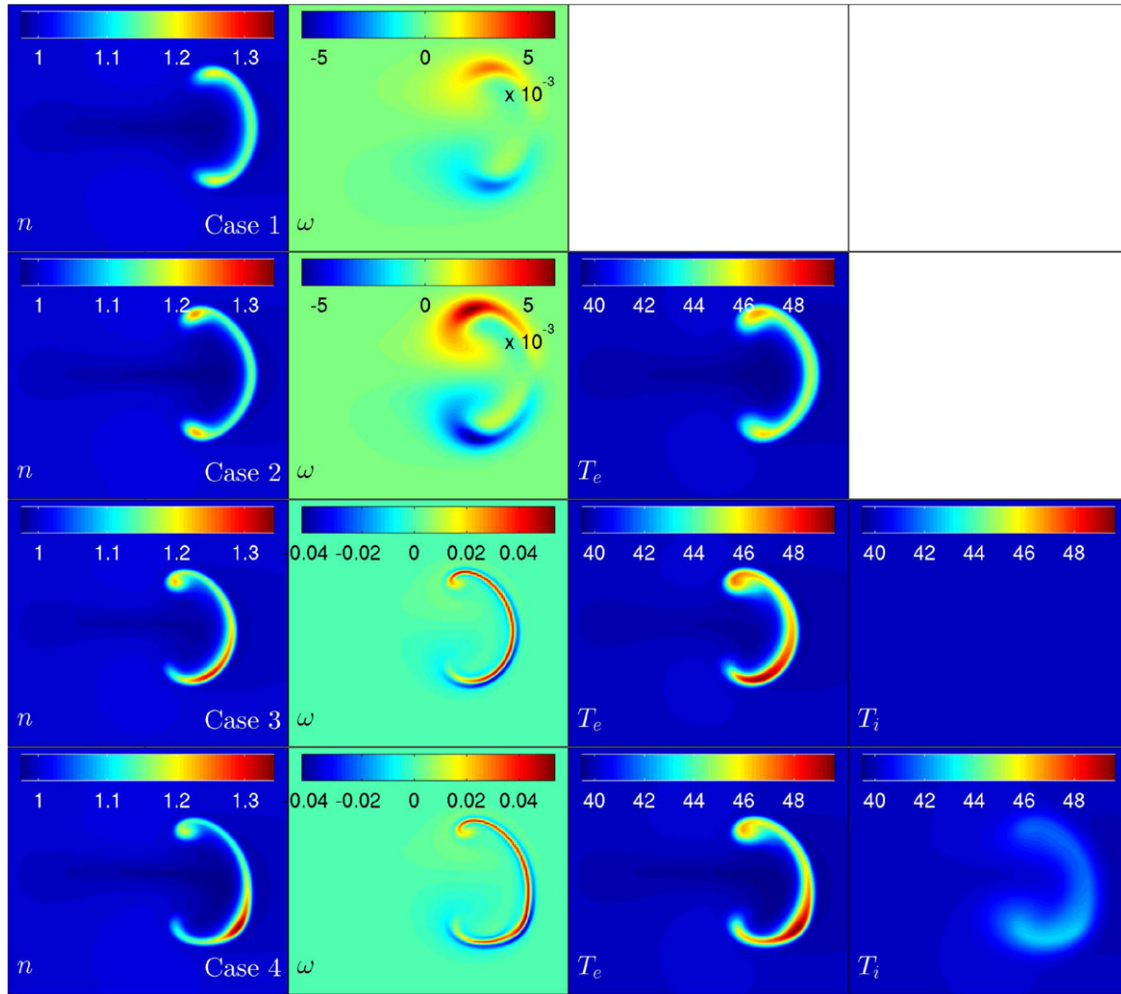
Figure 1. Contour plots of the four fields at $t = 20\gamma^{-1}$. All blobs are initialised with the same parameters, but solved including different degrees of temperature dynamics and perturbations (see table 1). The boxes only show part of the simulation domain displaying a square box of size $5\sigma \times 5\sigma$.

The compactness [33], defined as

$$I_c(t) \equiv \frac{\left(\int (n(x,y,t) - n_0)\mathrm{d}\mathbf{x}\right)h(x,y,t)}{\left(\int (n(x,y,0) - n_0)\mathrm{d}\mathbf{x}\right)h(x,y,0)}, \qquad (22)$$

is a measure of blob coherence. Here, h is a Heaviside function given by

$$h(x,y,t) \equiv \begin{cases} 1 & \text{if } (x - x_{\max}(t))^2 + (y - y_{\max}(t))^2 < \sigma^2 \\ 0 & \text{else,} \end{cases} \qquad (23)$$

The integration is over the entire domain, and $x_{\max}$, $y_{\max}$ denote the positions of the radial and poloidal maximal particle densities, respectively. I_c thus describes the integrated particle density in a ball of radius σ centred at $(x_{\max}, y_{\max})$, normalised to $I_c(t=0) = 1$. When the particle density is preserved, $I_c = 1$, whereas $I_c \to 0$ for a completely dispersed blob.

In [33, 34] it was observed that the defining parameter for the blob coherence resulting from FLR effects depends on both initial ion temperature, blob width and blob particle density perturbations. A dimensionless quantity, r, containing these parameters was introduced to quantify the different regimes of the dynamics:

$$r \equiv \frac{\rho_i \Delta n}{\sigma n_0}. \qquad (24)$$

The compactness, I_C, at time $t = 10\gamma^{-1}$ is plotted as a function of r in figure 4. We observe a transition in blob compactness between $r = 0$ and $r = 0.1$, as was also seen in [33, 34]. By inspection of the simulation results, this is consistent with a transition from plume-like to more coherent structures. The black symbols, which denote the compactness of small blobs, do not show the same transition as the larger blobs. Instead the small blobs show high compactness for all values of r after $10\ \gamma^{-1}$. We believe this is due to a breakdown of the interchange scaling in the extreme cases of very low particle density perturbations and small blob widths, as will be discussed in section 5. At very low Rayleigh number this mismatch of the inertial scaling was also observed by Garcia *et al* [14].

5. Velocity scaling laws

We now wish to investigate the validity of two different existing scaling laws for the maximum radial centre of mass
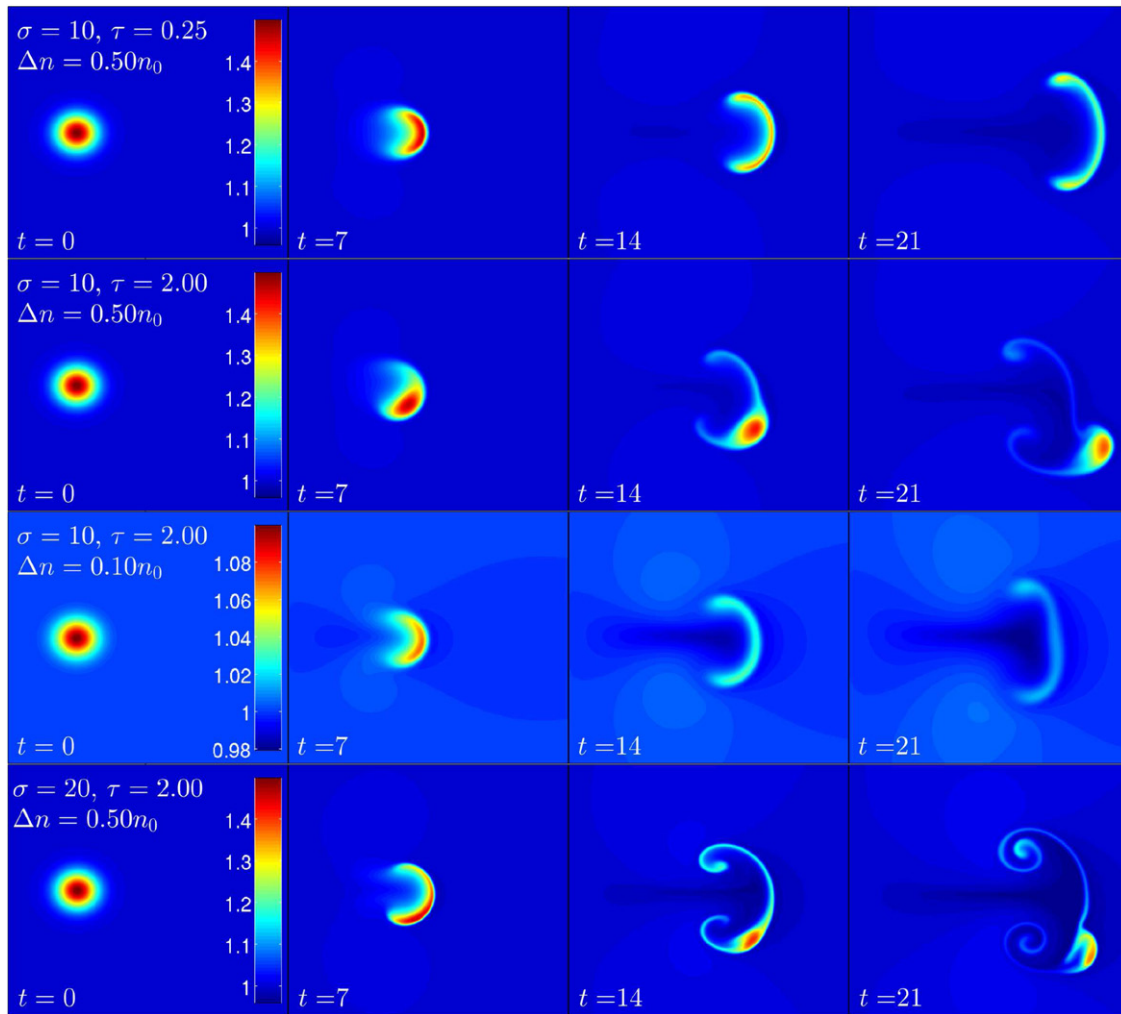
Figure 2. Particle density of four different blobs in time steps of $7\gamma^{-1}$. The displayed domain is a square of size $5\sigma \times 5\sigma$, which is only part of the full simulation domain. The colour scheme is kept constant in each row, and the parameters used in each simulation are stated in the respective rows.
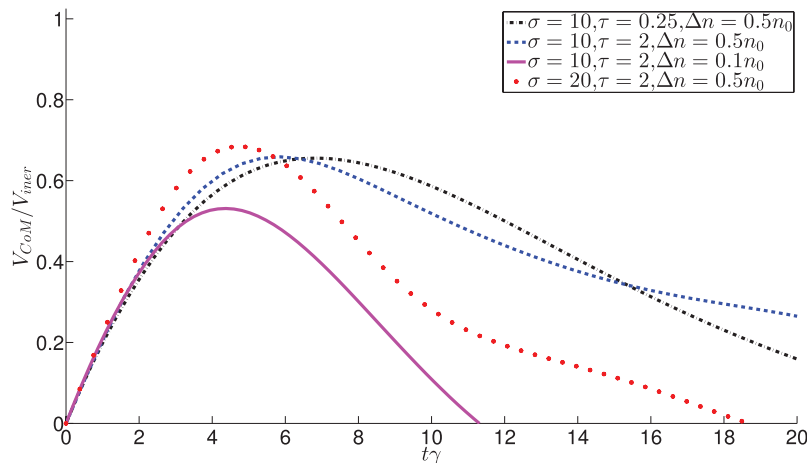

Figure 3. Evolution of the radial centre of mass velocity with time for the four different cases shown in figure 2.

velocity, $V_{\max}$. Both scalings are derived based on assumptions similar to what is assumed in the HESEL model, i.e. magnetic perturbations and parallel dynamics are neglected. In particular sheath damping is not included. It is therefore reasonable to compare the results from the simulations with the scaling laws.

The first scaling we compare with was introduced in [28] and is found by balancing the compression of the polarization and diamagnetic currents. It is given by equation (14) which, when both ion and electron pressure perturbations are included, is given by
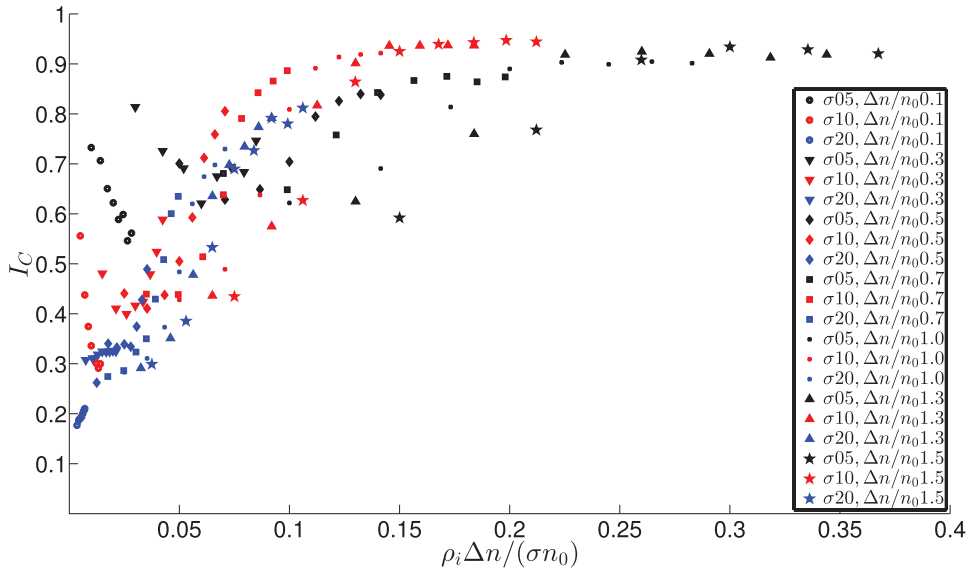
Figure 4. Compactness, I_c, of blobs as a function of $r = \rho_i \Delta n/(\sigma n_0)$ at $t = 10\gamma^{-1}$. A transition from plume-like blobs to more coherent structures between $r = 0$ and $r = 0.1$ is observed.

$$1: \frac{V_{\text{iner}}}{c_s} = \left(\frac{\sigma}{R} \frac{(\Delta p_e + \Delta p_i)}{p_0} \right)^{1/2}, \qquad (25)$$

where $p_0 = T_{e0} n_0$ is the background electron pressure, and Δp_e and Δp_i are the electron and ion pressure perturbations, respectively. This means that both the particle density perturbation and the electron and ion temperature perturbations contribute to V_{max}, e.g. $\Delta p = n_0 \Delta T + T_0 \Delta n + \Delta n \Delta T$. For all simulations we have initialised the blobs according to equations (18)–(20). With this initialisation, assuming the same form of the electron and ion pressures, equation (25) can be rewritten as

$$\frac{V_{\text{iner}}}{c_s} = \left(\frac{\sigma}{R} \frac{\Delta p_e}{p_0} \right)^{1/2} (1 + \tau)^{1/2}. \qquad (26)$$

The second scaling we consider is proposed in [27] and compared with experimental results in [49], where a convincing agreement between experiment and analytical scaling was not observed. It is derived from a model with electron temperature dynamics and finite but constant ion temperature assuming the ion and electron pressure perturbations to be of the same form. This scaling is given by

$$2: \frac{V_{\text{Manz}}}{c_s} = \sqrt{\frac{\sqrt{f^2 + g^2} - f}{2}}, \qquad (27)$$

where

$$f = \left(\frac{\tau \rho_s}{2\sigma} \frac{\Delta p_e}{p_0} \right)^2, \qquad \text{and} \qquad g = (1 + \tau) \frac{2\sigma}{R} \frac{\Delta p_e}{p_0}. \qquad (28)$$

It is worth noting that in the limit $g \gg f$ equation (27) reduces to the inertial scaling, equation (26). In the opposite limit, $g \ll f$, the scaling approaches

$$\frac{V_{\text{Manz}}}{c_s} \approx \frac{2(1 + \tau)\sigma^2}{\tau R \rho_s}. \qquad (29)$$

This means that for small blob widths, the limiting behaviour of scaling 2 is proportional to σ^2 and independent of Δp_e and independent of τ when $\tau \gg 1$.

The validity of these scalings is investigated by calculating V_{max}, normalising it with each scaling and plotting the normalised values. If the scaling captures the maximum velocity dependence on a parameter, the normalised values, $V_{\text{max}}/V_{\text{scaling}}$, should lie along a horizontal line when plotting them as a function of the given parameter. Here, V_{scaling} is the expected velocity calculated with equation (26) or (27). If the scaling fully captures the maximum velocity variation with all parameters, $V_{\text{max}}/V_{\text{scaling}}$, will be centred around 1.

In the following we investigate how V_{max} scales with the initial blob width, amplitude and ion temperature, and test the validity of the proposed scaling laws in equations (26) and (27). In sections 5.1 and 5.2 we have initialised the blobs with a particle density perturbation of $\Delta n/n_0 = 0.5$, which means that the temperature perturbations are initialised as $\Delta T/T_0 = 0.5$ as given in table 1.

5.1. Dependence on blob width

The first parameter dependence we investigate is the blob width, σ. We display two plots illustrating the general trends in figure 5, where figure 5(a) illustrates V_{max} normalised with c_s and figure 5(b) displays V_{max} normalised with V_{iner} (squares) and V_{Manz} (stars). To illustrate the differences in V_{max} with both weak and strong FLR effects, we have included simulations with two different initial ion temperatures. A case with weak FLR effects, $\tau = 0.5$ (red), and one with stronger FLR effects, $\tau = 2$ (black). It is evident from figure 5(b) that neither of the scalings capture the variations in maximum velocity for small blobs $\sigma < 10$ with large FLR effects. Scaling 1 is found to overestimate the velocity for small blobs, but does, however, overestimate it in the same way for both weak and strong FLR effects. Scaling 2, on the other hand, displays very different variations in V_{max} for
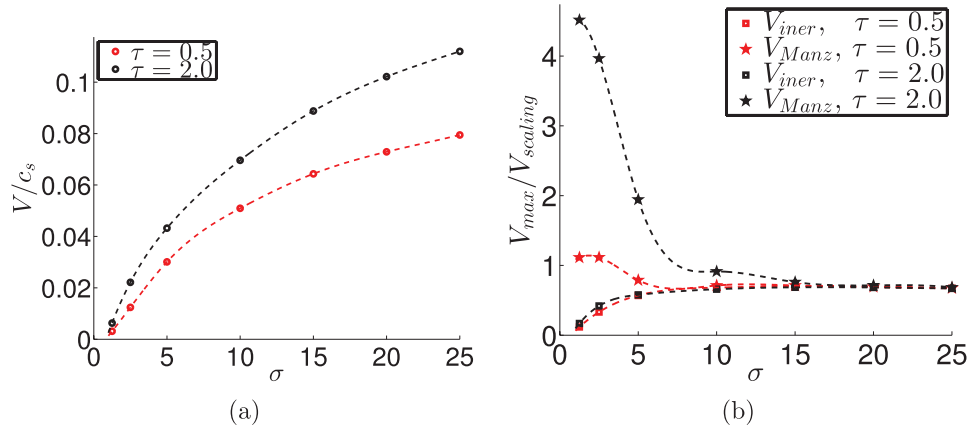
Figure 5. Maximum blob velocity as a function of initial blob width. The initial particle density perturbation is $\Delta n/n_0 = 0.5$. The red symbols are for $\tau = 0.5$ and the black symbols are for $\tau = 2$. The squares are the maximum velocities normalised by scaling 1 and the stars are the maximum velocities normalised by scaling 2.

Figure 6. Maximum blob velocity as a function of initial τ. The initial particle density perturbation is $\Delta n = 0.5n_0$, the red symbols are for $\sigma = 5$ and the black symbols are for $\sigma = 20$. The squares are the maximum velocities normalised by scaling 1 and the stars are the maximum velocities normalised by scaling 2.
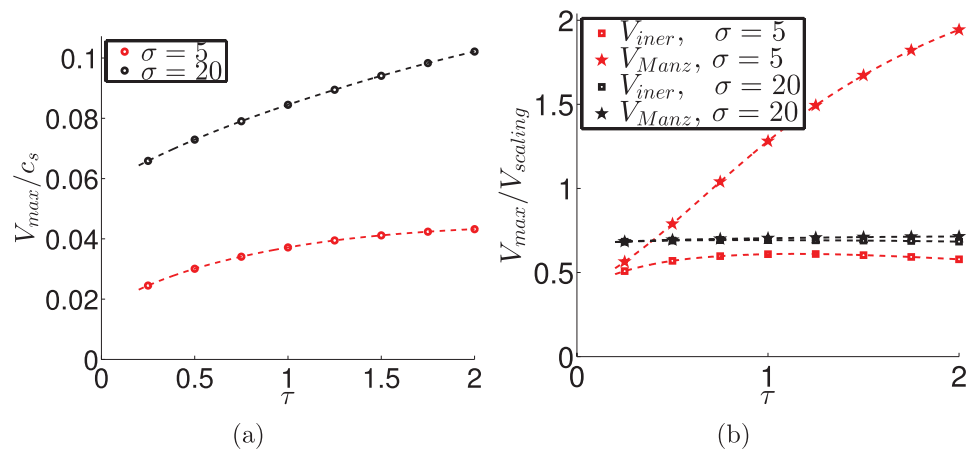
blobs with $\sigma < 10$ with different degrees of FLR effects. The scaling captures the velocity scaling well for weak FLR effects for this particular choice of ion temperature. Further investigations, which are not illustrated here, have, however, shown that the scaling significantly overestimates the blob velocity for $\tau < 0.5$ whereas the blob velocity is significantly underestimated for high ion temperatures. The scaling does thus not capture the velocity dependence on blob size for blobs with $\sigma < 10$. We note that HESEL assumes that $(\rho_i k_\perp)^3 \ll 1$, which means that it does not capture FLR induced blob dynamics for strong FLR effects correctly. But, since scaling 2 is based on assumptions similar to HESEL, this does not explain the observed discrepancies. However, both scalings capture the variations in maximum velocity with blob sizes of $\sigma > 10$ where the points approximately follow a horizontal line.

5.2. Dependence on ion temperature

Next, we investigate the influence of the initial ion temperature, τ, on V_{max}. Again we display two plots capturing the general trends here illustrated in figure 6. Figure 6(a) illustrates V_{max} normalised with c_s and figure 6(b) displays V_{max} normalised

with V_{iner} (squares) and V_{Manz} (stars). Since the scalings mainly differ for small blobs we examine how they depend on the initial blob ion temperature for two initial blob widths $\sigma = 5$ and $\sigma = 20$. For both blob sizes, it is seen that scaling 1 (squares) captures the dependence on τ well where the points are very close to being on a straight line for both blob sizes. Scaling 2 also captures the scaling well for large blobs, but does, however, underestimate the velocity dependence on τ for small blobs where it predicts no increase in V_{max} with increasing τ. This is in contrast to what is observed in the HESEL simulations, where the velocity is seen to increase with increasing τ (figure 6(a)). This indicates that scaling 2 is partly valid when FLR effects are weak, i.e. when $r < 0.05$, but does not match when FLR effects are strong, i.e. when $r > 0.05$.

5.3. Dependence on particle density perturbation

Finally we investigate the influence of the initial blob amplitude, Δn, on V_{max}. In the scalings the dependency on Δn is included in $\Delta p/p_0$. For blobs initialised according to equations (18)–(20) this is proportional to $\Delta n^2 + 2\Delta n$. Again, blobs with a small initial width, $\sigma = 5$, and a large initial
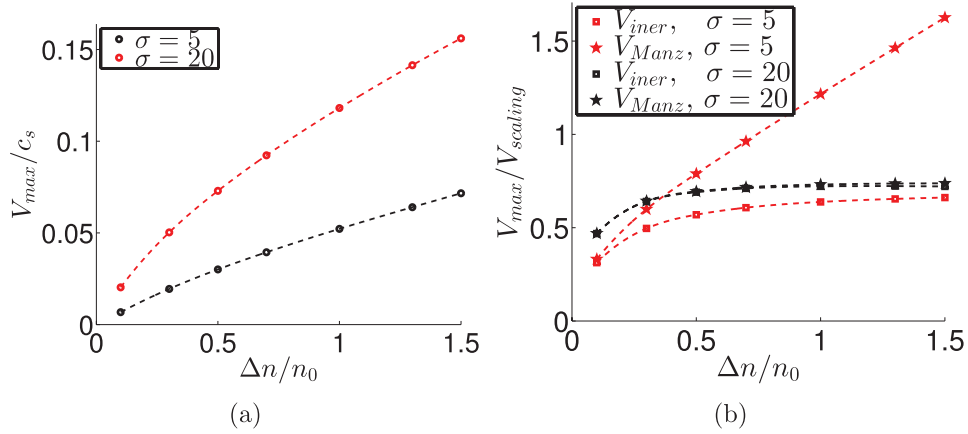
Figure 7. Maximum blob velocity as a function of initial Δn. The initial ion temperature is $\tau = 0.5$, the red symbols are for $\sigma = 5$ and the black symbols are for $\sigma = 20$. The squares are the maximum velocities normalised by scaling 1 and the stars are the maximum velocities normalised by scaling 2.

width, $\sigma = 20$, are examined. Figure 7 shows the maximum velocity as a function of Δn for blobs with an initial ion temperature of $\tau = 0.5$. For $\Delta n/n_0 < 0.5$ both scalings are observed to overestimate the maximum radial centre of mass velocity. For larger amplitudes $\Delta n/n_0 > 0.5$ scaling 1 describes the maximum velocity variations well for both blob sizes where the normalised points approximately follow a horizontal line. Scaling 2 also captures the maximum velocity variations well for large blobs, but does, however, underestimate the dependence on Δn for small blobs, as seen in figure 7(b), where the scaling predicts no increase in velocity with Δn. This limiting behaviour is opposite of what is observed in the HESEL simulations, which is displayed in figure 7(a).

6. Conclusion

In this paper we have examined the effects of dynamic temperatures on the evolution of interchange driven blobs and maximum centre of mass velocity by means of numerical simulations. We have employed a 2D drift fluid model dubbed HESEL which describes the dynamics in a plane perpendicular to the magnetic field at the outboard midplane of a Tokamak. We have observed that the inclusion of dynamic ion temperatures do not significantly alter the evolution of the seeded blobs compared to blobs with constant ion temperature. The inclusion of finite ion temperatures does, however, significantly alter the dynamics of the blobs. Finite ion temperatures introduce asymmetries in the blobs due to a contribution of the ion pressure to the vorticity equation. Blobs with zero ion temperature generate the typical mushroom shape, seen in for example [28], whereas the inclusion of finite ion temperatures introduces finite larmor radius (FLR) effects causing blobs to stay more coherent and propagating not only radially, but also poloidally in the $\mathbf{B} \times \nabla B$ direction. This transition from mushroom-like structures to coherent filaments can be described by the dimensionless parameter $r = \rho_i \Delta n/(\sigma n_0)$, where a transition is seen between $r = 0$ and $r = 0.1$. Here ρ_i is the ion gyroradius, Δn is the particle density perturbation of

the blob, σ is the initial blob width and n_0 is the background particle density.

Despite the qualitative differences in the cross-field convection, all blobs initially accelerate radially, reach a maximum velocity and slow down due to stretching and collisional diffusion. We have investigated how this maximum radial velocity scales with different initial parameters, since a scaling estimate of the maximum blob velocities is, e.g. important for estimating power loads. The blob velocity is directly related to the convective density flux carried by the blobs. In this respect we have compared two different scaling laws with the simulation results from HESEL. The first scaling is the inertial scaling given in equation (26), and is denoted as scaling 1. It is derived by balancing the compression of the polarization and the diamagnetic currents and predicts an increase in the maximum centre of mass velocity proportional to $\sqrt{\sigma}$. The second scaling, given in equation (27), is denoted as scaling 2 and is an extension of the inertial scaling aiming at capturing the influence of FLR effects on blob convection. The two scalings coincide when FLR effects are weak, but differ when the blob is subjected to strong FLR effects, where scaling 2 predicts an increase in maximum centre of mass velocity proportional to σ^2. We have observed that none of the suggested scaling laws cover the whole spectrum of parameters. For blobs larger than $\sigma = 10$ and for blobs with weak FLR effects both scaling laws describe the evolution with initial blob width well, but for blobs with $\sigma < 10$ subjected to strong FLR effects scaling 2 greatly underestimates the velocity, whereas scaling 1 slightly overestimates the velocity. The dependence on ion-electron temperature ratio, τ is observed to be described well by scaling 1 for all parameters, whereas scaling 2 predicts no increase in maximum velocity when strong FLR effects are present. This is opposite of what is observed in the HESEL simulations. For small initial blob particle density perturbations, $\Delta n/n_0 < 0.5$, both scaling laws overestimate the maximum velocity, whereas for large Δn, scaling 1 describes the variations in maximum velocity well. Scaling 2, on the other hand, predicts a constant maximum velocity with increasing particle density perturbation when strong FLR effects are

present, which is again not what is observed in the HESEL simulations, where the velocity is seen to increase with increasing particle density perturbations. We have thus concluded that although it does not cover the entire parameter range, scaling 1, which is also the simplest scaling model, is the most successful in describing the maximum radial centre of mass velocity with initial parameters.

We note that the thin-layer approximation has been invoked in the HESEL model, which may influence the evolution of the blobs at later stages. Previous studies [34] have, however, shown that the approximation does not significantly alter the evolution of blobs in the early stages of the propagation. Since the purpose of this paper is to investigate the influence of temperature dynamics and to test the validity of scalings of the maximum radial centre of mass velocity, which occurs in the early stages of propagation, we believe that the effects in this respect are not essential.

We recognise that the present investigation on seeded blobs does not necessarily carry over to self-consistently generated blobs in the turbulence at the edge-SOL region. However, we do believe that once the blobs have been created, they will obey the scalings observed here for seeded blobs. We therefore believe that future investigations in the interaction of blobs with neutrals in the SOL (both impurities and fuelling neutrals) will benefit from the results including temperature dynamics presented here. Both types of neutral interactions are of great interest, where the enhanced ionization by the hot and dense blobs may lead to outward shift of the ionization profiles [50]. This is desired with regard to the impurities resulting from sputtering, which then may not penetrate into the plasma. This is, however, problematic for the fuelling gas which remains in the SOL.

Acknowledgments

References

[1] Goldston R J 2012 Heuristic drift-based model of the power scrape-off width in low-gas-puff H-mode tokamaks *Nucl. Fusion* **52** 013009

[2] Eich T *et al* 2013 Scaling of the tokamak near the scrape-off layer H-mode power width and implications for ITER *Nucl. Fusion* **53** 093031

[3] Zweben S J 2007 Edge turbulence measurements in toroidal fusion devices *Plasma Phys. Control. Fusion* **49** S1

[4] Naulin V 2007 Turbulent transport and the plasma edge *J. Nucl. Mater.* **363–5** 24–31

[5] Boedo J *et al* 2001 Transport by intermittent convection in the boundary of the DIII-D tokamak *Phys. Plasmas* **8** 4826–33

[6] Antar G Y, Counsell G, Yu Y, Labombard B and Devynck P 2003 Universality of intermittent convective transport in the scrape-off layer of magnetically confined devices *Phys. Plasmas* **10** 419–28

[7] Garcia O *et al* 2006 Interchange turbulence in the TCV scrape-off layer *Plasma Phys. Control. Fusion* **48** L1

[8] Grulke O, Terry J, LaBombard B and Zweben S 2006 Radially propagating fluctuation structures in the scrape-off layer of Alcator C-Mod *Phys. Plasmas* **13** 012306

[9] Garcia O 2009 Blob transport in the plasma edge: a review *Plasma Fusion Res.* **4** 019–9

[10] Dippolito D, Myra J and Krasheninnikov S 2002 Cross-field blob transport in tokamak scrape-off-layer plasmas *Phys. Plasmas* **9** 222–33

[11] D'Ippolito D, Myra J, Krasheninnikov S, Yu G and Pigarov A 2004 Blob transport in the tokamak scrape-off-Layer *Contrib. Plasma Phys.* **44** 205–16

[12] Krasheninnikov S, D'ippolito D and Myra J 2008 Recent theoretical progress in understanding coherent structures in edge and SOL turbulence *J. Plasma Phys.* **74** 679–717

[13] Xu G S *et al* 2009 Blob/hole formation and zonal-flow generation in the edge plasma of the JET tokamak *Nucl. Fusion* **49** 092002

[14] Garcia O E, Bian N H and Fundamenski W 2006 Radial interchange motions of plasma filaments *Phys. Plasmas* **13** 082309

[15] Fundamenski W, Naulin V, Neukirch T, Garcia O E and Rasmussen J J 2007 On the relationship between ELM filaments and solar flares *Plasma Phys. Control. Fusion* **49** R43

[16] Kirk A *et al* 2006 Evolution of filament structures during edge-localized modes in the MAST tokamak *Phys. Rev. Lett.* **96** 185001

[17] Zohm H 1996 Edge localized modes (ELMs) *Plasma Phys. Control Fusion* **38** 105

[18] Kirk A *et al* 2004 Spatial and temporal structure of edge-localized modes *Phys. Rev. Lett.* **92** 245002

[19] Rudakov D *et al* 2002 Fluctuation-driven transport in the DIII-D boundary *Plasma Phys. Control Fusion* **44** 717

[20] Gonçalves B *et al* 2003 Edge localized modes and fluctuations in the JET SOL region *Plasma Phys. Control. Fusion* **45** 1627

[21] Rudakov D *et al* 2005 Far SOL transport and main wall plasma interaction in DIII-D *Nucl. Fusion* **45** 1589

[22] Greenwald M *et al* 1988 A new look at density limits in tokamaks *Nucl. Fusion* **28** 2199

[23] Kočan M *et al* 2012 Ion temperature fluctuations in the ASDEX Upgrade scrape-off layer *Plasma Phys. Control. Fusion* **54** 085009

[24] Kočan M *et al* 2009 Measurements of scrape-off layer ion-to-electron temperature ratio in tore supra ohmic plasmas *J. Nucl. Mater.* **390** 1074–7

[25] Marandet Y *et al* 2011 Transport of neutral particles in turbulent scrape-off layer plasmas *Nucl. Fusion* **51** 083035

[26] Kube R and Garcia O E 2011 Velocity scaling for filament motion in scrape-off layer plasmas *Phys. Plasmas* **18** 102314

[27] Manz P *et al* 2013 Filament velocity scaling laws for warm ions *Phys. Plasmas* **20** 102307.

[28] Garcia O, Bian N, Naulin V, Nielsen A and Rasmussen J J 2005 Mechanism and scaling for convection of isolated structures in nonuniformly magnetized plasmas *Phys. Plasmas* **12** 090701

[29] Yu G, Krasheninnikov S and Guzdar P 2006 Two-dimensional modelling of blob dynamics in tokamak edge plasmas *Phys. Plasmas* **13** 042508

[30] Windisch T, Grulke O and Klinger T 2006 Radial propagation of structures in drift wave turbulence *Phys. Plasmas* **13** 122303

[31] Furno I, Spolaore M, Theiler C, Vianello N, Cavazzana R and Fasoli A 2011 Direct two-dimensional measurements of the

field-aligned current associated with plasma blobs *Phys. Rev. Lett.* **106** 245001

[32] Happel T, Greiner F, Mahdizadeh N, Nold B, Ramisch M and Stroth U 2009 Generation of intermittent turbulent events at the transition from closed to open field lines in a toroidal plasma *Phys. Rev. Lett.* **102** 255001

[33] Madsen J, Garcia O E, Stæ rk Larsen J, Naulin V, Nielsen A H and Rasmussen J J 2011 The influence of finite Larmor radius effects on the radial interchange motions of plasma filaments *Phys. Plasmas* **18** 112504

[34] Wiesenberger M, Madsen J and Kendl A 2014 Radial convection of finite ion temperature, high amplitude plasma blobs *Phys. Plasmas* **21** 092301

[35] Kendl A 2015 Inertial blob-hole symmetry breaking in magnetised plasma filaments *Plasma Phys. Control. Fusion* **57** 045012

[36] Jovanović D, Shukla P and Pegoraro F 2008 Effects of the parallel electron dynamics and finite ion temperature on the plasma blob propagation in the scrape-off layer *Phys. Plasmas* **15** 112305

[37] Bisai N and Kaw P 2013 Role of ion temperature on scrape-off layer plasma turbulence *Phys. Plasmas* **20** 042509

[38] Maqueda R J 2003 Gas puff imaging of edge turbulence (invited) *Rev. Sci. Instrum* **74** 2020–6

[39] Kube R and Garcia O E 2012 Effect of dynamical friction on interchange motion of plasma filaments *Phys. Plasmas* **19** 042305

[40] Carralero D *et al* 2014 An experimental investigation of the high density transition of the scrape-off layer transport in ASDEX Upgrade *Nucl. Fusion* **54** 123005

[41] Madsen J, Nielsen A H, Naulin V and Rasmussen J J Cross-field collisional effects in low-frequency fluid models manuscript in preparation (arXiv: 1512.07425)

[42] Rasmussen J J, Nielsen A H, Madsen J, Naulin V and Xu G S 2015 Numerical modeling of the transition from low to high confinement in magnetically confined plasma *Plasma Phys. Control. Fusion* **58** 014031

[43] Nielsen A H, Xu G S, Madsen J, Naulin V, Rasmussen J J and Wan B N 2015 Simulation of transition dynamics to high confinement in fusion plasmas *Phys. Lett.* A **47–8** 3097–101

[44] Garcia O E 2001 Two-field transport models for magnetized plasmas *J. Plasma Phys.* **65** 81–96

[45] Scott B D 2007 Nonlinear polarization and dissipative correspondence between low-frequency fluid and gyrofluid equations *Phys. Plasmas* **14** 102318

[46] Garcia O E, Naulin V, Nielsen A H and Rasmussen J J 2005 Turbulence and intermittent transport at the boundary of magnetized plasmass *Phys. Plasmas* **12** 062309

[47] Fundamenski W *et al* 2007 Dissipative processes in interchange driven scrape-off layer turbulence *Nucl. Fusion* **47** 417

[48] Bian N, Benkadda S, Paulsen J V and Garcia O 2003 Blobs and front propagation in the scrape-off layer of magnetic confinement devices *Phys. Plasmas* **10** 671–6

[49] Manz P *et al* 2015 The influence of finite ion temperature on plasma blob dynamics *Plasma Phys. Control. Fusion* **57** 014012

[50] Thrysøe A S, Tophøj L E H, Naulin V, Rasmussen J J, Madsen J and Nielsen A H 2015 The influence of blobs on neutral particles in the scrape-off layer *Plasma Phys. Control. Fusion* submitted

4.2.3 Summary

In the paper we investigated the effects of temperature dynamics on blob propagation and investigated the validity of two existing velocity scaling laws. The study was carried out using the HESEL model described in sec. 2.7 with all parallel dynamics removed using seeded blobs initialised as Gaussian perturbations on a flat background.

First the effects of temperature dynamics were investigated with four different cases;

1: Ions were assumed cold, $T_i = 0$, and electrons were assumed isothermal, $T_e = T_{e0}$.

2: Ions were assumed cold, $T_i = 0$, and electrons were evolved dynamically, $T_e = T_e(x, y, t)$.

3: Ions were assumed isothermal but with a finite temperature, $T_i = T_{i0}$, and electrons were evolved dynamically, $T_e = T_e(x, y, t)$.

4: Both electrons and ions were evolved dynamically, $T_{e(i)} = T_{e(i)}(x, y, t)$.

In all four cases, the blobs were initialised with a density perturbation of $\Delta n = 0.5 n_0$, an ion to electron temperature ratio of $\tau = 1$ and a size of $\sigma = 10 \rho_s$. We observed that the inclusion of dynamic electron temperatures did not significantly alter the qualitative dynamics of the blob compared to the isothermal electron case. However, the inclusion of finite ion temperatures significantly altered the blob motion due to the contribution from the ion pressure to the interchange drive in the generalised vorticity. The inclusion of finite ion temperatures broke the up-down symmetry observed for the cold ion blobs, and instead of a symmetric vorticity dipole around the blob, the vorticity was elongated along the blob and the blob itself started propagating in the $\mathbf{B} \times \nabla B$-direction and remained more coherent than in the case with cold ions. The inclusion of dynamic ion temperatures enhanced the effects of finite ion temperatures, but otherwise no major qualitative differences were observed compared to the isothermal ion case.

With these results at hand, we moved on to investigate how different initial parameters affected the propagation of blobs using the model with both electron and ion temperature dynamics included. We observed that the ion to electron temperature ratio, τ, had a large influence on the blob propagation. For low τ the blobs generated a mushroom-like shape as was also seen in the cold ion simulations. For high τ the blobs remained more coherent and propagated in the $\mathbf{B} \times \nabla B$-direction as would be expected from the analysis of the effects of temperature dynamics above. We found that the amplitude of the blob, Δn, also significantly affects the blob propagation. Low Δn showed the same effects as low τ, likely due to the reduced contribution to the ion pressure in the generalised vorticity. Finally we found that the size of the blob, σ, also influenced the propagation of blobs. Large blobs leave behind much of the initial mass and propagate on as smaller more coherent structures. Furthermore, the secondary instabilities observed in the later stages of blob propagation like the Kelvin-Helmholz instability were more profound in large blobs compared to smaller blobs, which was attributed to stronger finite larmor radius (FLR) effects in smaller blobs stabilising sheared flows.

We then moved on to investigate the so-called compactness of the blob, I_c, which is a measure of how coherent the blob is after a given time. It is defined so $I_c = 1$ corresponds

to a blob, which remains fully coherent and $I_c = 0$ corresponds to a fully dispersed blob. We found a transition from mushroom-like structures to more coherent structures between $0 < r < 0.1$, where $r = \rho_{i0} \Delta n / (\sigma n_0)$ is a measure of the strength of the FLR effects, consistent with what was also observed in ref. [33, 61, 65].

The final investigation we conducted in the paper was how the blob radial centre of mass velocities scaled with a range of different parameters. We compared the radial centre of mass velocities with two scalings, the inertial scaling[66]

$$\frac{V_{iner}}{c_s} = \left(\frac{\sigma}{R_0} \frac{(\Delta p_e + \Delta p_i)}{p_0} \right)^{1/2}, \tag{4.35}$$

and a scaling proposed in ref. [67], given by

$$\frac{V_{Manz}}{c_s} = \sqrt{\frac{\sqrt{f^2 + g^2} - f}{2}}, \tag{4.36}$$

where

$$f = \left(\frac{\tau \rho_s}{2\sigma} \frac{\Delta p_e}{p_0} \right)^2, \qquad \text{and} \qquad g = (1 + \tau) \frac{2\sigma}{R_0} \frac{\Delta p_e}{p_0}, \tag{4.37}$$

and $p_0 = n_0 T_{e0}$ is a background pressure. The parameters we investigated with respect to the radial centre of mass velocities were the blob size, σ, the ion to electron temperature ratio, τ, and the blob amplitude, Δn. It was found that neither of the two scalings described the velocity well for small blobs, but for large blobs both scalings proved to fit well with the observed velocities when scanning the blob size. It was also found that the scaling given in eq. (4.35) fit well for all values of τ investigated, while the scaling given in eq. (4.36) consistently underestimated the velocity for smaller blobs, while it fit well for larger blobs. Finally the blob amplitude was scanned and again it was found that the scaling given in eq. (4.35) fit well for most values of Δn investigated, while the scaling given in eq. (4.36) consistently underestimated the velocity for smaller blobs, while it fit well for larger blobs. It should be noted, however, that neither of the scalings described the velocity of very low amplitude blobs well, likely due to the blobs dispersing before reaching their maximum velocity. This lead us to conclude that, although the scaling in eq. (4.35) did not cover the full parameter spectrum scanned, it mostly captured the blob velocities well and it was the most successful in describing filament velocities.

Chapter 5

Three dimensional blobs

In the previous section we saw how blobs propagate when three-dimensional effects are either parametrised or neglected. However, we also saw in the code validation studies in sec. 4.1 that 3D effects are important when modelling blob propagation, for example when the blob is affected by a sheath. We therefore set out to investigate how adding a third dimension changes the blob dynamics. This chapter is dedicated to preliminary, not yet published results using the implementation of the equations derived in sec. 2.6 in the BOUT++ framework described in sec. 3.1.

5.1   Implementation and initialisation

The three-dimensional model described in sec. 2.6 resembles that presented in ref. [68]. Both models solve for the density, vorticity and parallel electron and ion velocities. The main differences between the models are found in the vorticity equation, where the model in ref. [68] includes a perpendicular diffusion term using $T_{i0} = T_{e0}$ in the evaluation of the diffusion coefficient in an otherwise cold ion model, a diffusion which is not present in the model stated in sec. 2.6. Furthermore the term involving the source in eq. (2.47) has been neglected in ref. [68]. Finally, a parallel damping term is present in eq. (2.49), which is not included in ref. [68] and the curvature operator in the model described in sec. 2.6 is only half of that presented in ref. [68]. However, these are minor differences, and are not expected to strongly influence the propagation of coherent filaments, so if our implementation is correct, the solution should be similar to what is observed in ref. [68]. We acknowledge that this comparison does not verify our implementation and only renders the results presented in this section slightly more plausible. However, the results in this section are merely preliminary results meant as a foundation for future work, and thus thorough verification and validation should be conducted before final conclusions can be drawn.

With this in mind, we move on to define the parameters used for the simulations. In order to be able to compare our simulations with ref. [68], we use parameters relevant for the MAST tokamak also used in the paper; $T_{e0} = 40$ eV, $B_0 = 0.5$ T, $n_0 = 0.8 \times 10^{19}$ m^{-3}, $L_{\parallel} = 10$ m, $R_0 = 1.5$ m, $q = 7$ and the simulations are for a deuterium plasma, which means that $\mu = 3672$. What is needed in eqs. (2.47) to (2.50) are the corresponding nor-

malised quantities. For the parameters stated here, we have the normalisation quantities $c_{s0} = 4.4 \times 10^4$ m/s, $\rho_s = 1.8$ mm, $\rho_{e0} = 3.0 \times 10^{-2}$ mm and $\omega_{ci} = 2.4 \times 10^7$ s^{-1}.

The electron-ion collision frequency is calculated based on the expressions found in ref. [54] and is given by

$$\nu_{ei0} = \frac{\sqrt{2}}{12\pi^{3/2}} \frac{Z^2 e^{5/2} \ln \Lambda}{\sqrt{m_e}\epsilon_0^2} \frac{n_0}{T_{e0}^{3/2}}, \tag{5.1}$$

where $\ln \Lambda$ is the Coulomb logarithm and λ_D is the Debye length given by

$$\ln \Lambda = \ln \left(\frac{12\pi n_0 \lambda_D^3}{Z} \right), \qquad \lambda_D = \left(\frac{\epsilon_0 T_{e0}}{n_0 e} \right)^{1/2}. \tag{5.2}$$

With the parameters above, we have $\nu_{ei0} = 1.2 \times 10^6$ s^{-1}, which means that the normalised collision parameters are given by

$$D_n = 1.4 \times 10^{-5}, \qquad \nu_\parallel = 0.02, \qquad \nu_{e\parallel}^{-1} = 20. \tag{5.3}$$

Before we move on to state how the simulations are initialised, we need to make a short remark on the coordinate system used in BOUT++. All equations derived in sec. 2 assume the axisymmetric direction to be y and the magnetic field to be aligned along z. However, in BOUT++, the axisymmetric direction is z and the magnetic field is by default aligned with y. This means that in order to implement the equations in sec. 2.6 in BOUT++, we need to make the coordinate transformation[45]

$$x \to x, \qquad y \to -z, \qquad z \to y \tag{5.4}$$

for the implementation. However, we will keep the coordinate system described in sec. 2.1 when discussing the results in this section. This means that the magnetic field is aligned with the z-coordinate and the axisymmetric direction is the y-direction in this section.

Since the simulation domain is not infinite, we need to set boundary conditions. Per default in BOUT++ the axisymmetric coordinate employs periodic boundary conditions on all fields. In the radial direction we use Neumann boundary conditions on $n, \omega, u_{i\parallel}$ and $u_{e\parallel}$ with the gradient set to zero for both the inner and outer radial boundaries. Since a Laplace inversion needs to be done to determine φ, it is not possible to use Neumann boundary conditions on both the inner and outer radial boundaries on φ since the system will then not be uniquely defined. Du to this constraint we set the boundaries for φ to a Neumann boundary with zero gradient at the inner radial boundary and we set the outer radial boundary to a Dirichlet boundary with the value zero. This means that we are effectively setting the outer radial boundary to emulate the effect of a wall, where the potential of the system is defined with respect to the wall potential, φ_w. In the parallel direction, z, sheath boundary conditions are employed for the parallel velocities, so

$$u_{i\parallel}\big|_{z=\pm\tilde{L}_\parallel} = \pm 1, \qquad \text{and} \qquad u_{e\parallel}\big|_{z=\pm\tilde{L}_\parallel} = \pm \exp\left(-\varphi\big|_{z=\pm\tilde{L}_\parallel}\right), \tag{5.5}$$

where the potential of the system is defined with respect to the wall potential. Free boundary conditions were applied on both the upper and lower parallel boundaries on n, ω and φ to avoid overconstraining the system as described in ref. [68].

Finally to be able to solve the system of equations we need to define the source term. The sources used in the multicode validation studies proved to have the desired effect on the system with minimal impact on the blob propagation in the center of the domain. We therefore use the same source as that stated in eq. (4.31), where we set $C_1 = 1$ for simplicity. This means that the normalised source used is

$$S_n = \frac{10\exp(10z/\tilde{L}_\parallel)}{\tilde{L}_\parallel\left(\exp(10)-1\right)} + \frac{10\exp(-10z/\tilde{L}_\parallel)}{\tilde{L}_\parallel\left(\exp(10)-1\right)}, \tag{5.6}$$

where $z \in \left[-\tilde{L}_\parallel, \tilde{L}_\parallel\right]$ and $\tilde{L}_\parallel = 5500$ is the normalised parallel length, so that the source is primarily located at the upper and lower boundaries of the domain.

The numerical schemes used for discretising the set of equations are a second order finite difference scheme for the diffusive terms of the form $\partial_x f$ and $\partial_x^2 f$, and a first order upwinding scheme for advective terms of the from $v\partial_x f$.

5.2 The steady state

Before we investigate how seeded blobs move in three dimensions we start by investigating the steady-state of the system. The simulations are run from an initial input profile, similar to the steady-state solution stated in ref. [68], and are run until the solutions no longer change, which occurs after a normalised time $t = 40000$. Since the simulations need to run until a steady-state is reached, and since the steady-state solution does not depend on the dimensions perpendicular to the magnetic unless a perturbation is imposed, the number of spatial points in the poloidal direction are reduced to $n_y = 2$, while the number of radial points is kept at $n_x = 192$ for these simulations. The size of the domain is $L_x \times L_y \times L_z = 150 \times 100 \times 11000$ in normalised units.

5.2.1 Convergence of the steady state

We start by investigating how the steady-state solution depends on the number of grid-points used in the parallel direction. In this regard we have run the simulations with $n_z = 8, 16, 32, 64, 128$ and $n_z = 256$ until a steady-state was reached for each of the resolutions. The parallel domain was set to $[-\tilde{L}_\parallel, \tilde{L}_\parallel]$. The solutions for n and φ in the middle of the radial domain, $x = L_x/2$, are plotted in fig. 5.1, and the solutions in the middle of the radial domain, $x = L_x/2$, for $u_{i\parallel}$ and $u_{e\parallel}$ are plotted in fig. 5.2. We observe that the the steady-state solutions with low resolution, $n_z = 8$ and $n_z = 16$ display remarkably different profiles from the rest of the simulations both in fig. 5.1 and fig. 5.2.

In the fields with free boundary conditions, namely n and φ, the low resolutions profiles are observed to generate profiles opposite of what is observed in the higher resolutions cases. We expect this to be due to the very steep gradients at the sheath boundaries, which cannot be resolved properly in the low resolution simulations. Furthermore, we observe that both n and φ are asymmetric at the sheath boundaries. This asymmetry decreases with the number of points in the parallel direction, so we expect it to be due to a numerical issue, possibly the upwinding scheme used. However, the issue still needs to
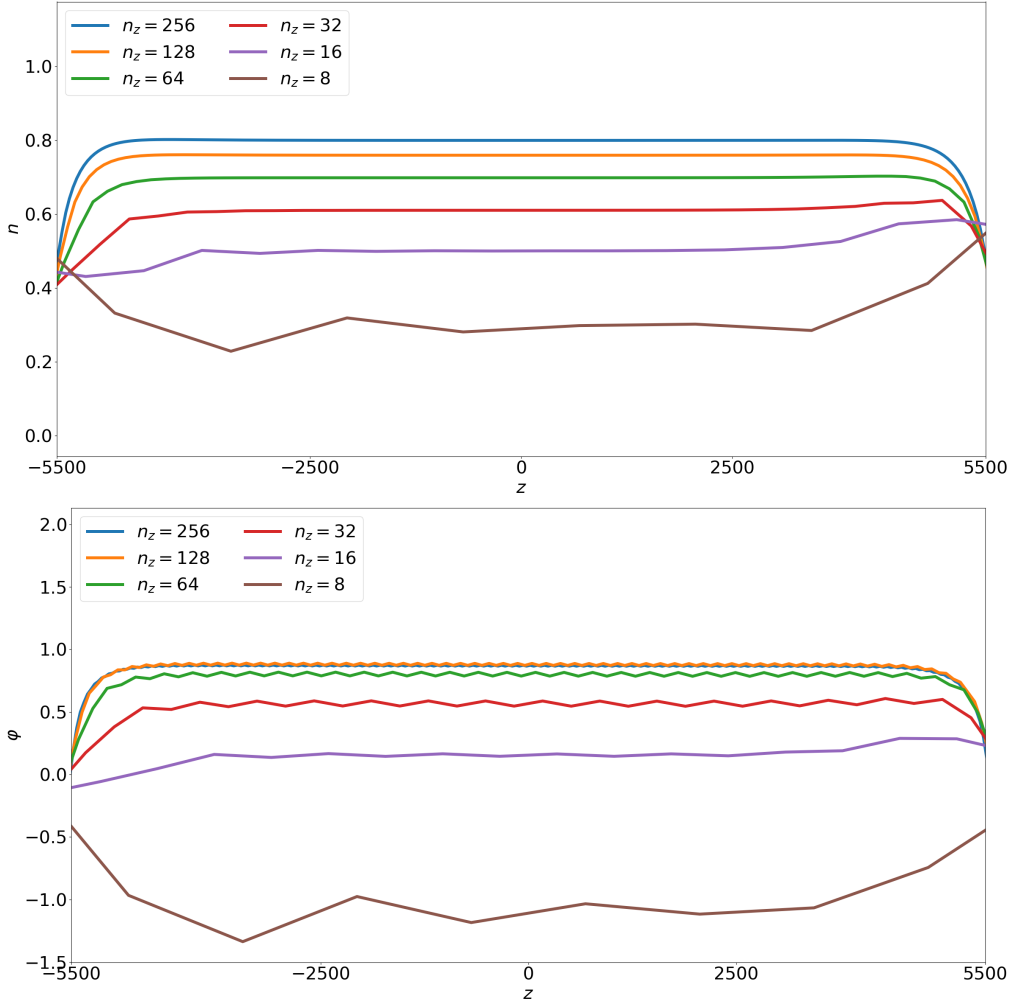
Figure 5.1: Steady-state profiles of n and φ at $x = L_x/2$ and $y = 0$ with different number of grid points in the parallel direction, n_z.

be investigated further, but the investigation is left for future studies due to the limited time available for this project. Furthermore, we observe a grid-sized see-sawing pattern in the potential as seen in fig. 5.1, which has also been observed in other plasma fluid codes with sheath boundaries[69]. The see-saw pattern relates to the resolution in the direction with the sheath boundaries and can be reduced by increasing the resolution[69].

The large discrepancy seen between the low resolution solutions and the higher resolution solutions for n and φ is also observed for the parallel ion velocity, $u_{i\parallel}$, seen in fig. 5.2. The low resolution profiles are seen to be asymmetric and are significantly below zero at the stagnation point, $z = 0$. This discrepancy is expected to be due to the very high numerical dissipation induced by the upwinding scheme used[36], which decreases with the number of points used. The trends seen with a discrepancy between the low and high resolution simulations are also observed for the parallel electron velocity, $u_{e\parallel}$. $u_{e\parallel}$, is observed to be antisymmetric as would be expected, however, it is not zero at the stagnation point, $z = 0$. This is due to the inherent asymmetry seen in fig. 5.1 in the potential at the sheath boundaries which influences the sheath boundaries of the parallel
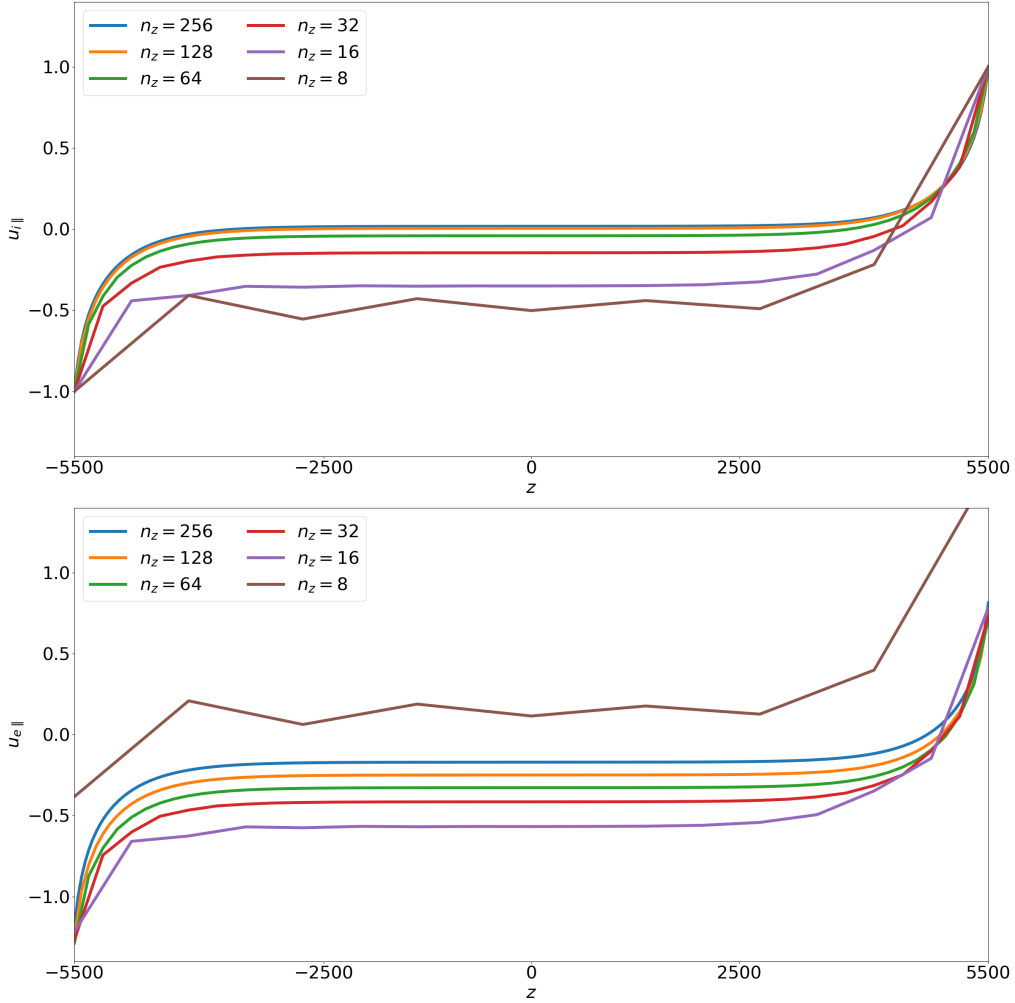
67

Figure 5.2: Steady-state profiles of $u_{i\parallel}$ and $u_{e\parallel}$ at $x = L_x/2$ and $y = 0$ with different number grid of points in the parallel direction, n_z.

electron velocity, eq. (5.5). As was the case with the potential, we observe that the solution becomes more symmetric as we increase the number of grid points, which also means that the solution to $u_{e\parallel}$ moves closer to zero at $z = 0$, again leading us to believe the behaviour observed to be numerically founded.

5.2.2 Order of steady-state error

Up until now we have qualitatively investigated how the steady-state solutions change with the number of grid points. The next investigation we wish to make is how the errors change quantitatively with the number of grid-points. The errors of the steady-state solutions are calculated with respect to the steady-state solution of the $n_z = 256$ simulation, since an analytical solution of the system in sec. 2.6 is not readily available with the boundary conditions used. Due to the lowest order scheme used in the simulations being the first order upwinding scheme, we expect the relative errors of all fields to be of order $\mathcal{O}(d_z)$, where d_z is the step-size. The errors can be determined using any suitable norm,

where we have chosen to examine the 2-norm

$$\|E\|_2 = \sqrt{\sum_{i=1}^{n_z} (f_i - f)^2}, \tag{5.7}$$

and the infinity norm

$$\|E\|_\infty = \max \left(|f_i - f| \right), \tag{5.8}$$

where f_i is the function at index i and f is the value of the true solution, which in our case is the value of the $n_z = 256$ steady-state at the same parallel location as index i. We observe that the errors do not completely follow the expected trend, where especially the two last points display different trends from the $\mathcal{O}(d_z)$ line. We expect this to be due to the low resolution, which is not able to capture the steep gradients near the sheath entrance and thus results in very large errors. Furthermore, we observe differences between the 2-norm and the infinity norm in the convergence rate for the potential, which needs further investigation, since the convergence rate should be independent of the norm used. However, for the remaining fields, we observe trends close to the expected convergence if we exclude the two largest step-sizes.

Despite the asymmetry in the solutions and the solutions not following the expected order of convergence for large step-sizes, we do observe that the solutions converge and that the asymmetry decreases as the number of grid-points in the parallel direction is increased. Furthermore, this deviance from the expected order of convergence was also observed in ref. [45], and it was stated that this issue appears to be caused by gradients at the sheath boundary which tend to infinity, leading to an ill-posed problem. We acknowledge that the trends shown here are not ideal, and further investigation should be carried out using the verification processes described in ref. [70] and more specifically using the method of manufactured solutions [71]. However, due to the limited time available, we settle for the steady-state profiles stated here and use the largest acceptable step-size for investigations on seeded blobs, while we leave resolving the issues and the verification procedures for future work. Despite the shortcomings, we believe that the analysis of blobs seeded on top of the steady-state solutions stated above can shed some light on the influence of 3D dynamics on blob propagation, although the conclusions should be made with care until verification of the code has been conducted.

5.3 Seeded blob simulations

With a steady state reached for the simulations, we can now turn to investigating blobs initialised on top of the steady-state background solutions. We use the resolution $n_z = 64$ in the parallel direction, since this is the lowest resolution we can use, while still getting a smooth steady-state profile as was observed in the previous section. This allows us to get a reasonable solution, while avoiding massive save-files and lengthy computation times. The steady-state profiles are extended uniformly to $n_x \times n_y \times n_z = 192 \times 128 \times 64$, and
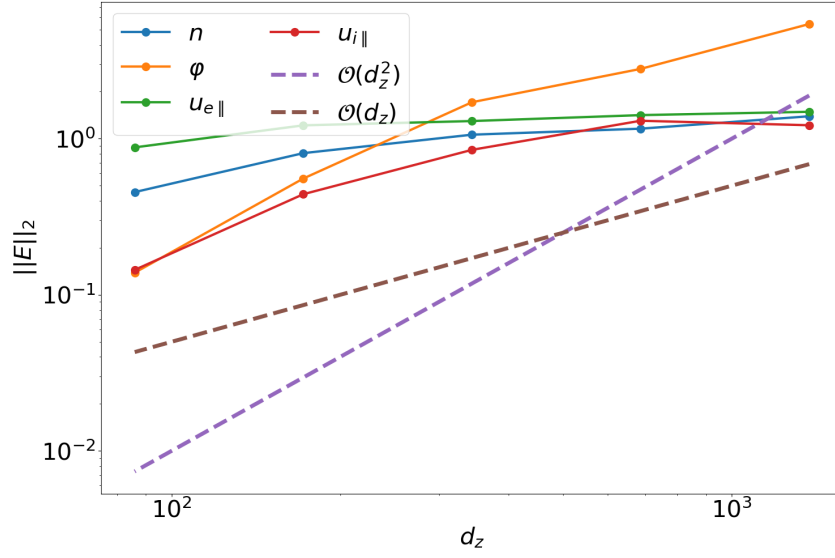
(a) The 2-norm of the steady-state solutions at $x = L_x/2$ and $y = 0$.
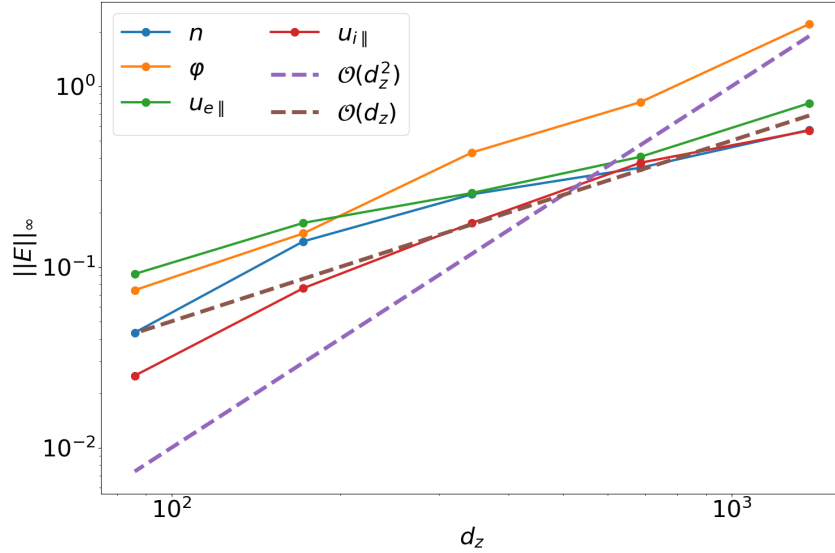
(b) The infinity norm of the steady-state solutions at $x = L_x/2$ and $y = 0$.

Figure 5.3: The magnitude of the rms error (a) and maximum error (b) of the steady-state solutions at the middle of the radial domain. The errors are calculated with respect to the $n_z = 256$ steady-state and are plotted along with the $\mathcal{O}(d_z)$ and $\mathcal{O}(d_z^2)$ lines.

a perturbation of the form

$$
\begin{aligned}
n_b(x, y, z) = \frac{1}{2} A \exp & \left(\frac{-(x - x_0)^2 - (y - y_0)^2}{d_\perp^2} \right) \\
& \times \left(\tanh \left(\frac{(z + d_\parallel)}{w_\parallel} \right) - \tanh \left(\frac{(z - d_\parallel)}{w_\parallel} \right) \right)
\end{aligned}
\tag{5.9}
$$

is added on top of the steady-state background. Here A is the blob amplitude, $d_\perp$ is the width of Gaussian perturbation in the perpendicular domain, $d_\parallel$ is the parallel length of

Figure 5.4: The propagation of n and φ for a blob in the $x - y$ plane at $z = 0$. The blob is initialised with $A = 2$, $d_\perp = 10$, $w_\parallel = \tilde{L}_\parallel/10$ and $d_\parallel = \tilde{L}_\parallel/2$.

the blob and $w_\parallel$ is the width of the hyperbolic tangent.

5.3.1 Comparison with previous work

We start by examining a blob with the normalised parameters $A = 2$, $x_0 = L_x/3$, $y_0 = 0$, $d_\perp = 10$, $d_\parallel = 2250$ a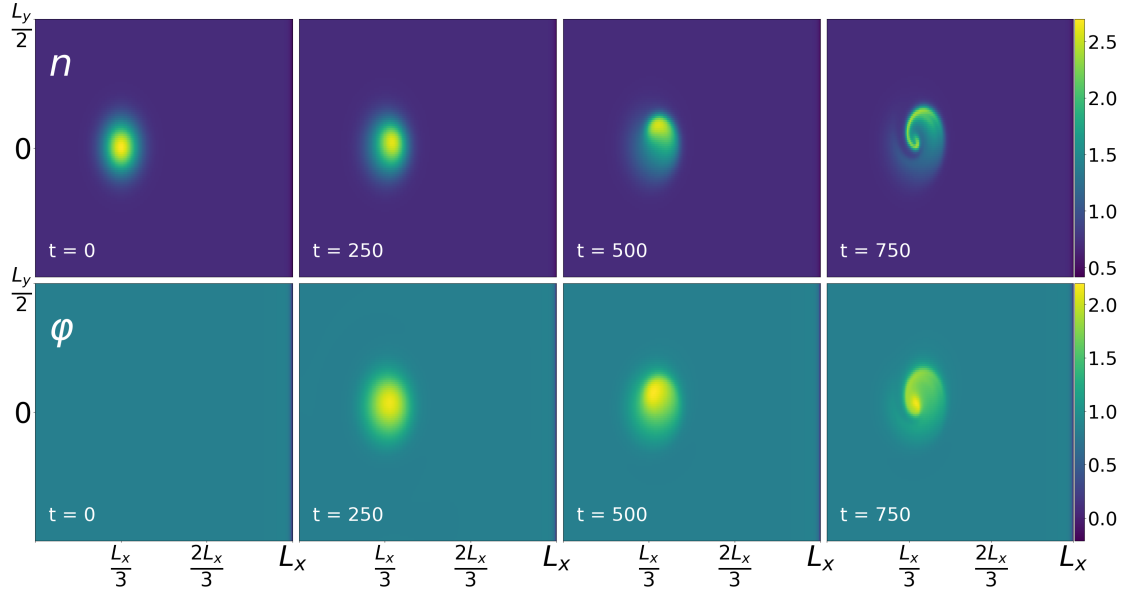nd $w_\parallel = \tilde{L}_\parallel/10$, which corresponds to the parameters used in ref. [68] in order to be able to compare our simulations with those presented in the paper. The propagation of the filament density and potential in the x-y-plane can be seen in fig. 5.4, where we observe a blob propagating in a very similar manner to what was observed in ref. [68].

The up-down symmetry observed in the cold ion simulations in sec. 4.2 is broken when parallel dynamics are included in the simulations due to a connection to the sheath. The blobs propagate not only radially, but also in the poloidal direction, which can be attributed to the so-called Boltzmann spinning. We observe minor differences between the simulations presented here and those presented in ref. [68]. The blob in fig. 5.4 rotates further in the later stages of propagation where those in ref. [68] break into smaller parts and disperse. These differences, however, can be attributed to the curvature term of the model stated in sec. 2.6 only being half of the one presented in ref. [68] and the fact that we have not used a neoclassical correction on the perpendicular diffusion term D_n.

The fact that the results for the radial propagation of the blobs compare well with the results presented in ref. [68] when using the same parameters leads us to conclude that although the analysis of the steady-state solutions did not show the expected trends, the propagation of blobs with 3D dynamics can still provide useful results, which are comparable to what is found in other numerical models. Furthermore, the rotation seen in fig. 5.4 is also observed in a wide range of other 3D models[72, 73, 74, 75]. We therefore turn to investigate the propagation of the blob parallel to the magnetic field. For the
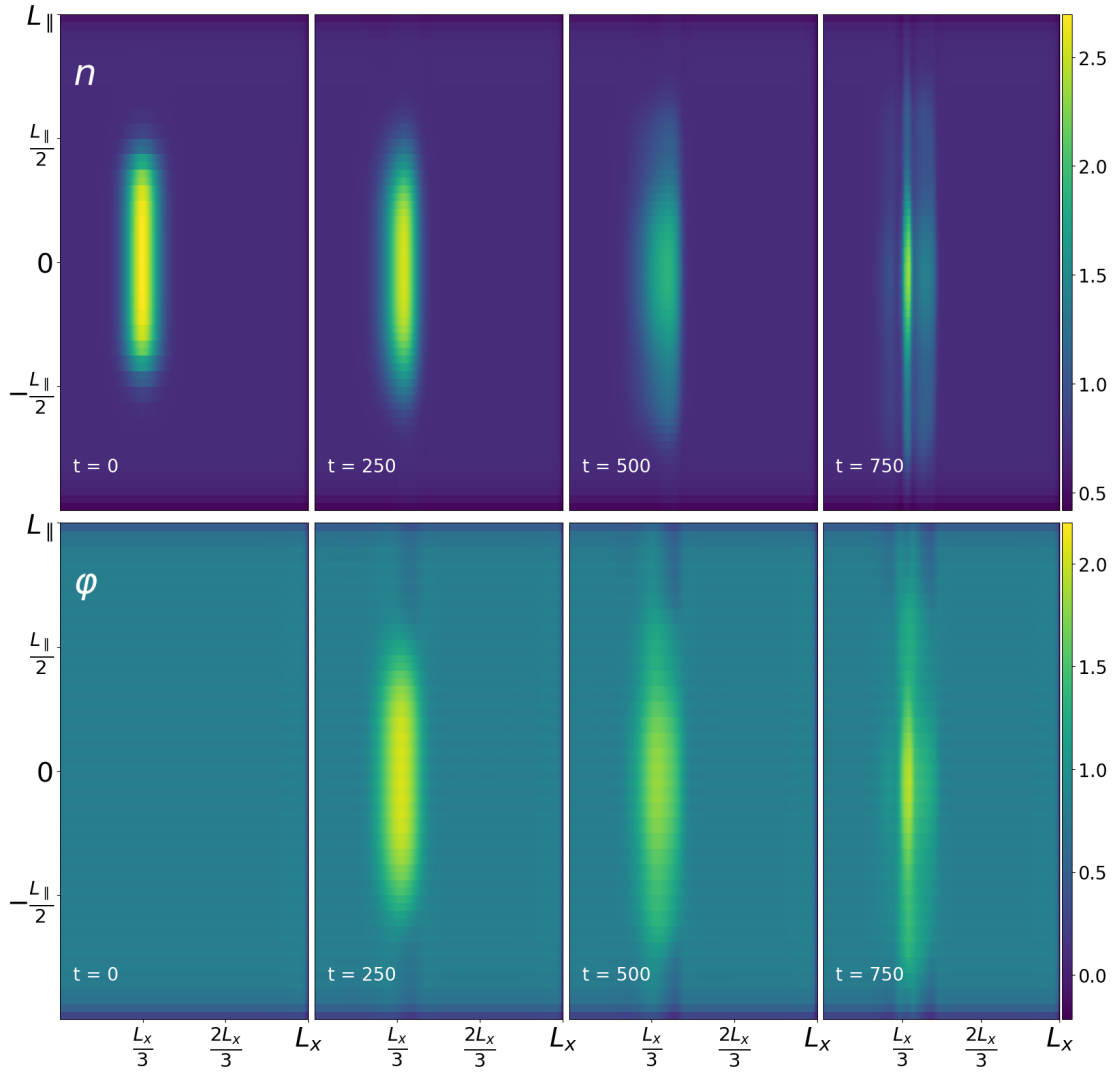
Figure 5.5: The propagation of n and φ for a blob in the $x - z$ plane at $y = 0$. The blob is initialised with $A = 2$, $d_\perp = 10$, $w_\parallel = \tilde{L}_\parallel/10$ and $d_\parallel = \tilde{L}_\parallel/2$.
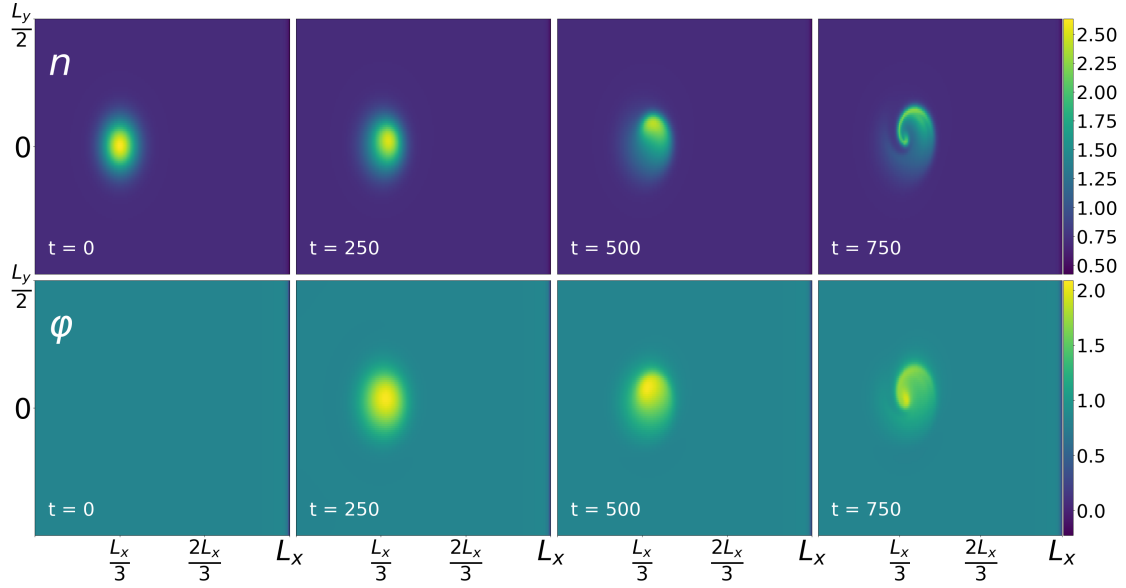
Figure 5.6: The propagation of n and φ for a blob in the $x - y$ plane at $z = 0$. The blob is initialised with $A = 2$, $d_\perp = 10$, $w_\parallel = \tilde{L}_\parallel/5$ and $d_\parallel = \tilde{L}_\parallel/2$.

parameters stated above, we get the $x - z$ profile of n and φ seen in fig. 5.5 for the same parameters as those stated in fig. 5.4. We observe that the blob quickly expands in the parallel direction, where a potential builds up and a connection to the sheath is rapidly established. In the later stages of propagation, the maximum density is seen as a narrow thin line behind the blob front, which is due to secondary instabilities, where the blobs curl up, generating lobes behind the blob centre of mass.

5.3.2 Dependence on parallel gradient

With the observation that the blobs presented in the previous section resembled those in ref. [68], we now move on to investigate how parallel dynamics influence blob propagation. The first investigation we wish to carry out is how the width of the hyperbolic tangent in the blob initialisation affects the blob propagation. We scan $w_\parallel$ in the range $w_\parallel \in [\tilde{L}_\parallel/25, \tilde{L}_\parallel/5]$. In fig. 5.6 we have plotted the $x - y$ cross-section at $z = 0$ for a blob with $A = 2$, $d_\perp = 10$, $w_\parallel = \tilde{L}_\parallel/5$ and $d_\parallel = \tilde{L}_\parallel/2$. We observe that the propagation of the blob is almost identical to that seen in fig. 5.4, where the blob propagates both in the radial and poloidal directions and undergoes strong rotation due to Boltzmann spinning. In fig. 5.7 we have plotted the $x - y$ cross-section of a blob with the same parameters as in fig. 5.6, except for the width of the hyperbolic tangent, which is initialised much narrower with $w_\parallel = \tilde{L}_\parallel/25$. We observe that the propagation of the blobs in the two figures are almost identical, which indicates that the initial width of the parallel extent of the blob, $w_\parallel$, does not have a strong influence on blob propagation. The rotation of the blob is slightly stronger in fig. 5.7 compared to fig. 5.6 otherwise no great differences are observed. The similarities between the blobs is expected to be due to a rapid propagation of the parallel edges of the blob, which quickly causes steep gradients to become smoother.

Figure 5.7: The propagation of n and φ for a blob in the $x - y$ plane at $z = 0$. The blob is initialised with $A = 2$, $d_\perp = 10$, $w_\parallel = \tilde{L}_\parallel/25$ and $d_\parallel = \tilde{L}_\parallel/2$.
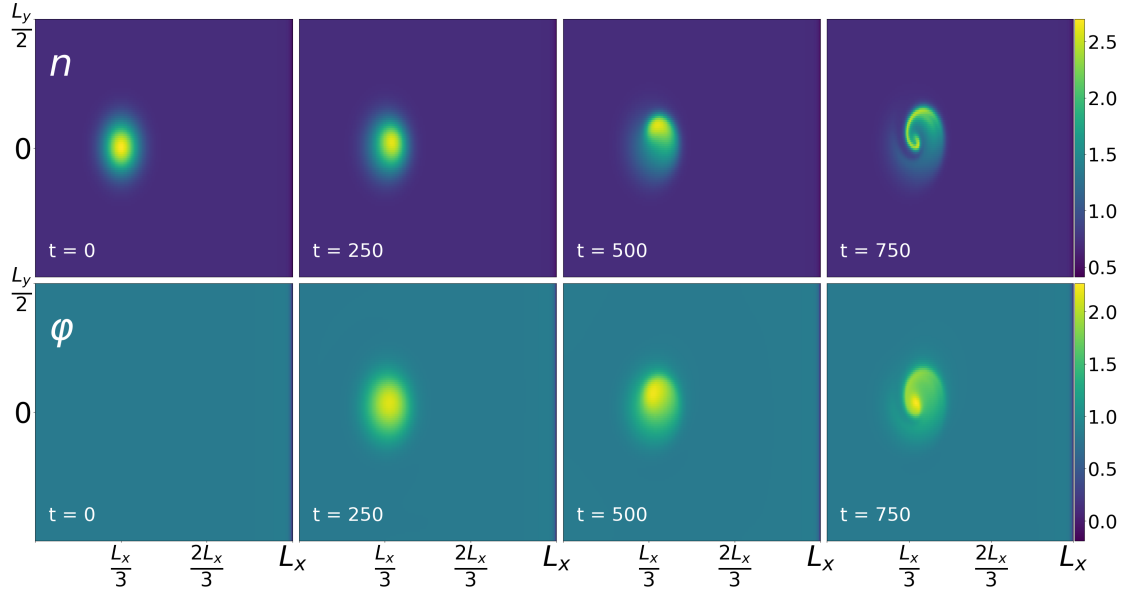
This trend with the rapid propagation of the edges of the blob is clearly seen in the parallel profiles, which are plotted in fig. 5.8 for the two blobs described above. The plot displays the parallel profile of n at $y = 0$ and at the radial location where $n = n_{max}$. We observe that the blobs with the steep parallel gradient quickly flatten, creating a smooth structure. This can describe the similarities observed between the blobs with initial smooth and initial steep gradients. However, one should note that the evolution in the parallel direction is not symmetric, likely due to the asymmetry also seen in the steady-state in sec. 5.2, which appears to be a numerical issue, so the results presented here should be thoroughly tested before final conclusions are made.

With this in mind, we move on to investigate the similarities in the propagation of the blobs. In order to carry out this investigation, we track the centre of mass position as a function of time. The centre of mass position is defined as

$$\mathbf{x}_{CoM}(t) \equiv \frac{1}{\int (n(x, y, z, t) - n_0(x, y, z)) \mathrm{d}V} \int (n(x, y, z, t) - n_0(x, y, z)) \mathbf{x} \mathrm{d}V, \qquad (5.10)$$

where $\mathrm{d}V = \mathrm{d}x\mathrm{d}y\mathrm{d}z$ and $\mathbf{x} = (x, y, z)$. A plot of the evolution of the radial and poloidal centre of mass position for blobs initialised with $A = 2$, $d_\perp = 10$, $d_\parallel = \tilde{L}_\parallel/2$ and a range of $w_\parallel$ is plotted in fig. 5.9. We observe no great difference between the different values of $w_\parallel$, where only the smallest gradient blob displays behaviour different from the other curves in fig. 5.9. This is likely due to the fact that the edges of the blob with small gradient quickly reaches the sheath entrance and is influenced by the connection.

Another way to examine the motion of plasma filaments is by examining the centre of mass velocity defined as

$$\mathbf{V}_{CoM} \equiv \frac{\mathrm{d}}{\mathrm{d}t}\mathbf{x}_{CoM}, \qquad (5.11)$$

where $\mathbf{V}_{CoM} = (V_{x,CoM}, V_{y,CoM}, V_{z,CoM})$, and the derivative is calculated using a second

(a) $w_\parallel = \tilde{L}_\parallel/5$

(b) $w_\parallel = \tilde{L}_\parallel/25$
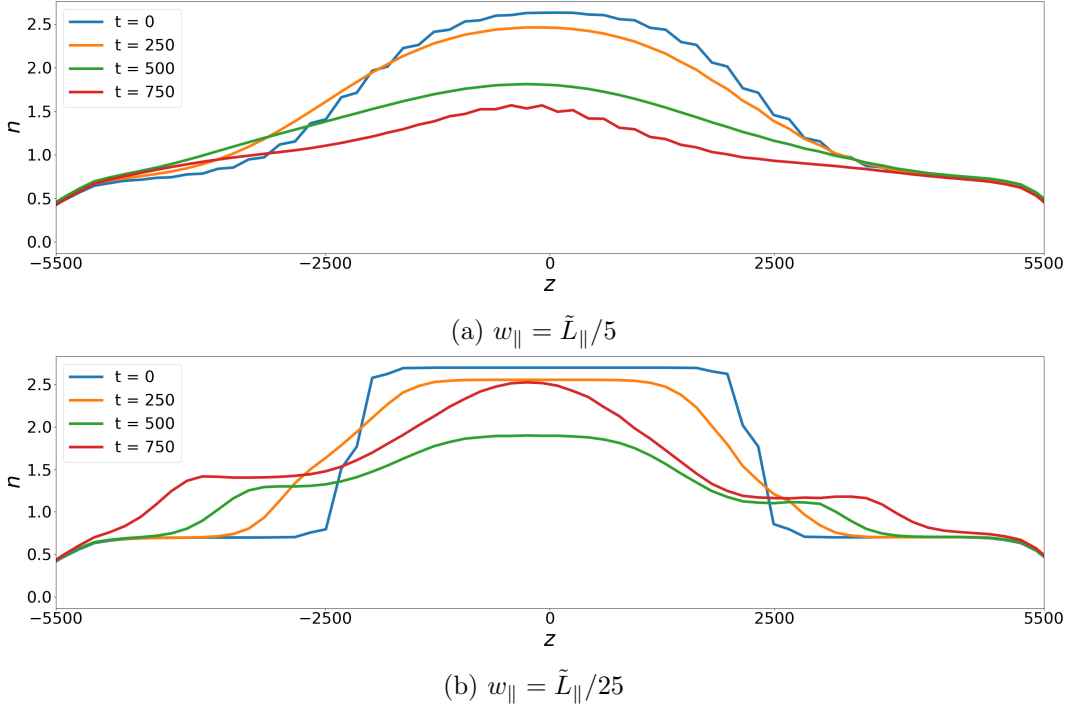
Figure 5.8: The parallel profiles of the maximum radial position at $y = 0$ for a filament initialised with $A = 2$, $d_\perp = 10$, $d_\parallel = \tilde{L}_\parallel/2$. Figure (a) is for a width of the hyperbolic tangent of $w_\parallel = \tilde{L}_\parallel/5$ and (b) is for a width of the hyperbolic tangent of $w_\parallel = \tilde{L}_\parallel/25$.
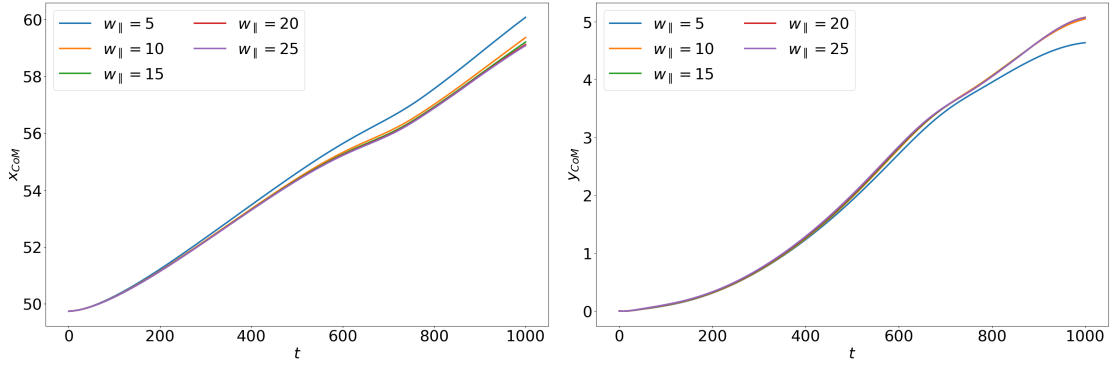
Figure 5.9: Radial and poloidal center of mass position as a function of time for blobs initialised with $A = 2$, $d_\perp = 10$, $d_\parallel = \tilde{L}_\parallel/2$ and a range of $w_\parallel$ as stated in the legends.

order finite difference scheme given by eq. (3.1). Both the radial and poloidal velocities as a function of time are plotted in fig. 5.10. Here we observe that the velocities initially accelerate, both in the radial and poloidal direction, slow down around $t = 400$ and then accelerate again. This second acceleration peak was not observed for the 2D blobs in sec. 4.2, and is likely due to the blob rotation, where the blob center of mass slowly stagnates around $t = 400$ and at $t = 700$, the blob lobe has rotated far enough for it to drag the centre of mass forward again.
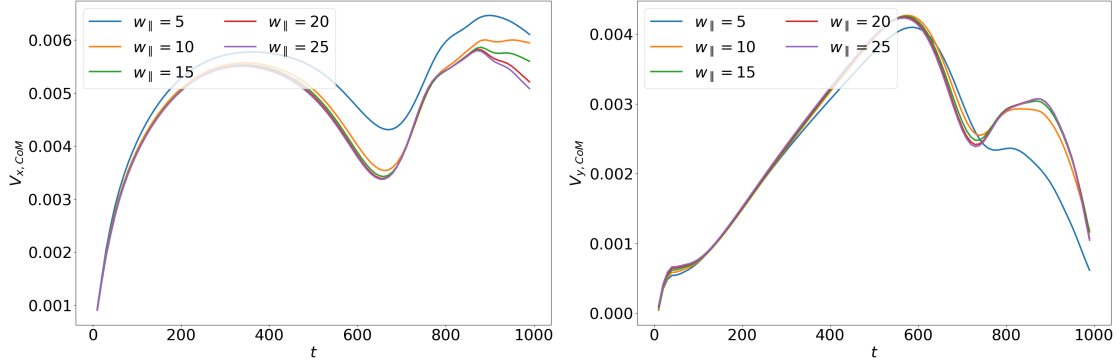
Figure 5.10: Radial and poloidal center of mass velocities as a function of time for blobs initialised with $A = 2$, $d_\perp = 10$, $d_\parallel = \tilde{L}_\parallel/2$ and a range of $w_\parallel$ as stated in the legends.

5.3.3 Dependence on parallel length

The last investigation of blobs in a 3D geometry we wish to carry out is how the parallel length of the blob influences the blob propagation. In this respect we have used the parameters $A = 2$, $d_\perp = 10$, $w_\parallel = \tilde{L}_\parallel/10$ and scanned $d_\parallel$ in the range $d_\parallel \in [2250, 4000]$. We have plotted the $x - y$ cross-section at $z = 0$ for a blob with $d_\parallel = 2500$ in fig. 5.11 and for a blob with $d_\parallel = 4000$ in fig. 5.12. Upon comparing the two plots we observe a significant difference, especially in the later stages of blob propagation. The smaller blob with $d_\parallel = 2500$ generates the rotating spiral also seen in the previous section, whereas the large blob with $d_\parallel = 4000$ initially starts to spin, but then breaks into smaller fragments instead of generating the spiral seen for the smaller blob. We expect this to be due to the edges of the large blob quickly reaching the sheath entrance, which in turn damps the potential causing secondary instabilities to develop, as was also observed in ref. [74].

The quick connection to the sheath is seen when comparing the parallel profiles at $z = 0$ and at the radial position where $n = n_{max}$ of the filament with $d_\parallel = 2500$ and the filament with $d_\parallel = 4000$, which is plotted in fig. 5.13. We observe in fig. 5.13 (a) that the parallel fronts of the small filaments propagate towards the sheath and then develop steep gradients when the front reaches the sheath, after which the filament dissipates. In fig. 5.13 (b), we observe the same effect, however, the connection to the sheath is established much faster and the dissipation in turn also happens faster. Again we observe an inherent asymmetry in the parallel evolution of the blobs, which needs to be investigated further before final conclusions can be drawn.

The radial and poloidal centre of mass positions for blobs with parallel lengths of $d_\parallel \in [2250, 4000]$ is seen in fig. 5.14. We observe similar trends for all filaments, but unlike with the parallel width, significant differences between the blobs are observed. We note that the radial centre of mass position initially decreases for the blobs with $d_\parallel \neq 2250$ due to an initial rotation of the filament, only to increase again and propagate in the positive radial direction. Finally it is observed that the largest blobs propagate further than the smaller blobs, both in the radial and poloidal direction, which can be attributed to the blob depleting slower in the direction parallel to the magnetic field. This leaves more of the initial mass in the centre of the blob at $z = 0$, contributing to a larger drive
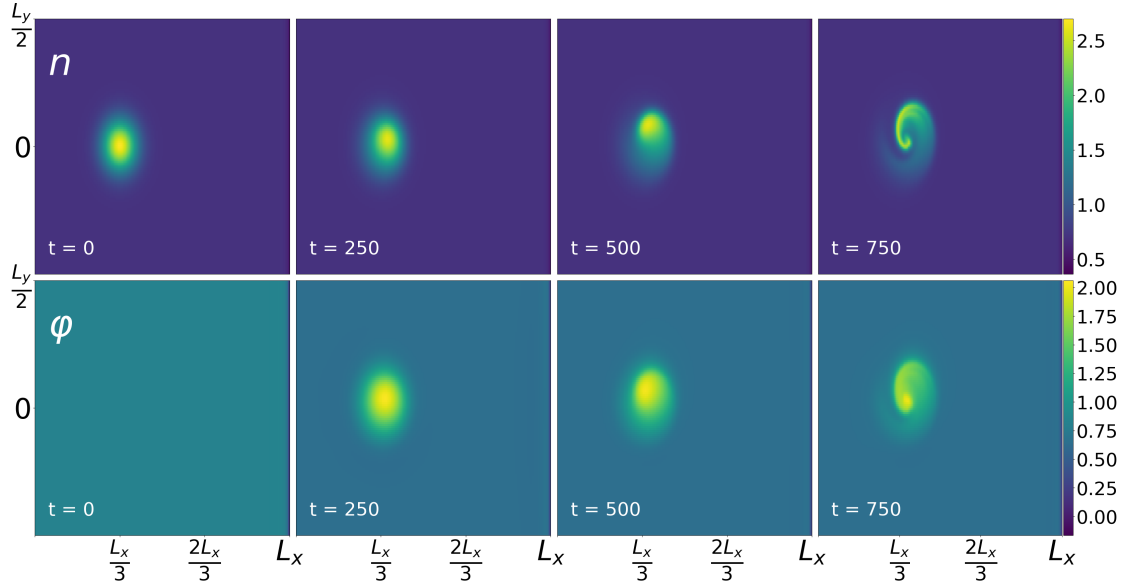
Figure 5.11: The propagation of n and φ for a blob in the $x - y$ plane at $z = 0$. The blob is initialised with $A = 2$, $d_\perp = 10$, $w_\parallel = \tilde{L}_\parallel/10$ and $d_\parallel = 2500$.
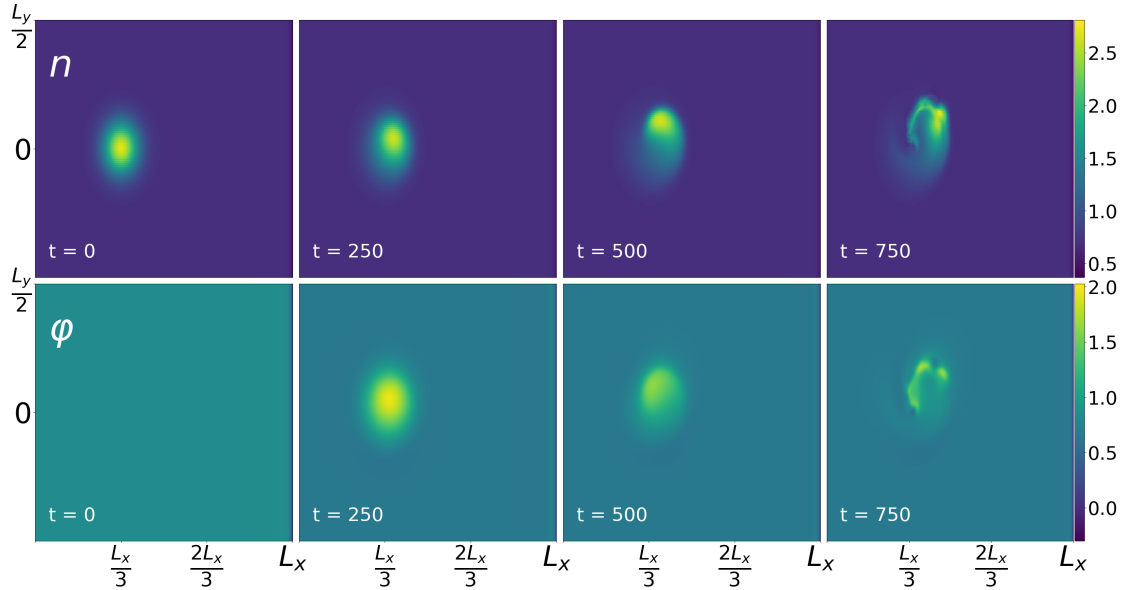
Figure 5.12: The propagation of n and φ for a blob in the $x - y$ plane at $z = 0$. The blob is initialised with $A = 2$, $d_\perp = 10$, $w_\parallel = \tilde{L}_\parallel/10$ and $d_\parallel = 4000$.

following the inertial scaling described in sec. 4.2.

The radial and poloidal centre of mass velocities are plotted in fig. 5.15, and here we observe that the blob with $d_\parallel = 2250$ displays different behaviour from the other filaments, initially accelerating, where the other filaments initially decelerate. This behaviour is, to the best of the authors knowledge, not observed in other 3D fluid models, and thus needs to be investigated further. We also observe that the filament with $d_\parallel = 2250$ propagates much slower than the other filaments both radially and poloidally. The other
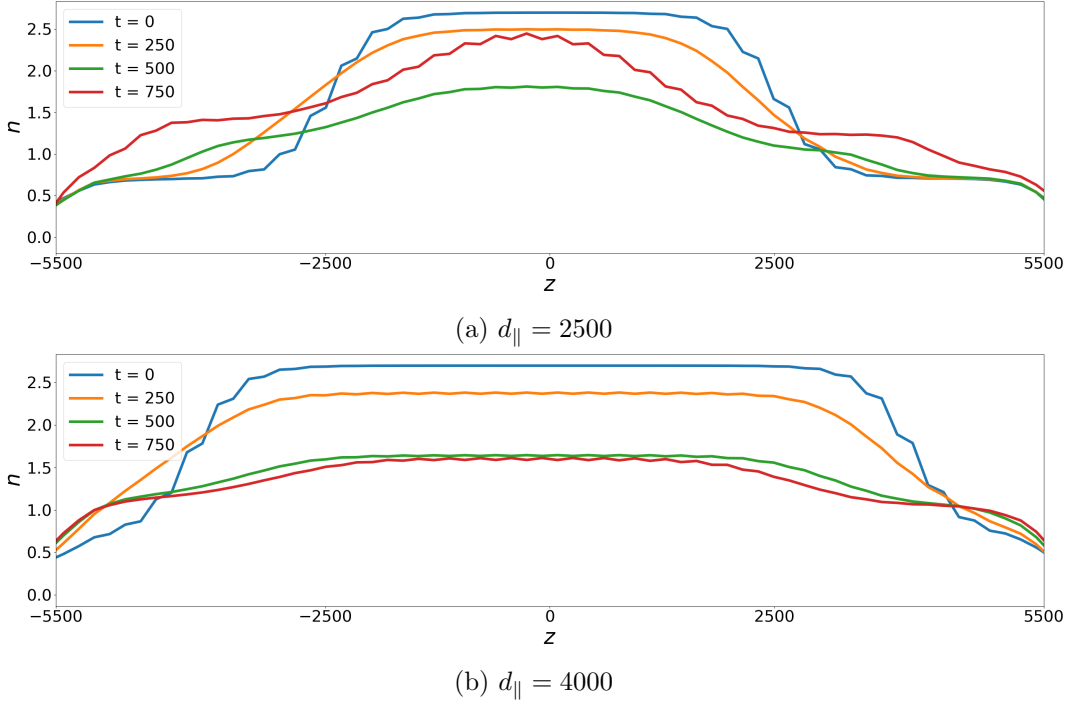
(a) $d_\parallel = 2500$

(b) $d_\parallel = 4000$

Figure 5.13: The parallel profiles of the maximum radial position at $y = 0$ for a filament initialised with $A = 2$, $d_\perp = 10$, $w_\parallel = \tilde{L}_\parallel/10$. Figure (a) is for a width of the hyperbolic tangent of $d_\parallel = 2500$ and (b) is for a width of the hyperbolic tangent of $d_\parallel = 4000$.
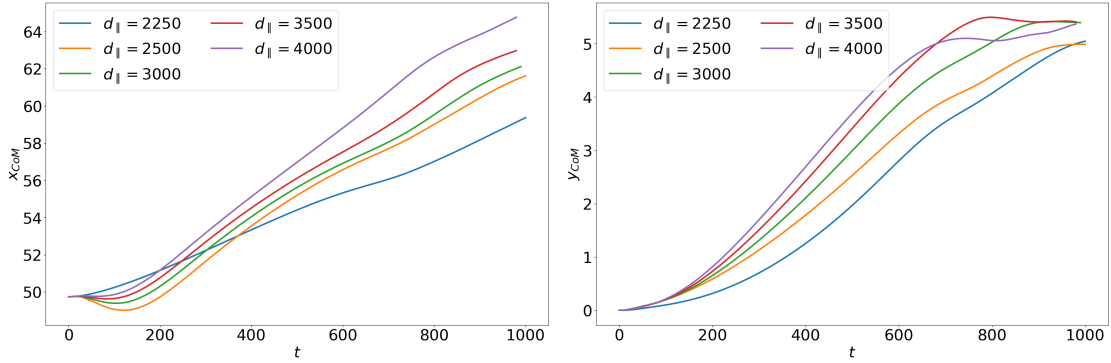
Figure 5.14: Radial and poloidal center of mass position as a function of time for blobs initialised with $A = 2$, $d_\perp = 10$, $w_\parallel = \tilde{L}_\parallel/10$ and a range of $d_\parallel$ as stated in the legends.

filaments all initially decelerate in the radial direction, then accelerate until they reach a maximum velocity, then decelerate and accelerate again creating a bump in the velocity profile, which occurs at the time when the blob starts to break apart. In the poloidal direction illustrated in the left plot in fig. 5.14, all blobs initially accelerate upward, reach a maximum velocity, and then decelerate. As was also observed with the radial velocity, a bump in the poloidal velocity profile is seen around the time when the blob begins to break apart.

In summary the trends for all blobs in the velocity profiles are very similar, except for the initial radial deceleration of the larger blobs, and bumps in the centre of mass velocities

are seen in all cases. These bumps in the velocity profiles were also observed for three-dimensional simulations in ref. [75], and this behaviour was not observed for the 2D filaments described in sec. 4.2, leading us to believe that they are an attribute of the 3D dynamics.
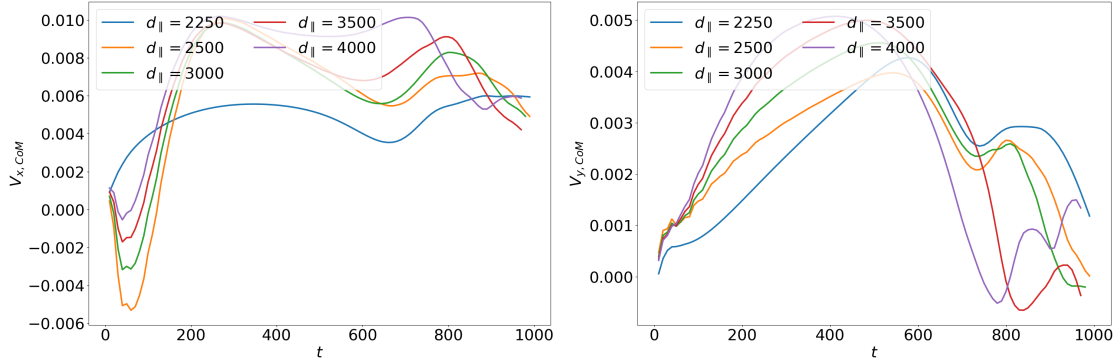
Figure 5.15: Radial and poloidal center of mass velocities as a function of time for blobs initialised with $A = 2$, $d_\perp = 10$, $w_\parallel = \tilde{L}_\parallel/10$ and a range of $d_\parallel$ as stated in the legends.

5.4   Summary

In this chapter we investigated the influence of a three-dimensional geometry on the dynamics of seeded blobs. We started by examining the steady-state solution to the system of equations described in sec. 2.6, where we observed an asymmetry in the solutions for all fields. This asymmetry in the steady-state decreased with the number of grid-points in the parallel direction, which lead us to believe that the asymmetry is founded in numerical issues. However, we did observe that the steady-state solutions converged towards a symmetric solution and when examining the convergence rate of the numerical errors, we observed a convergence rate close to the expected value when excluding the lowest resolution cases. Although the behaviour observed is not ideal, we have left the investigation of the asymmetries to future work due to a limitation on the time available for this project. Instead we moved on to investigate how blobs initialised on top of the steady-state backgrounds evolve with different initial parameters. We observed that the width of the hyperbolic tangent used to initialise the filaments does not strongly influence the filament propagation, however we did observe that the parallel extent of the filaments has an influence on how the blob propagates. Larger filaments propagate faster both in the radial and poloidal direction and larger filaments initially rotate, but break into smaller fragments at the later stages of propagation. On the other hand smaller blobs continued to rotate, generating a spiral structure in the later stages of propagation.

Again we should state that the results presented here are preliminary and that thorough verification and validation of the code should be carried out before final conclusions are drawn.

Chapter 6

Scrape-off Layer Power fall-off length

Throughout this thesis, we have seen how both 2D and 3D dynamics affect blob propagation when studying isolated plasma filaments. However, in real tokamak plasmas, blobs are not spontaneously generated as Gaussian perturbations in the SOL on a flat background. They are self-consistently generated in the edge region and propagate across the LCFS into the SOL. The filaments do not only result in perpendicular transport. Since they are elongated along the magnetic field lines, they eventually reach the divertor, thus contributing to the so-called scrape-off layer power fall-off length, λ_q. The scrape-off layer power fall-off length is a measure for the radial width of the parallel channel transporting plasma from the outboard mid-plane to the divertor. In the final part of this thesis, we have therefore set out to investigate how λ_q scales with different parameters, highlighting the effects of the intermittent transport carried by blobs.

6.1 Scrape-off layer power fall-off length from turbulence simulations of ASDEX Upgrade L-mode

6.1.1 Introduction

The study of the λ_q scaling has been accepted in *Plasma Phys. Contr. Fusion* at the time of writing. It was carried out using an extended version of the HESEL model described in sec. 2.7, and a thorough description of the extensions to the model can be found in ref. [25]. Since HESEL is designed to model low confinement mode (L-mode) plasmas in medium sized tokamaks, we have restricted the analysis of λ_q to parameters relevant for ASDEX Upgrade (AUG) L-mode. Furthermore, the investigation carried out in this study was not focused on individual blobs, like what was done in the previous sections of this thesis, but rather on self consistently generated blobs and their impact on λ_q. The simulations for this study were carried out using an edge region with profiles resembling those seen in experiments, forced at the inner boundaries of the domain, and with a full SOL and a wall-region included in the simulation domain. The simulations were run long

enough for approximately 100 blob events to occur, so the average effect of intermittent blobs and their contribution to λ_q could be modelled.

This paper sets out to determine the contributions from different heat flux channels to λ_q. Through the use of turbulence simulations, the parallel losses due to advection and conduction for both electrons and ions are determined. Then a series of parameter scans are carried out to determine the scaling of λ_q. The parameters included in the scalings were determined based on their mutual correlation, where parameters with a correlation of more than 50% were excluded from the same fits of λ_q.

Scrape-off layer power fall-off length from turbulence simulations of ASDEX Upgrade L-mode

Jeppe Olsen

PPFE, Department of Physics, Technical University of Denmark, Building 309, 2800 Kgs. Lyngby

E-mail: `jmbols@fysik.dtu.dk`

Anders Henry Nielsen

PPFE, Department of Physics, Technical University of Denmark, Building 309, 2800 Kgs. Lyngby

E-mail: `ahnie@fysik.dtu.dk`

Jens Juul Rasmussen

PPFE, Department of Physics, Technical University of Denmark, Building 309, 2800 Kgs. Lyngby

E-mail: `jjra@fysik.dtu.dk`

Jens Madsen

PPFE, Department of Physics, Technical University of Denmark, Building 309, 2800 Kgs. Lyngby

E-mail: `jmad@fysik.dtu.dk`

Thomas Eich

Max-Planck Institute for Plasma Physics, Boltzmannstrasse 2, Garching, Germany

E-mail: `thomas.eich@ipp.mpg.de`

Bernhard Sieglin

Max-Planck Institute for Plasma Physics, Boltzmannstrasse 2, Garching, Germany

E-mail: `bernhard.sieglin@ipp.mpg.de`

Volker Naulin

PPFE, Department of Physics, Technical University of Denmark, Building 309, 2800 Kgs. Lyngby

E-mail: `vona@fysik.dtu.dk`

Abstract. The scrape-off layer power fall-off length, λ_q, for parameters relevant to ASDEX Upgrade (AUG) L-mode discharges is examined by means of numerical simulations. The simulation data is acquired using synthetic probe data from turbulence simulations, which gives a high temporal resolution on the full density and pressure fields, required for an accurate evaluation of λ_q due to the strongly intermittent signals in the scrape-off layer (SOL). Electron conduction is found to dominate the parallel heat flux close to the separatrix, while ion convection dominates in the far SOL. Good agreement is found with the experimental scaling for AUG L-mode [Sieglin et al., Plasma Phys. Contr. Fusion 2016;58(5):055015], where λ_q is found to scale almost linearly with the safety factor, q, and to be weakly dependent on the power across the last-closed flux surface (LCFS), P. However, P depends on a wide range of parameters. In this paper we trace this dependence and the resulting fit of λ_q reveals a scaling proportional to the inverse square root of the electron temperature at the LCFS, $T_{e,LCFS}^{-1/2}$, and a linear dependence on q.

1. Introduction

In magnetic confinement fusion devices most of the power across the last-closed flux surface (LCFS) is transported towards the divertor along magnetic field lines in a narrow region close to the separatrix [1]. The width of this channel is denoted as λ_q and it is crucial to know this parameter when determining the divertor peak heat load, which for ITER steady state operation needs to be kept below 10 MWm^{-2} due to material constraints. To estimate λ_q for ITER, several empirical scaling laws have been derived based on engineering parameters and extrapolated to ITER relevant parameters, both for limited plasmas [2–4] and for divertor plasmas [5–8].

The different scaling laws, however, do not all agree and it is not yet clear how much individual heat flux channels contribute to λ_q. In the experimental scaling laws, λ_q is either determined at the outer mid-plane using reciprocating Langmuir probes (as in [3]) or at the divertor using infra-red spectrometry and then mapping it to the outboard mid-plane (as in [1]). Neither of these methods provide insight into the individual contributions from electrons and ions to λ_q, and both are subject to large uncertainties when estimating λ_q and the corresponding parameters, e.g., when determining the position of the LCFS. For larger machines like AUG, it has been shown that the width of the parallel heat flux channel, λ_q, and the width of the parallel electron temperature channel, λ_{Te}, even when in L-Mode conditions, are well correlated by Spitzer-Härm conduction and hence $\lambda_q/\lambda_{Te} = 2/7$ is found [9, 10]. This correlation, however, is doubtful for smaller machines like TCV and Compass, so an experimental

multi-machine scaling for the power width in L-Mode conditions is difficult to establish and prone to artefacts; therefore this paper focuses on AUG L-mode relevant parameters. To identify the contributions from different heat flux channels to λ_q and to gain further understanding for the physical processes determining the scrape-off layer power fall-off length, numerical simulations are employed. The advantage of simulations is that every parameter is known exactly, and thus contributions to λ_q can be identified and held up against experiments to validate the results. Several papers have investigated how λ_q scales with different parameters using numerical simulations [11–14], but these studies used either steady-state transport codes or turbulence codes assuming cold ions. In the present paper we investigate the parameter dependence of λ_q by means of numerical simulations using the HESEL model [15], a 2D drift-fluid model. The model parametrises 3D dynamics with parallel heat fluxes and a sheath connection closure to incorporate the effects along the magnetic field lines as well as drift-wave terms in the region of closed field lines. Although this approach does not capture the full dynamics between the outboard midplane and the divertor, where full 3D codes such as HERMES [16], GBS [17] and TOKAM3X [18] are needed to incorporate these effects, the scaling found in this paper compares well with experimental results found for AUG L-mode [19]. Through turbulence simulations we deduce the parallel losses due to advection and conduction for both electrons and ions, and through parameter scans, with parameters chosen based on statistical significance using an approach similar to that in [3], we calculate numerical scalings for λ_q.

The outline of the paper is as follows; in section 2 we introduce the HESEL model used for the simulations and the methods used for calculating λ_q, in section 3 we present how the scaling parameters are chosen and the derived numerical scaling laws, and finally in section 4 we summarise and conclude the work.

2. The HESEL model

The HESEL model [15] is used for simulations throughout the paper. HESEL is a 2D model derived from the Braginskii two-fluid equations [20] solving for the density, n, generalised vorticity, $\omega^* = \nabla^2\varphi + \nabla^2 p_i$, electron pressure, p_e and ion pressure, p_i. 3D dynamics are parametrised following the approach and assumptions given in [21]. The simulations are conducted in a domain at the out-board midplane of a tokamak, as illustrated in Fig. 1. For all equations, Bohm normalisation has been imposed;

$$\omega_{ci}t \to t, \quad \frac{\mathbf{x}}{\rho_s} \to \mathbf{x}, \quad \frac{e\varphi}{T_{e0}} \to \varphi, \quad \frac{n}{n_0} \to n, \quad \frac{T_e}{T_{e0}} \to T_e, \quad \frac{T_i}{T_{e0}} \to T_i, \qquad (1)$$

where T_e is the electron temperature, T_i is the ion temperature, n is the density, φ is the electrostatic potential and t is time. The normalisation parameters are the ion cyclotron frequency, $\omega_{ci} = eB_0/m_i$, the ion gyroradius at electron temperature, $\rho_s = c_{s0}/\omega_{ci}$, the electron charge, e, the reference electron temperature, T_{e0}, the reference density, n_0, the magnetic field strength at the outboard mid-plane, B_0, the ion mass, m_i, and the constant sound speed at the reference electron temperature, $c_{s0} = (T_{e0}/m_i)^{1/2}$.

Figure 1: The cross-section of AUG with the HESEL domain indicated to scale by the red box.

The HESEL model reads

$$d_t n + n\mathcal{K}(\varphi) - \mathcal{K}(p_e) = \Lambda_n, \tag{2}$$

$$d_t^0 \omega^* + \{\nabla\varphi, \nabla p_i\} - \mathcal{K}(p_e + p_i) = \Lambda_{\omega^*}, \tag{3}$$

$$\frac{3}{2}d_t p_e + \frac{5}{2}p_e\mathcal{K}(\varphi) - \frac{5}{2}\mathcal{K}\left(\frac{p_e^2}{n}\right) = \Lambda_{p_e}, \tag{4}$$

$$\frac{3}{2}d_t p_i + \frac{5}{2}p_i\mathcal{K}(\varphi) + \frac{5}{2}\mathcal{K}\left(\frac{p_i^2}{n}\right) - p_i\mathcal{K}(p_e + p_i) = \Lambda_{p_i}, \tag{5}$$

where $d_t = (\partial_t + B(x)^{-1}\hat{\mathbf{z}} \times \nabla\varphi \cdot \nabla)$ is a material derivative, with $B(x) = B_0(R_0 + a)/(R_0 + a + x)$ being the magnetic field modulus, R_0 is the device major radius, a is the device minor radius, x is the radial coordinate from the LCFS and $\partial_t = \partial/\partial_t$. $d_t^0 = (\partial_t + B_0^{-1}\hat{\mathbf{z}} \times \nabla\varphi \cdot \nabla)$ denotes the material derivative with constant magnetic field. $\mathcal{K} = \nabla(B(x)^{-1})\cdot\hat{\mathbf{z}}\times\nabla$ is the curvature operator, where $\hat{\mathbf{z}}$ is a unit vector in the direction of the magnetic field. The Poisson bracket is

$$\{\varphi, f\} = \frac{\partial\varphi}{\partial x}\frac{\partial f}{\partial y} - \frac{\partial f}{\partial x}\frac{\partial\varphi}{\partial y}. \tag{6}$$

The right-hand sides of Eqs. (2)-(5) consist of perpendicular dissipation terms and parametrised parallel dynamics, given by

$$\Lambda_n = D_e \nabla_\perp^2 n - \frac{n}{\tau_d} - \alpha \left(\tilde{T}_e + \frac{\tilde{T}_e}{\bar{n}} \tilde{n} - \tilde{\varphi} \right) - \frac{n - n_p}{\tau_p} \tag{7}$$

$$\Lambda_{\omega^*} = D_i \nabla_\perp^2 \omega^* - \frac{\omega^*}{\tau_\omega} + \frac{\rho_s}{L_\parallel} \left[1 - \exp \left(\varphi_w - \frac{\varphi_s}{T_{e,s}} \right) \right] - \alpha \left(\tilde{T}_e + \frac{\tilde{T}_e}{\bar{n}} \tilde{n} - \tilde{\varphi} \right) \tag{8}$$

$$\Lambda_{p_e} = \frac{5}{2} D_e \nabla_\perp^2 p_e + \left(\frac{16}{6} - \frac{5}{2}\tau \right) \nabla \cdot (n \nabla_\perp T_e) - \frac{9}{2} \frac{p_e}{\tau_d} - \frac{T_e}{\tau_{SH,e}}$$

$$- \alpha \tilde{T}_e \left(\tilde{T}_e + \frac{\tilde{T}_e}{\bar{n}} \tilde{n} - \tilde{\varphi} \right) - \Theta - \frac{p_e - p_{e,p}}{\tau_p} \tag{9}$$

$$\Lambda_{p_i} = D_i \nabla_\perp^2 p_i - D_i T_i \nabla_\perp^2 n - \frac{9}{2} \frac{p_i}{\tau_d} + \Theta - \frac{p_i - p_{i,p}}{\tau_p} - \frac{T_i}{\tau_{SH,i}} + p_i \Lambda_{\omega^*}, \tag{10}$$

with the neoclassical diffusion coefficients given by

$$D_i = \left(1 + \frac{R_0}{a} q^2 \right) \frac{\rho_{i0}^2 \nu_{ii0}}{\rho_s^2 \omega_{ci}}, \tag{11}$$

$$D_e = (1 + \tau) \left(1 + \frac{R_0}{a} q^2 \right) \frac{\rho_{e0}^2 \nu_{ei0}}{\rho_s^2 \omega_{ci}}, \tag{12}$$

as derived in [21] where ρ_{i0} is the ion gyroradius and ρ_{e0} is the electron gyroradius both at reference temperatures. ν_{ii0} is the ion-ion collision frequency at reference temperature, ν_{ei0} is the electron-ion collision frequency at reference temperature, q is the safety factor, and $\tau = T_{i0}/T_{e0}$, where T_{i0} is a reference ion temperature. $L_\parallel$ is the parallel connection length, $\varphi_w = \ln \left(\sqrt{m_i/(2\pi m_e)} \right)$ is the Bohm potential and $\alpha = 2T_{e0}/(\nu_{ei0} m_e L_\parallel^2 \omega_{ci})$ is the drift-wave coefficient. φ_s is the potential at the sheath entrance and $T_{e,s}$ is the electron temperature at the sheath entrance. In this paper we have assumed that the plasma is connected to the sheath, which is modelled using $T_{e,s} = T_e(x, y, t)$ and $\varphi_s = \varphi(x, y, t)$, i.e. the sheath dissipation depends on the full temperature and potential fields.

The term $\Theta = 3(m_e/m_i)\nu_{ei0} (p_e - p_i)$ is the energy transfer between electrons and ions. The tilde $\tilde{f}$ denotes a fluctuating term of the field f and $\bar{f}$ denotes the poloidal average, defined as

$$\tilde{f} \equiv \bar{f} - f, \qquad \bar{f} \equiv \frac{1}{L_y} \int_0^{L_y} f \mathrm{d}y, \tag{13}$$

where L_y is the poloidal length of the domain. At the inner boundary, the profiles are forced with the characteristic time τ_p towards prescribed profiles, n_p , $p_{e,p}$, $p_{i,p}$. τ_p is kept shorter than the interchange time, and the profiles are made to resemble typical profiles measured in the edge region of tokamak experiments and thus act as particle and energy sources, while avoiding unphysical steep gradients generated at the inner boundary when using constant particle and energy sources [15].

The parallel dynamics are parametrised in the form of parallel loss terms due to advection and electron and ion heat conduction (Spitzer-Härm conduction) with loss
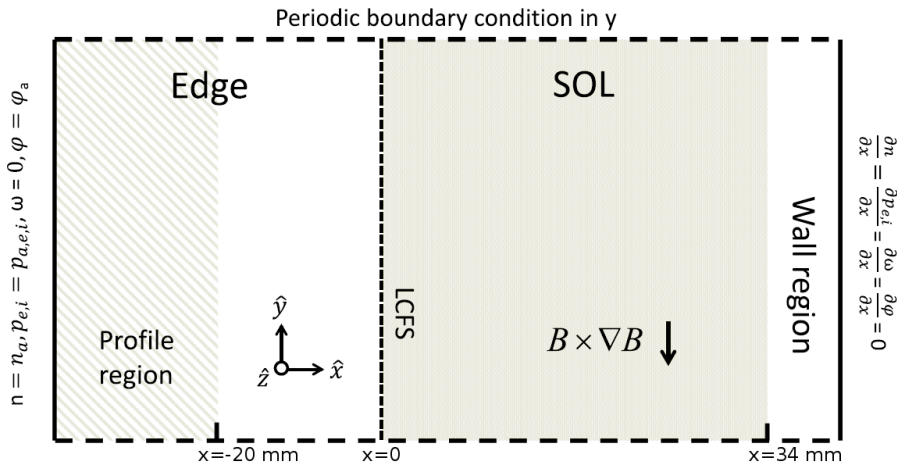
Figure 2: An illustration of the HESEL domain (not to scale) with boundary conditions and geometry illustrated in the plot.

rates given by

$$\tau_{SH,e} = \frac{L_B^2 \nu_{ee}}{3.2 v_e^2}, \qquad \tau_{SH,i} = \frac{L_B^2 \nu_{ii}}{3.2 v_i^2}, \qquad \tau_d = \frac{L_B}{2M c_s}, \tag{14}$$

where $L_B = q R_0$ is the parallel ballooning length. $v_{e(i)}$ is the electron (ion) thermal speed, $\nu_{ee(ii)}$ is the electron-electron (ion-ion) collision frequency, both depending on the local values of $T_{e(i)}$ so that $\tau_{SH,e(i)}^{-1} \propto T_{e(i)}^{5/2}$ and M is the parallel Mach number assumed to be $M = 0.5$ at the outboard mid-plane (see [22] for a thorough description of this assumption). Finally $c_s = \sqrt{(T_e + T_i)/m_i}$ is the sound speed, which depends on the local electron and ion temperatures. We note that in order for Spitzer-Härm conduction to be valid, the electron collisionality [23]

$$\nu_e^* \equiv \frac{L_{\parallel} \nu_{ei}}{v_e} \gg 10, \tag{15}$$

which is fulfilled for all simulations in this paper.

2.1. Evaluation of λ_q

Assuming that the transport across the LCFS originates from ballooning-like turbulence in a poloidal extend of 60° at the out-board mid plane [15], given approximately by $2\pi a/6 \approx a$, and assuming that the power is evenly distributed in this region, we can calculate the radial profile of the parallel heat fluxes. This is done using data from from synthetic probes in the HESEL domain illustrated in Fig. 2, where $n_a, p_{a,e,i}$ is the value of the fixed profile at the inner boundary for the density and the electron and ion pressures, respectively, and φ_a (see Fig. 2) is chosen so that $\omega^* = 0$ at the inner boundary.

The parallel heat flux at the outboard mid-plane is calculated from the parametrised parallel dynamics, and following the parametrisation stated in [21] as well as the contribution from the ion Spitzer-Härm conduction, we get four contributions to the

parallel heat flux. The approach used in HESEL assumes quasineutrality, which consequently means that only small variation between the parallel velocities is allowed, and as a result, the thermal heat flux is assumed small compared to the other four contributions and has been neglected. The contributions to the parallel heat flux are thus a contribution from the electron advection, $q_{\parallel,a,e}$, the ion advection, $q_{\parallel,a,i}$, the electron conduction (also known as Spitzer-Härm conduction), $q_{\parallel,SH,e}$ and the ion conduction, $q_{\parallel,SH,i}$, given by

$$q_{\parallel,a,e} \quad = a \left\langle \frac{9}{2}\frac{p_e}{\tau_d} \right\rangle_t, \qquad q_{\parallel,a,i} \quad = a \left\langle \frac{9}{2}\frac{p_i}{\tau_d} \right\rangle_t \tag{16}$$

$$q_{\parallel,SH,e} = a \left\langle \frac{p_e}{\tau_{SH,e}} \right\rangle_t, \qquad q_{\parallel,SH,i} = a \left\langle \frac{p_i}{\tau_{SH,i}} \right\rangle_t, \tag{17}$$

where $\langle \cdot \rangle_t$ denotes a temporal average. All terms are multiplied by the poloidal extent of the ballooning region, a, following the assumption above. We should state that macroscopic heat fluxes have been neglected since the mean fluid velocity at the outboard mid-plane is negligible. However, when approaching the divertor target, part of the thermal energy in expanding filaments will be converted to kinetic energy of the ions streaming toward the target plates at the filament fronts and this contribution to the heat flux would have to be evaluated. However, at the outboard mid-plane the parallel heat flux is described by the four contributions stated above. It is important to note that the full temperature and pressure fields are used for computing the parallel fluxes in Eqs. (16) and (17). Since a significant fraction of the transport across the LCFS is intermittent [24], the parallel heat fluxes can not be calculated solely based on temporally averaged profiles, but need to be evaluated using the full temporal signals to capture the contributions from the intermittent bursts. To illustrate the importance of using the full fields, we have plotted the electron temperature at the LCFS in the poloidal centre of the domain as a function of time in Fig. 3a. Here it is seen that the electron temperature is subject to large fluctuations varying by more than a factor of five. This inevitably influences the value of the parallel heat flux, as is illustrated in Fig. 3b, where we have plotted the electron contributions to the parallel heat flux evaluated using Eqs. (16) and (17) using the full fields (blue) and the temporally averaged fields (magenta). The difference is most pronounced in the Spitzer-Härm conduction, where the averaged profile leads to an estimation of the heat flux, which is a factor of two smaller at the LCFS than the profile found using the full fields.

The total parallel heat flux is the sum of all four contributions in Eqs. (16) and (17), so

$$q_{\parallel} = q_{\parallel,a,e} + q_{\parallel,a,i} + q_{\parallel,SH,e} + q_{\parallel,SH,i} \tag{18}$$

The scrape-off layer power fall-off length is then calculated as

$$\lambda_q = \frac{\int_0^\infty x q_{\parallel}(x)\mathrm{d}x}{\int_0^\infty q_{\parallel}(x)\mathrm{d}x}, \tag{19}$$

where 0 is the location of the separatrix.
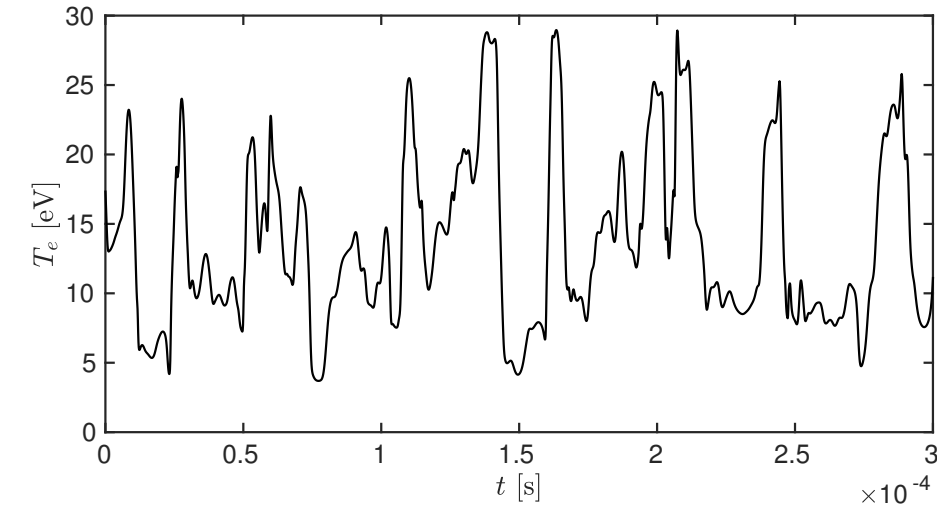
(a)
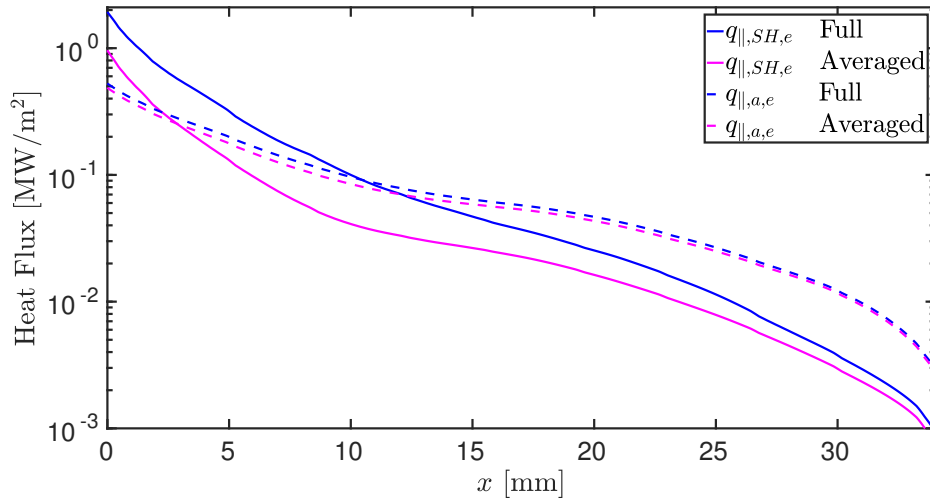
(b)

Figure 3: (a) Fluctuation level at the LCFS in the poloidal centre of the domain for a simulation with AUG relevant parameters. Only part of the temporal domain is shown. The full simulation is an order of magnitude longer. (b) The electron conduction (solid) and electron advection (dashed) contributions to the parallel heat flux for a typical simulation with AUG relevant parameters. The blue lines indicate the contributions calculated using the full fields and the magenta lines indicate the contributions calculated using averaged profiles.
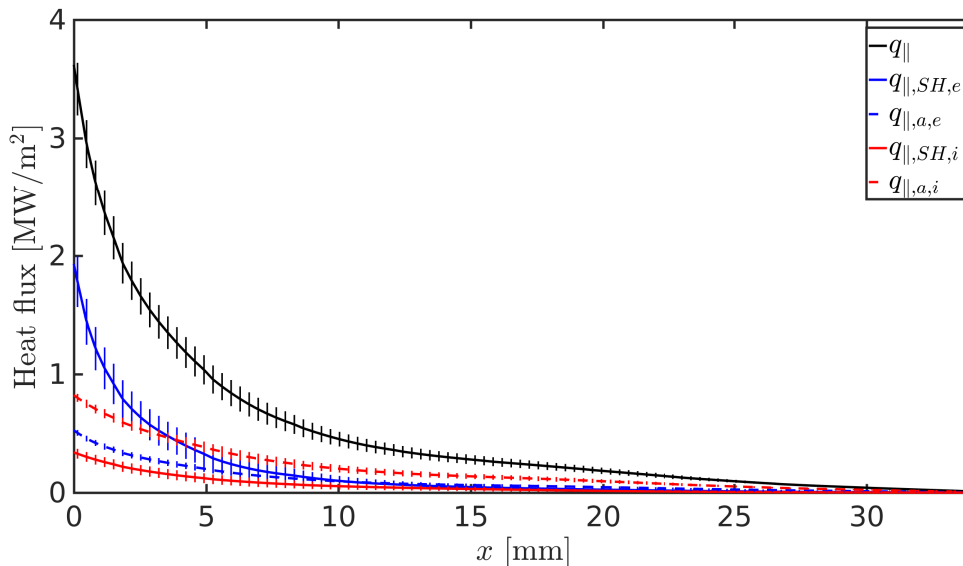
Figure 4: A typical parallel heat flux profile for AUG relevant parameters. The vertical lines indicate the 95% confidence limits on the averaged values.

A typical heat flux profile for parameters relevant for ASDEX Upgrade is seen in Fig. 4. The four contributions to the total heat flux are illustrated in the plot, and as seen from the figure, the electron conduction dominates the parallel transport close to the LCFS, while the ion advection and electron advection become the dominant terms in the far SOL, where the ion conduction remains insignificant throughout the SOL. This is made more evident when looking at the ratio of the individual contributions with respect to the full heat flux profile as a function of the radial position, which is illustrated in Fig. 5. Here we see that the contribution from ion advection becomes dominant a few millimetres into the SOL. Note that the illustrated domain does not show the full simulation domain, but only depicts the SOL.

3. Scrape-off layer power fall off length

The simulations, from which the heat flux profiles are calculated are repeated scanning several AUG relevant L-mode parameters. This is done in order to derive a numerical scaling law for λ_q in L-mode. λ_q is calculated using Eq. (19) for every scanned parameter, and a fit of λ_q is made as a function of different combinations of parameters. The scans are performed by varying the parameters one at a time while all other parameters are kept fixed at typical AUG L-mode values, $R_0 = 1.65$ m, $a = 0.5$ m, $q = 4.5$ and $B_0 = 1.9$ T. Since the total power across the LCFS, P, and the LCFS values of n, T_e and T_i are not input parameters, but depend on the forced profiles and the scanned input parameters, they vary slightly when the other parameters are scanned and they themselves are scanned by varying their respective forced profiles. The range of the scans are listed in table 1.
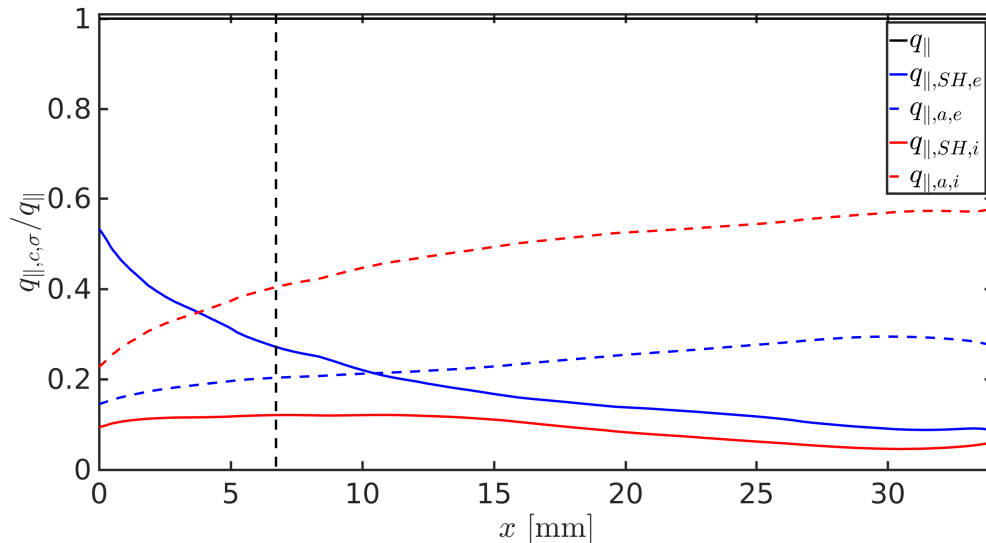
Figure 5: The fraction of the total heat flux for each of the four contributions. The dashed black line indicates the extent of the power fall-off length, λ_q, as calculated using Eq. (19).

Table 1: The scaled parameters with corresponding ranges.

Parameter	units	range
R_0	[m]	1-5
a	[m]	0.3-1.2
q		3.8-9.0
B_0	[T]	1.5-2.3
P	[MW]	0.04-1.27
n_{LCFS}	[10^{19} m^3]	1.1-2.8
$T_{e,LCFS}$	[eV]	11-22
$T_{i,LCFS}$	[eV]	14-43

Here $P = 2\pi(R_0 + a)\int_0^\infty q_\parallel(x)\mathrm{d}x$ is the total power across the LCFS, where the $2\pi(R_0 + a)$ accounts for the circumference of the tokamak, n_{LCFS} is the density at the LCFS and $T_{e(i),LCFS}$ is the electron(ion) temperature at the LCFS. We are aware that the electron and ion temperatures are low compared to usual AUG parameters, however, it should be noted that the LCFS is at the bottom of a steep gradient and moving the position 0.5 cm further in (which is less than the precision with which the position of the LCFS is determined in experiments) increases the temperatures by more than 50%.

3.1. Comparison with experimental scaling

First we investigate the experimental L-mode scaling from AUG derived in [19]. In this paper, a scan of P and q is performed, while the fit of B_0 is taken from a study of an
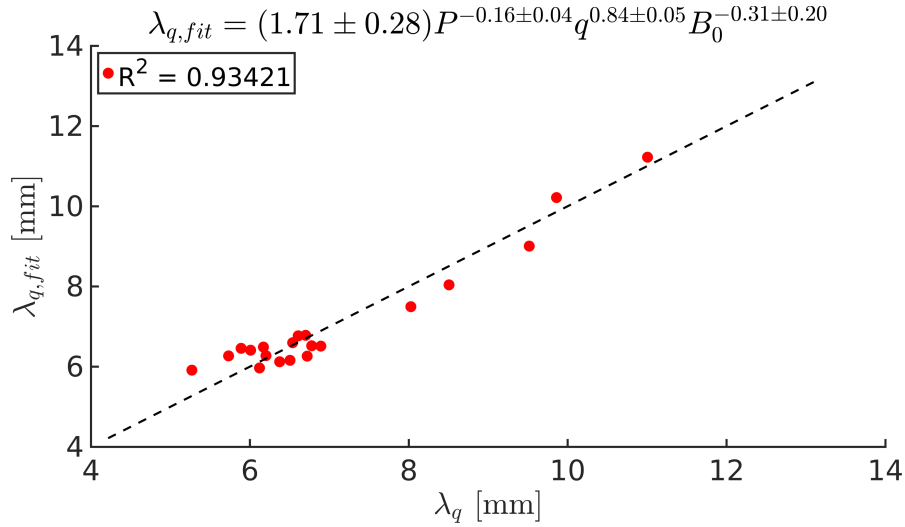
Figure 6: The nonlinear fit of λ_q with the parameters P, q and B_0 plotted with respect to the numerically found λ_q, given by Eq. (19). Note that each dot corresponds to a separate simulation.

H-mode scaling at AUG in [5] and the parameter was thus not scanned in the paper. The scaling arrived at is given by

$$\lambda_{q,Sieg} = (1.45 \pm 0.38)P^{-0.14\pm0.10}q^{1.07\pm0.07}B_0^{-0.78}, \tag{20}$$

where B_0 is highlighted in red since it is not a scanned parameter.

In order to compare our numerical results with the experiments, we include scans with the same parameters as in [19]. This means that $R_0 = 1.65$ m and $a = 0.5$ m are kept constant, while the variation in n_{LCFS} is kept small using a range of 1.2×10^{19} m^3 to 1.4×10^{19} m^3. A fit is then made using

$$\lambda_{q,fit} = AP^b q^c B_0^d, \tag{21}$$

where a nonlinear fitting routine using an iterative least squares estimation (nlinfit in MATLAB) is used to determine the parameters A, b, c and d. $\lambda_{q,fit}$ is plotted as a function of the numerically found value for λ_q in Fig. 6, where the best fit is found to be

$$\lambda_{q,fit} = (1.71 \pm 0.28)P^{-0.16\pm0.04}q^{0.84\pm0.05}B_0^{-0.31\pm0.20}. \tag{22}$$

We observe a fit with a coefficient of determination of $R^2 = 0.93$. The fit is weakly dependent on the power across the last closed flux surface, P, it scales almost linearly with the safety factor, q, and it is weakly dependent on the toroidal magnetic field, B_0. Comparing this scaling to Eq. (20) we observe a match within the error bars on P and we observe the same trend with an almost linear dependence with q. The scaling with toroidal magnetic field, B_0, differs between the two scalings, however, it should be noted that B_0 was not a scaled parameter in [19], so the two scalings cannot be directly compared with respect to this parameter.

3.2. Choice of scaling parameters

The scaling in the previous section was derived in order to compare the results with the experimental scaling from AUG. This meant that the scanned parameters were limited to P, q and B_0. Now, in order to make a more systematic investigation of the parameter dependence of λ_q, we fit it to all parameters listed in Tab. 1. However, some of the parameters have strong mutual correlation, so, following the approach in [3], we calculate the correlation between the different parameters. Since the correlation coefficient describes a linear correlation between two quantities, we determine the coefficient by making a linear fit between the logarithms of the two parameters in question. The mutual correlation between each parameter is illustrated in Tab. 2, and any parameters with a correlation of more than 50% are highlighted in bold face and are not included in the same scalings. We observe that the total power across

Table 2: Mutual correlation between the logarithms of the different fitting parameters.

Corr. (%)	a	n_{LCFS}	q	$T_{e,LCFS}$	$T_{i,LCFS}$	B_0	P	a/R_0
R_0	**63**	24	0	49	19	1	**71**	0
a		24	0	35	15	1	**79**	9
n_{LCFS}			7	23	12	3	**53**	0
q				37	32	1	6	13
$T_{e,LCFS}$					**89**	5	**76**	0
$T_{i,LCFS}$						6	**50**	0
B_0							5	0
P								0

the LCFS depends on a wide variety of scaling parameters, so in order to get a better understanding of what determines λ_q, it is fruitful to make a fit, where P is neglected and the other mutually independent parameters are included instead. Revisiting the scaling in Eq. (22) where P is replaced with the parameters n_{LCFS} and $T_{e,LCFS}$, we again apply the nonlinear fitting routine to get $\lambda_{q,fit}$. All parameter exponents in the fit are subject to uncertainties and are accompanied with 95% confidence intervals as calculated by the fitting routine. If the interval encompasses 0, then the parameter has no statistical significance and can be omitted from the scaling. When a parameter is omitted the fit is redone without this parameter and the process is repeated until only parameters with statistical significance remain. The outcome of this iterative routine is shown in Tab. 3. We observe a very good fit with a coefficient of determination of $R^2 = 0.96$ when including all parameters, which leads to a scaling given by

$$\lambda_{q,fit} = (8.06 \pm 2.14) n_{LCFS}^{0.54 \pm 0.32} q^{0.85 \pm 0.07} B_0^{-0.20 \pm 0.15} T_{e,LCFS}^{-0.58 \pm 0.11}, \qquad (23)$$

as illustrated in Fig. 7. However, we can, without significantly deteriorating the coefficient of determination, remove the parameters with the largest uncertainties, which is what we have done in the last two iterations in Tab. 3. This leads to a simple scaling,

Table 3: Scaling where P, q and B_0 are scanned.

A	n_{LCFS}	q	B_0	$T_{e,LCFS}$	R^2
8.06 ± 2.14	0.54 ± 0.32	0.85 ± 0.07	-0.20 ± 0.15	-0.58 ± 0.11	0.96
6.16 ± 1.38	-	0.93 ± 0.05	-0.28 ± 0.15	-0.45 ± 0.08	0.96
5.02 ± 1.04	-	0.92 ± 0.05	-	-0.44 ± 0.09	0.95
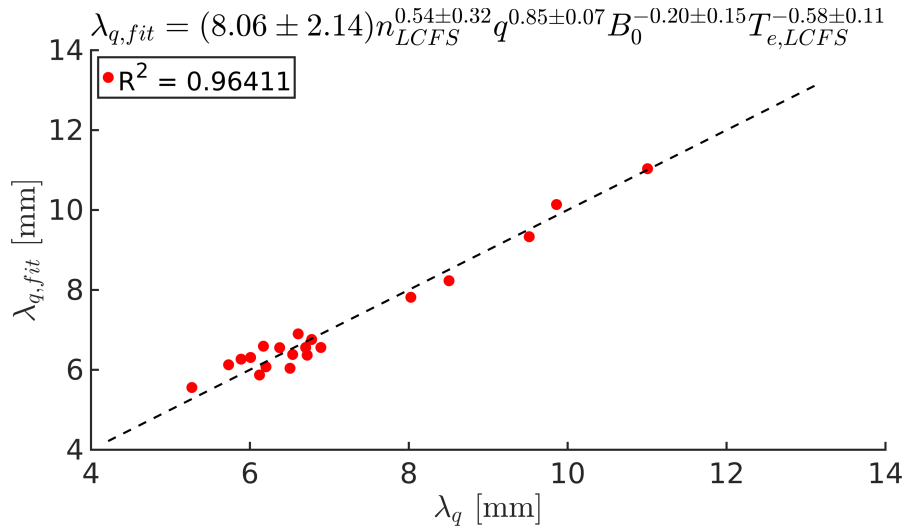
Figure 7: The nonlinear fit λ_q with respect to the parameters n_{LCFS}, q, B_0 and $T_{e,LCFS}$ for simulations where P, q and B_0 are scanned.

where λ_q is solely determined by the electron temperature at the LCFS and the safety factor;

$$\lambda_{q,fit} = (5.02 \pm 1.04)q^{0.92 \pm 0.05}T_{e,LCFS}^{-0.44 \pm 0.09} \tag{24}$$

with a coefficient of determination of $R^2 = 0.95$, which is plotted in Fig. 8. Comparing this fit, to Fig. 7, we do not observe any major improvements to the fit quality with more parameters. This means that the extra parameters in the fit in Eq. (23) compared to Eq. (24) merely add complexity, but do not significantly improve how well λ_q is described by the parameters.

3.3. Scaling with n_{LCFS}

The λ_q scalings found in Eqs. (22) and (24) were derived with a scan over P, q and B_0 to be able to compare with experimentally found values. However, we observed large uncertainties on the exponents of several parameters in the scalings, so in order to reduce the range of the confidence interval for the parameter exponents, a dedicated scan of n_{LCFS} with the range given in Tab. 1 was conducted and included in the λ_q fits. The nonlinear fitting routine described previously is applied with the extra parameter scan and the result is seen in Tab. 4. We get a match within the errorbars on all parameters compared to the fit in seen in Eq. (23). However, we still get large uncertainties on B_0
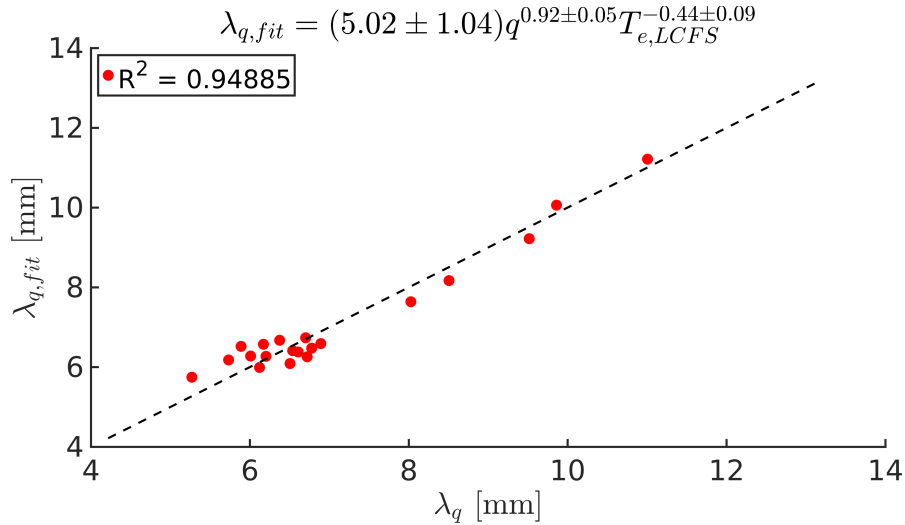
Figure 8: The nonlinear fit λ_q with respect to the parameters $T_{e,LCFS}$ and q for simulations where P, q and B_0 are scanned.

Table 4: Scaling where P, q, B_0 and n_{LCFS} are scanned.

A	n_{LCFS}	q	B_0	$T_{e,LCFS}$	R^2
5.57 ± 1.28	0.23 ± 0.05	0.86 ± 0.05	-0.23 ± 0.18	-0.41 ± 0.08	0.93
4.74 ± 0.92	0.24 ± 0.05	0.86 ± 0.05	-	-0.40 ± 0.08	0.93

and when removing this parameter from the scaling, as is done in the last step in Tab. 4, we do not observe a significant reduction in the fit quality. This leads to a fit given by

$$\lambda_{q,fit} = (4.74 \pm 0.92)n_{LCFS}^{0.24\pm0.05}q^{0.86\pm0.05}T_{e,LCFS}^{-0.40\pm0.06} \tag{25}$$

with a coefficient of determination of $R^2 = 0.93$. The fit is plotted in Fig. 9 and we observe that the points lie very close to the straight line indicating that λ_q is described well by the fourth root of n_{LCFS}, which compares well with [6], the inverse square root of $T_{e,LCFS}$ and linearly with q.

3.4. Scaling with R_0

Finally, we investigate the dependence of λ_q on the major radius, where all parameter scans from Tab. 1 are included. R_0 enters the calculations in a wide range of ways. First it enters in the curvature operator $\propto 1/R_0$, so a larger major radius decreases the amount of turbulence. The connection lengths and ballooning lengths are $\propto R_0$ and the neoclassical corrections in the diffusivities are $\propto R_0 q^2$. This means that the perpendicular diffusivities increase with R_0, whereas the sheath loss and the other parallel losses decrease. It is therefore difficult to predict exactly how R_0 will affect λ_q.

The parameter scan of R_0 is conducted both with a fixed aspect ratio, a/R_0 of

$$\lambda_{q,fit} = (4.74 \pm 0.92) n_{LCFS}^{0.24 \pm 0.05} q^{0.86 \pm 0.05} T_{e,LCFS}^{-0.40 \pm 0.08}$$

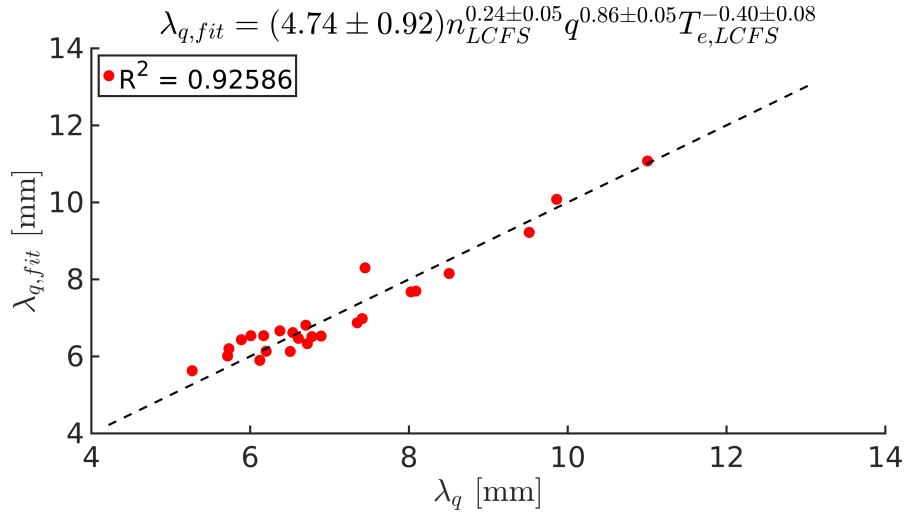Figure 9: The nonlinear fit of λ_q with respect to the parameters n_{LCFS}, q and $T_{e,LCFS}$ for simulations where P, q, B_0 and n_{LCFS} are scanned.

0.3, varying both a and R_0 to keep the ratio fixed, and with a fixed minor radius of $a = 0.5$ m, so the aspect ratio varies between 0.1 and 0.3. The scaling is seen in Tab. 5.

Table 5: Scaling where P, q, B_0, n_{LCFS} and R_0 are scanned.

A	n_{LCFS}	q	B_0	$T_{e,LCFS}$	R_0	R^2
3.70 ± 1.04	0.27 ± 0.06	0.84 ± 0.07	-0.21 ± 0.24	-0.37 ± 0.10	0.64 ± 0.04	0.93
3.19 ± 0.72	0.27 ± 0.06	0.84 ± 0.07	-	-0.36 ± 0.10	0.63 ± 0.04	0.93

The best fit is found to be

$$\lambda_{q,fit} = (3.19 \pm 0.72) n_{LCFS}^{0.27 \pm 0.06} q^{0.84 \pm 0.07} T_{e,LCFS}^{-0.36 \pm 0.10} R_0^{0.63 \pm 0.04}, \tag{26}$$

with $R^2 = 0.93$. As illustrated in Fig. 10, the fit is very close to the straight line with the exception of two outliers for very small major radii. This scaling with the major radius is in sharp contrast to what was found in the multimachine scaling in [5], where λ_q was found to be independent of the major radius, but agrees well with Halpern [8], Militello [13] and Myra [25]. The discrepancy with the experimental multi machine scaling may be attributed to the decrease in parallel losses with increasing major radius, which broadens λ_q. However, these parallel loss terms are 2D parametrisations of a 3D field, and therefore do not capture the dynamics between the outboard midplane and the divertor region, where the parallel heat flux is measured in [5]. In order to capture these dynamics and describe the heat flux at the divertor, a full 3D model will be necessary. The effects of such 3D models on filamentary transport are discussed in [26] and [27] and the inclusion of 3D effects on the SOL width is discussed in [28].
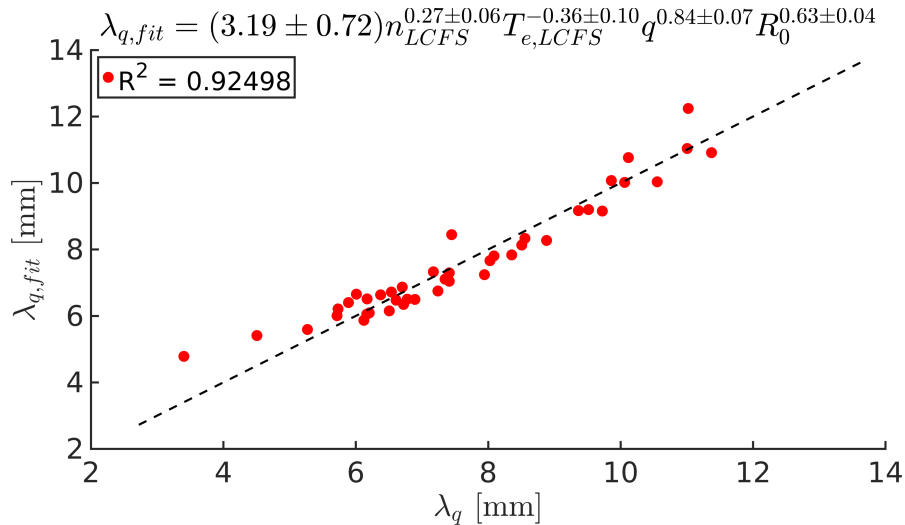
Figure 10: The nonlinear fit of λ_q with respect to the parameters n_{LCFS}, q, $T_{e,LCFS}$ and R_0 for simulations where n, P, q, B_0.

4. Conclusion

In this paper, we have investigated the SOL power fall-off length, λ_q, by means of numerical simulations using the HESEL model. Since plasma transport in a tokamak is strongly intermittent, it is crucial to account for this intermittency when determining λ_q and averaged profiles can thus not be used. We have calculated the SOL power fall-off length by determining the parallel heat fluxes using full fields. Assuming that both advection and conduction for ions and electrons constitute the parallel heat flux, we get four individual contributions. We observe for typical AUG L-mode parameters, that electron conduction dominates the parallel heat flux close to the separatrix, but further into the SOL electron and ion advection take over, with the ion advection being dominant in the far SOL, and broaden λ_q, which is determined by the weighted average position of the parallel heat flux.

In order to compare with experimentally found scaling laws for λ_q, we initially made a parameter scan using parameters comparable to those used in AUG L-mode discharges. From this, we found a scaling law given by

$$\lambda_{q,fit} = (1.71 \pm 0.28)P^{-0.16\pm0.04}q^{0.84\pm0.05}B_0^{-0.31\pm0.20}, \tag{27}$$

which is close to the L-mode scaling in [19] with a weak dependence on the total power across the LCFS, P, and an almost linear dependence on the safety factor, q. The dependence on the toroidal magnetic field differs between the experimental and numerical scalings, but since it was not a scaled parameter in [19] we cannot compare the two.

The experimental scaling laws were derived on the basis of engineering parameters, which influence the properties of the plasma, but do not tell us much about the physical processes behind the SOL power fall-off length. To get a better understanding of what

dictates λ_q, we examined the correlation between parameters which influence λ_q. It was found that P depends on a number of different parameters, so to understand what determines λ_q, the scaling was redone with P replaced by the density at the LCFS, n_{LCFS}, and the electron temperature at the LCFS $T_{e,LCFS}$. Here it was found that λ_q can be described by the two parameters q and $T_{e,LCFS}$ and that λ_q scales almost linearly with q and as one over the square root of $T_{e,LCFS}$.

Moving on to include a wider range of scanned parameters, including a dedicated scan of n_{LCFS} and the major radius, R_0, revealed a dependence of λ_q on n_{LCFS} and R_0 in addition to the dependence on q and $T_{e,LCFS}$. The best fit for λ_q was found to be

$$\lambda_{q,fit} = (3.19 \pm 0.72) n_{LCFS}^{0.27\pm0.06} q^{0.84\pm0.07} T_{e,LCFS}^{-0.36\pm0.10} R_0^{0.63\pm0.04}. \tag{28}$$

The dependence on R_0 conflicts with what was found in [5], where λ_q was found to be independent of R_0. Since the major radius enters the HESEL model both in the parallel loss-terms, the diffusivities and in the curvature operator, it is not straightforward to determine which term this inconsistency arises from and this analysis is therefore left for future studies.

Despite this we do observe a good fit with the experimental L-mode scaling for AUG, and we believe that the λ_q scalings we have found in this paper can act as a guideline for future experiments. In all scaling laws derived in this paper, it is important to note that the theory used is only valid for strongly collisional plasmas. The extrapolation of λ_q to ITER, however, needs to be done with care, since ITER is not expected to be dominated by Spitzer-Härm conduction due to it operating in a low collisional regime.

5. Acknowledgements

References

[1] Eich T, Sieglin B, Scarabosio A, Fundamenski W, Goldston RJ, Herrmann A, et al. Inter-ELM power decay length for JET and ASDEX Upgrade: measurement and comparison with heuristic drift-based model. Phys. Rev. Lett. 2011;107(21):215001.

[2] Kocan M, Pitts R A, Arnoux G, Balboa I, de Vries P C, et al. Impact of a narrow limiter SOL heat flux channel on the ITER first wall panel shaping Nucl. Fusion 2015;55:033019.

[3] Horacek J, Pitts R A, Adamek J, Arnoux G, Bak J-G, et al. Multi-machine scaling of the main SOL parallel heat flux width in tokamak limiter plasmas Plasma Phys. Contr. Fusion. 2016;58:074005.

[4] Silva C, Arnoux G, Devaux S, Frigione D, Groth M, et al. Characterization of scrape-off layer transport in JET limiter plasmas Nucl. Fusion. 2014;54:083022.

[5] Eich T, Leonard AW, Pitts RA, Fundamenski W, Goldston RJ, Gray TK, Herrmann A, Kirk A, Kallenbach A, Kardaun O, et al. Scaling of the tokamak near the scrape-off layer H-mode power width and implications for ITER. Nucl. Fusion. 2013;53(9):093031.

[6] Sieglin B, Eich T, Faitsch M, Herrmann A, Nille D, Scarabosio A, et al. Density dependence of SOL power width in ASDEX upgrade L-Mode Nucl. Mater. Energy. 2017;12:216-220.

[7] Faitsch M, Sieglin B, Eich T, Sun HJ, Herrmann A, et al. Change of the scrape-off layer power width with the toroidal B-field direction in ASDEX upgrade Plasma Phys. Contr. Fusion. 2015;57:075005.

[8] Halpern FD, Horacek J, Pitts RA, Ricci P. A theoretical interpretation of the main scrape-off layer heat-flux width scaling for tokamak inner-wall limited plasmas Plasma Phys. Contr. Fusion. 2016;58(8):084003.

[9] Sun HJ, Wolfrum E, Eich T, et al. Study of near scrape-off layer (SOL) temperature and density gradient lengths with Thomson scattering Plasma Phys. Contr. Fusion. 2015;57:125001.

[10] Eich T, Goldston RJ, Kallenbach A, Sieglin B, et al. Correlation of the tokamak H-mode density limit with ballooning stability at the separatrix Nucl. Fusion. 2018;58:034001.

[11] Myra JR, Russell DA, D'Ippolito DA, Ahn, JW, Maingi R, et al. Reduced model simulations of the scrape-off-layer heat-flux width and comparison with experiment Phys. Plasmas. 2011;18:012305.

[12] Stangeby PC, Canik JM, Whyte DG. The relation between upstream density and temperature widths in the scrape-off layer and the power width in an attached divertor. Nucl. Fusion. 2010;50(12):125003.

[13] Militello F, Naulin V, Nielsen AH. Numerical scalings of the decay lengths in the scrape-off layer. Plasma Phys. Contr. Fusion. 2013;55:074010.

[14] Halpern F D, Ricci P. Velocity shear, turbulent saturation, and steep plasma gradients in the scrape-off layer of inner-wall limited tokamaks Nucl. Fusion. 2017;57:034001.

[15] Nielsen AH, Juul Rasmussen J, Madsen J, Xu GS, Naulin V, Olsen JMB, Løiten M, Hansen SK, Yan N, Tophøj L, Wan BN. Numerical simulations of blobs with ion dynamics Plasma Phys. Contr. Fusion. 2017;59(2):025012.

[16] Dudson BD, Leddy, B. Hermes: global plasma edge fluid turbulence simulations Plasma Phys. Contr. Fusion. 2017;59(5):054010

[17] Halpern FD, Ricci P, Jolliet S, Loizu J, Morales J, Mosetto A, et al. The GBS code for tokamak scrape-off layer simulations J. Comput. Phys. 2016;315:388-408

[18] Tamain P, Bufferand H, Ciraolo G, Colin C, Galassi D, Ghendrih Ph, Schwander F, Serre E. The TOKAM3X code for edge turbulence fluid simulations of tokamak plasmas in versatile magnetic geometries J. Comput. Phys. 2016;321:606-623

[19] Sieglin B, Eich T, Faitsch M, Herrmann A, Scarabosio A, et al. Investigation of scrape-off layer and divertor heat transport in ASDEX Upgrade L-mode Plasma Phys. Contr. Fusion 2016;58(5):055015.

[20] Braginskii SI. Transport processes in a plasma Rev. Plasma Phys. 1965;1:205

[21] Madsen J, Naulin V, Nielsen AH, Juul Rasmussen J. Collisional transport across the magnetic field in drift-fluid models Phys. Plasmas. 2016;23(3):032306.

[22] Fundamenski W, Garcia OE, Naulin V, Pitts RA, Nielsen AH, Juul Rasmussen J, Horacek J, Graves JP et. al. Dissipative processes in interchange driven scrape-off layer turbulence Nucl. Fusion 2007;47(5):417

[23] Fundamenski W. Parallel heat flux limits in the tokamak scrape-off layer Plasma Phys. Control. Fusion. 2005;47:R163.

[24] Zweben SJ, Boedo JA, Grulke O, et. al. Edge turbulence measurements in toroidal fusion devices Plasma Phys. Control. Fusion. 2007;49(7):S1.

[25] Myra JR, D'Ippolito DA, Russel DA. Turbulent transport regimes and the scrape-off layer heat flux width Phys. Plasmas 2015;22:042516.

[26] Riva F, Colin C, Denis J, Easy L, Furno I, Madsen J, et al. Blob dynamics in the TORPEX experiment: a multi-code validation Plasma Phys. Control. Fusion. 2016;58(4):044005

[27] Militello F, Walkden NR, Farley T, Gracias WA, Olsen J, Riva F et al. Multi-code analysis of scrape-off layer filament dynamics in MAST Plasma Phys. Control. Fusion. 2016;58(10):105002.

[28] Jorge R, Ricci P, Halpern FD, Loureiro NF, Silva C. Plasma turbulence in the scrape-off layer of the ISTTOK tokamak Phys. Plasmas. 2016;23(10):102511.

6.1.3 Summary

In the paper we investigated the scrape-off layer power fall-off length, λ_q, by means of numerical simulations. The analysis was restricted to parameters relevant to ASDEX Upgrade (AUG) L-mode. Since 3D dynamics are parametrised in HESEL, the parallel heat fluxes were determined by assuming ballooning-like turbulence, where the transport across the LCFS is located in a poloidal plane spanning 60° at the outboard mid-plane. The poloidal extent of this region is thus $2\pi a/6 \approx a$, where a is the minor radius, which is used when evaluating the different contributions to λ_q. The data is acquired using synthetic probes with a high acquisition rate to get the full signals of the fields needed to evaluate the parallel heat fluxes.

As previously mentioned, the parallel heat fluxes are calculated using parametrised parallel dynamics, where we have identified four contributions; a contribution from the electron advection

$$q_{\parallel,a,e} = a \left\langle \frac{9}{2} \frac{p_e}{\tau_d} \right\rangle_t, \tag{6.1}$$

a contribution from the ion advection

$$q_{\parallel,a,i} = a \left\langle \frac{9}{2} \frac{p_i}{\tau_d} \right\rangle_t, \tag{6.2}$$

a contribution from the electron conduction, also known as Spitzer-Härm conduction

$$q_{\parallel,SH,e} = a \left\langle \frac{p_e}{\tau_{SH,e}} \right\rangle_t, \tag{6.3}$$

and a contribution from the ion conduction

$$q_{\parallel,SH,i} = a \left\langle \frac{p_i}{\tau_{SH,i}} \right\rangle_t. \tag{6.4}$$

Here a accounts for the ballooning-like turbulence, $p_{e(i)}$ is the electron (ion) pressure and $\langle . \rangle_t$ denotes a temporal average. The parallel losses are parametrised by

$$\tau_d = \frac{L_B}{2Mc_s}, \qquad \tau_{SH,i} = \frac{L_B^2 \nu_{ii}}{3.2 v_i^2}, \qquad \text{and} \qquad \tau_{SH,e} = \frac{L_B^2 \nu_{ee}}{3.2 v_e^2}, \tag{6.5}$$

where $L_B = qR_0$ is the ballooning length, $M = 0.5$ is the parallel mach number at the outboard mid-plane, $c_s = \sqrt{(T_e + T_i)/m_i}$ is the sound speed, $\nu_{ii(ee)}$ is the ion-ion (electron-electron) collision frequency and $v_i(e)$ is the ion (electron) thermal velocity. Here it is important to note that the temporal average is taken on the full fields, since intermittent transport in the form of blobs contribute significantly to the parallel losses. In the paper we highlighted the importance of intermittent transport by calculating $q_{\parallel,a,e}$ and $q_{\parallel,SH,e}$ using the full fields and using averaged profiles. Large differences were found, especially in $q_{\parallel,SH,e}$, where using the averaged profiles lead to parallel heat conduction at the LCFS at half the value of what was found when using the full fields. Furthermore, we found that the electron conduction dominated parallel transport close to the LCFS, where electron and ion advection became the dominant terms in the far SOL, again due to intermittent transport.

Next we investigated how λ_q scales with different parameters. The full heat flux, $q_\parallel(x) = q_{\parallel,a,e}(x) + q_{\parallel,a,i}(x) + q_{\parallel,SH,e}(x) + q_{\parallel,SH,i}(x)$ was used to evaluate the scrape-off layer power fall-off length as

$$\lambda_q = \frac{\int_0^\infty x q_\parallel(x)\mathrm{d}x}{\int_0^\infty q_\parallel(x)\mathrm{d}x}, \tag{6.6}$$

and a series of parameters were scanned to get a numerical scaling for λ_q. First we made a scan with the magnetic field strength at the outboard mid-plane, B_0, the safety factor, q, and the total power across the LCFS, P, where we found a scaling very close to that found in an experimental study of λ_q in AUG L-mode [76]. In the experimental work, B_0 was not varied, so the scaling with respect to this parameter could not be compared, but the scaling with P fit within the error bars and the scaling with q showed the same trends with an almost linear dependence of λ_q on this parameter.

However, by examining the mutual correlation between the scanned parameters, we found that P depends on a wide range of other parameters. We therefore redid the fitting of λ_q with the other parameters, where parameters with a mutual correlation of more than 50% were excluded from the same fits. Scanning the same parameters as done when comparing with the experimental scaling, we found

$$\lambda_{q,fit} = (5.02 \pm 1.04)q^{0.92\pm0.05}T_{e,LCFS}^{-0.44\pm0.09}, \tag{6.7}$$

where $T_{e,LCFS}$ is the electron temperature at the LCFS. This fit had a degree of description of $R^2 = 0.95$, which indicates that λ_q is described well with just the two parameters q and $T_{e,LCFS}$.

Finally we included scans of the density at the LCFS, n_{LCFS} and the major radius, R_0, where we found

$$\lambda_{q,fit} = (3.19 \pm 0.72)n_{LCFS}^{0.27\pm0.06}q^{0.84\pm0.07}T_{e,LCFS}^{-0.36\pm0.10}R_0^{0.63\pm0.04}, \tag{6.8}$$

with a degree of description of $R^2 = 0.93$, which again was a very good fit. The scaling with the major radius did not fit with what was observed in an experimental multimachine scaling [21], where λ_q was found to be independent of R_0. However, since R_0 enters in a variety of ways in HESEL, it is not yet clear why this discrepancy arises and a dedicated study is left for future works.

Chapter 7

Conclusion and outlook

The need for a new, sustainable and clean energy source was discussed in chapter 1. The process of nuclear fusion was presented as a possible candidate for such an energy source. However, it was also illustrated that there are challenges, which need to be overcome before such a nuclear fusion power plant can be realised. One of the challenges comes in the form of coherent plasma filaments, also known as blobs. This thesis therefore set out to investigate coherent plasma filaments by means of numerical simulations, specifically studying the effects of temperature dynamics and the effects of a three-dimensional geometry on blob propagation. Finally we set out to study the so-called scrape-off layer power fall-off length, how it is influenced by coherent filaments and how it scales with different parameters.

7.1 Conclusion

In order to carry out investigations of coherent plasma filaments, we first needed to derive a set of equations. The set of equations were derived from first principles in chapter 2. Through a series of assumptions, including the assumption of isothermal electrons and cold ions, we reached a set of coupled differential equations for the evolution of the density, vorticity and parallel electron and ion velocities. The derived equations were designed to model the three-dimensional effects on blob propagation. To investigate the effects of dynamic electron and ion temperatures we turned to the two-dimensional drift-fluid model, HESEL, which we described in sec. 2.7.

The set of equations in the two models described in chapter 2 cannot be solved analytically, therefore numerical methods were employed to get approximate numerical solutions. The numerical methods used for solving the two models were described in chapter 3 with a thorough description of the BOUT++ framework and a brief discussion of the numerical methods used to implement the HESEL model. These numerical implementations of the models were then used to examine how coherent plasma filaments propagate with different initial parameters. In chapter 4 we investigated how filaments propagated when three-dimensional dynamics were either parametrised or excluded altogether using the HESEL model. In sec. 4.1, two validation studies were carried out. Five different numerical models, each derived using different assumptions, were held up against experimental

results from the TORPEX plasma experiment and the MAST tokamak. We found that none of the models fully captured the experimental results, both due to lacking diagnostics in the experimental results and due to assumptions that were not applicable to the experimental scenarios in question. However, we did illuminate the effects of some of the assumptions commonly used in plasma physics models by comparing the results from the different numerical models. We found that background temperature profiles and three-dimensional dynamics are essential to model correctly if one is to fully capture the evolution of plasma filaments. Especially the connection to the sheath was shown to greatly influence how blobs propagate, where a strong connection to the sheath causes the blob to propagate slower in the radial direction than blobs with a weak connection to the sheath. Furthermore, a strong connection to the sheath causes the blob to remain more coherent than is the case for blobs with a weak sheath connection.

With these results at hand, we moved on to investigate how temperature dynamics influenced the propagation of blobs. This investigation is presented in a published paper, which is reprinted in sec. 4.2. The study concerned the effects of temperature dynamics on the evolution of blobs and the effect of different initial parameters on blob propagation and centre of mass velocity when three-dimensional effects were neglected all together. We observed that dynamic temperatures do not significantly change the qualitative evolution of plasma filaments, but the inclusion of finite ion temperatures greatly influence the blob evolution. Instead of generating a mushroom-like structure, as is observed when ions are assumed cold, the blobs remain more coherent and propagate faster through the scrape-off layer. The influence of different initial parameters when ion temperature dynamics were included showed that the hot ion blobs remained more coherent due to finite ion Larmor radius effects. Finally, we found that the so-called inertial scaling described the maximum centre of mass velocity well with a range of initial parameters of the seeded blob perturbations.

We then turned to investigate the effects of a three-dimensional slab geometry on the evolution of blobs. The three-dimensional effects were studied in chapter 5 with preliminary, not yet published results using a numerical implementation in BOUT++ of the model described in sec. 2.6. The first investigation we carried out with the three-dimensional model was on the steady-state of the system. We observed an unexpected asymmetry in the steady-state, which decreased when increasing the resolution. Based on this observation, the asymmetry was recognised as a numerical issue that still needs to be investigated further. However, we observed that the steady-state solutions converged towards symmetric profiles, so we continued the investigation by initialising seeded blobs on top of the steady-state backgrounds. Here we observed that the parallel gradient of the blob edges did not significantly influence the propagation of blobs, whereas the parallel extend of the blobs influenced the filament dynamics. The larger blobs in the parallel direction were observed to propagate faster than smaller blobs and to break into smaller fragments at the later stages of propagation, whereas the smaller blobs generated a spiral-like structure. All filaments were observed to rotate due to Boltzmann spinning and the velocity profiles of the filaments consisted of two bumps, where the blobs initially accelerated, then decelerated only to accelerate again. This behaviour was not observed for two-dimensional blobs, so the effect was attributed to the inclusion of three-dimensional dynamics.

The final investigation we carried out was the examination how the scrape-off layer (SOL)

power fall-off length, λ_q, depends on a range of different parameters using the HESEL model. The results of the λ_q scalings were presented in an accepted paper, which is reprinted in chapter 6. In the paper we noted that it was crucial to account for intermittent transport when determining λ_q. When neglecting intermittent transport in the form of blobs from the evaluation of the parallel heat flux, the heat flux at the last closed flux surface (LCFS) was underestimated by a factor of two. This underestimation correspondingly leads to a wrong evaluation of λ_q. It was also observed that the main parameter determining λ_q was the safety factor, q, with which λ_q scaled almost linearly. We found a numerical scaling, which fit well with what was observed in comparable experimental results [Sieglin et al. Plasma Phys. Contr. Fusion 2016;58(5):055015]. However, we also observed that the scaling parameters used in the experimental results depended on a wide range of other parameters. We therefore investigated the mutual correlation of the parameters in the system. Excluding parameters with a high mutual correlation from the same fits, we arrived at a simpler scaling for λ_q with a higher coefficient of determination. This fit showed that λ_q is determined by a linear dependence on q and the inverse of the square root of the electron temperature at the LCFS, $T_{e,LCFS}$. The experimental data did not include dedicated scans of the density at the LCFS, n_{LCFS}, or the major radius, R_0. When including scans of R_0 and n_{LCFS} in the numerical simulations, we found that λ_q scales as the fourth root of n_{LCFS}, almost linearly with q, as the inverse of the square root of $T_{e,LCFS}$ and as R_0 to the power of two thirds.

In summary, we have shed light on the influence of electron and ion temperature dynamics on the propagation of coherent filaments. We have derived a three-dimensional model from first principles and used it to conduct numerical simulations on the influence of three-dimensional dynamics on blob evolution. Finally we have investigated the importance of blobs on the SOL power fall-off length, λ_q, and how λ_q scales with a range of different parameters.

7.2 Outlook

The results presented in this thesis have concerned coherent filaments in magnetically confined plasmas, and we believe that this thesis can act as a foundation for future studies dedicated to gaining a better understanding of these coherent structures, which can eventually act as a small step towards realising a nuclear fusion power plant. However, there are still many topics concerning coherent filaments that need to be addressed before a fusion power plant can be realised.

In the model derived in sec. 2.6 we made several assumptions motivated by computational expediency. The assumptions of cold ions, isothermal electrons and the so-called local approximation, i.e., small density gradient length scales, greatly simplified the model used in this thesis. The simplifications allowed us to investigate the dynamics of coherent filaments in three dimensions. However, we observed that the assumption of cold ions and isothermal electrons have an impact on how the blobs propagate, where especially the assumption of cold ions strongly influences the blob dynamics. The study of blobs in a three-dimensional geometry would therefore greatly benefit from a full three-dimensional model where these assumptions are omitted and the electron and ion temperature fields are evolved dynamically.

Furthermore, the local approximation significantly speeds up the simulations of numerical plasma models, but the approximation may not be suitable for studies of blobs. In scrape-off layer plasmas, blobs typically have density amplitudes that are much larger than the background plasma. In a future study it would therefore shed light on blob propagation in the SOL if dedicated simulations omitting the local approximation were conducted and it was investigated how significant this assumption is.

Real tokamaks have a complex magnetic geometry with an X-point, which strongly influences the propagation of filaments between the outboard mid-plane and the divertor. In this thesis we have assumed a slab geometry since it significantly simplifies the numerical implementation of the derived model. However, understanding the influence of the magnetic geometry on filament propagation is of great importance in fusion research since it would allow the magnetic field to be tailored so heat loads to the divertor can be minimised. The implementation of a realistic geometry is thus also a step which needs to be done in future numerical studies, examining the effects of an X-point on filament propagation.

Before the above improvements can be implemented we note that the results presented in chapter 5 showed an unexpected asymmetry in the system, which still needs to be investigated. Ideally the implementation of a numerical model needs to be both verified and validated against experiments. This means that a first step in future work is to verify and validate the current model, and only when this has been done can the inclusion of ion and electron temperature dynamics and a realistic geometry start to be implemented.

Finally, with a verified three-dimensional model with ion and electron temperature dynamics included in a realistic tokamak geometry, the study of how λ_q scales with different parameters should be redone and the effects of the dynamics between the outboard mid-plane and the divertor should be investigated and compared directly with experimental λ_q measurements at the divertor plates. These results will shed light on the heat loads at the divertor, a parameter which is crucial to know if a fusion power plant is to be realised.

Appendix A

Perpendicular dynamics

A.1 Derivation of lowest order perpendicular drifts

In order to derive equations for the perpendicular drifts of order 1 and ϵ, we start from the perpendicular part of the momentum equation, eq. (2.8);

$$\frac{\partial}{\partial t}\mathbf{u}_{\sigma\perp} + (\mathbf{u}_{\sigma\perp} \cdot \nabla_\perp)\mathbf{u}_{\sigma\perp} + \left(\mathbf{u}_{\sigma\parallel} \cdot \nabla_\parallel\right)\mathbf{u}_{\sigma\perp} = \frac{q_\sigma}{m_\sigma}\left(\mathbf{E}_\perp + \mathbf{u}_{\sigma\perp} \times \mathbf{B}\right) - \frac{\left(\nabla \cdot \overline{\overline{\mathbf{P}}}_\sigma\right)_\perp}{n_\sigma m_\sigma}$$
$$- \frac{\mathbf{R}_{\perp\sigma\alpha}}{n_\sigma m_\sigma} - \frac{\mathbf{u}_{\sigma\perp} S_n}{n_\sigma}. \tag{A.1}$$

We expand $\mathbf{u}_{\sigma\perp}$ as stated in eq. (2.14) and retain only $\mathbf{u}_{\sigma\perp 0}$ and $\mathbf{u}_{\sigma\perp 1}$, neglecting all higher order terms and expanding $\overline{\overline{\mathbf{P}}}_\sigma$ using eq. (2.3);

$$\frac{\partial}{\partial t}\left(\mathbf{u}_{\sigma\perp 0} + \mathbf{u}_{\sigma\perp 1}\right) + \left(\left(\mathbf{u}_{\sigma\perp 0} + \mathbf{u}_{\sigma\perp 1}\right) \cdot \nabla_\perp\right)\left(\mathbf{u}_{\sigma\perp 0} + \mathbf{u}_{\sigma\perp 1}\right) + \left(\mathbf{u}_{\sigma\parallel} \cdot \nabla_\parallel\right)\left(\mathbf{u}_{\sigma\perp 0} + \mathbf{u}_{\sigma\perp 1}\right)$$
$$= \frac{q_\sigma}{m_\sigma}\left(\mathbf{E}_\perp + \left(\mathbf{u}_{\sigma\perp 0} + \mathbf{u}_{\sigma\perp 1}\right) \times \mathbf{B}\right) - \frac{\nabla_\perp p_\sigma}{n_\sigma m_\sigma} - \frac{\left(\nabla \cdot \overline{\overline{\mathbf{\Pi}}}_\sigma\right)_\perp}{n_\sigma m_\sigma} - \frac{\mathbf{R}_{\perp\sigma\alpha}}{n_\sigma m_\sigma} - \frac{\left(\mathbf{u}_{\sigma\perp 0} + \mathbf{u}_{\sigma\perp 1}\right) S_n}{n_\sigma}. \tag{A.2}$$

With the assumptions in eqs. (2.10) to (2.13), we have that the perpendicular momentum equation to order 1 is given by

$$\mathbf{0} = \frac{q_\sigma}{m_\sigma}\mathbf{E}_\perp + \frac{q_\sigma}{m_\sigma}\mathbf{u}_{\sigma\perp 0} \times \mathbf{B} - \frac{\nabla_\perp p_\sigma}{n_\sigma m_\sigma}. \tag{A.3}$$

This equation can now be solved to give us an expression for $\mathbf{u}_{\sigma\perp 0}$;

$$\mathbf{0} = \frac{q_\sigma}{m_\sigma}\mathbf{E}_\perp + \frac{q_\sigma}{m_\sigma}\mathbf{u}_{\sigma\perp 0} \times \mathbf{B} - \frac{\nabla_\perp p_\sigma}{n_\sigma m_\sigma}$$

$$\Rightarrow \frac{q_\sigma}{m_\sigma}\mathbf{u}_{\sigma\perp 0} \times \mathbf{B} = -\frac{q_\sigma}{m_\sigma}\mathbf{E}_\perp + \frac{\nabla_\perp p_\sigma}{n_\sigma m_\sigma}$$

$$\Rightarrow (\mathbf{u}_{\sigma\perp 0} \times \mathbf{B}) \times \mathbf{B} = -\mathbf{E}_\perp \times \mathbf{B} + \frac{\nabla_\perp p_\sigma \times \mathbf{B}}{n_\sigma q_\sigma}$$

$$\Rightarrow \underbrace{(\mathbf{u}_{\sigma\perp 0} \cdot \mathbf{B})\mathbf{B}}_{0} - (\mathbf{B} \cdot \mathbf{B})\mathbf{u}_{\sigma\perp 0} = -\mathbf{E}_\perp \times \mathbf{B} + \frac{\nabla_\perp p_\sigma \times \mathbf{B}}{n_\sigma q_\sigma}$$

$$\Rightarrow -B^2 \mathbf{u}_{\sigma\perp 0} = -\mathbf{E}_\perp \times \mathbf{B} + \frac{\nabla_\perp p_\sigma \times \mathbf{B}}{n_\sigma q_\sigma}$$

$$\Rightarrow \mathbf{u}_{\sigma\perp 0} = \frac{\mathbf{E}_\perp \times \mathbf{B}}{B^2} - \frac{\nabla_\perp p_\sigma \times \mathbf{B}}{B^2 n_\sigma q_\sigma}, \tag{A.4}$$

where $B = |\mathbf{B}|$. Next we return to eq. (A.2) and collect terms of order ϵ, again following the assumptions in eqs. (2.10) to (2.13), which gives

$$\frac{\partial}{\partial t}\mathbf{u}_{\sigma\perp 0} = -(\mathbf{u}_{\sigma\perp 0} \cdot \nabla_\perp)\mathbf{u}_{\sigma\perp 0} - (\mathbf{u}_{\sigma\parallel} \cdot \nabla_\parallel)\mathbf{u}_{\sigma\perp 0} + \frac{q_\sigma}{m_\sigma}\mathbf{u}_{\sigma\perp 1} \times \mathbf{B}$$

$$- \frac{\mathbf{u}_{\sigma\perp 0}S_n}{n_\sigma} - \frac{\mathbf{R}_{\perp\sigma\alpha}}{n_\sigma m_\sigma} - \frac{\left(\nabla \cdot \overline{\overline{\mathbf{\Pi}}}_\sigma\right)_\perp}{n_\sigma m_\sigma}. \tag{A.5}$$

Inserting the expression for $\mathbf{u}_{\sigma\perp 0}$, eq. (A.4), into eq. (A.5), we get

$$\frac{\partial}{\partial t}\left(-\frac{\nabla_\perp p_\sigma \times \mathbf{B}}{q_\sigma n_\sigma B^2} + \frac{\mathbf{E}_\perp \times \mathbf{B}}{B^2}\right)$$

$$+ \left(\left[-\frac{\nabla_\perp p_\sigma \times \mathbf{B}}{q_\sigma n_\sigma B^2} + \frac{\mathbf{E}_\perp \times \mathbf{B}}{B^2}\right] \cdot \nabla_\perp\right)\left(-\frac{\nabla_\perp p_\sigma \times \mathbf{B}}{q_\sigma n_\sigma B^2} + \frac{\mathbf{E}_\perp \times \mathbf{B}}{B^2}\right)$$

$$+ (\mathbf{u}_{\sigma\parallel} \cdot \nabla_\parallel)\left(-\frac{\nabla_\perp p_\sigma \times \mathbf{B}}{q_\sigma n_\sigma B^2} + \frac{\mathbf{E}_\perp \times \mathbf{B}}{B^2}\right) + \frac{\left(\nabla \cdot \overline{\overline{\mathbf{\Pi}}}_\sigma\right)_\perp}{n_\sigma m_\sigma}$$

$$= \frac{q_\sigma}{m_\sigma}\mathbf{u}_{\sigma\perp 1} \times \mathbf{B} - \left(-\frac{\nabla_\perp p_\sigma \times \mathbf{B}}{q_\sigma n_\sigma B^2} + \frac{\mathbf{E}_\perp \times \mathbf{B}}{B^2}\right)\frac{S_n}{n_\sigma} - \frac{\mathbf{R}_{\perp\sigma\alpha}}{n_\sigma m_\sigma}$$

$$\Rightarrow \mathbf{u}_{\sigma\perp 1} \times \mathbf{B} = \frac{\partial}{\partial t}\left(-\frac{m_\sigma \nabla_\perp p_\sigma}{q_\sigma^2 n_\sigma B^2} + \frac{m_\sigma \mathbf{E}_\perp}{q_\sigma B^2}\right) \times \mathbf{B}$$

$$+ \left(\left[-\frac{\nabla_\perp p_\sigma \times \mathbf{B}}{q_\sigma n_\sigma B^2} + \frac{\mathbf{E}_\perp \times \mathbf{B}}{B^2}\right] \cdot \nabla_\perp\right)\left(-\frac{m_\sigma \nabla_\perp p_\sigma}{q_\sigma^2 n_\sigma B^2} + \frac{m_\sigma \mathbf{E}_\perp}{q_\sigma B^2}\right) \times \mathbf{B}$$

$$+ (\mathbf{u}_{\sigma\parallel} \cdot \nabla_\parallel)\left(-\frac{m_\sigma \nabla_\perp p_\sigma}{q_\sigma^2 n_\sigma B^2} + \frac{m_\sigma \mathbf{E}_\perp}{q_\sigma B^2}\right) \times \mathbf{B}$$

$$+ \frac{S_n}{n_\sigma}\left(-\frac{m_\sigma \nabla_\perp p_\sigma}{q_\sigma^2 n_\sigma B^2} + \frac{m_\sigma \mathbf{E}_\perp}{q_\sigma B^2}\right) \times \mathbf{B} + \frac{\left(\nabla \cdot \overline{\overline{\mathbf{\Pi}}}_\sigma\right)_\perp}{n_\sigma q_\sigma} + \frac{\mathbf{R}_{\perp\sigma\alpha}}{n_\sigma q_\sigma}.$$

Crossing both sides with $\mathbf{B}$ we get

$$
\begin{aligned}
(\mathbf{u}_{\sigma\perp 1} \times \mathbf{B}) \times \mathbf{B} = &\left(\frac{\partial}{\partial t} \left(-\frac{m_\sigma \nabla_\perp p_\sigma}{q_\sigma^2 n_\sigma B^2} + \frac{m_\sigma \mathbf{E}_\perp}{q_\sigma B^2} \right) \times \mathbf{B} \right. \\
&+ \left(\left[-\frac{\nabla_\perp p_\sigma \times \mathbf{B}}{q_\sigma n_\sigma B^2} + \frac{\mathbf{E}_\perp \times \mathbf{B}}{B^2} \right] \cdot \nabla_\perp \right) \left(-\frac{m_\sigma \nabla_\perp p_\sigma}{q_\sigma^2 n_\sigma B^2} + \frac{m_\sigma \mathbf{E}_\perp}{q_\sigma B^2} \right) \times \mathbf{B} \\
&+ \left(\mathbf{u}_{\sigma\|} \cdot \nabla_\| \right) \left(-\frac{m_\sigma \nabla_\perp p_\sigma}{q_\sigma^2 n_\sigma B^2} + \frac{m_\sigma \mathbf{E}_\perp}{q_\sigma B^2} \right) \times \mathbf{B} \\
&\left. + \frac{S_n}{n_\sigma} \left(-\frac{m_\sigma \nabla_\perp p_\sigma}{q_\sigma^2 n_\sigma B^2} + \frac{m_\sigma \mathbf{E}_\perp}{q_\sigma B^2} \right) \times \mathbf{B} + \frac{\left(\nabla \cdot \overline{\overline{\boldsymbol{\Pi}}}_\sigma \right)_\perp}{n_\sigma q_\sigma} + \frac{\mathbf{R}_{\perp\sigma\alpha}}{n_\sigma q_\sigma} \right) \times \mathbf{B}.
\end{aligned}
$$

Finally, using the same relation as in the derivation of $\mathbf{u}_{\sigma\perp 0}$, we get an expression for $\mathbf{u}_{\sigma\perp 1}$

$$
\begin{aligned}
-\mathbf{u}_{\sigma\perp 1} B^2 = &-\frac{\partial}{\partial t} \left(-\frac{m_\sigma \nabla_\perp p_\sigma}{q_\sigma^2 n_\sigma B^2} + \frac{m_\sigma \mathbf{E}_\perp}{q_\sigma B^2} \right) B^2 \\
&- \left(\left[-\frac{\nabla_\perp p_\sigma \times \mathbf{B}}{q_\sigma n_\sigma B^2} + \frac{\mathbf{E}_\perp \times \mathbf{B}}{B^2} \right] \cdot \nabla_\perp \right) \left(-\frac{m_\sigma \nabla_\perp p_\sigma}{q_\sigma^2 n_\sigma B^2} + \frac{m_\sigma \mathbf{E}_\perp}{q_\sigma B^2} \right) B^2 \\
&- \left(\mathbf{u}_{\sigma\|} \cdot \nabla_\| \right) \left(-\frac{m_\sigma \nabla_\perp p_\sigma}{q_\sigma^2 n_\sigma B^2} + \frac{m_\sigma \mathbf{E}_\perp}{q_\sigma B^2} \right) B^2 \\
&- \frac{S_n}{n_\sigma} \left(-\frac{m_\sigma \nabla_\perp p_\sigma}{q_\sigma^2 n_\sigma B^2} + \frac{m_\sigma \mathbf{E}_\perp}{q_\sigma B^2} \right) B^2 + \frac{\left(\nabla \cdot \overline{\overline{\boldsymbol{\Pi}}}_\sigma \right)_\perp \times \mathbf{B}}{n_\sigma q_\sigma} + \frac{\mathbf{R}_{\perp\sigma\alpha} \times \mathbf{B}}{n_\sigma q_\sigma} \\
\Rightarrow \mathbf{u}_{\sigma\perp 1} = &\frac{\partial}{\partial t} \left(-\frac{m_\sigma \nabla_\perp p_\sigma}{q_\sigma^2 n_\sigma B^2} + \frac{m_\sigma \mathbf{E}_\perp}{q_\sigma B^2} \right) \\
&+ \left(\left[-\frac{\nabla_\perp p_\sigma \times \mathbf{B}}{q_\sigma n_\sigma B^2} + \frac{\mathbf{E}_\perp \times \mathbf{B}}{B^2} \right] \cdot \nabla_\perp \right) \left(-\frac{m_\sigma \nabla_\perp p_\sigma}{q_\sigma^2 n_\sigma B^2} + \frac{m_\sigma \mathbf{E}_\perp}{q_\sigma B^2} \right) \\
&+ \left(\mathbf{u}_{\sigma\|} \cdot \nabla_\| \right) \left(-\frac{m_\sigma \nabla_\perp p_\sigma}{q_\sigma^2 n_\sigma B^2} + \frac{m_\sigma \mathbf{E}_\perp}{q_\sigma B^2} \right) \\
&+ \frac{S_n}{n_\sigma} \left(-\frac{m_\sigma \nabla_\perp p_\sigma}{q_\sigma^2 n_\sigma B^2} + \frac{m_\sigma \mathbf{E}_\perp}{q_\sigma B^2} \right) - \frac{\left(\nabla \cdot \overline{\overline{\boldsymbol{\Pi}}}_\sigma \right)_\perp \times \mathbf{B}}{n_\sigma q_\sigma B^2} - \frac{\mathbf{R}_{\perp\sigma\alpha} \times \mathbf{B}}{n_\sigma q_\sigma B^2}.
\end{aligned} \tag{A.6}
$$

A.2 The viscous drift

In order to derive an expression for $\mathbf{u}_{\Pi\sigma}$, we first need to take a look at the stress-tensor $\mathbf{\Pi}_\sigma$, defined in ref. [27] as

$$\Pi_{xx}^\sigma = -\frac{\eta_0^\sigma}{2}\left(W_{xx}^\sigma + W_{yy}^\sigma\right) - \frac{\eta_1^\sigma}{2}\left(W_{xx}^\sigma - W_{yy}^\sigma\right) - \eta_3^\sigma W_{xy}^\sigma,$$

$$\Pi_{yy}^\sigma = -\frac{\eta_0^\sigma}{2}\left(W_{xx}^\sigma + W_{yy}^\sigma\right) - \frac{\eta_1^\sigma}{2}\left(W_{yy}^\sigma - W_{xx}^\sigma\right) + \eta_3^\sigma W_{xy}^\sigma,$$

$$\Pi_{zz}^\sigma = -\eta_0^\sigma W_{zz}^\sigma,$$

$$\Pi_{xy}^\sigma = \Pi_{yx}^\sigma = -\eta_1^\sigma W_{xy}^\sigma + \frac{\eta_3^\sigma}{2}\left(W_{xx}^\sigma - W_{yy}^\sigma\right),$$

$$\Pi_{xz}^\sigma = \Pi_{zx}^\sigma = -\eta_2^\sigma W_{xz}^\sigma - \eta_4^\sigma W_{yz}^\sigma,$$

$$\Pi_{yz}^\sigma = \Pi_{zy}^\sigma = -\eta_2^\sigma W_{yz}^\sigma + \eta_4^\sigma W_{xz}^\sigma,$$

where $W_{ij}^\sigma = \frac{\partial u_{\sigma i}}{\partial x_j} + \frac{\partial u_{\sigma j}}{\partial x_i} - \frac{2}{3}\delta_{ij}\nabla\cdot\mathbf{u}_\sigma$ is the rate-of-strain tensor.

This means that

$$\begin{aligned}
\Pi_{xx}^\sigma = & -\frac{\eta_0^\sigma}{2}\left(W_{xx}^\sigma + W_{yy}^\sigma\right) - \frac{\eta_1^\sigma}{2}\left(W_{xx}^\sigma - W_{yy}^\sigma\right) - \eta_3^\sigma W_{xy}^\sigma \\
= & -\frac{\eta_0^\sigma}{2}\left(2\partial_x u_{\sigma x} - \frac{2}{3}\nabla\cdot\mathbf{u}_\sigma + 2\partial_y u_{\sigma y} - \frac{2}{3}\nabla\cdot\mathbf{u}_\sigma\right) \\
& -\frac{\eta_1^\sigma}{2}\left(2\partial_x u_{\sigma x} - \frac{2}{3}\nabla\cdot\mathbf{u}_\sigma - 2\partial_y u_{\sigma y} + \frac{2}{3}\nabla\cdot\mathbf{u}_\sigma\right) \\
& -\eta_3^\sigma\left(\partial_y u_{\sigma x} + \partial_x u_{\sigma y}\right) \\
= & -\frac{\eta_0^\sigma}{3}\left(\nabla_\perp\cdot\mathbf{u}_{\sigma\perp} - 2\nabla_\parallel\cdot\mathbf{u}_{\sigma\parallel}\right) - \eta_1^\sigma\left(\partial_x u_{\sigma x} - \partial_y u_{\sigma y}\right) - \eta_3^\sigma\left(\partial_y u_{\sigma x} + \partial_x u_{\sigma y}\right)
\end{aligned}$$

$$\begin{aligned}
\Pi_{yy}^\sigma = & -\frac{\eta_0^\sigma}{2}\left(W_{xx}^\sigma + W_{yy}^\sigma\right) - \frac{\eta_1^\sigma}{2}\left(W_{yy}^\sigma - W_{xx}^\sigma\right) + \eta_3^\sigma W_{xy}^\sigma \\
= & -\frac{\eta_0^\sigma}{3}\left(\nabla_\perp\cdot\mathbf{u}_{\sigma\perp} - 2\nabla_\parallel\cdot\mathbf{u}_{\sigma\parallel}\right) - \eta_1^\sigma\left(\partial_y u_{\sigma y} - \partial_x u_{\sigma x}\right) + \eta_3^\sigma\left(\partial_y u_{\sigma x} + \partial_x u_{\sigma y}\right)
\end{aligned}$$

$$\begin{aligned}
\Pi_{zz}^\sigma = & -\eta_0^\sigma W_{zz}^\sigma \\
= & -\frac{2\eta_0^\sigma}{3}\left(2\partial_z u_{\sigma z} - \partial_x u_{\sigma x} - \partial_y u_{\sigma y}\right) \\
= & -\frac{2\eta_0^\sigma}{3}\left(2\nabla\cdot\mathbf{u}_{\sigma\parallel} - \nabla_\perp\cdot\mathbf{u}_{\sigma\perp}\right)
\end{aligned}$$

$$\begin{aligned}
\Pi_{xy}^\sigma = \ & \Pi_{yx}^\sigma = -\eta_1^\sigma W_{xy} + \frac{\eta_3^\sigma}{2}\left(W_{xx}^\sigma - W_{yy}^\sigma\right) \\
= & -\eta_1^\sigma\left(\partial_y u_{\sigma x} + \partial_x u_{\sigma y}\right) + \frac{2\eta_3^\sigma}{2}\left(\partial_x u_{\sigma x} - \partial_y u_{\sigma y}\right)
\end{aligned}$$

$$\begin{aligned}
\Pi_{xz}^\sigma = \ & \Pi_{zx}^\sigma = -\eta_2^\sigma W_{xz} - \eta_4^\sigma W_{yz}^\sigma \\
= & -\eta_2^\sigma\left(\partial_z u_{\sigma x} + \partial_x u_{\sigma z}\right) - \eta_4^\sigma\left(\partial_z u_{\sigma y} + \partial_y u_{\sigma z}\right)
\end{aligned}$$

$$\begin{aligned}
\Pi_{yz}^\sigma = \ & \Pi_{zy}^\sigma = -\eta_2^\sigma W_{yz} + \eta_4^\sigma W_{xz}^\sigma \\
= & -\eta_2^\sigma\left(\partial_z u_{\sigma y} + \partial_y u_{\sigma z}\right) + \eta_4^\sigma\left(\partial_z u_{\sigma x} + \partial_x u_{\sigma z}\right),
\end{aligned}$$

where $\partial_x = \partial/\partial_x$. Now, since what is present in the $\mathbf{u}_{\Pi\sigma}$ is $\nabla\cdot\overline{\overline{\mathbf{\Pi}}}_\sigma$, we evaluate this term

$$\nabla \cdot \overline{\overline{\mathbf{\Pi}}}_\sigma = \begin{bmatrix} \partial_x \Pi_{xx}^\sigma + \partial_y \Pi_{xy}^\sigma + \partial_z \Pi_{xz}^\sigma \\ \partial_x \Pi_{yx}^\sigma + \partial_y \Pi_{yy}^\sigma + \partial_z \Pi_{yz}^\sigma \\ \partial_x \Pi_{zx}^\sigma + \partial_y \Pi_{zy}^\sigma + \partial_z \Pi_{zz}^\sigma \end{bmatrix}$$

$$= \left(\partial_x \left[-\frac{\eta_0^\sigma}{3} \left(\nabla_\perp \cdot \mathbf{u}_{\sigma\perp} - 2\nabla_\parallel \cdot \mathbf{u}_{\sigma\parallel} \right) - \eta_1^\sigma \left(\partial_x u_{\sigma x} - \partial_y u_{\sigma y} \right) - \eta_3^\sigma \left(\partial_y u_{\sigma x} + \partial_x u_{\sigma y} \right) \right] \right.$$
$$+ \partial_y \left[-\eta_1^\sigma \left(\partial_y u_{\sigma x} + \partial_x u_{\sigma y} \right) + \eta_3^\sigma \left(\partial_x u_{\sigma x} - \partial_y u_{\sigma y} \right) \right]$$
$$\left. + \partial_z \left[-\eta_2^\sigma \left(\partial_z u_{\sigma x} + \partial_x u_{\sigma z} \right) - \eta_4^\sigma \left(\partial_z u_{\sigma y} + \partial_y u_{\sigma z} \right) \right] \right) \hat{\mathbf{x}}$$

$$+ \left(\partial_x \left[-\eta_1^\sigma \left(\partial_y u_{\sigma x} + \partial_x u_{\sigma y} \right) + \eta_3^\sigma \left(\partial_x u_{\sigma x} - \partial_y u_{\sigma y} \right) \right] \right.$$
$$+ \partial_y \left[-\frac{\eta_0^\sigma}{3} \left(\nabla_\perp \cdot \mathbf{u}_{\sigma\perp} - 2\nabla_\parallel \cdot \mathbf{u}_{\sigma\parallel} \right) - \eta_1^\sigma \left(\partial_y u_{\sigma y} - \partial_x u_{\sigma x} \right) + \eta_3^\sigma \left(\partial_y u_{\sigma x} + \partial_x u_{\sigma y} \right) \right]$$
$$\left. + \partial_z \left[-\eta_2^\sigma \left(\partial_z u_{\sigma y} + \partial_y u_{\sigma z} \right) + \eta_4^\sigma \left(\partial_z u_{\sigma x} + \partial_x u_{\sigma z} \right) \right] \right) \hat{\mathbf{y}}$$

$$+ \left(\partial_x \left[-\eta_2^\sigma \left(\partial_z u_{\sigma x} + \partial_x u_{\sigma z} \right) - \eta_4^\sigma \left(\partial_z u_{\sigma y} + \partial_y u_{\sigma z} \right) \right] \right.$$
$$+ \partial_y \left[-\eta_2^\sigma \left(\partial_z u_{\sigma y} + \partial_y u_{\sigma z} \right) + \eta_4^\sigma \left(\partial_z u_{\sigma x} + \partial_x u_{\sigma z} \right) \right]$$
$$\left. + \partial_z \left[-\frac{2\eta_0^\sigma}{3} \left(2\partial_z u_{\sigma z} - \partial_x u_{\sigma x} - \partial_y u_{\sigma y} \right) \right] \right) \hat{\mathbf{z}}. \tag{A.7}$$

Next we have that $\mathbf{u}_{\mathbf{\Pi}\sigma}$ is given by eq. (2.20), and inserting the above expression for $\nabla \cdot \overline{\overline{\mathbf{\Pi}}}_\sigma$, we get

$$\mathbf{u}_{\mathbf{\Pi}\sigma} = -\frac{\left(\nabla \cdot \overline{\overline{\mathbf{\Pi}}}_\sigma \right)_\perp \times \mathbf{b}}{n_\sigma q_\sigma B}$$

$$= -\frac{1}{n_\sigma q_\sigma B} \left(\hat{\mathbf{x}} \left(\partial_x \left[-\eta_1^\sigma \left(\partial_y u_{\sigma x} + \partial_x u_{\sigma y} \right) + \eta_3^\sigma \left(\partial_x u_{\sigma x} - \partial_y u_{\sigma y} \right) \right] \right. \right.$$
$$+ \partial_y \left[-\frac{\eta_0^\sigma}{3} \left(\nabla_\perp \cdot \mathbf{u}_{\sigma\perp} - 2\nabla_\parallel \cdot \mathbf{u}_{\sigma\parallel} \right) - \eta_1^\sigma \left(\partial_y u_{\sigma y} - \partial_x u_{\sigma x} \right) + \eta_3^\sigma \left(\partial_y u_{\sigma x} + \partial_x u_{\sigma y} \right) \right]$$
$$\left. + \partial_z \left[-\eta_2^\sigma \left(\partial_z u_{\sigma y} + \partial_y u_{\sigma z} \right) + \eta_4^\sigma \left(\partial_z u_{\sigma x} + \partial_x u_{\sigma z} \right) \right] \right)$$
$$- \hat{\mathbf{y}} \left(\partial_x \left[-\frac{\eta_0^\sigma}{3} \left(\nabla_\perp \cdot \mathbf{u}_{\sigma\perp} - 2\nabla_\parallel \cdot \mathbf{u}_{\sigma\parallel} \right) - \eta_1^\sigma \left(\partial_x u_{\sigma x} - \partial_y u_{\sigma y} \right) \right. \right.$$
$$\left. - \eta_3^\sigma \left(\partial_y u_{\sigma x} + \partial_x u_{\sigma y} \right) \right] + \partial_y \left[-\eta_1^\sigma \left(\partial_y u_{\sigma x} + \partial_x u_{\sigma y} \right) + \eta_3^\sigma \left(\partial_x u_{\sigma x} - \partial_y u_{\sigma y} \right) \right]$$
$$\left. \left. + \partial_z \left[-\eta_2^\sigma \left(\partial_z u_{\sigma x} + \partial_x u_{\sigma z} \right) - \eta_4^\sigma \left(\partial_z u_{\sigma y} + \partial_y u_{\sigma z} \right) \right] \right) \right), \tag{A.8}$$

which is the simplest expression we can get for $\mathbf{u}_{\mathbf{\Pi}\sigma}$ without making further assumptions and specifying the species.

A.3 The electron continuity equation

In order to expand each term separately in the electron continuity equation, we start by looking at eq. (2.26), which is restated here to give a better overview;

$$\frac{\partial}{\partial t}n_e + \nabla_\parallel \cdot \left(n_e \mathbf{u}_{e\parallel}\right) + \nabla_\perp \cdot \left(n_e \mathbf{u}_E + n_e \mathbf{u}_{de} + n_e \mathbf{u}_{Rei} + n_e \mathbf{u}_{\mathbf{\Pi}e}\right) = S_n.$$

The evaluation is the done by inserting the drifts given by eqs. (2.17) to (2.23).

A.3.1 Evaluation of the ExB and diamagnetic terms

The first term we look at is

$$
\begin{aligned}
\nabla_\perp \cdot (n_e \mathbf{u}_E) &= \mathbf{u}_E \cdot \nabla_\perp n_e + n_e \nabla_\perp \cdot \mathbf{u}_E \\
&= \mathbf{u}_E \cdot \nabla_\perp n_e - n_e \nabla_\perp \cdot \left(\frac{\nabla_\perp \phi \times \mathbf{b}}{B}\right) \\
&= \mathbf{u}_E \cdot \nabla_\perp n_e - n_e \frac{\mathbf{b}}{B} \cdot \overset{0}{\cancel{(\nabla \times \nabla_\perp \phi)}} + n_e \nabla_\perp \phi \cdot \left(\nabla \times \frac{\mathbf{b}}{B}\right) \\
&= \mathbf{u}_E \cdot \nabla_\perp n_e + n_e \left(\nabla_\perp \times \frac{\mathbf{b}}{B}\right) \cdot \nabla_\perp \phi
\end{aligned}
$$

Next we have

$$
\begin{aligned}
\nabla_\perp \cdot (n_e \mathbf{u}_{de}) &= \nabla_\perp \cdot \frac{\nabla_\perp p_e \times \mathbf{b}}{eB} \\
&= \frac{\mathbf{b}}{B} \cdot \overset{0}{\cancel{\left(\nabla_\perp \times \frac{\nabla_\perp p_e}{e}\right)}} - \frac{\nabla_\perp p_e}{e} \cdot \left(\nabla_\perp \times \frac{\mathbf{b}}{B}\right) \\
&= -\left(\nabla_\perp \times \frac{\mathbf{b}}{B}\right) \cdot \frac{\nabla_\perp p_e}{e}.
\end{aligned}
$$

Since $(\nabla_\perp \times \mathbf{b}/B) \cdot \nabla_\perp$ is a recurring term, we define the curvature operator

$$\left(\nabla_\perp \times \frac{\mathbf{b}}{B}\right) \cdot \nabla_\perp f \equiv \mathcal{K}(f). \tag{A.9}$$

A.3.2 Evaluation of the resistive term

Now, in order to evaluate $\nabla_\perp \cdot (n_e \mathbf{u}_{Rei})$, we need an expression for $\mathbf{R}_{\perp ei}$. We again refer to [27], where $\mathbf{R}_{ei}$ is given by eq. (2.4)

$$\mathbf{R}_{ei} = -\mathbf{R}_{ie} = \mathbf{R}_{uei} + \mathbf{R}_{Tei},$$

with $\mathbf{R}_{uei}$ being a momentum transfer due to a relative velocity between the electrons and ions, and $\mathbf{R}_{Tei}$ being a thermal force. For $Z = 1$ the friction force is given by eq. (2.5)

$$\mathbf{R}_{uei} = \nu_{ei} m_e n_e \left(0.51 \left(\mathbf{u}_{e\parallel} - \mathbf{u}_{i\parallel}\right) + (\mathbf{u}_{e\perp} - \mathbf{u}_{i\perp})\right),$$

and the thermal force is given by eq. (2.6)

$$\mathbf{R}_{Tei} = 0.71 n_e \nabla_\parallel T_e + \frac{3}{2} \frac{n_e \nu_{ei}}{\omega_{ceB}} \mathbf{b} \times \nabla T_e,$$

where ν_{ei} is the electron-ion collision frequency and $\omega_{ceB} = eB/m_e$ is the electron gyrofrequency. This means that $\mathbf{R}_{\perp ei}$ is given by

$$\mathbf{R}_{\perp ei} = \nu_{ei} m_e n_e \left(\mathbf{u}_{e\perp} - \mathbf{u}_{i\perp} \right) + \frac{3}{2} \frac{n_e \nu_{ei}}{\omega_{ceB}} \mathbf{b} \times \nabla T_e. \tag{A.10}$$

Since $\mathbf{R}_{\perp ei} \propto \epsilon$ following the assumption in eq. (2.11), we only include $\mathbf{u}_{\sigma 0}$ in the velocities, since all other terms will be of order ϵ^2. This means that

$$
\begin{aligned}
\mathbf{R}_{\perp ei} &\approx \nu_{ei} m_e n_e \left(\mathbf{u}_{e\perp 0} - \mathbf{u}_{i\perp 0} \right) + \frac{3}{2} \frac{n_e \nu_{ei}}{\omega_{ceB}} \mathbf{b} \times \nabla T_e \\
&= \nu_{ei} m_e n_e \left(\frac{\mathbf{E}_\perp \times \mathbf{B}}{B^2} + \frac{\nabla_\perp p_e \times \mathbf{B}}{B^2 n_e e} - \frac{\mathbf{E}_\perp \times \mathbf{B}}{B^2} + \frac{\nabla_\perp p_i \times \mathbf{B}}{B^2 n_i e} \right) + \frac{3}{2} \frac{n_e \nu_{ei}}{\omega_{ceB}} \mathbf{b} \times \nabla T_e \\
&= \nu_{ei} m_e n_e \left(\frac{\nabla_\perp p_e \times \mathbf{B}}{B^2 n_e e} + \frac{\nabla_\perp p_i \times \mathbf{B}}{B^2 n_i e} \right) + \frac{3}{2} \frac{n_e \nu_{ei}}{\omega_{ceB}} \mathbf{b} \times \nabla T_e \\
&= \nu_{ei} m_e n_e \left(\frac{\nabla_\perp p_e}{B^2 n_e e} + \frac{\nabla_\perp p_i}{B^2 n_i e} \right) \times \mathbf{B} + \frac{3}{2} \frac{n_e \nu_{ei}}{\omega_{ceB}} \mathbf{b} \times \nabla T_e.
\end{aligned}
$$

This finally leads to

$$
\begin{aligned}
\nabla_\perp \cdot (n_e \mathbf{u}_{Rei}) &= \nabla_\perp \cdot \frac{\mathbf{R}_{\perp ei} \times \mathbf{b}}{eB} \\
&\approx \nabla_\perp \cdot \left(\frac{\nu_{ei} m_e n_e}{eB^2} \left(\frac{\nabla_\perp p_e}{B^2 n_e e} + \frac{\nabla_\perp p_i}{B^2 n_i e} \right) \times \mathbf{B} - \frac{3}{2} \frac{n_e \nu_{ei}}{\omega_{ceB} B} \nabla_\perp T_e \times \mathbf{B} \right) \times \mathbf{B} \\
&= -\nabla_\perp \cdot \left(\frac{\nu_{ei} m_e n_e}{eB^2} \left(\frac{\nabla_\perp p_e}{B^2 n_e e} + \frac{\nabla_\perp p_i}{B^2 n_i e} \right) - \frac{3}{2} \frac{n_e \nu_{ei}}{\omega_{ceB} e B^3} \nabla_\perp T_e \right) B^2 \\
&= -\nabla_\perp \cdot \left(\frac{\nu_{ei} m_e n_e}{eB^2} \left(\frac{\nabla_\perp p_e}{n_e e} + \frac{\nabla_\perp p_i}{n_i e} \right) - \frac{3}{2} \frac{n_e \nu_{ei}}{\omega_{ceB} e B} \nabla_\perp T_e \right) \\
&= -\nabla_\perp \cdot \left(\frac{\nu_{ei} n_e}{m_e \omega_{ceB}^2} \left(\frac{\nabla_\perp p_e}{n_e} + \frac{\nabla_\perp p_i}{n_i} \right) - \frac{3}{2} \frac{\nu_{ei} n_e}{m_e \omega_{ceB}^2} \nabla_\perp T_e \right)
\end{aligned}
$$

Without more assumptions, this expression cannot be simplified further.

A.3.3 Evaluation of the viscous term

Finally, we look at the last term in the electron continuity equation, namely $\nabla_\perp \cdot (n_e \mathbf{u_{\Pi e}})$. We have that $\mathbf{u_{\Pi\sigma}}$ is given by eq. (A.8). In order to evaluate $\nabla_\perp \cdot (n_e \mathbf{u_{\Pi e}})$, we first evaluate

$$
\begin{aligned}
\nabla_\perp \cdot (n_e \mathbf{u_{\Pi e}}) =& \nabla_\perp \cdot \left(\frac{(\nabla \cdot \mathbf{\Pi}_e)_\perp \times \mathbf{b}}{eB} \right) \\
=& \partial_x \bigg(\frac{1}{eB} \bigg(\partial_x \left[-\eta_1^e (\partial_y u_{ex} + \partial_x u_{ey}) + \eta_3^e (\partial_x u_{ex} - \partial_y u_{ey}) \right] \\
& + \partial_y \left[-\frac{\eta_0^e}{3} (\nabla_\perp \cdot \mathbf{u}_{e\perp} - 2\nabla_\parallel \cdot \mathbf{u}_{e\parallel}) - \eta_1^e (\partial_y u_{ey} - \partial_x u_{ex}) \right. \\
& \left. + \eta_3^e (\partial_y u_{ex} + \partial_x u_{ey}) \right] \\
& + \partial_z \left[-\eta_2^e (\partial_z u_{ey} + \partial_y u_{ez}) + \eta_4^e (\partial_z u_{ex} + \partial_x u_{ez}) \right] \bigg) \bigg) \\
& - \partial_y \bigg(\frac{1}{eB} \bigg(\partial_x \left[-\frac{\eta_0^e}{3} (\nabla_\perp \cdot \mathbf{u}_{e\perp} - 2\nabla_\parallel \cdot \mathbf{u}_{e\parallel}) - \eta_1^e (\partial_x u_{ex} - \partial_y u_{ey}) \right. \\
& \left. -\eta_3^e (\partial_y u_{ex} + \partial_x u_{ey}) \right] \\
& + \partial_y \left[-\eta_1^e (\partial_y u_{ex} + \partial_x u_{ey}) + \eta_3^e (\partial_x u_{ex} - \partial_y u_{ey}) \right] \\
& + \partial_z \left[-\eta_2^e (\partial_z u_{ex} + \partial_x u_{ez}) - \eta_4^e (\partial_z u_{ey} + \partial_y u_{ez}) \right] \bigg) \bigg).
\end{aligned}
$$

Now we have from [27], that for $Z = 1$, the coefficients are given by

$$
\begin{aligned}
\eta_0^e &= 0.73 \frac{p_e}{\nu_{ei}}, \qquad \eta_1^e = 0.51 \frac{p_e \nu_{ei}}{\omega_{ceB}^2}, \qquad \eta_2^e = 2.04 \frac{p_e \nu_{ei}}{\omega_{ceB}^2} \\
\eta_3^e &= -0.5 \frac{p_e}{\omega_{ceB}}, \quad \eta_4^e = \frac{p_e}{\omega_{ceB}}.
\end{aligned} \tag{A.11}
$$

Where $1/\omega_{ceB} = m_e/(eB)$, which means that due to the small electron mass compared to the ion mass η_1^e to η_4^e will be very small compared to all other terms and can be neglected. This leaves us with

$$
\begin{aligned}
\nabla_\perp \cdot (n_e \mathbf{u_{\Pi e}}) =& \nabla_\perp \cdot \left(\frac{(\nabla \cdot \mathbf{\Pi}_e)_\perp \times \mathbf{b}}{eB} \right) \\
\approx& \partial_x \left(\frac{1}{eB} \partial_y \left[-\frac{\eta_0^e}{3} (\nabla_\perp \cdot \mathbf{u}_{e\perp} - 2\nabla_\parallel \cdot \mathbf{u}_{e\parallel}) \right] \right) \\
& - \partial_y \left(\frac{1}{eB} \partial_x \left[-\frac{\eta_0^e}{3} (\nabla_\perp \cdot \mathbf{u}_{e\perp} - 2\nabla_\parallel \cdot \mathbf{u}_{e\parallel}) \right] \right) \\
=& \frac{1}{e} \left(\nabla \times \frac{\mathbf{b}}{B} \right) \cdot \nabla_\perp \left(\frac{\eta_0^e}{3} (\nabla_\perp \cdot \mathbf{u}_{e\perp} - 2\nabla_\parallel \cdot \mathbf{u}_{e\parallel}) \right),
\end{aligned} \tag{A.12}
$$

where we in the last term have used

$$\left(\frac{1}{eB} \partial_x \partial_y \left[-\frac{\eta_0^e}{3} \left(\nabla_\perp \cdot \mathbf{u}_{e\perp} - 2\nabla_\parallel \cdot \mathbf{u}_{e\parallel} \right) \right] \right)$$
$$- \left(\frac{1}{eB} \partial_y \partial_x \left[-\frac{\eta_0^e}{3} \left(\nabla_\perp \cdot \mathbf{u}_{e\perp} - 2\nabla_\parallel \cdot \mathbf{u}_{e\parallel} \right) \right] \right) = 0.$$

However, it follows from the assumption given in eq. (2.12), that $\nabla \cdot \mathbf{u}_e$ is of order ϵ, which means that eq. (A.12) is of order ϵ^2, and we thus neglect this term, which leaves us with the electron continuity equation

$$\frac{\partial}{\partial t} n_e + \nabla_\parallel \cdot \left(n_e \mathbf{u}_{e\parallel} \right) + \mathbf{u}_E \cdot \nabla_\perp n_e + n_e \mathcal{K}(\phi) - \frac{\mathcal{K}(p_e)}{e}$$
$$= \frac{1}{m_e} \nabla_\perp \cdot \left(\frac{1}{\omega_{ceB}^2} \nu_{ei} n_e \left(\frac{\nabla_\perp p_e}{n_e} + \frac{\nabla_\perp p_i}{n_i} \right) - \frac{3}{2} \frac{1}{\omega_{ceB}^2} \nu_{ei} n_e \nabla_\perp T_e \right) + S_n. \qquad \text{(A.13)}$$

A.4 The ion continuity equation

We wish to evaluate the individual terms of the ion continuity equation, eq. (2.32), so to get a better overview, we restate the equation;

$$\partial_t n_i + \nabla_\parallel \cdot \left(n_i \mathbf{u}_{i\parallel} \right) + \nabla_\perp \cdot \left(n_i \left(\mathbf{u}_E + \mathbf{u}_{di} + \mathbf{u}_{pi} + \mathbf{u}_{\Pi i} + \mathbf{u}_{\nabla_\parallel i} + \mathbf{u}_{S_n i} + \mathbf{u}_{\mathbf{R}_{ie}} \right) \right) = S_n.$$

A.4.1 Evaluation of ExB, diamagnetic and resistive terms

The evaluation of the $\nabla \cdot (n_i \mathbf{u}_E)$ and $\nabla \cdot (n_i \mathbf{u}_{di})$ is almost identical to the approach for the electron continuity equation in Appendix A.3, so we simply state the results here, which are

$$\nabla_\perp \cdot (n_i \mathbf{u}_E) = n_i \nabla_\perp \cdot \mathbf{u}_E + \mathbf{u}_E \cdot \nabla_\perp n_i = n_i \mathcal{K}(\phi) + \mathbf{u}_E \cdot \nabla_\perp n_i$$

and

$$\nabla_\perp \cdot (n_i \mathbf{u}_{di}) = \frac{\mathcal{K}(p_i)}{e}.$$

Since both momentum and energy must be conserved, we have that $\mathbf{R}_{ie} = -\mathbf{R}_{ei}$, which means that we again can use the result from the electron continuity equation in Appendix A.3 for the resistive drift. With the assumptions stated in sec. 2.4.1 this gives;

$$\nabla_\perp \cdot (n_i \mathbf{u}_{\mathbf{R}_{ie}}) = -\nabla_\perp \cdot \left(\frac{\mathbf{R}_{\perp ie} \times \mathbf{b}}{eB} \right) = \nabla_\perp \cdot \left(\frac{\mathbf{R}_{\perp ei} \times \mathbf{b}}{eB} \right)$$

$$= -\frac{\nu_{ei0} \rho_{e0}^2}{T_{e0}} \nabla_\perp \cdot \left(n_e \left(\frac{T_{e0} \nabla_\perp n}{n_e} + \frac{\nabla_\perp p_i}{n_i} \right) \right),$$

when only including terms of order 1 and order ϵ.

A.4.2 Evaluation of the parallel gradient term

The next drift we wish to evaluate is $\nabla_\perp \cdot \left(n_i \mathbf{u}_{\nabla_\parallel i} \right)$, which gives

$$\nabla_\perp \cdot \left(n_i \mathbf{u}_{\nabla_\parallel i} \right) = \nabla_\perp \cdot \left(n_i \left(\mathbf{u}_{i\parallel} \cdot \nabla_\parallel \right) \left(-\frac{m_i \nabla_\perp p_i}{e^2 n_i B^2} - \frac{m_i \nabla_\perp \phi}{eB^2} \right) \right)$$

$$= \nabla_\perp \cdot \left(n_i \left(\mathbf{u}_{i\parallel} \cdot \nabla_\parallel \right) \left(-\frac{1}{\omega_{ciB} B} \left(\frac{\nabla_\perp p_i}{e n_i} + \nabla_\perp \phi \right) \right) \right)$$

$$= -\nabla_\perp \cdot \left(\frac{n_i}{\omega_{ciB} B} \left(\mathbf{u}_{i\parallel} \cdot \nabla_\parallel \right) \left(\frac{\nabla_\perp p_i}{e n_i} + \nabla_\perp \phi \right) \right),$$

since by definition there is no parallel gradient of the magnetic field and $\omega_{ciB} = eB/m_i$. This expression cannot be simplified without further assumptions, so we leave it as is for now.

A.4.3 Evaluation of the source term

The next term we wish to evaluate is $\nabla_\perp \cdot (n_i \mathbf{u}_{S_n i})$, which is given by

$$\nabla_\perp \cdot (n_i \mathbf{u}_{S_n i}) = -\nabla_\perp \cdot \left(\frac{S_n}{\omega_{ciB} B} \left(\frac{\nabla_\perp p_i}{e n_i} + \nabla_\perp \phi \right) \right)$$

$$= -S_n \nabla_\perp \cdot \left(\frac{1}{\omega_{ciB} B} \left(\frac{\nabla_\perp p_i}{e n_i} + \nabla_\perp \phi \right) \right),$$

since we have defined the source to be located at the sheath entrance and thus does not vary in the direction perpendicular to the magnetic field as stated in sec. 2.3.

A.4.4 Evaluation of the polarisation term

Now, the last two terms we wish to evaluate require extensive calculations. The first of these is the polarisation drift. We have that $\nabla \cdot (n_i \mathbf{u}_{pi})$ is given by

$$\nabla_\perp \cdot (n_i \mathbf{u}_{pi}) = \nabla_\perp \cdot \left(n_i \left(\partial_t + \left[-\frac{\nabla_\perp p_i \times \mathbf{b}}{e n_i B} - \frac{\nabla_\perp \phi \times \mathbf{b}}{B} \right] \cdot \nabla_\perp \right) \left(-\frac{\nabla_\perp p_i}{\omega_{ciB} e B n_i} - \frac{\nabla_\perp \phi}{\omega_{ciB} B} \right) \right).$$

This can be divided into a a temporal derivative part, $\mathbf{u}_{pit}$, and a diamagnetic part, $\mathbf{u}_{pid}$. These are given by

$$\nabla_\perp \cdot (n_i \mathbf{u}_{pit}) = -\nabla_\perp \cdot \left(n_i \left(\partial_t + \mathbf{u}_E \cdot \nabla_\perp \right) \left(\frac{1}{\omega_{ciB} B} \left(\frac{\nabla_\perp p_i}{e n_i} + \nabla_\perp \phi \right) \right) \right)$$

and

$$\nabla_\perp \cdot (n_i \mathbf{u}_{pid}) = \nabla_\perp \cdot \left(\frac{\nabla_\perp p_i \times \mathbf{b}}{e B} \nabla_\perp \cdot \left(\frac{1}{\omega_{ciB} B} \left(\frac{\nabla_\perp p_i}{e n_i} + \nabla_\perp \phi \right) \right) \right).$$

We start by looking at $\nabla_\perp \cdot (n_i \mathbf{u}_{pit})$, which gives

$$\nabla_\perp \cdot (n_i \mathbf{u}_{pit}) = -\nabla_\perp \cdot \left(n_i \left(\partial_t + \mathbf{u}_E \cdot \nabla_\perp \right) \left(\frac{1}{\omega_{ciB} B} \left(\frac{\nabla_\perp p_i}{e n_i} + \nabla_\perp \phi \right) \right) \right)$$

$$= -\nabla_\perp n_i \cdot \left(\left(\partial_t + \mathbf{u}_E \cdot \nabla_\perp \right) \left(\frac{1}{\omega_{ciB} B} \left(\frac{\nabla_\perp p_i}{e n_i} + \nabla_\perp \phi \right) \right) \right)$$

$$- n_i \nabla_\perp \cdot \left(\left(\partial_t + \mathbf{u}_E \cdot \nabla_\perp \right) \left(\frac{1}{\omega_{ciB} B} \left(\frac{\nabla_\perp p_i}{e n_i} + \nabla_\perp \phi \right) \right) \right)$$

$$= -\nabla_\perp n_i \cdot \left(\left(\partial_t + \mathbf{u}_E \cdot \nabla_\perp \right) \left(\frac{1}{\omega_{ciB} B} \left(\frac{\nabla_\perp p_i}{e n_i} + \nabla_\perp \phi \right) \right) \right)$$

$$- n_i \left(\partial_t \nabla_\perp + (\nabla_\perp \cdot \mathbf{u}_E) \nabla_\perp + (\mathbf{u}_E \cdot \nabla_\perp) \nabla_\perp \right) \cdot \frac{1}{\omega_{ciB} B} \left(\frac{\nabla_\perp p_i}{e n_i} + \nabla_\perp \phi \right)$$

$$= -\nabla_\perp n_i \cdot \left(\left(\partial_t + \mathbf{u}_E \cdot \nabla_\perp \right) \left(\frac{1}{\omega_{ciB} B} \left(\frac{\nabla_\perp p_i}{e n_i} + \nabla_\perp \phi \right) \right) \right)$$

$$- n_i \left(\partial_t + \mathcal{K}(\phi) + (\mathbf{u}_E \cdot \nabla_\perp) \right) \nabla_\perp \cdot \frac{1}{\omega_{ciB} B} \left(\frac{\nabla_\perp p_i}{e n_i} + \nabla_\perp \phi \right).$$

Next we look at $\nabla_\perp \cdot (n_i \mathbf{u}_{pid})$, which gives

$$
\begin{aligned}
\nabla_\perp \cdot (n_i \mathbf{u}_{pid}) =& \nabla_\perp \cdot \left(\frac{\nabla_\perp p_i \times \mathbf{b}}{eB} \nabla_\perp \cdot \left(\frac{1}{\omega_{ciB}B} \left(\frac{\nabla_\perp p_i}{en_i} + \nabla_\perp \phi \right) \right) \right) \\
=& \left(\nabla_\perp \cdot \frac{\nabla_\perp p_i \times \mathbf{b}}{eB} \right) \nabla_\perp \cdot \left(\frac{1}{\omega_{ciB}B} \left(\frac{\nabla_\perp p_i}{en_i} + \nabla_\perp \phi \right) \right) \\
&+ \left(\frac{\nabla_\perp p_i \times \mathbf{b}}{eB} \cdot \nabla_\perp \right) \nabla_\perp \cdot \frac{1}{\omega_{ciB}B} \left(\frac{\nabla_\perp p_i}{en_i} + \nabla_\perp \phi \right) \\
=& -\frac{\mathcal{K}(p_i)}{e} \nabla_\perp \cdot \left(\frac{1}{\omega_{ciB}B} \left(\frac{\nabla_\perp p_i}{en_i} + \nabla_\perp \phi \right) \right) \\
&+ \left(\frac{\nabla_\perp p_i \times \mathbf{b}}{eB} \cdot \nabla_\perp \right) \nabla_\perp \cdot \frac{1}{\omega_{ciB}B} \left(\frac{\nabla_\perp p_i}{en_i} + \nabla_\perp \phi \right).
\end{aligned}
$$

A.4.5 Evaluation of the viscous term

The final term we need to evaluate is the viscous term. Similar to the term in the electron continuity equation we have

$$
\begin{aligned}
\nabla_\perp \cdot (n_i \mathbf{u}_{\mathbf{\Pi}i}) =& -\nabla_\perp \cdot \left(\frac{(\nabla \cdot \mathbf{\Pi}_i)_\perp \times \mathbf{b}}{eB} \right) \\
=& -\partial_x \left(\frac{1}{eB} \left(\partial_x \left[-\eta_1^i (\partial_y u_{ix} + \partial_x u_{iy}) + \eta_3^i (\partial_x u_{ix} - \partial_y u_{iy}) \right] \right. \right. \\
&+ \partial_y \left[-\frac{\eta_0^i}{3} (\nabla_\perp \cdot \mathbf{u}_{i\perp} - 2\nabla_\parallel \cdot \mathbf{u}_{i\parallel}) - \eta_1^i (\partial_y u_{iy} - \partial_x u_{ix}) \right. \\
&+ \eta_3^i (\partial_y u_{ix} + \partial_x u_{iy}) \Big] \\
&+ \partial_z \left[-\eta_2^i (\partial_z u_{iy} + \partial_y u_{iz}) + \eta_4^i (\partial_z u_{ix} + \partial_x u_{iz}) \right] \bigg) \bigg) \\
&+ \partial_y \left(\frac{1}{eB} \left(\partial_x \left[-\frac{\eta_0^i}{3} (\nabla_\perp \cdot \mathbf{u}_{i\perp} - 2\nabla_\parallel \cdot \mathbf{u}_{i\parallel}) - \eta_1^i (\partial_x u_{ix} - \partial_y u_{iy}) \right. \right. \right. \\
&- \eta_3^i (\partial_y u_{ix} + \partial_x u_{iy}) \Big] \\
&+ \partial_y \left[-\eta_1^i (\partial_y u_{ix} + \partial_x u_{iy}) + \eta_3^i (\partial_x u_{ix} - \partial_y u_{iy}) \right] \\
&+ \partial_z \left[-\eta_2^i (\partial_z u_{ix} + \partial_x u_{iz}) - \eta_4^i (\partial_z u_{iy} + \partial_y u_{iz}) \right] \bigg) \bigg).
\end{aligned}
$$

From [27], we have that the ion viscosities are given by

$$
\begin{aligned}
\eta_0^i &= 0.96 \frac{p_i}{\nu_{ii}}, \qquad \eta_1^i = 0.3 \frac{p_i \nu_{ii}}{\omega_{ciB}^2}, \qquad \eta_2^i = 1.2 \frac{p_i \nu_{ii}}{\omega_{ciB}^2} \\
\eta_3^i &= 0.5 \frac{p_i}{\omega_{ciB}}, \qquad \eta_4^i = \frac{p_i}{\omega_{ciB}}.
\end{aligned}
\tag{A.14}
$$

This means that unlike for the electrons, none of the terms can be neglected. However, following the analysis in Appendix A.3, we still have that the terms involving η_0^i will be

of order ϵ^2, so these can be omitted from the calculations. This leaves us with

$$
\begin{aligned}
\nabla_\perp \cdot (n_i \mathbf{u_{\Pi i}}) = &- \nabla_\perp \cdot \left(\frac{(\nabla \cdot \mathbf{\Pi}_i)_\perp \times \mathbf{b}}{eB} \right) \\
\approx &- \partial_x \left(\frac{1}{eB} \left(\partial_x \left[-\eta_1^i \left(\partial_y u_{ix} + \partial_x u_{iy} \right) + \eta_3^i \left(\partial_x u_{ix} - \partial_y u_{iy} \right) \right] \right. \right. \\
&+ \partial_y \left[-\eta_1^i \left(\partial_y u_{iy} - \partial_x u_{ix} \right) + \eta_3^i \left(\partial_y u_{ix} + \partial_x u_{iy} \right) \right] \\
&\left. \left. + \partial_z \left[-\eta_2^i \left(\partial_z u_{iy} + \partial_y u_{iz} \right) + \eta_4^i \left(\partial_z u_{ix} + \partial_x u_{iz} \right) \right] \right) \right) \\
&+ \partial_y \left(\frac{1}{eB} \left(\partial_x \left[-\eta_1^i \left(\partial_x u_{ix} - \partial_y u_{iy} \right) - \eta_3^i \left(\partial_y u_{ix} + \partial_x u_{iy} \right) \right] \right. \right. \\
&+ \partial_y \left[-\eta_1^i \left(\partial_y u_{ix} + \partial_x u_{iy} \right) + \eta_3^i \left(\partial_x u_{ix} - \partial_y u_{iy} \right) \right] \\
&\left. \left. + \partial_z \left[-\eta_2^i \left(\partial_z u_{ix} + \partial_x u_{iz} \right) - \eta_4^i \left(\partial_z u_{iy} + \partial_y u_{iz} \right) \right] \right) \right).
\end{aligned}
$$

Inserting the viscosities, we get

$$
\begin{aligned}
\nabla_\perp \cdot (n_i \mathbf{u_{\Pi i}}) = &- \nabla_\perp \cdot \left(\frac{(\nabla \cdot \mathbf{\Pi}_i)_\perp \times \mathbf{b}}{eB} \right) \\
\approx &- \partial_x \left(\frac{1}{eB} \left(\partial_x \left[-\frac{3}{10} \frac{p_i \nu_{ii}}{\omega_{ciB}^2} \left(\partial_y u_{ix} + \partial_x u_{iy} \right) + \frac{1}{2} \frac{p_i}{\omega_{ciB}} \left(\partial_x u_{ix} - \partial_y u_{iy} \right) \right] \right. \right. \\
&+ \partial_y \left[-\frac{3}{10} \frac{p_i \nu_{ii}}{\omega_{ciB}^2} \left(\partial_y u_{iy} - \partial_x u_{ix} \right) + \frac{1}{2} \frac{p_i}{\omega_{ciB}} \left(\partial_y u_{ix} + \partial_x u_{iy} \right) \right] \\
&\left. \left. + \partial_z \left[-\frac{12}{10} \frac{p_i \nu_{ii}}{\omega_{ciB}^2} \left(\partial_z u_{iy} + \partial_y u_{iz} \right) + \frac{p_i}{\omega_{ciB}} \left(\partial_z u_{ix} + \partial_x u_{iz} \right) \right] \right) \right) \\
&+ \partial_y \left(\frac{1}{eB} \left(\partial_x \left[-\frac{3}{10} \frac{p_i \nu_{ii}}{\omega_{ciB}^2} \left(\partial_x u_{ix} - \partial_y u_{iy} \right) - \frac{1}{2} \frac{p_i}{\omega_{ciB}} \left(\partial_y u_{ix} + \partial_x u_{iy} \right) \right] \right. \right. \\
&+ \partial_y \left[-\frac{3}{10} \frac{p_i \nu_{ii}}{\omega_{ciB}^2} \left(\partial_y u_{ix} + \partial_x u_{iy} \right) + \frac{1}{2} \frac{p_i}{\omega_{ciB}} \left(\partial_x u_{ix} - \partial_y u_{iy} \right) \right] \\
&\left. \left. + \partial_z \left[-\frac{12}{10} \frac{p_i \nu_{ii}}{\omega_{ciB}^2} \left(\partial_z u_{ix} + \partial_x u_{iz} \right) - \frac{p_i}{\omega_{ciB}} \left(\partial_z u_{iy} + \partial_y u_{iz} \right) \right] \right) \right).
\end{aligned}
$$

We now collect terms, which gives

$$\nabla_\perp \cdot (n_i \mathbf{u_{\Pi i}}) = - \partial_x \left(-\frac{3}{10eB}\left(\partial_x \left[\frac{p_i \nu_{ii}}{\omega_{ciB}^2}\left(\partial_y u_{ix} + \partial_x u_{iy}\right) \right] + \partial_y \left[\frac{p_i \nu_{ii}}{\omega_{ciB}^2}\left(\partial_y u_{iy} - \partial_x u_{ix}\right) \right] \right. \right.$$

$$\left. + 4\partial_z \left[\frac{p_i \nu_{ii}}{\omega_{ciB}^2}\left(\partial_z u_{iy} + \partial_y u_{iz}\right) \right] \right) + \frac{1}{2eB}\left(\partial_x \left[\frac{p_i}{\omega_{ciB}}\left(\partial_x u_{ix} - \partial_y u_{iy}\right) \right] \right.$$

$$\left. \left. +\partial_y \left[\frac{p_i}{\omega_{ciB}}\left(\partial_y u_{ix} + \partial_x u_{iy}\right) \right] + 2\partial_z \left[\frac{p_i}{\omega_{ciB}}\left(\partial_z u_{ix} + \partial_x u_{iz}\right) \right] \right) \right)$$

$$+ \partial_y \left(-\frac{3}{10eB}\left(\partial_x \left[\frac{p_i \nu_{ii}}{\omega_{ciB}^2}\left(\partial_x u_{ix} - \partial_y u_{iy}\right) \right] + \partial_y \left[\frac{p_i \nu_{ii}}{\omega_{ciB}^2}\left(\partial_y u_{ix} + \partial_x u_{iy}\right) \right] \right. \right.$$

$$\left. + 4\partial_z \left[\frac{p_i \nu_{ii}}{\omega_{ciB}^2}\left(\partial_z u_{ix} + \partial_x u_{iz}\right) \right] \right) + \frac{1}{2eB}\left(-\partial_x \left[\frac{p_i}{\omega_{ciB}}\left(\partial_y u_{ix} + \partial_x u_{iy}\right) \right] \right.$$

$$\left. \left. + \partial_y \left[\frac{p_i}{\omega_{ciB}}\left(\partial_x u_{ix} - \partial_y u_{iy}\right) \right] - 2\partial_z \left[\frac{p_i}{\omega_{ciB}}\left(\partial_z u_{iy} + \partial_y u_{iz}\right) \right] \right) \right).$$

Without further assumptions, this cannot be simplified further. However, in tokamak plasmas it is usually the case that $|\nabla B| \propto 1/R_0$, where R_0 is the major radius, while $\nabla \cdot \mathbf{u}_i \propto 1/L$, where L is the typical perpendicular length scale. The major radius in tokamaks is typically in the order of a meter, whereas the typical perpendicular length scale is on the order of a centimetre. With this in mind we can neglect ∇B and in turn that we can neglect the variation of B in ω_{ciB}. This means that $\omega_{ciB} \approx \omega_{ci} = eB_0/m_i$. Furthermore we assume ν_{ii} to be constant, i.e. $\nu_{ii} = \nu_{ii0}$, which leads to

$$\nabla_\perp \cdot (n_i \mathbf{u_{\Pi i}}) \approx \frac{3}{10}\frac{\nu_{ii0}}{eB\omega_{ci}^2}\left[\left(\partial_x^2 p_i - \partial_y^2 p_i\right)\left(\partial_y u_{ix} + \partial_x u_{iy}\right) \right.$$

$$+2\partial_x \partial_y p_i \left(\partial_y u_{iy} - \partial_x u_{ix}\right)$$

$$+4\partial_x \partial_z p_i \left(\partial_z u_{iy} + \partial_y u_{iz}\right)$$

$$-4\partial_y \partial_z p_i \left(\partial_z u_{ix} + \partial_x u_{iz}\right)$$

$$+ 2\partial_x p_i \left(\partial_x^2 u_{iy} + \partial_y^2 u_{iy} + 2\partial_z^2 u_{iy} + 2\partial_z \partial_y u_{iz}\right)$$

$$- 2\partial_y p_i \left(\partial_x^2 u_{ix} + \partial_y^2 u_{ix} + 2\partial_z^2 u_{ix} + 2\partial_x \partial_z u_{iz}\right)$$

$$+4\partial_z p_i \left(\partial_x \partial_z u_{iy} - \partial_y \partial_z u_{ix}\right)$$

$$+ p_i \left(\partial_x^3 u_{iy} - \partial_y^3 u_{ix} - \partial_x^2 \partial_y u_{ix} + \partial_x \partial_y^2 u_{iy} \right.$$

$$\left. \left. +4\partial_x \partial_z^2 u_{iy} - 4\partial_y \partial_z^2 u_{ix}\right)\right]$$

$$-\frac{1}{2eB\omega_{ci}}\left[\left(\partial_x^2 p_i - \partial_y^2 p_i\right)\left(\partial_x u_{ix} - \partial_y u_{iy}\right) \right.$$

$$+ 2\partial_x \partial_y p_i \left(\partial_y u_{ix} + \partial_x u_{iy}\right)$$

$$+ 2\partial_x \partial_z p_i \left(\partial_z u_{ix} + \partial_x u_{iz}\right)$$

$$+ 2\partial_y \partial_z p_i \left(\partial_z u_{iy} + \partial_y u_{iz}\right)$$

$$+2\partial_x p_i \left(\partial_x^2 u_{ix} + \partial_y^2 u_{ix} + \partial_z^2 u_{ix} + \partial_x \partial_z u_{iz}\right)$$

$$+2\partial_y p_i \left(\partial_x^2 u_{iy} + \partial_y^2 u_{iy} + \partial_z^2 u_{iy} + \partial_z \partial_y u_{iz}\right)$$

$$+ 2\partial_z p_i \left(\partial_x^2 u_{iz} + \partial_y^2 u_{iz} + \partial_x \partial_z u_{ix} + \partial_y \partial_z u_{iy}\right)$$

$$+ p_i \left(\partial_x^3 u_{ix} + \partial_y^3 u_{iy} + \partial_x^2 \partial_y u_{iy} + \partial_x \partial_y^2 u_{ix} \right.$$

$$\left. \left. +2\partial_x \partial_z^2 u_{ix} + 2\partial_x^2 \partial_z u_{iz} + 2\partial_y \partial_z^2 u_{iy} + 2\partial_y^2 \partial_z u_{iz}\right)\right],$$

where the first term is due to the ion viscosity, and the second terms is the ion finite Larmor radius (FLR) effect. We split these into two different contributions, the viscous term $\mathbf{u}_{\mathbf{\Pi}i\nu}$ and the FLR term $\mathbf{u}_{\mathbf{\Pi}iFLR}$, so

$$
\begin{aligned}
\nabla \cdot (n_i \mathbf{u}_{\mathbf{\Pi}i\nu}) = \frac{3\nu_{ii0}}{10\omega_{ci}^2 eB} \Big[& (\partial_x^2 p_i - \partial_y^2 p_i)(\partial_y u_{ix} + \partial_x u_{iy}) \\
& + 2\partial_x\partial_y p_i (\partial_y u_{iy} - \partial_x u_{ix}) \\
& + 4\partial_x\partial_z p_i (\partial_z u_{iy} + \partial_y u_{iz}) \\
& - 4\partial_y\partial_z p_i (\partial_z u_{ix} + \partial_x u_{iz}) \\
& + 2\partial_x p_i (\partial_x^2 u_{iy} + \partial_y^2 u_{iy} + 2\partial_z^2 u_{iy} + 2\partial_z\partial_y u_{iz}) \\
& - 2\partial_y p_i (\partial_x^2 u_{ix} + \partial_y^2 u_{ix} + 2\partial_z^2 u_{ix} + 2\partial_x\partial_z u_{iz}) \\
& + 4\partial_z p_i (\partial_x\partial_z u_{iy} - \partial_y\partial_z u_{ix}) \\
& + p_i \big(\partial_x^3 u_{iy} - \partial_y^3 u_{ix} - \partial_x^2\partial_y u_{ix} + \partial_x\partial_y^2 u_{iy} \\
& \qquad + 4\partial_x\partial_z^2 u_{iy} - 4\partial_y\partial_z^2 u_{ix} \big) \Big] ,
\end{aligned}
\tag{A.15}
$$

and

$$
\begin{aligned}
\nabla \cdot (n_i \mathbf{u}_{\mathbf{\Pi}iFLR}) = -\frac{1}{2\omega_{ci} eB} \Big[& (\partial_x^2 p_i - \partial_y^2 p_i)(\partial_x u_{ix} - \partial_y u_{iy}) \\
& + 2\partial_x\partial_y p_i (\partial_y u_{ix} + \partial_x u_{iy}) \\
& + 2\partial_x\partial_z p_i (\partial_z u_{ix} + \partial_x u_{iz}) \\
& + 2\partial_y\partial_z p_i (\partial_z u_{iy} + \partial_y u_{iz}) \\
& + 2\partial_x p_i (\partial_x^2 u_{ix} + \partial_y^2 u_{ix} + \partial_z^2 u_{ix} + \partial_x\partial_z u_{iz}) \\
& + 2\partial_y p_i (\partial_x^2 u_{iy} + \partial_y^2 u_{iy} + \partial_z^2 u_{iy} + \partial_z\partial_y u_{iz}) \\
& + 2\partial_z p_i (\partial_x^2 u_{iz} + \partial_y^2 u_{iz} + \partial_x\partial_z u_{ix} + \partial_y\partial_z u_{iy}) \\
& + p_i \big(\partial_x^3 u_{ix} + \partial_y^3 u_{iy} + \partial_x^2\partial_y u_{iy} + \partial_x\partial_y^2 u_{ix} \\
& \qquad + 2\partial_x\partial_z^2 u_{ix} + 2\partial_x^2\partial_z u_{iz} + 2\partial_y\partial_z^2 u_{iy} + 2\partial_y^2\partial_z u_{iz} \big) \Big] .
\end{aligned}
\tag{A.16}
$$

A.4.6 Gyroviscous cancellation

Before moving on to state the ion continuity equation, we look at the so-called gyroviscous cancellation[24, 77, 78]. Here parts of the diamagnetic term in the polarisation drift cancels with parts of the FLR term in the viscous drift.

In order to identify which terms cancel, we first need to look at the components of the velocity vector. We have that the velocity vector to order 1, is given by

$$
\begin{aligned}
\mathbf{u}_{\sigma\perp0} &= -\frac{\nabla_\perp (p_\sigma + q_\sigma n_\sigma \phi) \times \mathbf{b}}{q_\sigma n_\sigma B} \\
&= -\frac{1}{B}\left(\frac{\partial_y p_\sigma}{n_\sigma q_\sigma} + \partial_y \phi\right)\hat{\mathbf{x}} + \frac{1}{B}\left(\frac{\partial_x p_\sigma}{n_\sigma q_\sigma} + \partial_x \phi\right)\hat{\mathbf{y}},
\end{aligned}
$$

which means that

$$
u_{\sigma x0} = -\frac{1}{B}\left(\frac{\partial_y p_\sigma}{n_\sigma q_\sigma} + \partial_y \phi\right) \qquad \text{and} \qquad u_{\sigma y0} = \frac{1}{B}\left(\frac{\partial_x p_\sigma}{n_\sigma q_\sigma} + \partial_x \phi\right).
\tag{A.17}
$$

Neglecting ∇B terms, we have that the diamagnetic term of the polarisation equation in terms of the individual spatial components can be written as

$$\nabla \cdot (n_i \mathbf{u}_{pid}) = \frac{1}{\omega_{c\sigma} q_\sigma B^2} \left(-\partial_x^2 p_i \left(\partial_y \frac{\partial_x p_\sigma}{q_\sigma n_\sigma} + \partial_x \partial_y \phi \right) + \partial_y^2 p_\sigma \left(\partial_x \frac{\partial_y p_\sigma}{n_\sigma q_\sigma} + \partial_x \partial_y \phi \right) \right.$$
$$+ \partial_x \partial_y p_i \left(\partial_x \frac{\partial_x p_\sigma}{n_\sigma q_\sigma} + \partial_x^2 \phi - \partial_y \frac{\partial_y p_\sigma}{n_\sigma q_\sigma} - \partial_y^2 \phi \right)$$
$$- \partial_x p_i \left(\partial_x \partial_y \frac{\partial_x p_\sigma}{n_\sigma q_\sigma} + \partial_x^2 \partial_y \phi + \partial_y^2 \frac{\partial_y p_\sigma}{n_\sigma q_\sigma} + \partial_y^3 \phi \right)$$
$$\left. + \partial_y p_i \left(\partial_x^2 \frac{\partial_x p_\sigma}{n_\sigma q_\sigma} + \partial_x^3 \phi + \partial_x \partial_y \frac{\partial_y p_\sigma}{n_\sigma q_\sigma} + \partial_x \partial_y^2 \phi \right) \right).$$

With the expressions for the velocity components to order 1 given in eq. (A.17), we can rewrite this to

$$\nabla \cdot (n_i \mathbf{u}_{pid}) = \frac{1}{\omega_{ci} e B} \left(-\partial_x^2 p_i \left(\partial_y u_{iy0} \right) - \partial_y^2 p_i \left(\partial_x u_{ix0} \right) + \partial_x \partial_y p_i \left(\partial_x u_{iy0} + \partial_y u_{ix0} \right) \right.$$
$$\left. - \partial_x p_i \left(\partial_x \partial_y u_{iy0} - \partial_y^2 u_{ix0} \right) + \partial_y p_i \left(\partial_x^2 u_{iy0} - \partial_x \partial_y u_{ix0} \right) \right). \quad \text{(A.18)}$$

Since $\mathbf{u}_{\Pi i}$ is already of order ϵ, we only include $\mathbf{u}_{i\perp 0}$ in the expressions, since all other terms will be of order ϵ^2 or higher. Adding eq. (A.16) and eq. (A.18) thus gives

$$\nabla \cdot (n_i (\mathbf{u}_{pid} + \mathbf{u}_{\Pi iFLR})) = -\frac{1}{2\omega_{ci} e B} \left[\partial_x^2 p_i \left(\partial_x u_{ix0} + \partial_y u_{iy0} \right) + \partial_y^2 p_i \left(\partial_x u_{ix0} + \partial_y u_{iy0} \right) \right.$$
$$+ 2 \partial_x \partial_z p_i \left(\partial_z u_{ix0} + \partial_x u_{iz0} \right)$$
$$+ 2 \partial_y \partial_z p_i \left(\partial_z u_{iy0} + \partial_y u_{iz0} \right)$$
$$+ 2 \partial_x p_i \left(\partial_x^2 u_{ix0} + \partial_x \partial_y u_{iy0} + \partial_z^2 u_{ix0} + \partial_x \partial_z u_{iz0} \right)$$
$$+ 2 \partial_y p_i \left(\partial_y^2 u_{iy0} + \partial_x \partial_y u_{ix0} + \partial_z^2 u_{iy0} + \partial_y \partial_z u_{iz0} \right)$$
$$+ 2 \partial_z p_i \left(\partial_x^2 u_{iz0} + \partial_y^2 u_{iz0} + \partial_x \partial_z u_{ix0} + \partial_y \partial_z u_{iy0} \right)$$
$$+ p_i \left(\partial_x^3 u_{ix0} + \partial_y^3 u_{iy0} + \partial_x^2 \partial_y u_{iy0} + \partial_x \partial_y^2 u_{ix0} \right.$$
$$\left. \left. + 2 \partial_x \partial_z^2 u_{ix0} + 2 \partial_x^2 \partial_z u_{iz0} + 2 \partial_y \partial_z^2 u_{iy0} + 2 \partial_y^2 \partial_z u_{iz0} \right) \right].$$

which can be rewritten as

$$\nabla \cdot (n_i (\mathbf{u}_{pid} + \mathbf{u}_{\Pi iFLR})) = -\frac{1}{2\omega_{ci} e B} \left[\nabla_\perp^2 p_i \left(\nabla_\perp \cdot \mathbf{u}_{i\perp 0} \right) \right.$$
$$+ 2 \nabla_\perp \left(\nabla_\parallel p_i \cdot \nabla_\parallel \right) \mathbf{u}_{i\perp 0} + 2 \nabla_\parallel \left(\nabla_\perp p_i \cdot \nabla_\perp \right) \mathbf{u}_{i\parallel}$$
$$+ 2 \left(\nabla p_i \cdot \nabla \right) \left(\nabla \cdot \mathbf{u}_{i0} \right) - 2 \nabla_\parallel p_i \cdot \nabla_\parallel^2 \mathbf{u}_{i\parallel}$$
$$+ 2 \nabla_\perp p_i \cdot \nabla_\parallel^2 \mathbf{u}_{i\perp 0} + 2 \nabla_\parallel p_i \cdot \nabla_\perp^2 \mathbf{u}_{i\parallel}$$
$$+ p_i \left(\nabla^2 \left(\nabla \cdot \mathbf{u}_{i0} \right) - \nabla_\parallel^2 \left(\nabla_\parallel \cdot \mathbf{u}_{i\parallel} \right) \right.$$
$$\left. \left. + \nabla_\parallel^2 \left(\nabla_\perp \cdot \mathbf{u}_{i\perp 0} \right) + \nabla_\perp^2 \left(\nabla_\parallel \cdot \mathbf{u}_{i\parallel} \right) \right) \right].$$

Reinserting the expression for $\mathbf{u}_{i\perp 0}$ leads to

XVI

$$\nabla \cdot (n_i (\mathbf{u}_{pid} + \mathbf{u}_{\mathbf{\Pi}iFLR})) = -\frac{1}{2\omega_{ci}eB} \left[\nabla_\perp^2 p_i \left(\nabla_\perp \cdot \left(-\frac{\nabla_\perp p_i \times \mathbf{b}}{n_i eB} - \frac{\nabla_\perp \phi \times \mathbf{b}}{B} \right) \right) \right.$$

$$+ 2 \left(\nabla_\perp \left(\nabla_\| p_i \cdot \nabla_\| \right) \right) \cdot \left(-\frac{\nabla_\perp p_i \times \mathbf{b}}{n_i eB} - \frac{\nabla_\perp \phi \times \mathbf{b}}{B} \right)$$

$$+ 2\nabla_\| \left(\nabla_\perp p_i \cdot \nabla_\perp \right) \mathbf{u}_{i\|}$$

$$+ 2 \left(\nabla_\perp p_i \cdot \nabla_\perp + \nabla_\| p_i \cdot \nabla_\| \right) \left(\nabla_\| \cdot \mathbf{u}_{i\|0} \right)$$

$$+ 2 \left(\nabla_\perp p_i \cdot \nabla_\perp \right) \left(\nabla_\perp \cdot \left(-\frac{\nabla_\perp p_i \times \mathbf{b}}{n_i eB} - \frac{\nabla_\perp \phi \times \mathbf{b}}{B} \right) \right)$$

$$+ 2 \left(\nabla_\| p_i \cdot \nabla_\| \right) \left(\nabla_\perp \cdot \left(-\frac{\nabla_\perp p_i \times \mathbf{b}}{n_i eB} - \frac{\nabla_\perp \phi \times \mathbf{b}}{B} \right) \right)$$

$$- 2\nabla_\| p_i \cdot \nabla_\|^2 \mathbf{u}_{i\|} + 2\nabla_\| p_i \cdot \nabla_\perp^2 \mathbf{u}_{i\|}$$

$$+ 2\nabla_\perp p_i \cdot \nabla_\|^2 \left(-\frac{\nabla_\perp p_i \times \mathbf{b}}{n_i eB} - \frac{\nabla_\perp \phi \times \mathbf{b}}{B} \right)$$

$$+ p_i \left(\nabla^2 \left(\nabla_\perp \cdot \left(-\frac{\nabla_\perp p_i \times \mathbf{b}}{n_i eB} - \frac{\nabla_\perp \phi \times \mathbf{b}}{B} \right) \right) \right.$$

$$+ \nabla_\|^2 \left(\nabla_\perp \cdot \left(-\frac{\nabla_\perp p_i \times \mathbf{b}}{n_i eB} - \frac{\nabla_\perp \phi \times \mathbf{b}}{B} \right) \right)$$

$$\left. \left. + 2\nabla_\perp^2 \left(\nabla_\| \cdot \mathbf{u}_{i\|} \right) \right) \right].$$

Now, we have already defined

$$\nabla \cdot \left(-\frac{\nabla_\perp \phi \times \mathbf{b}}{B} \right) = \nabla_\perp \cdot \left(-\frac{\nabla_\perp \phi \times \mathbf{b}}{B} \right) = \mathcal{K}(\phi)$$

and

$$\nabla \cdot \left(-\frac{\nabla_\perp p_i \times \mathbf{b}}{eB} \right) = \nabla_\perp \cdot \left(-\frac{\nabla_\perp p_i \times \mathbf{b}}{eB} \right) = \frac{\mathcal{K}(p_i)}{e},$$

which can be inserted to give

$$
\nabla \cdot (n_i (\mathbf{u}_{pid} + \mathbf{u}_{\Pi iFLR})) = -\frac{1}{2\omega_{ci}eB} \left[\nabla_\perp^2 p_i \left(\frac{\nabla_\perp n_i \cdot \nabla_\perp p_i \times \mathbf{b}}{n_i^2 eB} + \frac{\mathcal{K}(p_i)}{e} + \mathcal{K}(\phi) \right) \right.
$$

$$
+ 2\nabla_\perp \left(\nabla_\| p_i \cdot \nabla_\| \right) \cdot \left(-\frac{\nabla_\perp p_i \times \mathbf{b}}{n_i eB} - \frac{\nabla_\perp \phi \times \mathbf{b}}{B} \right)
$$

$$
+ 2\nabla_\| \left(\nabla_\perp p_i \cdot \nabla_\perp \right) \cdot \mathbf{u}_{i\|}
$$

$$
+ 2 \left(\nabla_\perp p_i \cdot \nabla_\perp + \nabla_\| p_i \cdot \nabla_\| \right) \left(\nabla_\| \cdot \mathbf{u}_{i\|} \right)
$$

$$
+ 2 \left(\nabla_\perp p_i \cdot \nabla_\perp \right) \left(\frac{\nabla_\perp n_i \cdot \nabla_\perp p_i \times \mathbf{b}}{n_i^2 eB} + \frac{\mathcal{K}(p_i)}{e} + \mathcal{K}(\phi) \right)
$$

$$
+ 2 \left(\nabla_\| p_i \cdot \nabla_\| \right) \left(\frac{\nabla_\perp n_i \cdot \nabla_\perp p_i \times \mathbf{b}}{n_i^2 eB} + \frac{\mathcal{K}(p_i)}{e} + \mathcal{K}(\phi) \right)
$$

$$
- 2\nabla_\| p_i \cdot \nabla_\|^2 \mathbf{u}_{i\|} + 2\nabla_\| p_i \cdot \nabla_\perp^2 \mathbf{u}_{i\|}
$$

$$
+ 2\nabla_\perp p_i \cdot \nabla_\|^2 \left(-\frac{\nabla_\perp p_i \times \mathbf{b}}{n_i eB} - \frac{\nabla_\perp \phi \times \mathbf{b}}{B} \right)
$$

$$
+ p_i \left(\nabla_\perp^2 \left(\frac{\nabla_\perp n_i \cdot \nabla_\perp p_i \times \mathbf{b}}{n_i^2 eB} + \frac{\mathcal{K}(p_i)}{e} + \mathcal{K}(\phi) \right) \right.
$$

$$
+ 2\nabla_\|^2 \left(\frac{\nabla_\perp n_i \cdot \nabla_\perp p_i \times \mathbf{b}}{n_i^2 eB} + \frac{\mathcal{K}(p_i)}{e} + \mathcal{K}(\phi) \right)
$$

$$
\left. \left. + 2\nabla_\perp^2 \left(\nabla_\| \cdot \mathbf{u}_{i\|} \right) \right) \right] . \tag{A.19}
$$

With this at hand we can now write an expression for the ion continuity equation, assuming that ν_{ei} and ν_{ii} are constant, so $\nu_{ei} = \nu_{ei0}$ and $\nu_{ii} = \nu_{ii0}$ and assuming $|\nabla B| \ll \epsilon$;

$$
\partial_t n_i + \mathbf{u}_E \cdot \nabla n_i + \nabla_\| \cdot \left(n_i \mathbf{u}_{i\|} \right) + n_i \mathcal{K}(\phi) + \frac{\mathcal{K}(p_i)}{e} - \frac{S_n}{\omega_{ci}B} \nabla_\perp \cdot \left(\frac{\nabla_\perp p_i}{en_i} + \nabla_\perp \phi \right)
$$

$$
- \frac{\rho_{e0}^2 \nu_{ei0}}{T_{e0}} \nabla_\perp \cdot \left(n_e \left(\frac{\nabla_\perp p_e}{n_e} + \frac{\nabla_\perp p_i}{n_i} \right) - \frac{3}{2} n_e \nabla_\perp T_e \right)
$$

$$
- \frac{1}{\omega_{ci}B} \nabla_\perp \cdot \left(n_i \left(\mathbf{u}_{i\|} \cdot \nabla_\| \right) \left(\frac{\nabla_\perp p_i}{en_i} + \nabla_\perp \phi \right) \right) - \frac{\mathcal{K}(p_i)}{e\omega_{ci}B} \nabla_\perp \cdot \left(\frac{\nabla_\perp p_i}{en_i} + \nabla_\perp \phi \right)
$$

$$
+ \frac{1}{\omega_{ci}B} \left(\frac{\nabla_\perp p_i \times \mathbf{b}}{eB} \cdot \nabla_\perp \right) \nabla_\perp \cdot \left(\frac{\nabla_\perp p_i}{en_i} + \nabla_\perp \phi \right)
$$

$$
- \frac{1}{\omega_{ci}B} \nabla_\perp \cdot \left(n_i \left(\partial_t + \mathbf{u}_E \cdot \nabla_\perp \right) \left(\frac{\nabla_\perp p_i}{en_i} + \nabla_\perp \phi \right) \right)
$$

$$
+ \nabla_\perp \cdot \left(n_i \left(\mathbf{u}_{pid} + \mathbf{u}_{\Pi iFLR} \right) \right) + \nabla_\perp \cdot \left(n_i \mathbf{u}_{\Pi i\nu} \right) = S_n, \tag{A.20}
$$

where the last two terms are given by eq. (A.19) and eq. (A.15), respectively.

Appendix B

Parallel dynamics

In order to derive the equations for the parallel dynamics of the system, we start by looking at the parallel momentum equation, eq. (2.9)

$$\frac{\partial}{\partial t}\mathbf{u}_{\sigma\parallel} + (\mathbf{u}_{\sigma\perp} \cdot \nabla_\perp)\,\mathbf{u}_{\sigma\parallel} + \left(\mathbf{u}_{\sigma\parallel} \cdot \nabla_\parallel\right)\mathbf{u}_{\sigma\parallel} = \frac{q_\sigma}{m_\sigma}\mathbf{E}_\parallel - \frac{\left(\nabla \cdot \overline{\overline{\mathbf{P}}}_\sigma\right)_\parallel}{n_\sigma m_\sigma} - \frac{\mathbf{R}_{\parallel\sigma\alpha}}{n_\sigma m_\sigma} - \frac{\mathbf{u}_{\sigma\parallel}S_n}{n_\sigma}.$$
$$\text{(B.1)}$$

Assuming an electrostatic field $\mathbf{E} = -\nabla\phi$, and only including terms of order 1 in the perpendicular dynamics gives

$$\Rightarrow \frac{\partial}{\partial t}\mathbf{u}_{\sigma\parallel} + (\mathbf{u}_{\sigma\perp 0} \cdot \nabla_\perp)\,\mathbf{u}_{\sigma\parallel} + \left(\mathbf{u}_{\sigma\parallel} \cdot \nabla_\parallel\right)\mathbf{u}_{\sigma\parallel} = -\frac{q_\sigma}{m_\sigma}\nabla_\parallel\phi - \frac{\nabla_\parallel p_\sigma}{n_\sigma m_\sigma} - \frac{\left(\nabla \cdot \overline{\overline{\mathbf{\Pi}}}_\sigma\right)_\parallel}{n_\sigma m_\sigma}$$
$$- \frac{\mathbf{R}_{\parallel\sigma\alpha}}{n_\sigma m_\sigma} - \frac{\mathbf{u}_{\sigma\parallel}S_n}{n_\sigma}.$$
$$\text{(B.2)}$$

This term can now be evaluated separately for electrons and ions, which gives us two separate equations.

B.1 Parallel electron equation

We start by looking at the parallel electron continuity equation, which is given by

$$\Rightarrow \frac{\partial}{\partial t}\mathbf{u}_{e\parallel} + (\mathbf{u}_{e\perp 0} \cdot \nabla_\perp)\,\mathbf{u}_{e\parallel} + \left(\mathbf{u}_{e\parallel} \cdot \nabla_\parallel\right)\mathbf{u}_{e\parallel} = \frac{e}{m_e}\nabla_\parallel\phi - \frac{\nabla_\parallel p_e}{nm_e} - \frac{\left(\nabla \cdot \overline{\overline{\mathbf{\Pi}}}_e\right)_\parallel}{nm_e}$$
$$- \frac{\mathbf{R}_{\parallel ei}}{nm_e} - \frac{\mathbf{u}_{e\parallel}S_n}{n}.$$
$$\text{(B.3)}$$

Inserting $\mathbf{u}_{e\perp 0}$, eq. (2.15) and eq. (2.5), we get

$$\frac{\partial}{\partial t}\mathbf{u}_{e\parallel} + \left((\mathbf{u}_E + \mathbf{u}_{de})\cdot\nabla_\perp\right)\mathbf{u}_{e\parallel} + \left(\mathbf{u}_{e\parallel}\cdot\nabla_\parallel\right)\mathbf{u}_{e\parallel} = \frac{e}{m_e}\nabla_\parallel\phi - \frac{\nabla_\parallel p_e}{nm_e} - \frac{\left(\nabla\cdot\overline{\overline{\mathbf{\Pi}}}_e\right)_\parallel}{nm_e}$$
$$- \frac{\mathbf{R}_{\parallel ei}}{nm_e} - \frac{\mathbf{u}_{e\parallel}S_n}{n},$$

$$\Rightarrow \frac{\mathrm{d}}{\mathrm{d}t}\mathbf{u}_{e\parallel} + \left(\mathbf{u}_{de}\cdot\nabla_\perp\right)\mathbf{u}_{e\parallel} + \left(\mathbf{u}_{e\parallel}\cdot\nabla_\parallel\right)\mathbf{u}_{e\parallel} = \frac{e}{m_e}\nabla_\parallel\phi - \frac{\nabla_\parallel p_e}{nm_e} - \frac{\left(\nabla\cdot\overline{\overline{\mathbf{\Pi}}}_e\right)_\parallel}{nm_e}$$
$$+ 0.51\nu_{ei}\left(\mathbf{u}_{i\parallel} - \mathbf{u}_{e\parallel}\right) - \frac{\mathbf{u}_{e\parallel}S_n}{n}$$
$$- 0.71n_e\nabla_\parallel T_e,$$

where $\mathrm{d}/\mathrm{d}t = \partial/\partial t + \mathbf{u}_E\cdot\nabla_\perp$. To simplify this expression further, we evaluate $\left(\nabla\cdot\overline{\overline{\mathbf{\Pi}}}_e\right)_\parallel/nm_e$, which is given by the $\mathbf{z}$-component of eq. (A.7),

$$-\frac{\left(\nabla\cdot\overline{\overline{\mathbf{\Pi}}}_e\right)_\parallel}{nm_e} = -\frac{1}{nm_e}\left(\partial_x\left[-\eta_2^\sigma\left(\partial_z u_{\sigma x} + \partial_x u_{\sigma z}\right) - \eta_4^\sigma\left(\partial_z u_{\sigma y} + \partial_y u_{\sigma z}\right)\right]\right.$$
$$+ \partial_y\left[-\eta_2^\sigma\left(\partial_z u_{\sigma y} + \partial_y u_{\sigma z}\right) + \eta_4^\sigma\left(\partial_z u_{\sigma x} + \partial_x u_{\sigma z}\right)\right]$$
$$\left.+ \partial_z\left[-\frac{2\eta_0^\sigma}{3}\left(2\partial_z u_{\sigma z} - \partial_x u_{\sigma x} - \partial_y u_{\sigma y}\right)\right]\right).$$

We have from eq. (A.11), that all parameters, except η_0^e depend on m_e, so we neglect these and insert the expression for η_0^e, which gives

$$-\frac{\left(\nabla\cdot\overline{\overline{\mathbf{\Pi}}}_e\right)_\parallel}{nm_e} \approx -\frac{1}{nm_e}\left(\partial_z\left[-\frac{0.73\cdot 2p_e}{3\nu_{ei}}\left(2\partial_z u_{ez} - \partial_x u_{ex} - \partial_y u_{ey}\right)\right]\right).$$

We have already assumed isothermal electrons and a constant ν_{ei} in section 2.4 and with these assumptions the expression can be rewritten as

$$-\frac{\left(\nabla\cdot\overline{\overline{\mathbf{\Pi}}}_e\right)_\parallel}{nm_e} \approx -\frac{1.46T_{e0}}{3nm_e\nu_{ei0}}\left(-\partial_z n\left(2\nabla_\parallel\cdot\mathbf{u}_{e\parallel} - \nabla_\perp\cdot\mathbf{u}_{e\perp 0}\right) - n\partial_z\left(2\nabla_\parallel\cdot\mathbf{u}_{e\parallel} - \nabla_\perp\cdot\mathbf{u}_{e\perp 0}\right)\right).$$

Inserting the expression for $\mathbf{u}_{e\perp 0}$ and using that $\nabla_\perp\cdot\mathbf{u}_E = \mathcal{K}(\phi)$, we get

$$-\frac{\left(\nabla\cdot\overline{\overline{\mathbf{\Pi}}}_e\right)_\parallel}{nm_e} \approx -\frac{1.46T_{e0}}{3nm_e\nu_{ei0}}\left(-\partial_z n\left(2\nabla_\parallel\cdot\mathbf{u}_{e\parallel} - \mathcal{K}(\phi) - \nabla_\perp\cdot\mathbf{u}_{de}\right)\right.$$
$$\left.- n\partial_z\left(2\nabla_\parallel\cdot\mathbf{u}_{e\parallel} - \mathcal{K}(\phi) - \nabla_\perp\cdot\mathbf{u}_{de}\right)\right).$$

With the assumptions of isothermal electrons we have have that $\mathbf{u}_{de} = T_{e0}\nabla_\perp n\times\mathbf{b}/(enB)$. This means that

$$\nabla_\perp\cdot\mathbf{u}_{de} = T_{e0}\nabla_\perp\cdot\frac{\nabla_\perp n\times\mathbf{b}}{enB} = -T_{e0}\left(\frac{\nabla_\perp n}{n^2}\frac{\nabla_\perp n\times\mathbf{b}}{eB} + \frac{1}{n}\nabla_\perp\cdot\left(\frac{\nabla_\perp n\times\mathbf{b}}{eB}\right)\right).$$

Using the local approximation, stated in sec. 2.4.3, we neglect the first term in $\nabla_\perp \cdot \mathbf{u}_{de}$ and in $\left(\nabla \cdot \overline{\overline{\mathbf{\Pi}}}_e \right)_\parallel$, which leaves us with

$$-\frac{\left(\nabla \cdot \overline{\overline{\mathbf{\Pi}}}_e \right)_\parallel}{nm_e} \approx -\frac{1.46T_{e0}}{3nm_e\nu_{ei0}}\left(-n\partial_z \left(2\nabla_\parallel \cdot \mathbf{u}_{e\parallel} - \mathcal{K}(\phi) - \frac{T_{e0}}{en}\mathcal{K}(n) \right) \right).$$

Furthermore, we have

$$\mathbf{u}_{de} \cdot \nabla_\perp = T_{e0}\frac{\nabla_\perp n \times \mathbf{b}}{enB} \cdot \nabla_\perp = T_{e0}\frac{\partial_y n \partial_x - \partial_x n \partial_y}{enB}, \tag{B.4}$$

which leads to

$$\frac{\mathrm{d}}{\mathrm{d}t}\mathbf{u}_{e\parallel} = -T_{e0}\frac{\partial_y n \partial_x - \partial_x n \partial_y}{enB}\mathbf{u}_{e\parallel} - \left(\mathbf{u}_{e\parallel} \cdot \nabla_\parallel \right)\mathbf{u}_{e\parallel} + \frac{e}{m_e}\nabla_\parallel\phi - \frac{T_{e0}\nabla_\parallel n}{nm_e}$$
$$-\frac{1.46T_{e0}}{3nm_e\nu_{ei0}}\left(-n\partial_z \left(2\nabla_\parallel \cdot \mathbf{u}_{e\parallel} - \mathcal{K}(\phi) - \frac{T_{e0}}{en}\mathcal{K}(n) \right) \right)$$
$$+0.51\nu_{ei}\left(\mathbf{u}_{i\parallel} - \mathbf{u}_{e\parallel} \right) - \frac{\mathbf{u}_{e\parallel}S_n}{n}.$$

Neglecting all cross-terms gives

$$\frac{\mathrm{d}}{\mathrm{d}t}\mathbf{u}_{e\parallel} = -\left(\mathbf{u}_{e\parallel} \cdot \nabla_\parallel \right)\mathbf{u}_{e\parallel} + \frac{e}{m_e}\nabla_\parallel\phi - \frac{T_{e0}\nabla_\parallel n}{nm_e} + 0.51\nu_{ei}\left(\mathbf{u}_{i\parallel} - \mathbf{u}_{e\parallel} \right) - \frac{\mathbf{u}_{e\parallel}S_n}{n}$$
$$-\frac{2.92T_{e0}}{3m_e\nu_{ei0}}\nabla_\parallel^2\mathbf{u}_{e\parallel}.$$

Similar to the approach for the perpendicular dynamics of the system, we wish to normalise the above equation;

$$\omega_{ci}c_s\frac{\mathrm{d}}{\mathrm{d}\tilde{t}}\tilde{\mathbf{u}}_{e\parallel} = -\frac{c_s^2}{\rho_s}\left(\tilde{\mathbf{u}}_{e\parallel} \cdot \tilde{\nabla}_\parallel \right)\tilde{\mathbf{u}}_{e\parallel} + \frac{T_{e0}}{\rho_s m_e}\tilde{\nabla}_\parallel\varphi - \frac{T_{e0}\tilde{\nabla}_\parallel\tilde{n}}{\rho_s\tilde{n}m_e}$$
$$+0.51\nu_{ei}c_s\left(\tilde{\mathbf{u}}_{e\parallel} - \tilde{\mathbf{u}}_{i\parallel} \right) - \frac{c_s\tilde{\mathbf{u}}_{e\parallel}S_n}{n_0\tilde{n}} + \frac{2.92T_{e0}c_s}{3m_e\nu_{ei0}\rho_s^2}\tilde{\nabla}_\parallel^2\tilde{\mathbf{u}}_{e\parallel}.$$

$$\Rightarrow \frac{\mathrm{d}}{\mathrm{d}\tilde{t}}\tilde{\mathbf{u}}_{e\parallel} = -\left(\tilde{\mathbf{u}}_{e\parallel} \cdot \tilde{\nabla}_\parallel \right)\tilde{\mathbf{u}}_{e\parallel} + \frac{m_i}{m_e}\tilde{\nabla}_\parallel\varphi - \frac{m_i\tilde{\nabla}_\parallel\tilde{n}}{\tilde{n}m_e}$$
$$+\frac{0.51\nu_{ei}}{\omega_{ci}}\left(\tilde{\mathbf{u}}_{e\parallel} - \tilde{\mathbf{u}}_{i\parallel} \right) - \frac{\tilde{\mathbf{u}}_{e\parallel}S_n}{\omega_{ci}n_0\tilde{n}} + \frac{2.92\rho_{e0}^2\omega_{ce}^2}{3\nu_{ei0}\omega_{ci}\rho_s^2}\tilde{\nabla}_\parallel^2\tilde{\mathbf{u}}_{e\parallel}.$$

Inserting the definitions for $\tilde{S}_n$, defining $\nu_\parallel = 0.51\nu_{ei0}/(\omega_{ci})$ and $\nu_{e\parallel}^{-1} = 2.92\rho_{e0}^2\omega_{ce}/(3\rho_s^2\nu_{ei0})$ we get the parallel electron equation

$$\frac{\mathrm{d}}{\mathrm{d}\tilde{t}}\tilde{\mathbf{u}}_{e\parallel} = -\left(\tilde{\mathbf{u}}_{e\parallel} \cdot \tilde{\nabla}_\parallel \right)\tilde{\mathbf{u}}_{e\parallel} + \mu\nabla_\parallel\varphi - \mu\frac{\tilde{\nabla}_\parallel\tilde{n}}{\tilde{n}} + \nu_\parallel\left(\tilde{\mathbf{u}}_{i\parallel} - \tilde{\mathbf{u}}_{e\parallel} \right) - \frac{\tilde{\mathbf{u}}_{e\parallel}\tilde{S}_n}{\tilde{n}} + \mu\nu_{e\parallel}^{-1}\tilde{\nabla}_\parallel^2\tilde{\mathbf{u}}_{e\parallel}, \tag{B.5}$$

where we have defined $\mu \equiv m_i/m_e$.

B.2   Parallel ion equation

Using the assumptions of cold ions, $T_i = 0$, quasineutrality, $n_i = n_e \equiv n$, and isothermal electrons, $\nabla T_e = \mathbf{0}$, and only include lowest order perpendicular terms, the parallel ion equation reads

$$\frac{\partial}{\partial t}\mathbf{u}_{i\parallel} + \left(\mathbf{u}_{i\perp 0} \cdot \nabla_\perp\right)\mathbf{u}_{i\parallel} + \left(\mathbf{u}_{i\parallel} \cdot \nabla_\parallel\right)\mathbf{u}_{i\parallel} = -\frac{e}{m_i}\nabla_\parallel \phi - \frac{\mathbf{R}_{\parallel ie}}{nm_i} - \frac{\mathbf{u}_{i\parallel}S_n}{n}.$$

From [27], we have

$$\mathbf{R}_{\parallel ie} = -\mathbf{R}_{\parallel ei} = 0.51\nu_{ei0}m_e n \left(\mathbf{u}_{i\parallel} - \mathbf{u}_{e\parallel}\right). \tag{B.6}$$

Inserting this and normalising with Bohm normalisation, eq. (2.38) we get

$$c_s\omega_{ci}\frac{\partial}{\partial \tilde{t}}\tilde{\mathbf{u}}_{i\parallel} + \frac{c_s^2}{\rho_s}\left(\tilde{\mathbf{u}}_E \cdot \tilde{\nabla}_\perp\right)\tilde{\mathbf{u}}_{i\parallel} = -\frac{c_s^2}{\rho_s}\left(\tilde{\mathbf{u}}_{i\parallel} \cdot \tilde{\nabla}_\parallel\right)\tilde{\mathbf{u}}_{i\parallel} - \frac{T_{e0}}{\rho_s m_i}\tilde{\nabla}_\parallel \varphi$$

$$-\frac{0.51\nu_{ei0}m_e c_s}{m_i}\left(\tilde{\mathbf{u}}_{i\parallel} - \tilde{\mathbf{u}}_{e\parallel}\right) - \frac{c_s\tilde{\mathbf{u}}_{i\parallel}S_n}{n_0\tilde{n}}$$

$$\Rightarrow \frac{\mathrm{d}}{\mathrm{d}\tilde{t}}\tilde{\mathbf{u}}_{i\parallel} = -\left(\tilde{\mathbf{u}}_{i\parallel} \cdot \tilde{\nabla}_\parallel\right)\tilde{\mathbf{u}}_{i\parallel} - \tilde{\nabla}_\parallel \varphi - \frac{0.51\nu_{ei0}}{\mu\omega_{ci}}\left(\tilde{\mathbf{u}}_{e\parallel} - \tilde{\mathbf{u}}_{i\parallel}\right) - \frac{\tilde{\mathbf{u}}_{i\parallel}S_n}{\omega_{ci}n_0\tilde{n}}.$$

Using the definition of $\tilde{S}_n$ given in eq. (2.40) and $\nu_\parallel = 0.51\nu_{ei}/\omega_{ci}$, we have the parallel ion equation given by

$$\frac{\mathrm{d}}{\mathrm{d}\tilde{t}}\tilde{\mathbf{u}}_{i\parallel} = -\left(\tilde{\mathbf{u}}_{i\parallel} \cdot \tilde{\nabla}_\parallel\right)\tilde{\mathbf{u}}_{i\parallel} - \tilde{\nabla}_\parallel \varphi - \frac{\nu_\parallel}{\mu}\left(\tilde{\mathbf{u}}_{i\parallel} - \tilde{\mathbf{u}}_{e\parallel}\right) - \frac{\tilde{\mathbf{u}}_{i\parallel}\tilde{S}_n}{\tilde{n}}. \tag{B.7}$$

Bibliography

[1] US EIA. International Energy Outlook 2017. Washington: U. S. Energy Information Administration; 2017.

[2] Pachauri RK, Allen MR, Barros VR, Broome J, Cramer W, Christ R, et al. Climate Change 2014: Synthesis Report. Contribution of Working Groups I, II and III to the Fifth Assessment Report of the Intergovernmental Panel on Climate Change. Pachauri RK, Meyer L, editors. Geneva, Switzerland: IPCC; 2014.

[3] Einstein A. A brief outline of the development of the theory of relativity. Nature. 1921;106(2677):782–784.

[4] Friedberg J. Plasma Physics and Fusion Energy. Cambridge University Press; 2010.

[5] F4E. The Merits of Fusion. Fusion For Energy; 2018. http://fusionforenergy.europa.eu/understandingfusion/merits.aspx, Visited: 2018.08.05.

[6] Bloom EE. The challenge of developing structural materials for fusion power systems. J Nucl Mater. 1998;258:7–17.

[7] McCracken GM, McCracken G, Stott PE. Fusion: the energy of the universe. Academic Press; 2005.

[8] Lawson JD. Some Criteria for a Power Producing Thermonuclear Reactor. Proc Phys Soc, Sec B. 1957;70(1):6.

[9] Wesson J. Tokamaks. 3rd ed. Oxford University Press; 2004.

[10] Haines M. A review of the dense Z-pinch. Plasma Phys Control Fusion. 2011;53(9):093001.

[11] Fowler T, Logan B. The tandem mirror reactor. Comments Plasma Phys Control Fusion. 1977;2(6):167–172.

[12] Spitzer Jr L. The stellarator concept. Phys Fluids. 1958;1(4):253–264.

[13] Clery D. The bizarre reactor that might save nuclear fusion. Science Magazine. 2015;.

[14] Peacock N, Robinson D, Forrest M, Wilcock P, Sannikov V. Measurement of the electron temperature by Thomson scattering in tokamak T3. Nature. 1969;224(5218):488.

[15] EUROfusion; 2011. https://www.euro-fusion.org/news/detail/tokamak-principle/?, Visited: 2018.08.05.

[16] Ongena J, Koch R, Wolf R, Zohm H. Magnetic-confinement fusion. Nature Phys. 2016;12(5):398.

[17] Boedo JA, Rudakov DL, Moyer RA, McKee GR, Colchin RJ, Schaffer MJ, et al. Transport by intermittency in the boundary of the DIII-D tokamak. Phys Plasmas. 2003;10(5):1670–1677.

[18] Zweben S, Boedo J, Grulke O, Hidalgo C, LaBombard B, Maqueda R, et al. Edge turbulence measurements in toroidal fusion devices. Plasma Phys Control Fusion. 2007;49(7):S1.

[19] Naulin V. Turbulent transport and the plasma edge. J Nucl Mater. 2007;363:24–31.

[20] Schuller F. Disruptions in tokamaks. Plasma Phys Control Fusion. 1995;37(11A):A135.

[21] Eich T, Leonard A, Pitts R, Fundamenski W, Goldston R, Gray T, et al. Scaling of the tokamak near the scrape-off layer H-mode power width and implications for ITER. Nucl Fusion. 2013;53(9):093031.

[22] Team AU, Eich T, Sieglin B, Scarabosio A, Fundamenski W, Goldston R, et al. Inter-ELM power decay length for JET and ASDEX Upgrade: measurement and comparison with heuristic drift-based model. Phys Rev Let. 2011;107(21):215001.

[23] CCFE; 2012. http://www.ccfe.ac.uk/images_detail.aspx?id=9, Visited: 2018.08.05.

[24] Madsen J, Naulin V, Nielsen AH, Rasmussen JJ. Collisional transport across the magnetic field in drift-fluid models. Phys Plasmas. 2016;23(3):032306.

[25] Nielsen AH, Rasmussen JJ, Madsen J, Xu G, Naulin V, Olsen JMB, et al. Numerical simulations of blobs with ion dynamics. Plasma Phys Control Fusion. 2017;59(2):025012.

[26] Bellan PM. Fundamentals of Plasma Physics. Cambridge; 2006.

[27] Braginskii SI. Transport Processes in a Plasma. Rev Plasma Phys. 1965;1:205.

[28] Hinton F, Horton Jr C. Amplitude limitation of a collisional drift wave instability. Phys Fluids. 1971;14(1):116–123.

[29] Hazeltine RD, Meiss JD. Plasma confinement. Courier Corporation; 2003.

[30] Kočan M, Gunn J, Pascal J, Bonhomme G, Fenzi C, Gauthier E, et al. Edge ion-to-electron temperature ratio in the Tore Supra tokamak. Plasma Phys Control Fusion. 2008;50(12):125009.

[31] Kočan M, Gennrich F, Kendl A, Müller H, et al. Ion temperature fluctuations in the ASDEX Upgrade scrape-off layer. Plasma Phys Control Fusion. 2012;54(8):085009.

[32] Fernsler R, Slinker S, Joyce G. Quasineutral plasma models. Phys Rev E. 2005;71(2):026401.

[33] Wiesenberger M, Madsen J, Kendl A. Radial convection of finite ion temperature, high amplitude plasma blobs. Phys Plasmas. 2014;21(9):092301.

[34] Held M. Full-F gyro-fluid modelling of the tokamak edge and scrape-off layer [PhD thesis]. University of Innsbruck; 2016.

[35] Dudson BD, Umansky MV, Xu XQ, Snyder PB, Wilson HR. BOUT++: A framework for parallel plasma fluid simulations. Comput Phys Commun. 2009;180(9):1467 – 1480. Available from: http://www.sciencedirect.com/science/article/pii/S0010465509001040.

[36] LeVeque RJ. Finite difference methods for ordinary and partial differential equations: steady-state and time-dependent problems. vol. 98. Siam; 2007.

[37] Levy D, Puppo G, Russo G. On the behavior of the total variation in CWENO methods for conservation laws. Appl Numer Math. 2000;33(1-4):407–414.

[38] Frigo M, Johnson SG. The design and implementation of FFTW3. Proceedings of the IEEE. 2005;93(2):216–231.

[39] Feng C, Ai-Guo X, Guang-Cai Z, Ying-Jun L. Three-Dimensional Lattice Boltzmann Model for High-Speed Compressible Flows. Commun Theor Phys. 2010;54(6):1121. Available from: http://stacks.iop.org/0253-6102/54/i=6/a=28.

[40] Arfken GB, Weber HJ. Mathematical methods for physicists. AAPT; 1999.

[41] Arakawa A. Computational design for long-term numerical integration of the equations of fluid motion: Two-dimensional incompressible flow. Part I. J Comput Phys. 1966;1(1):119–143.

[42] Phillips NA. The general circulation of the atmosphere: A numerical experiment. Q J Roy Meteor Soc. 1956;82(352):123–164.

[43] Byrne GD, Hindmarsh AC. PVODE, an ODE solver for parallel computers. Int J High Perform Comput Appl. 1999;13(4):354–365.

[44] Dudson BD, Allen A, Breyiannis G, Brugger E, Buchanan J, Easy L, et al. BOUT++: Recent and current developments. J Plasma Phys. 2015;81(1):365810104.

[45] Easy L. Three Dimensional Simulations of Scrape-Off Layer Filaments [PhD thesis]. University of York; 2016.

[46] Naulin V, Nielsen AH. Accuracy of spectral and finite difference schemes in 2D advection problems. SIAM J Sci Comput. 2003;25(1):104–126.

[47] Avino F, Fasoli A, Furno I. The new TORPEX in-vessel toroidal conductor for the generation of a poloidal magnetic field. Rev Sci Instrum. 2014;85(3):033506.

[48] Riva F, Colin C, Denis J, Easy L, Furno I, Madsen J, et al. Blob dynamics in the TORPEX experiment: a multi-code validation. Plasma Phys Control Fusion. 2016;58(4):044005.

[49] Olsen JMB. Investigation of coherent structures in magnetically confined plasmas [master thesis]. Technical University of Denmark (DTU); 2015.

[50] Zeiler A, Drake J, Rogers B. Nonlinear reduced Braginskii equations with ion thermal dynamics in toroidal plasma. Phys Plasmas. 1997;4(6):2134–2138.

[51] Easy L, Militello F, Omotani J, Dudson B, Havlíčková E, Tamain P, et al. Three dimensional simulations of plasma filaments in the scrape off layer: A comparison with models of reduced dimensionality. Phys Plasmas. 2014;21(12):122515.

[52] Ricci P, Halpern F, Jolliet S, Loizu J, Mosetto A, Fasoli A, et al. Simulation of plasma turbulence in scrape-off layer conditions: the GBS code, simulation results and code validation. Plasma Phys Control Fusion. 2012;54(12):124047.

[53] Tamain P, Bufferand H, Ciraolo G, Colin C, Ghendrih P, Schwander F, et al. 3D Properties of Edge Turbulent Transport in Full-Torus Simulations and their Impact on Poloidal Asymmetries. Contrib Plasma Phys. 2014;54(4-6):555–559.

[54] Fundamenski W, Garcia OE, Naulin V, Pitts R, Nielsen AH, Rasmussen JJ, et al. Dissipative processes in interchange driven scrape-off layer turbulence. Nucl fusion. 2007;47(5):417.

[55] Furno I, Theiler C, Chabloz V, Fasoli A, Loizu J. Pre-sheath density drop induced by ion-neutral friction along plasma blobs and implications for blob velocities. Phys Plasmas. 2014;21(1):012305.

[56] Militello F, Walkden N, Farley T, Gracias W, Olsen J, Riva F, et al. Multi-code analysis of scrape-off layer filament dynamics in MAST. Plasma Phys Control Fusion. 2016;58(10):105002.

[57] Allan S, Elmore S, Fishpool G, Dudson B, Team M, Team EM, et al. Ion temperature measurements of L-mode filaments in MAST by retarding field energy analyser. Plasma Phys Control Fusion. 2016;58(4):045014.

[58] Walkden N, Easy L, Militello F, Omotani J. Dynamics of 3D isolated thermal filaments. Plasma Phys Control Fusion. 2016;58(11):115010.

[59] Mosetto A, Halpern FD, Jolliet S, Loizu J, Ricci P. Finite ion temperature effects on scrape-off layer turbulence. Phys Plasmas. 2015;22(1):012308.

[60] Kube R, Garcia OE. Velocity scaling for filament motion in scrape-off layer plasmas. Phys Plasmas. 2011;18(10):102314.

[61] Madsen J, Garcia OE, Stærk Larsen J, Naulin V, Nielsen AH, Rasmussen JJ. The influence of finite Larmor radius effects on the radial interchange motions of plasma filaments. Phys Plasmas. 2011;18(11):112504.

[62] Rudakov D, Boedo J, Moyer R, Krasheninnikov S, Leonard A, Mahdavi M, et al. Fluctuation-driven transport in the DIII-D boundary. Plasma Phys Control Fusion. 2002;44(6):717.

[63] Rudakov D, Boedo J, Moyer R, Stangeby PC, Watkins J, Whyte D, et al. Far SOL transport and main wall plasma interaction in DIII-D. Nucl Fusion. 2005;45(12):1589.

[64] Olsen J, Madsen J, Nielsen AH, Rasmussen JJ, Naulin V. Temperature dynamics and velocity scaling laws for interchange driven, warm ion plasma filaments. Plasma Phys Control Fusion. 2016;58(4):044011.

[65] Held M, Wiesenberger M, Madsen J, Kendl A. The influence of temperature dynamics and dynamic finite ion Larmor radius effects on seeded high amplitude plasma blobs. Nucl Fusion. 2016;56(12):126005.

[66] Garcia O, Bian N, Naulin V, Nielsen A, Rasmussen JJ. Mechanism and scaling for convection of isolated structures in nonuniformly magnetized plasmas. Phys Plasmas. 2005;12(9):090701.

[67] Manz P, Carralero D, Birkenmeier G, Müller H, Müller S, Fuchert G, et al. Filament velocity scaling laws for warm ions. Phys Plasmas. 2013;20(10):102307.

[68] Easy L, Militello F, Omotani J, Dudson B, Havlíčková E, Tamain P, et al. Three dimensional simulations of plasma filaments in the scrape off layer: A comparison with models of reduced dimensionality. Phys Plasmas. 2014;21(12):122515.

[69] Løiten M. Global numerical modeling of magnetized plasma in a linear device [PhD thesis]. Technical University of Denmark; 2017.

[70] Oberkampf WL, Roy CJ. Verification and validation in scientific computing. Cambridge University Press; 2010.

[71] Salari K, Knupp P. Code verification by the method of manufactured solutions. Sandia National Labs., Albuquerque, NM (US); Sandia National Labs., Livermore, CA (US); 2000.

[72] Wiesenberger M. Gyrofluid computations of filament dynamics in tokamak scrape-off layers [PhD thesis]. University of Innsbruck; 2014.

[73] Meyer OHH, Kendl A. Isotope effect on filament dynamics in fusion edge plasmas. Plasma Phys Control Fusion. 2017;59(6):065001.

[74] Angus JR, Umansky MV, Krasheninnikov SI. Effect of drift waves on plasma blob dynamics. Phys Rev Lett. 2012;108(21):215002.

[75] Halpern FD, Cardellini A, Ricci P, Jolliet S, Loizu J, Mosetto A. Three-dimensional simulations of blob dynamics in a simple magnetized torus. Phys Plasmas. 2014;21(2):022305.

[76] Sieglin B, Eich T, Faitsch M, Herrmann A, Scarabosio A, et al. Investigation of scrape-off layer and divertor heat transport in ASDEX Upgrade L-mode. Plasma Phys Control Fusion. 2016;58(5):055015.

[77] Smolyakov A. Gyroviscous forces in a collisionless plasma with temperature gradients. Can J Phys. 1998;76(4):321.

[78] Hazeltine RD, Meiss JD. Shear-Alfvén dynamics of toroidally confined plasmas. Phys Rep. 1985;121(1-2):1–164.